Mass distribution in galaxy clusters: strong lensing and dynamical mass analysis

Mauricio Carrasco

Instituto de Astrofísica, Facultad de Física
Pontificia Universidad Católica de Chile

Institut für Theoretische Astrophysik
Zentrum für Astronomie der Universität Heidelberg

Santiago – Heidelberg 2014

Dissertation

submitted to the
Instituto de Astrofísica, Facultad de Física
Pontificia Universidad Católica de Chile, Chile
for the degree of
Doctor in Astrophysics

submitted to the
Combined Faculties for the Natural Sciences and for Mathematics
of the Ruperto-Carola University of Heidelberg, Germany
for the degree of
Doctor of Natural Sciences

presented by

Mauricio Carrasco
Born in Santiago, Chile

Oral examination: July 23^{rd} 2014

Mass distribution in galaxy clusters: strong lensing and dynamical mass analysis

Referees: Prof. Dr. L. Felipe Barrientos
Prof. Dr. Matthias Bartelmann

Abstract.
In this thesis we study the total mass distribution in galaxy cluster through detailed analysis of strong gravitational lensing (SL) signatures and dynamical mass information. We perform FORS2/VLT spectroscopic observations for a sample of 29 new SL selected galaxy clusters from the RCSGA survey. Our spectroscopic analysis reveals 51 lensed galaxies that correspond to 34 background sources. From the redshift measurements we derive 689 cluster members, which are used to compute velocity dispersion and dynamical masses resulting in a mass range of $0.28 \leq M_{200}/10^{14}h^{-1}M_{\odot} \leq 28.4$. We use these results to derive robust mass measurements of our 29 clusters by combining SL constraints with dynamical masses. We combine the best-fitting model parameters from 27 of these clusters with the recent analysis of 19 X-ray selected clusters from the CLASH survey, and also with concentration parameter measurements from 27 SL selected clusters from the SGAS survey. This leads us to the largest robust dataset of concentration parameters for a controlled sample of 73 galaxy clusters. We find that for massive clusters ($M_{200} \sim 8 \times 10^{14}h^{-1}M_{\odot}$), the concentration parameters are distributed around $c_{200} = 4.3 \pm 1.4$, which is consistent with theoretical expectations within the intrinsic scatter. In contrast, for less massive clusters ($M_{200} \sim 10^{14}h^{-1}M_{\odot}$), the concentrations are on average almost twice the mean expected value, even if the selection bias and projection effects are taken into account, resulting in a $c-M$ relation with a strong dependence on the cluster mass, $c \propto M^{\alpha}$, where $\alpha = -0.52 \pm 0.09$. We find that this steep mass slope is mainly due to 6 RCSGA clusters and ~ 16 clusters from the SGAS survey that are clearly describing a higher and steeper $c-M$ relation with $c_n = 8.9 \pm 1.12$ and $\alpha = -0.69 \pm 0.09$. This unusual relation is far from any theoretical expectation suggesting a bimodality in the $c-M$ relation. The rest of the sample is characterized by a mass slope of $\alpha = -0.24 \pm 0.11$, reconciling simulation results with observations. We also develop the first algorithm able to automatically find multiple-image systems in galaxy clusters.

Zusammenfassung.
In dieser Dissertation untersuchen wir die gesamte Massenverteilung in Galaxienhaufen anhand einer detaillierten Analyse der Auswirkungen des starken Gravitationslinseneffekts (strong lensing, SL) und anhand dynamischer Information über die Masse. Wir führen spektroskopische Beobachtungen mit FORS2/VLT von 29 Galaxienhaufen durch, die aufgrund ihrer SL-Eigenschaften aus der RCSGA-Durchmusterung ausgewählt wurden. Unsere spektroskopische Analyse deckt 51 Galaxienbilder auf, die durch den Gravitationslinseneffekt aus 34 Hintergrundgalaxien erzeugt werden. Anhand der Rotverschiebungsmessungen identifizieren wir 689 Haufenmitglieder, die wir verwenden, um Geschwindigkeitsdispersionen und dynamische Massen im Bereich von $0.28 \leq M_{200}/10^{14}$ $h^{-1}M_{\odot} \leq 28.4$ zu bestimmen. Diese Ergebnisse verwenden wir, um durch Kombination der dynamischen Messungen mit SL-Daten zuverlässige Massenwerte unserer 29 Galaxienhaufen zu bestimmen. Wir kombinieren die optimal angepassten Modellparameter von 27 dieser Haufen mit der jüngsten Analyse von 19 Galaxienhaufen, die aufgrund ihrer Röntgenemission in die Clash-Durchmusterung aufgenommen wurden. Ferner kombinieren wir sie mit den Messungen der Konzentrationsparameter von 27 Galaxienhaufen, die anhand ihrer SL-Effekte aus der SGAS-Durchmusterung ausgewählt wurden. Dies führt uns zum bisher größten Datensatz robuster Messungen des Konzentrationsparameters einer kontrollierten Stichprobe von 73 Galaxienhaufen. Wir finden, dass massereiche Galaxienhaufen ($M_{200} \approx 8 \times 10^{14}\, h^{-1}M_{\odot}$) Konzentrationsparameter von $c_{200} = 4.3 \pm 1.4$ aufweisen, was innerhalb der intrinsischen Streuung mit theoretischen Erwartungen verträglich ist. Demgegenüber sind die Konzentrationen weniger massereicher Haufen ($M_{200} \approx 10^{14}\, h^{-1}M_{\odot}$) im Mittel fast doppelt so groß wie die erwarteten Werte, selbst wenn Auswahl- und Projektionseffekte berücksichtigt werden. Dies ergibt eine c-M-Beziehung, die stark von der Haufenmasse abhängt, $c \propto M^{\alpha=0.52}$. Wir finden, dass diese steile Abhängigkeit von der Masse hauptsächlich von sechs Galaxienhaufen aus der RCSGA-Durchmusterung herrührt und dass ≈ 16 Galaxienhaufen aus der SGAS-Durchmusterung deutlich eine höhere und steilere c-M-Beziehung mit $c_n = 8.9 \pm 1.12$ und $\alpha = -0.69 \pm 0.09$ aufweisen. Diese ungewöhnliche Beziehung liegt weit ab von der theoretischen Erwartung und legt eine bimodale c-M-Relation nahe. Der Rest der Stichprobe ist durch einen Exponenten von $\alpha = -0.24 \pm 0.11$ gekennzeichnet, der im Einklang mit Simulationsergebnissen steht. Außerdem stellen wir den ersten Algorithmus vor, der Systeme von Mehrfachbildern in Galaxienhaufen auf automatische Weise findet.

para mi esposa y mi familia.

Acknowledgements

During the course of my PhD, many different people have supported me in one way or another and, here, I have the opportunity to acknowledge them.

First of all, I would like to thank my supervisors, Prof. Felipe Barrientos and Prof. Matthias Bartelmann, for their continuous encouragement and support. They have taught me many things, not only specific scientific topics but also a more general idea of how to conduct the research; they have taught me how to find a research theme, how to manage a collaboration well, how to conquer difficulties, and how to advertise my research. The scientific topics might become out-of-fashion some day, but such a general idea will continue to be useful throughout my life. In addition, they were always concerned about me and my future, and also about the financial support when it was needed. They have helped me to determine the course to be taken. I am sincerely grateful for their support. Thanks.

I also want to express my gratitude to my ESO supervisor, Dr. Michael West, for believing in me when I was just starting my PhD and for having accepted me as a student at ESO. He always had kind words of support and enthusiasm, even if my research was not moving as fast as we expected at the beginning. I am indebted with him for his kindness. Thanks Mike for everything! During my stay at ESO I met nice friends and colleagues that helped me grow as a scientist and person, thanks to everyone there.

Furthermore, I would like to thank Prof. Leopoldo Infante for providing me the opportunity to work with him in one of the most interesting and revolutionary science projects as is the CLASH survey, and also for being part of my examination committee. I have also to say that thanks to him and Prof. Thomas Puzia, I could obtain the Santiago-Heidelberg Doctoral Exchange Fellowship for a double degree ex-change program between the Heidelberg University and the Pontificia Universidad Católica de Chile, under the supervisions of Prof. Felipe Barrientos and Prof. Matthias Bartelmann.

I would also like to thank Prof. Michael Gladders and Prof. Marco Aurelio Díaz for kindly agreeing to form part of my examination committee.

My PhD could not have been possible without the financial and scientific support provided by the *Programa de Mejoramiento de la Calidad y Equidad de la Educación* (MECESUP program), the ESO studentship, the Santiago-Heidelberg Doctoral Exchange Fellowship by DAA, the *Proyecto Financiamiento* BASAL PFB06, and by FONDECYT under the project No. 1120676.

I would like to thank Timo Anguita for his consistent guidance, friendship and understanding. He has been an important support in many levels during my doctoral studies, with priceless help and advice in both scientific and practical issues. He has always been available to patiently answer the many questions I have had during these years. The results that I have gotten in my PhD would not be possible without his help. Thanks Timo.

I was lucky enough to have an opportunity to work with Adi Zitrin on lensing field. This changed my research life drastically. He was and he is a pillar in my researches. He taught me many things about sciences, life, and about how enjoy science and life.

This thesis could not have taken place without the tremendous help of you, my friends. I would like to thank Mauricio Ortiz, Daniela Carrasco, Fabrizio Arrigoni, Agnese Fabris, Paulina Céspedes, Eduardo Bañados, Nicolas Viaux, Elena Manjavacas, Eleonora Sarli, Matteo Maturi, Cristina García, Cristóbal Sifón, Juan Carlos Beamin, Jorge González, Gustavo Morales, and Nestor Espinoza for their friendship and scientific feedback. Thanks for everything. I would like to make a special recognition to some friends working at IA, ESO, ITA, and Heidelberg University, who helped me to solve many issues I have had during my PhD and who have supported me selflessly, many thanks to Giselle Ulloa, Juan Véliz, Mariela Villanueva, Carmen Gloria Cordovez, Mauricio Bars, Paulina Jiron, Teresita, Anna Zacheus, and Elisabeth Miller.

My family, both blood related and life acquired, have been the vital importance during these years. Thus, I want to thank Maylinh, Olga, Juan Luis, Lorena, Marcelo, Pedro, Sergio, Nora, Martina e Isabela. Thanks for sharing your lives with me. A special acknowledgement must go to my parents Efraín Carrasco and Rosa Venegas: all of the accomplishments in my life have been possible through the world of possibilities, love and understanding they have constantly provided for all my life.

Finally, I want to reserve this whole paragraph to tell Kathy, my wife, that nothing would have been possible without your support and love. You are the engine pushing me towards my most important goals. I am immensely thankful to have met you.

Contents

Chapter 1

Introduction

1.1 Introduction

The fascination with the cosmos has been present since the origins of human reasoning and over time it has turned into one of the most important disciplines of modern science. The main goal of modern cosmology is to address some very basic questions, regarding the composition of our Universe, its origin, evolution and eventual fate. During the past decades, enormous progress has been made towards this direction by the improvements in observational techniques as well as the development of new physical theories. Resulting in a standard cosmological model, according to which the Universe is, on large scales, homogeneous and isotropic and geometrically flat, with structures (like stars, galaxies, clusters of galaxies) generated by the growth of small primordial fluctuations through gravitational instability. In the standard scenario the Universe is mainly composed by the so-called dark energy, responsible for the observed accelerated expansion, and by non baryonic dark matter.

Even though this model is well supported by several independent cosmological observations, such as distant type-Ia supernovae, galaxy clusters, large-scale structure, big bang nucleosynthesis, and its most representative observation: the Cosmic Microwave Background (CMB) anisotropies, there are still important issues that can not be explained. Our Universe seems to be composed in great majority by unknown dark components. In fact, the ordinary matter we know accounts for only $\sim 4\%$ of the total density. The rest of the density is represented by dark energy ($\sim 70\%$) and dark matter ($\sim 26\%$), two components whose nature has not been determined yet. Over the next decades one of the main goals of cosmology will be, therefore, to unveil the nature of these dark components.

In this thesis we concentrate our attention on dark matter, whose composition is still very controversial. We specifically focus our research on the determination of how this unseen component is distributed on different scales. We carry out our investigation by studying galaxy clusters, since these objects are the largest gravitationally bound structures in our universe and their total mass consists for $\sim 80\%$ of pure dark matter, making them unique laboratories for our purposes.

Although, the main problem of studying dark matter in galaxy clusters lies in the fact that it is dark!, i.e. it cannot be observed by usual methods, nevertheless, there are different ways to probe the total mass distribution of galaxy clusters, such as X-ray profiles, dynamical mass and gravitational lensing. In particular, gravitational lensing is the only method that can directly probe dark matter without making any assumption about the composition, distribution or dynamical state of the underlying cluster mass.

The gravitational lensing phenomenon, described by General Relativity Theory, predicts that gravitational fields around massive objects, such as galaxies and galaxy clusters, distort space-time and curve the light rays passing through them. Gravitational lensing is the most robust way to probe the dark matter distribution because the light deflection is independent of the nature of the matter and of its state – lensing is equally sensitive to dark and luminous matter, as well as to matter in equilibrium or far out of it. Lensing effects can appear in different forms. Close to the center of galaxy clusters, the mass density can be high enough to noticeably modify the shape of background galaxies, producing giant elongated arcs or even multiple images of the background sources, this is the so-called strong lensing (SL) regime. Instead, in the outer regions of the clusters, the light deflection produces only tiny distortions that cannot be observed on single images, therefore statistical measurements of several of these distortions become necessary to reconstruct the mass of the cluster, this is the weak lensing (WL) regime. Since strong and weak lensing probe mass distributions at different radii, the combination of these two phenomena is an indispensable tool for cosmology to fully probe the dark matter distribution at two decades of radius.

The dynamics of galaxy clusters is another powerful method to determine the total mass of galaxy clusters through the measurement of the velocity dispersion of the cluster members, although it relies on equilibrium assumptions that could bias the conclusions. Nevertheless, it has been shown that dynamical masses are good tracers of the total mass of galaxy clusters, on the same level of other methods, such as the weak lensing approach. Therefore, the combination of velocity dispersion of the cluster members and strong gravitational signatures in the innermost region of the clusters becomes a powerful tool towards a complete understanding of the total mass distribution and density profile of galaxy clusters, providing important tests to the standard cosmological model.

In this thesis we focus our attention on the analysis of the underlying mass distribution of galaxy clusters, in order to put constraints on the understanding of the dark matter component of the Universe. This analysis is conducted via reconstructions of the mass distribution of the clusters, using an innovative technique which consists in combining strong lensing constraints, such as giant arcs and multiple-image systems, and dynamical information of the cluster members. Resulting in robust measurements of intrinsic properties of the galaxy clusters, such as their halo concentrations and density profiles.

The thesis is organized as follows. In chapter 2, we introduce the theoretical and observational framework which represents the starting point of this thesis. In particular, we place galaxy clusters into the cosmological picture, highlighting the currently accepted large scale structure scenario and describing how the mass of clusters is used as cosmological probe, as well as we introduce the basic concepts of gravitational lensing that will be used throughout the thesis. In chapter 3, we describe our strong lens modeling methodology and we introduce our innovative technique to probe mass distributions at larger radii by including dynamical information. In chapter 4, we present a new sample of 29 strong lensing selected clusters from the Red-sequence Cluster Survey Giant Arc (RCSGA) and we describe their spectroscopic features as well as their dynamical properties. In chapter 5, we review the results of the previous 29 clusters through their concentration−mass relation. In this chapter we also introduce the largest robust dataset of 73 concentration parameters for a controlled sample of galaxy clusters and we derive the most complete analysis of the concentration−mass relation hitherto. In chapter 6, we describe the strong lensing models for 7 clusters from the Cluster Lensing and Supernova survey with Hubble (CLASH) and we present the candidate for the most distant galaxy known to date. In chapter 7, we present the first automated Multiple-Image Finder ALgorithm (MIFAL) for strong-lens modeling. Finally, in chapter 8, we recapitulate the work presented in this manuscript as well as offer a scientific outlook.

Chapter 2

Theoretical and observational background

In this section, we review some of the fundamental cosmological concepts, as well as the basic aspects of gravitational lensing, that provides the basis of this thesis and that will be relevant for the subsequent discussions. Most of the concepts on this section are based on the work presented in Schneider et al. (1992), Pee (1994), Hogg (1999), Oguri (2004), Anguita (2009), and Falco (2013).

2.1 Cosmology

According to the current cosmological model, our Universe originated from a singularity in the space-time that began to expand about 13.7 billion years ago, the so-called "Big Bang". In this earliest phase the Universe was incredibly dense and hot and it was expanding and cooling very rapidly.

It is believed that around $10^{-35}s$ the Universe undergoes a spectacular acceleration known as inflation. When inflation stops, the Universe consists of a plasma of quark-gluon and other elementary particles. Particles and anti-particles are constantly being created and annihilated.

At some point an unknown process called baryogenesis violates the conservation of baryon number, leading to the a predominance of matter over anti-matter.

At about 3 minutes after the Big Bang, the drop in temperature due to the expansion allows the formation of the first elements (mostly hydrogen and helium), but most protons remain uncombined.

Only $\sim$ 379000 years later electrons and nuclei are able to combine into atoms, we are at the recombination. The drop of free electrons drastically decreases the possibility of Compton scattering for photons, which, therefore, decouple from matter and start traveling freely through space. This relic radiation is still detectable today and it is known as the Cosmic Microwave Background (CMB).

At this point, baryons, no longer impeded by the radiation pressure of the photons, are able to collapse in the potential wells previously created by the dark matter. In fact, since dark matter does not interact with photons, it is not affected by the radiation pressure and consequently it has started to collapse much before the recombination epoch. After recombination the Universe becomes neutral and enters a period of time called "The Dark Ages": there are no sources of light, apart from the emission of the 21-cm wavelength line of neutral hydrogen.

Meanwhile structure formation proceeds. Larger and larger structures are formed by gravitational collapse and merging of smaller objects. Eventually the first stars and galaxies form, they re-ionize the Universe and render it bright as it appears today.

2.1.1 The cosmic expansion and Hubble law

One of the most relevant discoveries in the history of cosmology has been the expansion of the Universe. This implies that all the objects appear to recede from the Earth and from each other with a recession velocity higher at higher distances.

The first observational evidence of the expansion of the Universe was made by Edwin Hubble in 1929 (Hubble, 1929). He described this phenomenon by a very simple equation, today known as the Hubble law. If galaxies are moving away from us, the light coming from a galaxy arrives with a wavelength larger than the one originally emitted. We define the redshift z of a galaxy as

$$z = \frac{\lambda_{obs}}{\lambda_{emi}} - 1, \tag{2.1}$$

where λ_{obs} corresponds to the observed wavelength and λ_{emi} is the wavelength at the time of emission. The redshift corresponds to a recession velocity v, which, for nearby objects, is given by a simple Doppler formula $v = cz$.

Hubble discovered that the recession velocity of the galaxies v is linearly correlated with their distance d from us, this being true at any distance (Hubble, 1929). The Hubble's

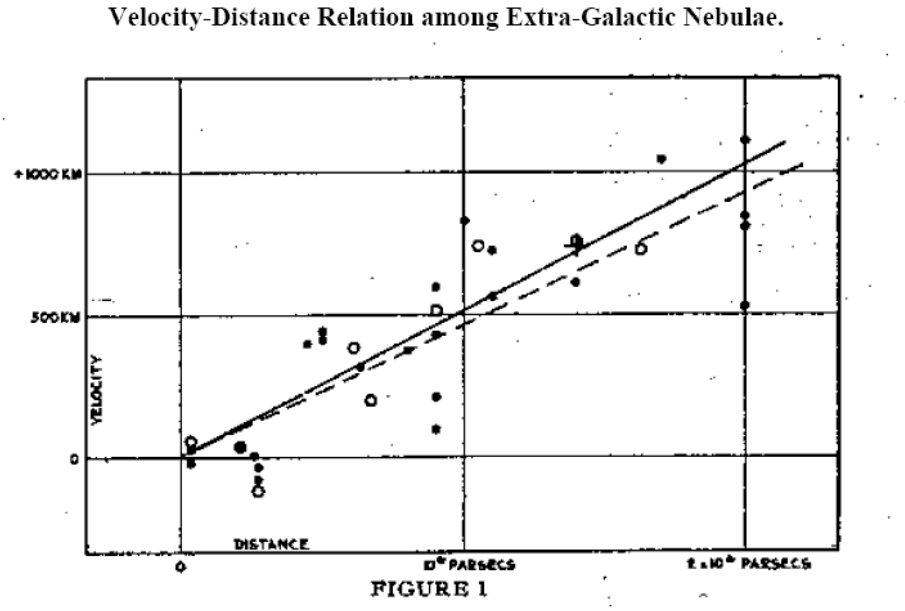

FIGURE 2.1: Original Hubble diagram from Hubble (1929).

law can be expressed in this way:

$$v = cz = H_0 d. \tag{2.2}$$

where the proportionality constant H_0 is called the Hubble constant and it quantifies the expansion rate of the Universe at the current time. A measurement of the Hubble constant requires the knowledge of both the distance of an object and its velocity, which is obtained through its redshift. One of the common methods is to use Type Ia Supernovae (SNeIa), since they are standard candles, i.e. sources with the same known luminosity. Fig. 2.1 shows the original Hubble diagram found in 1929, with an extremely high H_0. Current detailed observations suggest a lower value for the Hubble constant. It is convention to parametrize the Hubble constant in this way:

$$H_0 = 100\ h\ kms^{-1}Mpc^{-1}. \tag{2.3}$$

Current measurements of the WMPA (Spergel et al., 2007), gives $h = 0.7 \pm 0.022$, although, the recent Planck mission finds a significantly lower value of $h = 0.67 \pm 0.014$ (Planck Collaboration et al., 2013).

As we will describe below, at high redshifts, the luminosity distance departs from the linear Hubble law and shows that the Universe expansion is accelerating.

2.1.2 Fridmann-Robertson-Walker metric and expansion equations

The equations that govern the accelerating expansion of the Universe are derived by introducing a metric, which describes the space-time, and by using the formalism of General Relativity.

The Cosmological Principle states that the Universe around us, when averaged over sufficiently large angles and scales, is homogeneous and isotropic. This assertion was originally assumed and subsequently confirmed by observations for the very large scale of the Universe. Assuming homogeneity and isotropy, the unique form of the line element obeys the Friedmann-Robertson-Walker (FRW) metric and it is given by:

$$ds^2 = c^2dt^2 - a^2(t)\left(\frac{dr^2}{1-kr^2} + r^2(d\theta^2 + sin^2\theta d\phi^2)\right), \tag{2.4}$$

where ds is the line element, $[t, r, \theta, \phi]$ are the co-moving polar coordinates, c is the speed of light and $a(t)$ is a cosmological scale factor. The parameter k determines the curvature of the Universe and can assume different values: $k = 0$ corresponds to a flat space, $k = 1$ corresponds to a closed space, with finite volume and no boundary, and $k = -1$ corresponds to an open, infinite space.

Considering a light ray which travels along null geodesics (i.e., $ds = 0$) and taking a radial path (motivated by the radial expansion of the universe), Eq. 2.4 results in:

$$\frac{c\,dt}{a(t)} = \frac{dr}{\sqrt{1-kr^2}}. \tag{2.5}$$

By integrating the right side of Eq. 2.5 between an emission time t_e and an observed time t_o and equating to the same integral between $t_e + \delta t_e$ and $t_o + \delta t_o$ we obtain:

$$\int_{t_e}^{t_o} \frac{dt}{a(t)} = \int_{t_e+\delta t_e}^{t_o+\delta t_o} \frac{dt}{a(t)}, \tag{2.6}$$

if one assumes that the variation $\delta t \ll a(t)/\dot{a}(t)$, it results in:

$$\frac{a(t_o)}{a(t_e)} = \frac{\delta t_o}{\delta t_e} = \frac{\nu_e}{\nu_o}, \tag{2.7}$$

by replacing ν by the wavelength $\lambda = c/\nu$, we can relate the scale factor $a(t)$ with the cosmological redshift by:

$$\frac{a(t_o)}{a(t_e)} = \frac{\lambda_o}{\lambda_e} = 1 + z. \tag{2.8}$$

The General Relativity Theory uses 10 field equations to describe gravitational force through descriptions of the curvature of space-time caused by matter and energy. They have the form:

$$R_{\mu\nu} - \frac{1}{2} g_{\mu\nu} R + \Lambda g_{\mu\nu} = \frac{8\pi G}{c^4} T_{\mu\nu} \tag{2.9}$$

where the field curvature (composed by the Ricci tensor: $R_{\mu\nu}$, and Ricci curvature: $R = R_{\mu\nu} R^{\mu\nu}$) is related to the flux and density of energy and momentum (stress-energy tensor: $T_{\mu\nu}$). The metric is describe by $g_{\mu\nu}$ and Λ is the cosmological constant.

By inserting the FRW metric (Eq. 2.4) into the General Relativity, one can obtain two fundamental equations, called the expansion equations, and defined by:

- The Friedmann equation

$$H^2 \equiv \left(\frac{\dot{a}}{a}\right)^2 = \frac{8\pi G}{3}\rho - \frac{kc^2}{a^2} + \frac{\Lambda c^2}{3} \tag{2.10}$$

- The fluid equation

$$\dot{H} + H^2 = \frac{\ddot{a}}{a} = -\frac{4\pi G}{3}\left(\rho + \frac{3P}{c^2}\right) + \frac{\Lambda c^2}{3}, \tag{2.11}$$

where the quantities ρ and P are the total energy density and the pressure of the Universe. Furthermore, we have here introduced the Hubble parameter $H(t)$, which gives a measure of the expansion rate at the time t.

From observations we know that there are different components contributing to the energy density and pressure of the Universe, the terms ρ and P in equations 2.10 and 2.11 refer then to the sum of all the contributions from these various components. For each component the energy density evolves differently over time, reaching different values at the present time. In the next section, we will show how the Universe is described in terms of cosmological density parameters related to the different components.

2.1.3 Multi-component Universe

The total density of the Universe is composed by ordinary matter, dark matter and radiation. Moreover, in order to explain the accelerating expansion of the Universe, a fluid with negative pressure has been introduced as one of the species in the present

Universe, the so-called dark energy. This new component is associated to a non-null cosmological constant Λ and is defined by:

$$\rho_\Lambda = \frac{\Lambda c^2}{8\pi G} \tag{2.12}$$

Therefore, the total density of the Universe is given by:

$$\rho_{total} = \rho_M + \rho_r + \rho_\Lambda \tag{2.13}$$

where ρ_M and ρ_r corresponds to the density of the total matter and radiation, respectively.

The abundance of each density component can be expressed by the dimensionless parameter

$$\Omega_i = \frac{\rho_i}{\rho_{crit}} \tag{2.14}$$

with the critical density ρ_{crit} being the present energy density of a flat Universe:

$$\rho_{crit} = \frac{3H^2}{8\pi G} \tag{2.15}$$

We can derive the three dimensionless component parameters by multiplying the Eq. 2.10 with $(a/\dot{a})^2 = 1/H^2$ and writing it at the present time (t_0), we get:

$$\left(\frac{\Lambda c^2}{3H_0^2}\right) + \left(-\frac{kc^2}{a_0^2 H_0^2}\right) + \left(\frac{8\pi G}{3H_0^2}\rho_0\right) = 1, \tag{2.16}$$

where we can identify the cosmological constant parameter, the curvature parameter, and the matter and radiation parameters with these terms:

$$\Omega_\Lambda = \frac{\Lambda c^2}{3H_0^2}, \quad \Omega_k = -\frac{kc^2}{a_0^2 H_0^2}, \quad \Omega_M = \frac{8\pi G\rho_M}{3H_0^2}, \quad \text{and} \quad \Omega_r = \frac{8\pi G\rho_r}{3H_0^2}, \tag{2.17}$$

respectively. Therefore, we can rewrite Eq. 2.16 using the dimensionless parameters, by:

$$\Omega = \Omega_\Lambda + \Omega_M + \Omega_r = 1 - \Omega_k. \tag{2.18}$$

With the total sum of Ω determining the curvature of the Universe. If $\Omega > 1$, the curvature parameter k is greater than zero, resulting in a Universe with positive curvature. If $\Omega < 1$, then $k < 0$, corresponding to a negative curvature. A critical value is then obtained when $\Omega = 0$, which is the case of flat Universe, $k = 0$.

Moreover, the energy densities of the each component evolve with the pressure P according to the equation of state $\rho = wP$. The dimensionless parameter w depends on the corresponding component and, depending on this, it may vary with time. For constant w, plugging the equation of state into the fluid equation, one can obtain the energy density as a function of the scale factor:

$$\rho = \rho_0 a^{-3(1+w)}, \tag{2.19}$$

with $w = 0$ for non-relativistic particles, both dark matter and baryons. For radiation (relativistic matter), we have $w = +1/3$. An accelerating Universe requires a component with negative pressure, therefore, it needs $w < -1/3$. In the particular case in which the acceleration of the Universe is explained by the presence of vacuum energy by the cosmological constant, we have $w = -1$.

In order to determine how the individual components evolve we combine Eqs. 2.18 and 2.19, obtaining:

$$a(t) \propto t^{2/3(1+w)}, \tag{2.20}$$

for constant w.

Fig. 2.2 shows the evolution of the radiation, matter, and dark energy densities with redshift. In the early hot Universe ($z > 3000$), the radiation dominates and the Universe expands as $a(t) \propto t^{1/2}$. At redshifts in the interval $3000 > z > 0.5$, the Universe is dominated by matter and expands as $a(t) \propto t^{2/3}$. Finally, in the recent Universe ($z < 0.5$) the dark energy dominates and the Universe expands exponentially: $a(t) \propto exp(Ht)$.

To better understand the effect of the components on the expansion of the Universe, the deceleration parameter $q(z)$ has been introduced and defined as:

$$q(t) = -\frac{\ddot{a}a}{\dot{a}^2} \tag{2.21}$$

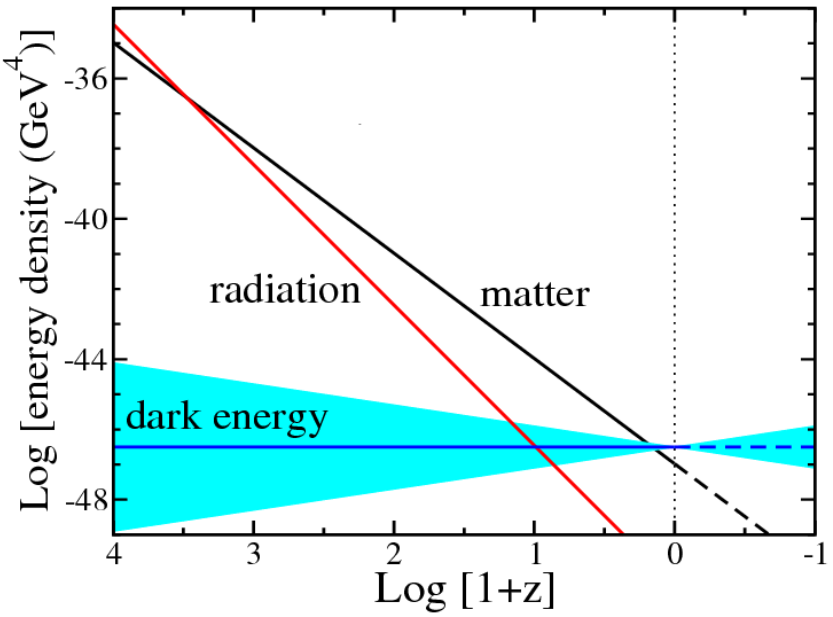

FIGURE 2.2: Evolution of the density of radiation, matter, and dark energy with redshift (Frieman and Dark Energy Survey Collaboration, 2013).

During the matter and radiation dominated eras, gravity slows the expansion, and thus $q > 0$ and $\ddot{a} < 0$. During the vacuum energy dominated era, the Universe starts to accelerate, given by $q < 0$ and $\ddot{a} > 0$.

Furthermore, in order to directly constrain the density components of the Universe with observables, we combine the FRW equations together with the expression for redshift derived in Eq. 2.8. In this way, one can provide a parametrization of the Hubble parameter $H(t) = \dot{a}(t)/a(t)$ in terms of the redshift z (Pee, 1994) as:

$$H(z)^2 = H_0^2 \left[\Omega_r(1+z)^4 + \Omega_M(1+z)^3 + \Omega_k(1+z)^2 + \Omega_\Lambda\right] . \tag{2.22}$$

Using this function we can parametrize, not only the Hubble parameter, but also the FRW equations and the metric as a function of the cosmological redshift z, a directly observable quantity.

2.1.4 Cosmological distances

Defining a metric in the spacetime allows us to locally define the distance between two events in the spacetime. In an Euclidean spacetime the concept of "distance" between two events is independent on the observable used to evaluate it. If the spacetime is not

Euclidean this is not true anymore and the distance between two events is no longer uniquely defined. This means, for example, that the distance calculated measuring the flux emitted by a source of known luminosity, has not the same value of the distances calculated from the ratio between the source's actual size and the angular size of the source as viewed from earth. In particular, distances will depend on the expansion rate of the universe and on its curvature. We give here a summary of the most used distance definitions utilized in cosmology.

Proper distance: This is the distance that the light covers to go from a source at z_2 to the observer at z_1, with $z_1 < z_2$:

$$D_p(z_1, z_2) = c \int_{a(z_1)}^{a(z_2)} \frac{da}{\dot{a}} = \frac{a}{H_0} \int_{a(z_1)}^{a(z_2)} \frac{da}{aE(a)} \tag{2.23}$$

Co-moving distance: This is the distance measured by an observer which is co-moving with the cosmic flow. The fact that it is measured in co-moving coordinates, implies that the distance traveled by the light ray needs to be scaled by the cosmological scale parameter $a(t)$:

$$D_c(z_1, z_2) = c \int_{a(z_1)}^{a(z_2)} \frac{da}{a\dot{a}} = \frac{a}{H_0} \int_{a(z_1)}^{a(z_2)} \frac{da}{a^2 E(a)} = \int_{z_1}^{z_2} \frac{cdz}{H(z_2)} \tag{2.24}$$

Angular diameter distance: This distance is defined as the ratio between the physical size of an object at redshift z and the angular size it displays at the current cosmological time:

$$D_A(z_1, z_2) = \frac{D_c(z_1, z_2)}{1 + z_2} = \frac{c}{1 + z_2} \int_{z_1}^{z_2} \frac{dz}{H(z_2)}. \tag{2.25}$$

The factor $(1 + z)$ makes $D_A(z)$ the only cosmological distance that does not grow indefinitely with redshift. This distance peaks around $z \simeq 1$ (depending on the choice of cosmological parameters). Consequently objects, at redshifts higher than the redshift where the angular diameter distance peaks, appear on the sky larger compared to objects of equivalent size at smaller redshifts.

Luminosity distance: This distance relates the intrinsic luminosity of an object with its observed flux. It is defined as:

$$D_L(z_1, z_2) = \sqrt{\frac{L}{4\pi F}}, \tag{2.26}$$

where L is the bolometric luminosity and F is the observed flux of an object. Luminosity distance is related to the co-moving and angular diameter distances in the following way:

$$D_L(z_1, z_2) = D_c(z_1, z_2)(1 + z_2) = D_A(z_1, z_2)(1 + z_2)^2 \tag{2.27}$$

2.1.5 The matter density parameter

The matter density parameter Ω_M was found to be close to $\Omega_M \sim 0.3$ by independent methods, such as gravitational lensing statistics (Chae et al., 2002), type-Ia supernovae (Riess et al., 2004), the galaxy power spectrum, and also by galaxy cluster studies. Allen (2002) derived Ω_M using the redshift evolution of cluster gas-mass fraction, finding $\Omega_M = 0.30^{+0.04}_{-0.03}$, in excellent agreement with SN and lensing statistics. Furthermore, CMB anisotropies can also constrain this parameter, by $\Omega_M h^2$. Spergel et al. (2003) constrained $\Omega_M = 0.29 \pm 0.07$ assuming $h \simeq 0.7$.

Even though we can measure Ω_M precisely, there are strong observational evidences that suggest that most of the matter in the Universe is unknown. Indeed, the ordinary matter we know accounts for only $\sim 4\%$ of the total Ω_M. The remaining matter is known as dark matter, since it does not emit/absorb light and can be detected only through its gravitational effects.

One of the main goals of this thesis is the study of the mass distribution of galaxy clusters. We are, therefore, interested in the properties of the total matter density, not only the visible one. Below, we will review in detail for which reasons dark matter has been proposed and how it has been investigated in the last years, as well as how it can be analyzed in the future.

2.1.5.1 Dark matter evidence

Dark matter was first proposed by Zwicky (1933) through an analysis of the mass of the Coma cluster from the peculiar velocities of the galaxies in the cluster. He found that the mass is about 400 times larger than the mass estimated by adding up all of the galaxy masses obtained from their luminosities. But only after the 1970's, this idea began to be considered more seriously. Rubin and Ford (1970) found that the velocities of the ionized clouds in the Andromeda galaxy do not decrease with increasing distance from the center and proposed as possible explanation the presence of extra mass in the outer part of the galaxy; Rubin et al. (1985) confirmed that this phenomenon is commonly seen in spiral galaxies; Ostriker and Peebles (1973) pointed out that the spherical halo

component is needed to stabilize the flatten disk galaxy. With all this new observational information, people had to pay more attention to this idea of dark matter.

Another proof for the existence of dark matter can be found through detailed analysis of the CMB anisotropies by combining the results from baryon matter density $\Omega_b h^2$ and the total matter parameter $\Omega_M h^2$. The former can be strongly constrained by the relative peak heights of the odd peaks respect to the even ones. While $\Omega_M h^2$ is sensitive to the amount of boost of the angular power spectrum around the first peak, which is caused by the potential decay during radiation dominated era (early integrated Sachs-Wolfe effect). The detailed angular power spectrum measurements by WMAP revealed that $\Omega_M h^2$ is about six times larger than $\Omega_b h^2$ (Spergel et al., 2003). This clearly indicates that most of the matter in the universe should be non-baryonic and dark.

The most significant evidence for dark matter comes from observations of cluster of galaxies. Due to their X-ray luminosity, the mass of the clusters can be estimated under the assumption of hydrodynamic equilibrium, which turns out to be much larger than the mass of the visible matter (i.e., gas + stars). Indeed, White et al. (1993) found that the fraction of the visible mass in Coma cluster compare to the total one is $M_b/Mt \simeq 0.01 \pm 0.05 h^{-3/2}$, implying that galaxy clusters must be dominated by invisible dark matter.

Now, the most direct evidence is offered by gravitational lensing phenomenon, because gravitational light deflection is independent of the nature of the matter and of its state – lensing is sensitive to the total matter, dark and luminous matter, and matter in equilibrium or far out of it. Squires et al. (1996) estimated an upper bound for the fraction of the gas mass to the total one, $M_{gas}/M_t < 0.04 \pm 0.02h$, using weak lensing method.

Dark matter candidates can be classified according to their collisionless damping (free streaming) scales. If we regard massive neutrinos ($m_\mu \geq 10eV$) as dominant component of dark matter, then they were relativistic until the horizon scale of ∼Mpc; therefore fluctuations below ∼Mpc were smoothed out due to their relativistic motions. Such dark matter is called hot dark matter (HDM). On the other hand, one can consider a possibility of very massive dark matter so that it became non-relativistic long time ago, a time when collisionless damping scale were much smaller than important scales for structure formation. This is called cold dark matter (CDM). There is also a possibility of warm dark matter (WDM) which has collisionless damping scale of ∼kpc. The difference between these dark matter models becomes evident in their power spectra. Now observations support the cold dark matter model. Fig. 2.3 shows the comparison of observed power spectrum with cold dark matter predictions. They are in good agreement

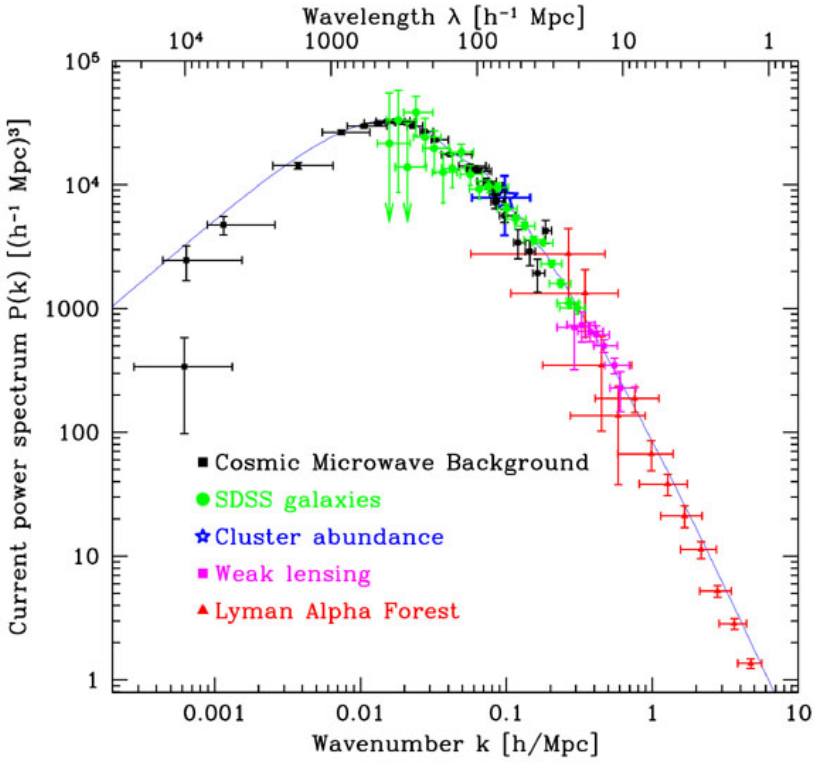

FIGURE 2.3: Comparison of several measurements on the power spectrum. The black solid line corresponds to the CDM prediction with $\Omega_M = 0.28$, $h = 0.72$, and $\Omega_b/\Omega_M = 0.16$. This Figure is taken from Tegmark et al. (2004).

at ≥Mpc scales. Therefore, now it is believed that most of dark matter is non-baryonic and cold.

The determination of the distribution and the amount of dark matter in the Universe has received significant attention in the recent years, representing one the most fundamental aspect of cosmology. As noted earlier, in this thesis we would like to perform a detailed analysis of the mass distribution in galaxy clusters, and therefore, contributing to the understanding of Dark Matter in the Universe.

2.1.6 The flat ΛCDM model

As mentioned earlier, the evolution of our universe is governed by the Friedmann and fluid equations (Eqs. 2.10 and 2.11 respectively). In this cosmological framework, the most fundamental parameters are the curvature and the density content of the Universe. Surprisingly, the current observations support a flat Universe, mainly dominated by unknown dark components; dark energy and cold dark matter. The observations support $\Omega_M \simeq 0.3$ and $\Omega_\Lambda \simeq 0.7$, which can be seen in the Fig. 2.4. This concordance model

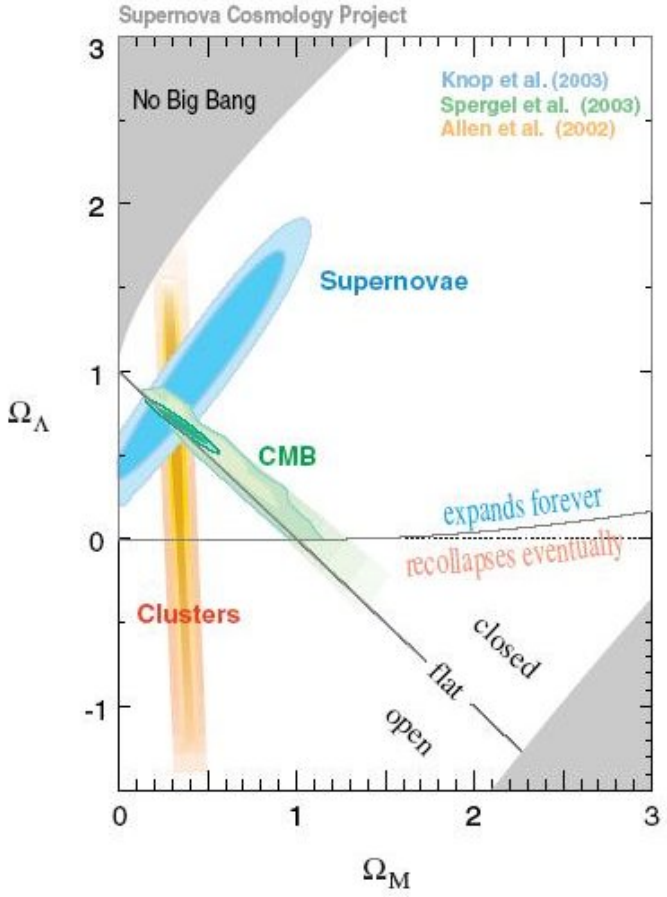

FIGURE 2.4: This figure shows three independent constraints on cosmological parameters projected in the $\Omega_\Lambda - \Omega_M$ plane. The CMB is constraints from CMB anisotropy observed by WMAP Spergel et al. (2003). Supernovae shows the results of type-Ia supernovae observations by Knop et al. (2003). Finally, the X-ray measurements of distant clusters (Allen, 2002) are denoted by Cluster. It is surprising that these three independent observations are well explained by a model with $\Omega_M \simeq 0.3$ and $\Omega_\Lambda \simeq 0.7$. This Figure is taken from http://www-supernova.lbl.gov/

is commonly called as the flat ΛCDM model. Its main features can be summarized as follows:

- The Universe is homogeneous and isotropic and governed by the General Relativity.
- The Universe is composed by baryons, dark matter, and dark energy, and it is flat. We also assume the densities of radiation components of photons and neutrinos as inferred from the CMB temperature and as calculated from the standard thermal history. We assume the three massless species of neutrinos.
- We assume that the adiabatic primordial fluctuations obey the Gaussian statistics. The primordial power spectrum can be described by a power law, $P_i(k) \propto k^{n_s}$.
- Dark matter is cold.

- We assume that the cosmological constant Λ describes the dark energy component, i.e., $w = -1$

All the work performed in this thesis is based on this concordance model: a flat ΛCDM cosmological framework, with $\Omega_M = 1 - \Omega_\Lambda = 0.3$ and $H_0 = 100h$ km s^{-1} Mpc^{-1}, with $h = 0 - 1.0$.

Furthermore, the cluster virial radius at redshift z is defined as the radius that encloses an average over density Δ_c times the critical density, $\rho_c(z)$, with:

$$\Delta_c = 18\pi^2 + 82(\Omega_m(z) - 1) - 39(\Omega_m(z) - 1)^2, \tag{2.28}$$

based on spherical collapse theory (Bryan and Norman, 1998) in a flat ΛCDM universe, where $\Omega_m(z)$ is defined as:

$$\Omega_m(z) = \frac{\Omega_m(1+z)^3}{\Omega_m(1+z)^3 + \Omega_\Lambda}, \tag{2.29}$$

and

$$\rho_c(z) = \frac{3H(z)}{8\pi G}, \tag{2.30}$$

In this thesis we denote the concentration parameter, virial radius and mass by c_{vir}, r_{vir}, and M_{vir} when using the theoretical value of Δ_c (equation 2.28), while by c_{200}, r_{200}, and M_{200}, respectively, when fixing Δ_c to 200, to compare with previous observational works and simulations.

2.2 Gravitational lensing

We review in this section the basic concepts of the gravitational lensing theory, which are indispensable for the complete understanding of this thesis.

As mentioned before, massive objects in the universe can act as lenses, distorting the images of distant sources. This phenomenon, which is explained by the General Relativity Theory, exists on a wide range of scales. From small compact objects in the halo of the Milky Way, to galaxy clusters, which represent the most powerful lenses in the universe, modifying the shape of distant galaxies and forming giant arcs as well as small arclets, which are the main topic of this work.

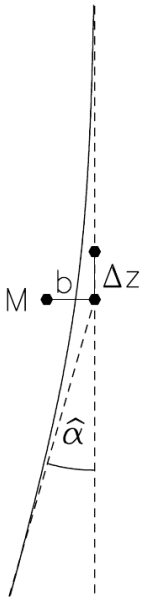

FIGURE 2.5: Deflection of a light ray by a point mass M. The light ray, which has an impact parameter b (b=ξ), is bent by the angle $\tilde{\alpha}$ (Figure from Narayan and Bartelmann 1996).

Although photons propagate along null geodesics of the space-time, as described by the General Relativity, in most of the astrophysically relevant situations a much simpler approximated description of light by means of light rays is enough. In particular, this is sufficient to properly describe the lensing phenomena produced by galaxy clusters, which will be discussed in the following chapters. For a more detailed and rigorous treatment, we refer the reader to the book by Schneider et al. (1992) and to the reviews by Narayan and Bartelmann (1996) and by Bartelmann and Schneider (2001).

2.2.1 The deflection angle

Consider first the deflection of a light ray by the exterior part of a spherically symmetric mass M, with the ray impact parameter ξ much larger than the Schwarzchild radius, $\xi \gg R_s \equiv 2GMc^{-2}$, then General Relativity predicts that the deflection angle $\tilde{\alpha}$ is:

$$\tilde{\alpha} = \frac{4GM}{c^2 \xi} \tag{2.31}$$

We now consider more realistic lens models, i.e. three dimensional distributions of matter with volume density $\rho(\boldsymbol{r})$, which can be divided into cells of size dV and mass $dm = \rho(\boldsymbol{r})dV$. We consider that the light ray passes this mass distribution and we

describe its spatial trajectory by (ξ_1, ξ_2, r_3), where the coordinates are chosen such that the incoming light ray propagates along r_3.

Now, when the physical size of the lens is much smaller than the distances between observer, lens and source and so the deflection arises along a very short section of the light path, we can consider the *thin screen approximation* (Fig. 2.6), Within this approximation, the lensing matter distribution is fully described by its surface density, given by:

$$\Sigma(\boldsymbol{\xi}) = \int dr_3 \; \rho(\xi_1, \xi_2, r_3) \tag{2.32}$$

where $\boldsymbol{\xi}$ is a two-dimensional vector on the lens plane.

As long as the thin screen approximation holds, the total deflection angle is obtained by summing the contribution of all the mass elements $\Sigma(\boldsymbol{\xi})d\boldsymbol{\xi}$, described by:

$$\tilde{\boldsymbol{\alpha}}(\boldsymbol{\xi}) = \frac{4G}{c^2} \int d^2\xi' \; \Sigma(\boldsymbol{\xi}') \; \frac{\boldsymbol{\xi} - \boldsymbol{\xi}'}{|\boldsymbol{\xi} - \boldsymbol{\xi}'|^2} \tag{2.33}$$

This condition is satisfied in virtually all astrophysically relevant situations, i.e., lensing by galaxies and galaxy clusters, unless the deflecting mass extends all the way from the source to the observer, which is the instance for some cases in WL.

2.2.2 The lens equation

In Fig. 2.6 we show the sketch of a typical gravitational lens system. The lens of mass distribution $\Sigma(\boldsymbol{\xi}')$ is located at redshift z_l, corresponding to an angular diameter distance D_l. This lens deflects the light rays coming from a source at redshift z_s, which corresponds to an angular distance D_s.

From the geometry of Fig. 2.6, one can derive the next relations (assuming $sin\tilde{\alpha} \approx \tilde{\alpha} \approx tan\tilde{\alpha}$, with $\tilde{\alpha} \ll 1$):

$$\boldsymbol{\eta} = D_s \boldsymbol{\beta}, \tag{2.34}$$

$$\boldsymbol{\xi} = D_l \boldsymbol{\theta}, \tag{2.35}$$

It can also be seen:

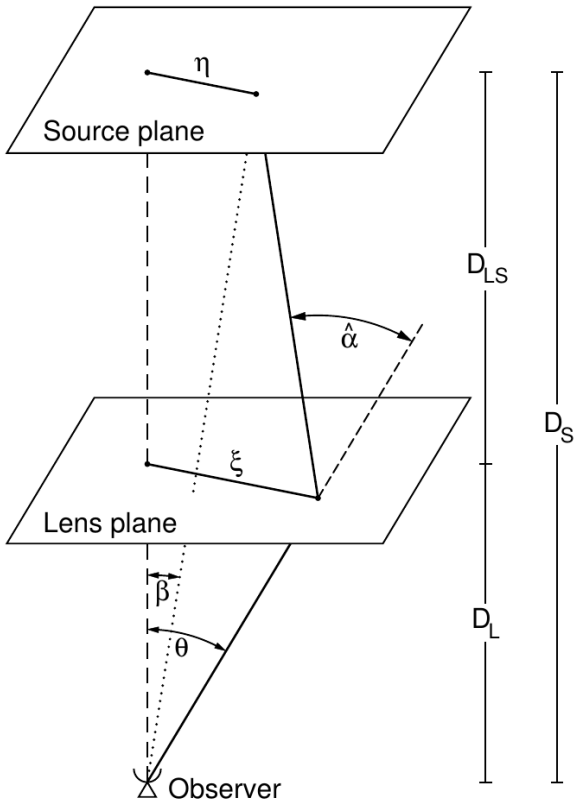

FIGURE 2.6: Sketch of a typical gravitational lensing system (Figure from Bartelmann and Schneider 2001).

$$\boldsymbol{\eta} = \frac{D_s}{D_l}\boldsymbol{\xi} - D_{ls}\tilde{\boldsymbol{\alpha}}(\boldsymbol{\xi}), \tag{2.36}$$

where D_{ls} corresponds to the angular distance between the lens and the source. Now combining the Eqs. 2.34, 2.35, and 2.36, one can derive the well known *lens equation*:

$$\boldsymbol{\beta} = \boldsymbol{\theta} - \boldsymbol{\alpha}(\boldsymbol{\theta}), \tag{2.37}$$

with

$$\boldsymbol{\alpha}(\boldsymbol{\theta}) \equiv \frac{D_{ls}}{D_s}\tilde{\boldsymbol{\alpha}}(D_l\boldsymbol{\theta}), \tag{2.38}$$

where we have defined the *scaled deflection angle* $\boldsymbol{\alpha(\theta)}$ in the last step. The *lens equation* describes the deviation $\boldsymbol{\alpha(\theta)}$ of the deflected light rays passing through the gravitational potential, which appear at the angular position $\boldsymbol{\theta} = (\theta_1, \theta_2)$ in the image plane, while originally come from an angular position in the source plane $\boldsymbol{\beta} = (\beta_1, \beta_2)$.

The *lens equation* can have more than one solution for a source at the fixed position $\boldsymbol{\beta} = (\beta_1, \beta_2)$, therefore, it source can have multiple images on the sky. When this happens, the lens is considered *strong*. Now, we can express the scaled deflection angle in terms of the surface mass density $\Sigma(\boldsymbol{\xi})$ as:

$$\alpha(\boldsymbol{\theta}) = \frac{1}{\pi} \int_{\mathbb{R}^2} d^2\theta' \, \kappa(\boldsymbol{\theta}') \, \frac{\boldsymbol{\theta} - \boldsymbol{\theta}'}{|\boldsymbol{\theta} - \boldsymbol{\theta}'|^2}, \tag{2.39}$$

where we have defined the *dimensionless surface mass density* or *convergence* $\kappa(\boldsymbol{\theta})$:

$$\kappa(\boldsymbol{\theta}) = \frac{\Sigma(\boldsymbol{\xi} = D_l\boldsymbol{\theta})}{\Sigma_{cr}} \qquad \text{with} \qquad \Sigma_{cr} = \frac{c^2}{4\pi G} \frac{D_s}{D_l D_{ls}}, \tag{2.40}$$

where Σ_{cr} is called the *critical surface density*. It is a function of the angular diameter distances of lens and source and therefore depends on their redshifts. A mass distribution which has $\kappa > 1$ somewhere, i.e. its surface density exceeds the critical value at some position, produces multiple images for some source position $\boldsymbol{\beta} = (\beta_1, \beta_2)$ (Schneider et al., 1992). Hence the critical surface density is a characteristic value of the surface density for discriminating between the strong and weak lensing regimes. The condition $\kappa > 1$ is only sufficient but not necessary for having multiple images: particular lenses may be strong even if their surface density never surpasses Σ_{cr}. Furthermore, since the lens equation (2.37) describes a mapping from the lens plane to the source plane $\boldsymbol{\theta} \to \boldsymbol{\beta}$, by solving this equation we can determine the projected mass distribution of the lens $\Sigma(D_l\boldsymbol{\theta})$. As the number of the images $\boldsymbol{\theta}$ for a given source $\boldsymbol{\beta}$ is not known a priori, the inversion of the lens equation is non-trivial in general, but it can be numerically solved and one can derive the mass distribution assuming some simple density profiles (as done in the case of parametric models).

2.2.3 Lensing potential

An extended distribution of matter is characterized by its effective lensing potential, obtained by projecting the three-dimensional Newtonian potential on the lens plane and by properly rescaling it:

$$\psi(\boldsymbol{\theta}) = \frac{D_{ls}}{D_l D_s} \frac{2}{c^2} \int_{\mathbb{R}^2} dr \; \Phi(D_l\boldsymbol{\theta}, r_3). \tag{2.41}$$

Using the identity $\boldsymbol{\nabla} \ln |\boldsymbol{\theta}| = \boldsymbol{\theta}/|\boldsymbol{\theta}|^2$, which is valid for any two-dimensional vector $\boldsymbol{\theta}$, we can rewrite the scaled deflection angle in terms of the effective lensing potential,

$$\psi(\boldsymbol{\theta}) = \frac{1}{\pi}\int_{\mathbb{R}^2} d^2\theta' \kappa(\boldsymbol{\theta'}) ln|\boldsymbol{\theta} - \boldsymbol{\theta'}|, \tag{2.42}$$

as

$$\boldsymbol{\alpha}(\boldsymbol{\theta}) = \boldsymbol{\nabla}\psi(\boldsymbol{\theta}), \tag{2.43}$$

2.2.4 Magnification and distortion

One of the main features of gravitational lensing is the magnification and distortion of the flux and shape of the sources, respectively. This is particularly evident when the source has no negligible apparent size. For example, background galaxies can appear as very long arcs in galaxy clusters.

The distortion arises because light bundles are deflected differentially. Ideally the shape of the images can be determined by solving the lens equation for all the points within the extended source. In particular, if the source is much smaller than the angular size on which the physical properties of the lens change, the relation between source and image positions can be linearized locally. In other words, the distortion of images can be described by the Jacobian matrix:

$$A(\boldsymbol{\theta}) = \frac{\partial \boldsymbol{\beta}}{\partial \boldsymbol{\theta}} = \left(\delta_{ij} - \frac{\partial^2\psi(\boldsymbol{\theta})}{\partial\theta_i\partial\theta_j}\right) = \begin{pmatrix} 1-\kappa-\gamma_1 & -\gamma_2 \\ -\gamma_2 & 1-\kappa+\gamma_1 \end{pmatrix}, \tag{2.44}$$

where we have introduced the components of the *shear* $\gamma \equiv \gamma_1 + \mathrm{i}\gamma_2 = |\gamma|e^{2i\varphi}$, with

$$\gamma_1 = \frac{1}{2}\left(\frac{\partial^2\psi(\boldsymbol{\theta})}{\partial^2\theta_1} - \frac{\partial^2\psi(\boldsymbol{\theta})}{\partial^2\theta_2}\right) = \gamma(\boldsymbol{\theta}) cos(2\varphi), \tag{2.45}$$

$$\gamma_2 = \frac{\partial^2\psi(\boldsymbol{\theta})}{\partial\theta_2\partial\theta_2} = \gamma(\boldsymbol{\theta}) sin(2\varphi), \tag{2.46}$$

and κ is related to ψ through the Poisson equation $\nabla^2\psi = 2\kappa$. By using the previous Eqs., the magnification matrix becomes

$$A(\boldsymbol{\theta}) = (1-\kappa)\begin{pmatrix} 1 & 0 \\ 0 & 1 \end{pmatrix} - \gamma\begin{pmatrix} cos(2\varphi) & sin(2\varphi) \\ sin(2\varphi) & -cos(2\varphi) \end{pmatrix}. \tag{2.47}$$

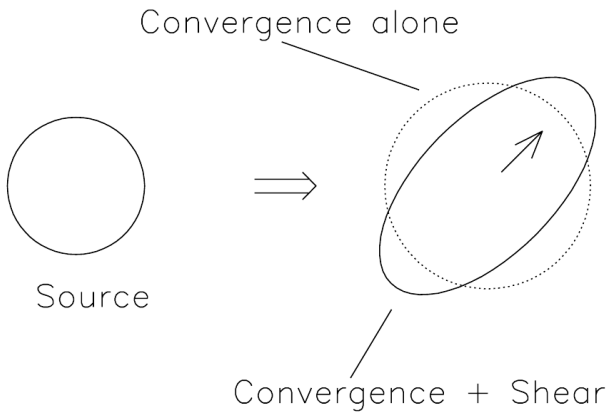

FIGURE 2.7: Distortion effects due to convergence and shear on a circular source (Figure from Narayan and Bartelmann 1996).

The last equation explains the meaning of both convergence and shear. The distortion induced by the convergence is isotropic, i.e. the images are only rescaled by a constant factor in all directions. On the other hand, the shear stretches the intrinsic shape of the source along one privileged direction. For this reason, a circular source like the one shown in Fig. 2.7 is mapped into an elongated image when κ and γ are both non-zero.

An important consequence of the lensing distortion is the magnification. Because of the Liouville theorem and the absence of emission and absorption of photons in gravitational light deflection, the conservation of the source surface brightness is ensured. This means that the change of the solid angle under which the source is seen implies that the flux received from a source will be magnified (or demagnified).

Given the magnification matrix (Eq. 2.44), the magnification is quantified by the inverse of the determinant of the Jacobian matrix. For this reason, the matrix $M(\boldsymbol{\theta}) = A^{-1}$ is called the magnification tensor, given by:

$$\mu \equiv detM = \frac{1}{detA} = \frac{1}{(1-\kappa)^2 - \gamma^2}. \tag{2.48}$$

The eigenvalues of the magnification tensor measure the amplification in the tangential and in the radial direction, given by:

$$\mu_t = \frac{1}{\lambda_t} = \frac{1}{1-\kappa-\gamma}. \tag{2.49}$$

$$\mu_r = \frac{1}{\lambda_r} = \frac{1}{1-\kappa+\gamma}. \tag{2.50}$$

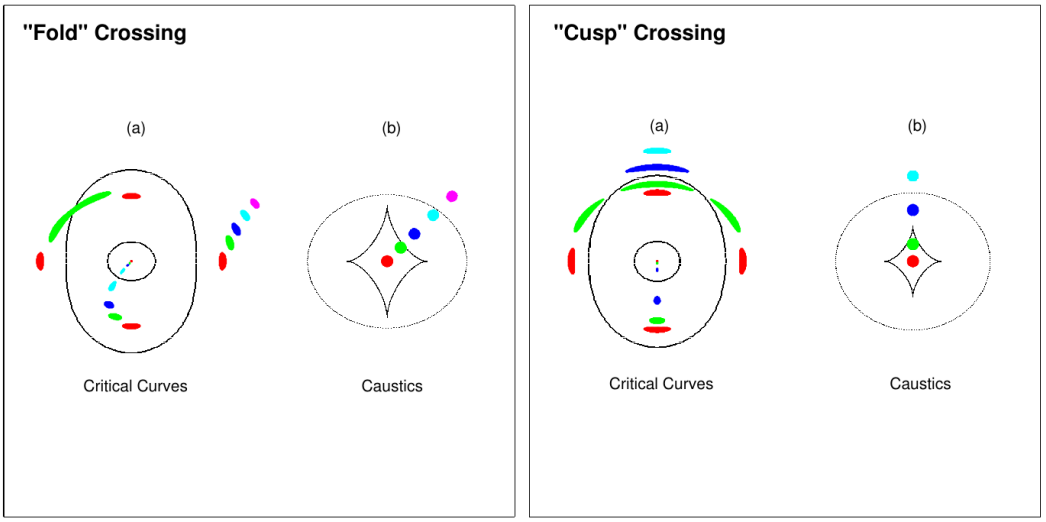

FIGURE 2.8: This figure shows the image (a) and source (b) positions with respect to critical curves (a) and caustics (b) curves. The left panel shows a fold caustic crossing configuration, while the right panel shows a cusp crossing configuration. The colored circles in panels (b) display the different source positions with respect to the caustics. These map to the distorted colored shapes in panels (a) shown with respect to the critical curves. Figure taken from Narayan and Bartelmann (1996).

The magnification is theoretically infinite where $\lambda_t = 0$ and where $\lambda_r = 0$. These two conditions define two curves in the lens plane, called the tangential and the radial critical curves, respectively. Images forming along the tangential critical line are strongly distorted tangentially to this line. On the other hand, images forming close to the radial critical curve are stretched in the direction perpendicular to the curve itself. When mapped to the source plane, these curves are called "caustic lines" or simply "caustics". Caustics can show more complicated patterns that intersect, but remain closed curves.

Fig. 2.8 shows critical curves (a: lens plane) and caustic lines (b: source plane) for an elliptical gravitational lens. A source at different positions with respect to the caustic lines maps to different image configurations in the lens plane. When the source is inside the area between the two caustic lines (e.g, blue spots in the figure), two images are mapped to the lens plane: one outside both critical curves and one between them. When the source is enclosed by both caustic curves, four images of the source are mapped (e.g., red spots in the figure): two outside the critical curves and two between them. If the source lies outside both caustic curves, there is no image splitting (e.g., pink spot in the figure).

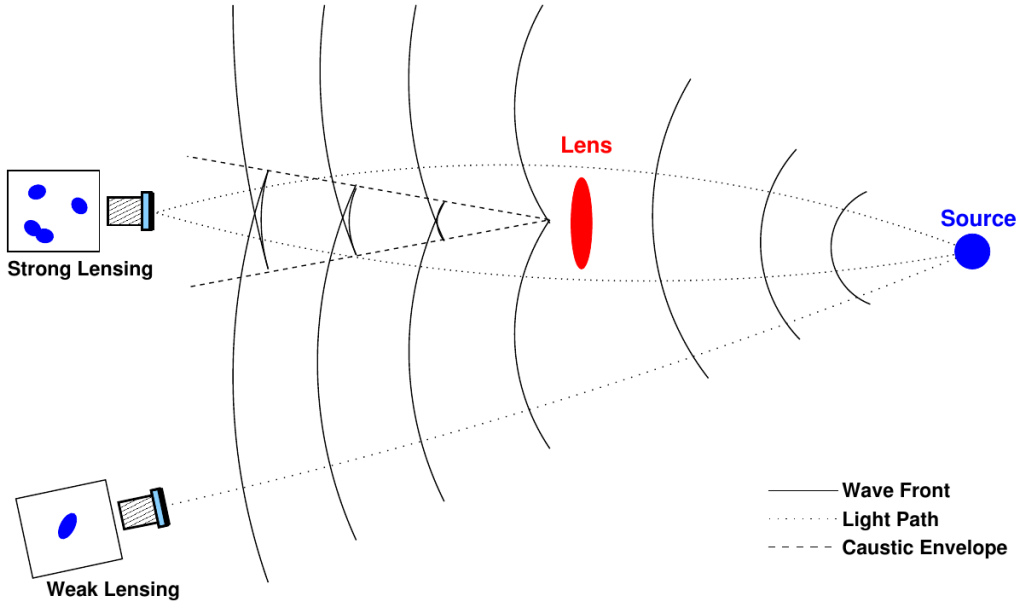

FIGURE 2.9: Strong and weak lensing regimes. The source wavefront is distorted by a lensing potential of the massive object. The caustic envelope indicates the region where image splitting can be seen (strong lensing). This image was taken from Anguita (2009).

2.2.5 Gravitational lensing regimes

In gravitational lensing we can distinguish two different regimes: strong and weak. The former is produced close to the centers of clusters, where mass density can be high enough to noticeably modify the shape of background galaxies, producing giant elongated arcs or even multiple images of the background sources (e.g. Bartelmann 2010; Kneib and Natarajan 2011, for reviews). The second regime is produced in the outer regions of the clusters, where the light deflection produces only tiny distortions that cannot be observed on single images, therefore statistical measurements of several of these distortions become necessary to reconstruct the mass of the cluster.

2.2.5.1 Strong lensing

Strong lensing arises when the surface mass density of the lens is larger than the Σ_{crit} together with an alignment (or vicinity) between the source and the optical axis of the lens. This case corresponds in Fig. 2.8 to the position of the source, in the source plane, inside the caustic lines, producing multiplicity of images and mirror inversion of images located at saddle points. In general, strong lensing refers to lensing systems in which the lens is a galaxy or galaxy cluster, and the source is a background galaxy or quasar.

Due to the (small) projected velocities of galaxies and galaxy clusters with respect to background sources, strong lensing is a static phenomenon in human time scales.

Strong lensing observables are the positions/orientation and brightnesses of the lensed images. Being a static phenomenon, the intrinsic brightness of the source is unobservable. Thus, individual brightnesses of lensed images do not give any information about the lensing system. However, the ratio between the brightnesses of multiple images does, as it corresponds to the ratio between the magnifications produced by the lensing potential.

Strong lensing effects in clusters show up in the form of giant luminous arcs, strongly distorted arclets and multiple images of background galaxies. Since strong lensing only occurs in the central part of the clusters, it can be used only to probe their inner mass distribution. However, strong lensing yields by far the most accurate central mass determinations in those cases where several strong lensing features can be identified. Therefore, strong lensing is the best cosmological tool to probe the total matter in the core of the galaxy clusters, making it ideal for our purpose.

Furthermore, clusters do act as a "natural telescope"; many of the most distant galaxies have been found by searching behind clusters, taking advantage of the lensing magnification. In the next chapters, we will present detailed analysis of the central mass distribution of galaxy clusters, as well as, a briefly description of how strong lensing help to find the most distant objects in the Universe hitherto, one found at $z \sim 9.6$ behind the CLASH cluster MACSJ1149+22 (Zheng et al., 2012) , and the other at $z \sim 11$ behind the CLASH cluster MACSJ0647.7+7015 (Coe et al., 2013).

2.2.5.2 Weak lensing

Weak lensing corresponds to the case where the light deflection produces only tiny distortions that cannot be observed on single images. In Fig. 2.9, it corresponds to sources that are outside of the caustic lines. There is a rather smooth transition between weak and strong lensing, where these sheared images begin to form arcs around the lens. Nonetheless, in the general weak lensing case, the background sources are sheared only by a few percent. If the original shape of a weakly lensed galaxy was known, the deformation induced by weak lensing could suffice to deduce the properties of the lens. However, the main problem weak lensing has to face is the fact that an exact knowledge of the intrinsic shape of distorted background galaxies does not exist. To get around this issue, massive clusters are observed at large scales and it is assumed that the distribution of the background galaxies is random. This fact compensates for the lack of knowledge of their exact shape and can constrain the mass distribution of the galaxy cluster with

high C.L. For a review of weak lensing and its applications see Bartelmann and Schneider (2001).

2.2.6 Strong lens modeling

The lens modeling refers to the modeling of the mass distribution (or effective lensing potential) of the lens, required to produce such a configuration of observational signatures, as image positions and brightnesses of the background sources. The lens equation (Eq. 2.37) describes the mapping from $\boldsymbol{\theta} \rightarrow \boldsymbol{\beta}$, that is from the lens plane to the source plane; for a given position $\boldsymbol{\theta}$ in the image plane and for a given mass distribution $\Sigma(\boldsymbol{\theta})$, we can easily calculate the source position $\boldsymbol{\beta}$. The problem arises when we want to do the mapping in the other way around, i.e., the inversion of the lens equation. Since the mapping $\boldsymbol{\theta} \rightarrow \boldsymbol{\beta}$ is not linear, finding all the image positions $\boldsymbol{\theta}$ for a given source position $\boldsymbol{\beta}$ is analytically possible only for some very simple mass models. As the number of the images $\boldsymbol{\theta}$ for a given source $\boldsymbol{\beta}$ is not known a priori, the inversion of the lens equation is non-trivial in general, but it can be numerically solved using sophisticated methods, which are described belows.

There are two ways by which the modeling of a mass potential can be accomplished: by performing a "parametric" or a "non-parametric" mass model.

2.2.6.1 Non-parametric lens modeling

In the so-called "non-parametric" methods the mass distribution or lens potential is reconstructed as a map defined on a grid of pixels. They have been initially developed to constrain the mass distribution of galaxy-scale lenses (Abdelsalam et al., 1998; Saha and Williams, 1997), at the beginning the purpose was to probe the large diversity of possible mass models with a view in particular at the modeling degeneracy present in the measurement of the Hubble constant. Since 1997, non-parametric modeling has been intensively tested and greatly improved to overcome the lack of constraints very common in strong lensing (e.g. Diego et al., 2005; Kochanek, 1996; Koopmans, 2005). However, the flexibility of these methods arising from their very large number of parameters has to be controlled to avoid over-fitting the data. Recent work on regularization techniques (Bradač et al., 2005; Coe et al., 2008; Merten et al., 2009; Suyu et al., 2006) has improved the situation in this regard somewhat. However, physical understanding often comes from the measurement of quantities such as total mass, profile slope, and so on, which still have to be extracted from the flexible reconstructed maps.

The most successful non-parametric approaches to mass modeling are: the multipole expansion method (e.g. Kochanek, 1991; Trotter et al., 2000) and the pixelization method (e.g. Abdelsalam et al., 1998; Diego et al., 2005; Saha and Williams, 1997). The multipole expansion method, as the name suggests, is a Taylor expansion of the lens potential. On the other hand, the pixelization method makes no strong assumptions on the mass density profile. In this case, the mass producing the deflection is defined on a grid of pixels. PIXELENS (Saha and Williams, 1997, 2004) is the most widely used code in this sub-class.

2.2.6.2 Parametric lens modeling

"Parametric" lens modeling techniques requires a parametric description of the potential. Therefore, these kinds of models have two advantages: the assumption of a physical model leads to inferences that are directly related to physical quantities and the model fits the data with relatively few free parameters compared to a "non-parametric" model. The basic philosophy in this technique is the following: first, a physically motivated mass profile for the lens, like the Pseudo Isothermal Elliptical Mass Distribution (PIEMD: Kassiola and Kovner, 1993) or the Navarro, Frenk and White profile (NFW: Navarro et al., 1997), is chosen. Then, the parameters of the chosen profile are modified (and subsequently the lensing potential) many times, until the observed images are reproduced. The parameters corresponding to the best-fit are then used to construct the mass distribution of the lens.

This technique requires a relatively good knowledge on what the system is composed of and it is therefore usually constrained by secondary observational signatures, that go from the ellipticity and position angle of the lensing galaxy to its effective light radius or stellar velocity dispersion. The fitting process generally consists of a χ^2 minimization of the weighted distances between the observed and predicted image positions. To carry out this process, a grid is created at the source plane and at the lens plane. By solving the lens equation (Eq. 2.37) with the chosen potential, a direct mapping between source and lens plane is obtained: for every cell of the grid in the lens plane a corresponding cell exists in the source plane grid.

The χ^2 minimization can be done either in the source plane or in the lens plane. In the first case, based on the fact that all multiple images in the lens plane come from a single source, the distance between the multiple (N) sources mapped to the source plane from the multiple (N) images in the lens plane are minimized. In the lens plane minimization, the process is inverted: one position at the source plan maps to multiple image positions and the χ^2 minimization is done based on the weighted difference between the modeled

and observed image positions on the lens plane. In both cases, this minimization can be complemented with constraints from the flux ratios between the images, as well as the time-delays. Image plane minimization provides a more precise result, but it is comparatively much more computationally demanding (for more information on parametric lens modeling see Jullo et al. 2007; Keeton 2001; Kneib 1993).

All the mass models that will be presented in this thesis were performed with the parametric method LENSTOOL (Jullo et al., 2007; Kneib, 1993). LENSTOOL does both source and image plane χ^2 minimization, using a Bayesian algorithm (prior based minimization), and a Markov Chain Monte-Carlo (MCMC) process that samples the probability distribution by random variations of the parameters. The scanning of the parameter space avoids hitting local χ^2 minima and allows robust results. The details of the algorithm and the underlying statistics are described in Jullo et al. (2007).

2.3 Galaxy clusters

Galaxy clusters occupy a special position in the hierarchical formation scenario as the most extended and recently formed systems in the Universe, that are held together by their own gravity. Their masses cover a range of roughly $10^{13} < M/h^{-1}M_{\odot} < 10^{15}$, and their spatial size spreads over $1 - 3$Mpc. As noted earlier, dark matter represents $\simeq 80\%$ of the total matter content in clusters. Stars and galaxies, which emit at visible wavelengths, make up only for a few percent of the whole mass content of clusters $(3 - 5\%)$. The most massive visible component is in diffuse hot gas $(15 - 25\%)$ (e.g. Kellogg et al., 1971).

Historically, galaxy clusters have been considered among the most important cosmological probes. In part, this is due to the fact that they occupy a unique and important intersection of physical scales. As mentioned above, they are the largest objects which are small enough to have come into dynamical equilibrium and conversely, they are probably the smallest objects which are big enough to contain a fair sample of the materials in the Universe, particularly of baryonic and non-baryonic matter.

As mentioned before, the total gravitational potential of clusters (due to both visible and dark matter) causes the deflection of light rays coming from distant galaxies, leading to distortions in the shapes of these objects, and sometimes producing giant elongated arcs or even multiple images of the background sources (e.g. Bartelmann 2010; Kneib and Natarajan 2011, for reviews). The gravitational lensing is therefore, one of the most important tools in cosmology for studying the total mass of the clusters. Fig. 2.11 shows the galaxy cluster MACSJ1206.2−0847 (Umetsu et al., 2012), from the CLASH

FIGURE 2.10: The galaxy cluster MACSJ1206.2−0847 (Umetsu et al., 2012), from the CLASH program, showing an impressive giant arc around its center due to its strong potential well. This figure was taken from the CLASH website http: // www.int.stsci.edu / ∼postman / CLASH / ForAstronomers.html.

program[1] , around the center of the image an impressive giant arc is visible. This arc is generated as a consequence of the strong potential well of the cluster.

Since the $\sim 80\%$ of the total mass in galaxy clusters corresponds to dark matter, detailed studies of dark matter in N-body simulations are extremely useful for the understanding of galaxy clusters. In the ΛCDM cosmological framework, numerical simulations have shown that the spherically averaged density profile of relaxed halos can be described by a universal functional form (Navarro et al. 1996, 1997). This function, known as the Navarro-Frenk-White (NFW) profile, is independent of the cluster mass, the spectrum of initial fluctuations and cosmological parameters.

This claim has been confirmed by detailed observational lensing measurements of massive cluster profiles (Umetsu et al. 2011), although some discrepancies concerning their inner slope still remain (Sand et al. 2004). As described below, we will assume a NFW profile

[1]The Cluster Lensing and SuperNova Survey con Hubble.

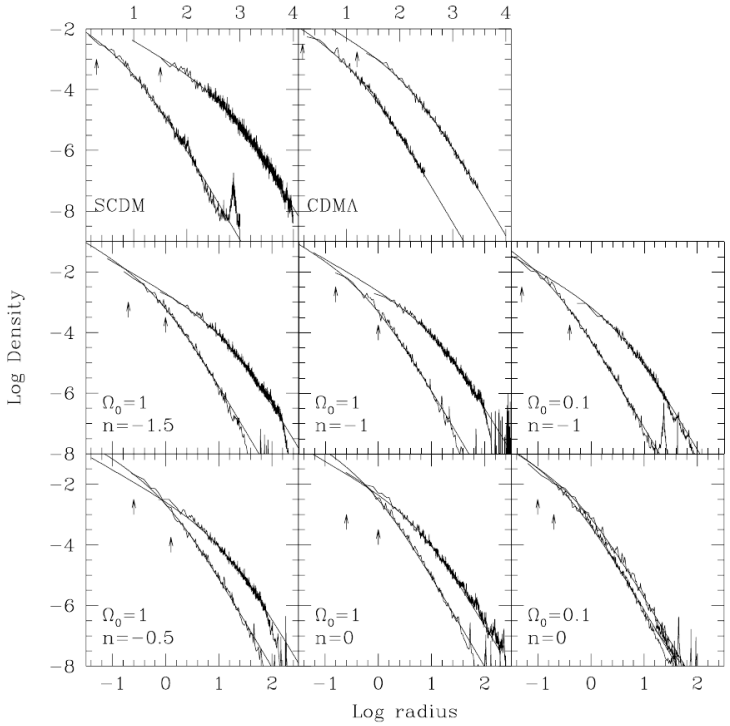

FIGURE 2.11: Density profiles of simulated dark matter halos. The different panels correspond to simulations for different cosmologies. Each panel shows the least and the most massive halos in each simulation (least massive to the left). Solid lines are the fits of the profiles to the NFW universal form. Figure from Navarro et al. (1997).

to characterize the cluster's density and to derive important parameters that describe their main properties.

Another important prediction of numerical simulations is the correlation between the concentration of the halos and their masses, called the $c - M$ relation in cosmological parlance. In particular, more massive halos are expected to be less concentrated than less massive ones. In the standard ΛCDM model, the halo concentration is determined by the mean density of the universe at the epoch when the halo is assembled, with higher concentrations corresponding to higher densities at earlier epochs (Bhattacharya et al. 2013; Bullock et al. 2001; Duffy et al. 2008; Macciò et al. 2008; Navarro et al. 1996; Neto et al. 2007). Therefore, halos build up at redshift $z \sim 0$ are expected to have a lower concentration than halos of lower mass formed at higher redshifts, when the mean density was higher. Observational studies of massive lensing clusters have generally shown qualitative agreement with the $c - M$ relations obtained from the simulations, although large discrepancies have been found in their normalizations (Comerford and Natarajan, 2007; Oguri et al., 2012, 2009) and slopes. The normalizations measured through lensing studies are surprisingly higher than the ones predicted by ΛCDM simulations, which means that lensing clusters are significantly more concentrated than what expected from

N-body simulations (Broadhurst et al., 2005b, 2008; Clowe and Schneider, 2001; King et al., 2002; Umetsu et al., 2011; Zitrin et al., 2011d). However, the lensing bias and projection effects should be taken into account before arriving to any conclusion. In fact, it has been shown that clusters having prominent arcs represent a strongly biased population such as that the masses and concentrations inferred from their projected mass distributions are on average much larger than in the normal population, mostly due to the halo triaxiality (Hennawi et al., 2007; Meneghetti et al., 2010; Oguri et al., 2012; Oguri and Blandford, 2009), with a typical major-to-minor axial ratio of $\sim 2:1$ (Jing and Suto, 2002). Furthermore, since lensing observables can only measure the projected mass distribution of the clusters, substructures and elongation along the line-of-sight may introduce a bias in the 3D mass distribution recovered from the projected mass (Meneghetti et al., 2003). It should be also noted that most of the N-body simulations mentioned above do not include a baryonic component, which dominate the mass in the cluster cores and makes the cluster halos more concentrated through adiabatic contraction.

In fact, one of the main goals of this thesis is to contribute to the understanding of the $c-M$ relation, as well as its possible redshift evolution, in order to put strong constraints in the current cosmological framework. We will dedicate a whole chapter to describe and interpret this relation.

2.3.1 The mass of galaxy clusters

Galaxy clusters are one of the most important probes of the large scale structure formation and the overall dynamical state of the Universe. The measurement of the total mass of clusters provides a direct way to estimate the amount of dark matter in the Universe, as well as a tool for the determination of the nature and evolution of dark energy. However, determining the total cluster mass is not an easy task, because the total mass of a cluster is not directly observable, but only its luminosity, or the temperature of the X-ray emitting intra-cluster medium. Therefore, in order to compare observed cluster with cosmological predictions, one needs a way to determine their masses. Among the most important methods for determining the mass of galaxy clusters are the following:

- Assuming virial equilibrium, the observed velocity distribution of galaxies in clusters can be converted into a mass estimate, using the virial theorem. This method typically requires assumptions about the statistical distribution of the anisotropy of the galaxy orbits.

- The hot intra-cluster gas, as visible through its Bremsstrahlung in X-rays, traces the gravitational potential of the cluster. Under certain assumptions, the mass profile can be constructed from the X-ray emission.
- Strong and weak gravitational lensing probes the projected mass distribution of the clusters at different radii, with strong lensing confined to the central region, whereas weak lensing can yield mass measurements for lager radii.

The three methods listed above are complementary; lensing yields the line-of-sight projected density of clusters, in contrast to the other two methods which probe the mass inside spheres. Those rely on equilibrium and symmetry conditions, which are not necessary for the lensig method.

In this section, we will briefly summarize the main features of two key methods to determine masses in galaxy clusters, to then introduce our innovative technique, which will be detailed in the next chapter.

2.3.1.1 Dynamical mass estimates from N-body simulations

The relationship between velocity dispersions and masses has been the focus of several studies. As a first-order approach, Heisler et al. (1985) studied simple variations of the virial theorem and found that they all behave similarly, and that it is not possible to distinguish among them. Carlberg et al. (1997) compared masses obtained from the virial theorem to those obtained with the Jeans equation in observed clusters. They found that the former are highly biased by a factor of $10 - 20\%$ and associated this bias with a surface pressure correction factor of the same order. More recently, large cosmological simulations Evrard et al. (2008) concluded that massive ($M_{200} > 10^{14} h^{-1} M_{\odot}$) clusters are, on average, consistent with a virialized state, with a best-fit scaling relation for dark matter halos described by NFW profiles in a variety of cosmologies. Accordingly, the mass enclosed within r_{200} is:

$$M_{200} = \frac{10^{15}}{h(z)} \left(\frac{\sigma_{DM}}{\sigma_{15}} \right)^{1/\alpha} M_{\odot} \tag{2.51}$$

where σ_{15} is the normalization at mass $10^{15} h^{-1} M_{\odot}$, α is the logarithmic slope, $h(z) = H(z)/100$ km s^{-1} Mpc^{-1} is the normalized Hubble parameter at redshift z for a flat universe, and σ_{DM} is the one-dimension velocity dispersion of the DM particles within r_{200}, which is related to the velocity dispersion of galaxies by a so-called velocity bias factor $b_v = \sigma_{cluster}/\sigma_{DM}$. The best-fit yields $\sigma_{15} = 1082.9 \pm 4.0$ km s^{-1} and $\alpha = 0.3361 \pm 0.0026$.

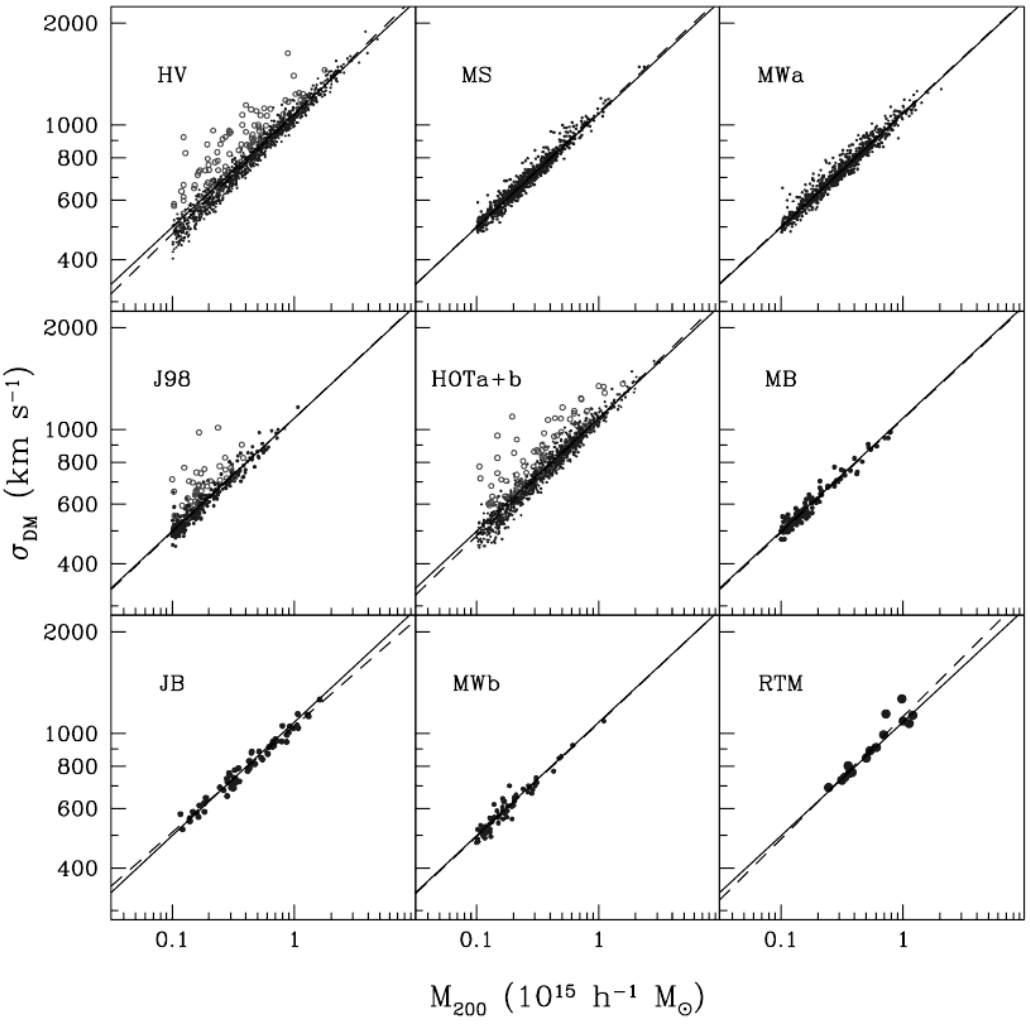

FIGURE 2.12: The figure shows the $\sigma_{DM} - M_{200}$ relation for several cosmologies, as well as the "universal" best-fit previously described by Eq. 2.51. This figure was taken from Evrard et al. (2008)

Recent theoretical works have indicated that the way in which subhalos are tracked and defined in simulations could affect the resulting velocity bias predictions (Evrard et al., 2008; White et al., 2010). In fact, Evrard et al. (2008) have shown no evidence for a velocity bias factor, $b_v = 1.00 \pm 0.05$. Thus, in this thesis we assume no velocity bias in the computing of dynamical masses. Fig. 2.12 shows the $\sigma_{DM} - M_{200}$ relation for several cosmologies, as well as the "universal" best-fit previously described by Eq. 2.51.

Therefore, with robust velocity dispersion measurements the total mass of a galaxy cluster can be determined by this scaling relation. In fact, this method was successfully applied in recent works, e.g. Bayliss et al. (2011) and Sifón et al. (2013). In this thesis, we use this technique to compute the dynamical masses of the galaxy clusters.

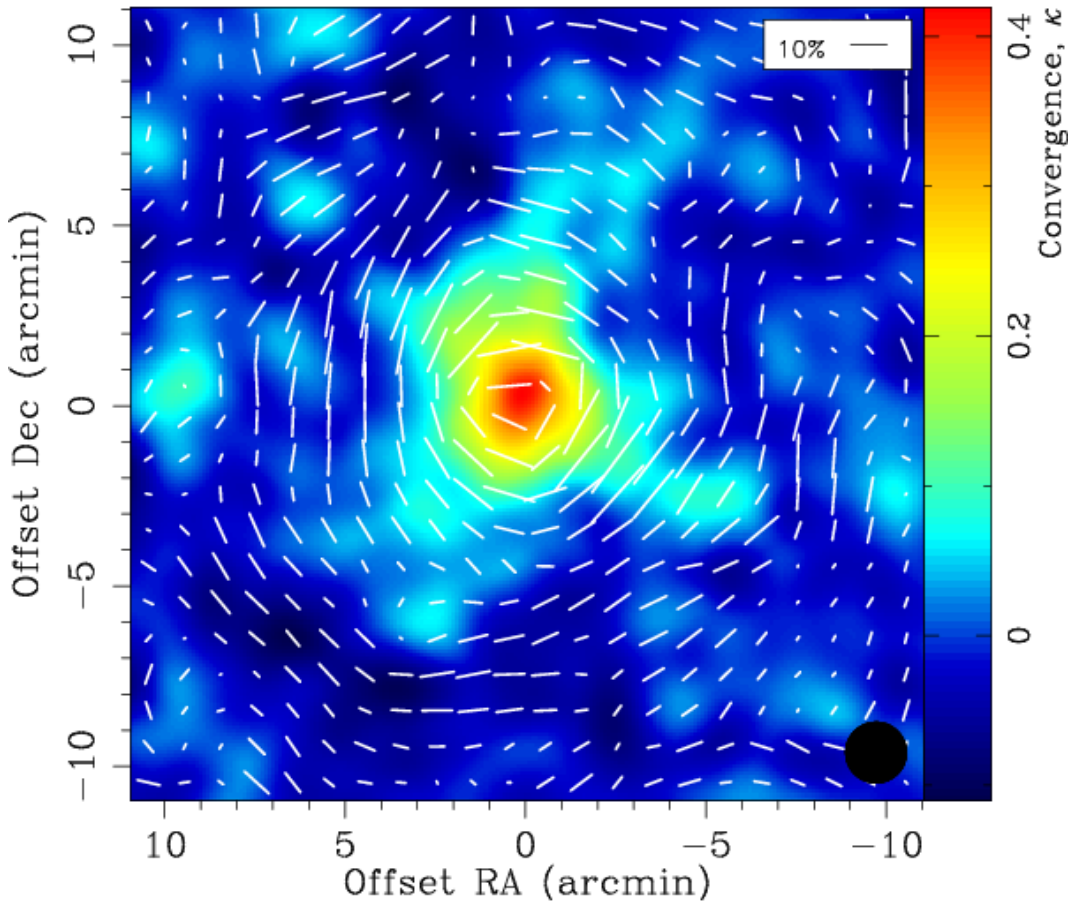

FIGURE 2.13: This figure shows the projected mass distribution (in terms of κ) of the cluster Abell 1689, reconstructed using the weak gravitational shear field γ measured from a color/magnitude-selected sample of red background galaxies registered in deep Subaru imaging observations. This figure was take from Umetsu and Broadhurst (2008a).

2.3.1.2 Gravitational lensing mass measurements

Gravitational lensing is the most robust way to probe the mass distribution of galaxy clusters because the gravitational light deflection is sensitive to the total cluster mass, regardless of its nature or state. As detailed in section 2.2.5, there are two regimes in gravitational lensing to probe the cluster mass distribution. Close to the center, we found the strong lensing phenomenon that yields the most precise measurements of the core mass of galaxy clusters. This is done by solving the lens equation (Eq. 2.37) and using the giant arcs and/or multiple-image systems as constraints in the modeling procedure. At larger radii, weak lensing probes the total mass of the clusters by deriving tangential shear profiles from the statistical measurements of several tiny distortions.

Several techniques for measuring the mass distribution of clusters up to large distances from the cluster center based on the application of weak lensing have been developed (e.g.

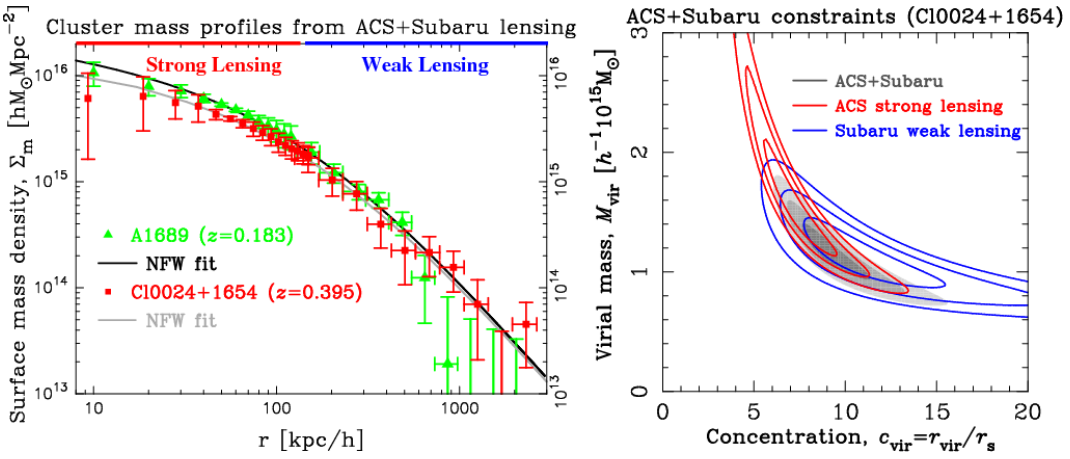

FIGURE 2.14: In the left panels is shown the cluster surface mass density profile for A1689 (*green triangles*) and CL0024+1654 (*red squares*) reconstructed from strong lensing (HST/ACS: $r \lesssim$200kpc) and weak lensing measurements (Subaru: $r \gtrsim$ 200kpc). The curvature of these profiles demonstrates that both strong and weak lensing data are required to make an accurate measurement of the cluster mass structure parameters, such as the halo virial mass, M_{vir}, and concentration, c_{vir}. Also shown as solid curves are the best-fitting NFW models, with a continuously steepening density profile for A1689 (*black*) and CL0024+1654 (*gray*). In the right panel is shown the joint constraints on the NFW model parameters (c_{vir}, M_{vir}) derived for CL0024+1654. The red and blue contours show the 68.3%, 95.4%, and 99.7% confidence limits for the inner strong lensing and outer weak lensing data, respectively. Combining strong and weak-lensing information (*gray contours*) significantly reduces the uncertainties on the profile parameters. This figures were taken from Umetsu and Broadhurst (2008a) and Umetsu et al. (2010).

Bertin and Lombardi, 2001; Hoekstra et al., 1998; Kaiser, 1995; Umetsu and Broadhurst, 2008b). Although almost all weak lensing methods suffer from the important problem of the mass sheet degeneracy. However, the fact that weak lensing methods do not need to make any assumption on the dynamical state of the matter, make them powerful tools anyway. In Fig. 2.13 we show the projected mass distribution (in terms of κ) of the cluster Abell 1689, reconstructed by using the weak gravitational shear field γ measured from a color/magnitude-selected sample of red background galaxies registered in deep Subaru imaging observations (Umetsu and Broadhurst, 2008a).

Since strong and weak lensing probe mass distributions at different radii, the combination of both methods results in precise measurements of the total cluster mass, as well as detailed density profile of galaxy clusters. In Fig. 2.14 we show two examples of the combination of these methods for the clusters A1689 and CL0024+1654. The figure shows the cluster surface mass density profiles reconstructed from strong lensing (HST/ACS: $r \lesssim$200kpc) and weak lensing measurements (Subaru: $r \gtrsim$ 200kpc), as well as the best-fit for the joint constraints. The curvature of these profiles demonstrates that both strong and weak lensing data are required to make an accurate measurement of the

cluster mass structure parameters, such as the halo virial mass M_{vir}, and concentration c_{vir}.

In the next Chapter, we will introduce an innovative technique to probe the mass distribution of galaxy clusters, which yields results as good as those obtained by combining strong and weak lensing constraints. The basic idea is to probe the innermost region of the mass distribution using strong lensing signatures, while at larger radii, the cluster mass is constrained by the velocity dispersion of the cluster members.

Chapter 3

Method: strong lensing and dynamical mass analysis

For all methods summarized in the previous chapter, an accurate estimation of the total cluster mass is crucial. The present thesis is devoted to contribute with new measurements of the total cluster mass for a large sample of galaxy clusters, as well as contributing to the development of progressive mass measurement techniques, which can be complementary to the existing ones.

In this chapter we present an innovative technique to determine the total cluster mass and to measure the concentration of the galaxy clusters, which is critical for a fully understanding of the current cosmological framework.

3.1 Strong lensing analysis

In this section we describe the strong lens modeling methodology that we have used for the mass reconstruction of all clusters studied in this thesis. We have used the parametric method described in Kneib (1993) and implemented in the Markov Chain Monte Carlo (MCMC) code: LENSTOOL (Jullo et al., 2007), to perform our models.

We start our models assuming an ellipsoidal NFW profile (Navarro et al., 1996, 1997) to describe the projected mass distribution for the main DM halo (ϕ_c), which is parameterized by the scale radius, r_s, and the halo characteristic density, ρ_s, by:

$$\rho(r) = \frac{\rho_s}{r/r_s(1 + r/r_s)^2} \tag{3.1}$$

where r_s corresponds to the region where the logarithmic slope of the density profile equals the isothermal value, namely $d\ln\rho(r)/d\ln r = -2$, and ρ_s is linked to the halo concentration parameter, c_{Δ_c}, by:

$$\rho_s = \rho_c(z) \times \frac{\Delta_c}{3} \frac{c_{\Delta_c}^3}{ln(1+c_{\Delta_c}) - c_{\Delta_c}/(1+c_{\Delta_c})}, \tag{3.2}$$

where $\rho_c(z)$ corresponds to the critical density of the Universe (Eq. 2.15) and Δ_c is the over density given by the Eq. 2.28. The concentration parameter is defined as the ratio of the virial radius to the scale radius,

$$c_{\Delta_c} \equiv \frac{r_{\Delta_c}}{r_s}. \tag{3.3}$$

The ellipticity of the projected mass distribution is then introduced in the NFW profile by substituting the radial coordinates $r = (x_1, x_2)$, by an elliptical radius r_ϵ, given by:

$$r_\epsilon = \sqrt{(1-\epsilon)x_1^2 + (1+\epsilon)x_2^2}, \tag{3.4}$$

where we assumed that the elliptical parameter ϵ is the ellipticity of the lens potential, $\varphi_\epsilon(x) \equiv \varphi(x_\epsilon)$. This quantity is linked to the ellipticity of the projected mass distribution, e_Σ, by assuming that $e_\Sigma = 3\epsilon$ (Golse and Kneib, 2002; Kneib, 1993), which in turn is defined by:

$$e_\Sigma = \frac{a^2 - b^2}{a^2 + b^2}, \tag{3.5}$$

with a and b corresponding to the "pseudo" semi major and semi minor axis, respectively. The direction of the elliptical mass distribution, θ_e, is measured counterclockwise from the West and is related to the position angle (P.A.) by P.A $= \theta_e - 90°$.

Therefore, the main DM halo can be fully characterized by six free parameters: the c_{Δ_c} and r_s parameters of the NFW profile, the center position (R.A., Dec.), the ellipticity e_Σ, and its direction θ_e. In some clusters, where there are not enough observational constraints, we fix the center of the main halo to the position of the brightest cluster galaxy (BCG), since the number of constraints has to be larger than the number of parameters in order to get a reliable fit.

Then, we add the mass contributions from the member galaxies ($\Sigma\phi_{gal_i}$) assuming a truncated Pseudo-Isothermal Elliptical Mass Distribution (PIEMD; Kassiola and Kovner,

1993; Kneib et al., 1996) with a constant mass-to-light ratio for all selected cluster members. The PIEMD profile is given by:

$$\rho(r) = \frac{\rho_0}{(1 + r^2/r_{core}^2)(1 + r^2/r_{cut}^2)} \tag{3.6}$$

where ρ_0 is the central density of the halo, which is related to the central velocity dispersion parameter, σ_0, by:

$$\rho_0 = \frac{\sigma_0^2}{2\pi G} \left(\frac{r_{cut} + r_{core}}{r_{core}^2 r_{cut}} \right). \tag{3.7}$$

The r_{core} and r_{cut} parameters define the changes of the slope in the density profile. In the inner region ($r < r_{core}$), the profile is described by a core of density ρ_0, while in the central region ($r_{core} < r < r_{cut}$) the profile is isothermal, with a logarithmic slope of $\sim 1/r^2$. In the outer region, the density progressively decays from $\rho(r) \sim 1/r^2$ to $\rho(r) \sim 1/r^4$, introducing a cutoff (for more details, see Limousin et al. 2005). The σ_0, r_{core}, and r_{cut} PIEMD profile parameters are given by (Jullo et al., 2007):

$$r_{core} = r_{core}^\star (L/L^\star)^{1/2}, \quad r_{cut} = r_{cut}^\star (L/L^\star)^{1/2}, \quad \text{and} \quad \sigma_0 = \sigma_0^\star (L/L^\star)^{1/4}, \tag{3.8}$$

where $L^\star$ is the typical luminosity of the galaxies at the cluster redshift, defined in this work as the break in the luminosity function of the cluster members, i.e., the characteristic luminosity of the Schechter function (Schechter, 1976). The total mass of each galaxy is then scaled by its luminosity L by:

$$M = (\pi/G)(\sigma_0^\star)^2 r_{cut}^\star (L/L^\star) \tag{3.9}$$

where $r_{cut}^\star$ and $\sigma_0^\star$ are free parameters in the optimization process, while $r_{core}^\star$ is set to a vanishing value of $0.15 - 0.30$ kpc to get a simple expression for the total mass (Eq. 3.9) (Eliasdottir et al., 2007; Kassiola and Kovner, 1993; Natarajan et al., 1998). Unlike the main DM halo, the center (R.A., Dec.), the ellipticity e_Σ and the direction θ_e of the galaxy-scale DM halos are assumed to be the same as those of the light distribution of the selected cluster galaxies. The cluster members were selected as those lying on ($\pm 1\sigma$) both red sequences ($r' - z'$) and ($g' - r'$), and brighter than $m^\star + 2$ (where $m^\star$ is the magnitude corresponding to $L^\star$).

Therefore, the total mass distribution for each galaxy cluster is fully described by eight free parameters (or six, depending on whether the center of the main DM halo is fixed);

the $r^{\star}_{cut}$ and $\sigma^{\star}_{0}$ parameters of the PIEMD galaxy-scale halos; the r_s and c_{Δ_c} parameters, as well as the center position, the ellipticity e_{Σ} and the direction θ_e of the main DM halo.

Then, we use the observational constraints, i.e., the positions of the multiple images and giant arcs, to optimize the parameters described above. The identification of the multiple-image systems is mainly based on the spectroscopically confirmed lensed galaxies (chapter 4), as well as on the colors of the lensed arcs measured from our groundbase imaging data. Depending of each lens configuration, giant arcs may correspond to the merging of two or three images of the same background source. Thus, we use the decrease in brightness of the spectroscopically confirmed giant arcs to separate them into multiple images, which are then used as constraints in the optimization procedure.

The optimization process is performed in the image plane. This minimizes the magnification bias introduced by the modeling procedure. The total SL χ^2 is given by:

$$\chi^2_{SL} = \sum_i \chi^2_{pos}(i) + \sum_k \chi^2_{cc}(k), \tag{3.10}$$

where the first component is the χ^2 of the predicted images by the model, defined by:

$$\chi^2_{pos}(i) = \sum_j \frac{(x^{obs}_{ij} - x^{pred}_{ij})^2}{\sigma^2_r}, \tag{3.11}$$

with x^{obs}_{ij} being the position of the multiple image j of the system i, while x^{pred}_{ij} is the position of its predicted image. This is obtained after solving the lens equation (Eq. 2.37) with the current model, i.e., by a specific projected mass distribution (Eq. 2.32). We fix the positional error in the image plane σ_r at $1.4''$, which has been found to be a reasonable value accounting for large-scale structure and matter along the line of sight (Coe et al., 2013; Zitrin et al., 2012b).

Depending on the number of confirmed multiple images and their configurations, we may also include the second component (χ^2_{cc}) in the total SL χ^2, which measures how well the location of some points in the critical curves (where $\Sigma(D_l\boldsymbol{\theta}) = \Sigma_{cr}$) are reproduced by the model. This constraint can be used in cases where we know with great confidence the location of the critical curve (Jullo et al., 2007; Limousin et al., 2007), e.g., in the cases where the giant arcs correspond to the merging of multiple images. In these cases, we use the observed critical curve position $(x^{obs}_{cc}, y^{obs}_{cc})$ to define the second component in the total SL χ^2, which is given by:

$$\chi^2_{cc}(k) = \sum_k \frac{(x^{obs}_{cc} - x^{pred}_{cc})^2 + (y^{obs}_{cc} - y^{pred}_{cc})^2}{\sigma^2_{x_{cc}} + \sigma^2_{y_{cc}}}, \tag{3.12}$$

where the coordinates x^{pred}_{cc} and y^{pred}_{cc} correspond to the predicted critical curve position by the current model. The uncertainties in the location of the critical curves are given by $\sigma^2_{x_{cc}}$ and $\sigma^2_{y_{cc}}$, which are set to $0.3''$, following the work of Limousin et al. (2007).

In order to avoid local minima in the image plane χ^2 optimization, we use the Bayesian MCMC implementation[1] of LENSTOOL. In brief, it starts randomly drawing mock models from a set of priors of the input parameters, and computing their χ^2. The sample progressively converges to the most likely parameter space, in where it draws $10,000$ realizations which are used to obtain the best-fitting model parameters, as well as to compute contours of confidence levels and error bars on the estimation of these parameters (for more details, see Jullo et al., 2007). The priors of the input parameters are assumed to be uniform and with very broad ranges, in order to explore all possible scenarios. We allow the concentration parameter c_{Δ_c} to vary between 0.1 and 40, and the scale radius r_s, from 10 kpc to 650 kpc; the velocity dispersion $\sigma^\star_0$ range spans between 50 and 400 km s^{-1}, whereas the cut radius $r^\star_{cut}$ is forced to be less than 200 kpc in order to account for tidal stripping of the galaxy-scale DM halos (e.g., Limousin et al., 2007; Natarajan et al., 2009; Wetzel and White, 2010, and references therein); the ellipticity e_Σ is allowed to reach values as high as 0.75 (Golse and Kneib, 2002), and its direction can take any value between 0° to 180°; finally, the position of the main DM halo is allowed to vary by $\pm 25''$ around to the BCG. We note that in some clusters, the redshift for some multiple-image systems is left as a free parameter in the optimization process, with a flat prior centered at $z_{input} = 2.0$, with a conservative 1σ error of $\sigma = ^{+3.0}_{-1.0}$ (Bayliss et al., 2011; Oguri et al., 2012).

3.2 Dynamical masses

In this section, we briefly describe the method used to calculate dynamical masses from velocity dispersions. The full details of this procedure can be found in chapter 4.

The redshift measurements were carried out by two independent methods: by cross-correlation of the spectra with spectral galaxy templates of the SDSS DR7, and by visual inspection of each spectrum, identifying a set of lines at a common redshift. Then, the cluster members as well as the redshift, z_{cl}, and velocity dispersion, $\sigma_{cluster}$, of each cluster were determined by applying a cut in (rest-frame) velocities space of

[1] http://www.inference.phy.cam.ac.uk/bayesys/

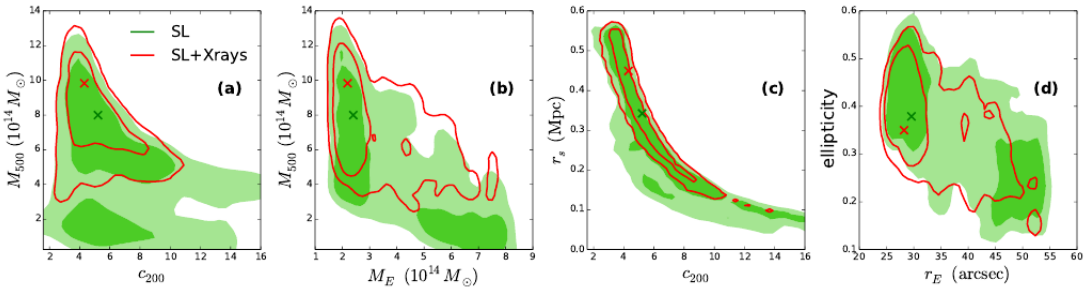

FIGURE 3.1: Filled green contours show parameter distributions from strong lensing alone while the red line contours show the parameter distributions when dynamical constrains are included. Crosses denote the corresponding maximum likelihood estimates. Contours are at the 68% and 95% levels. This figure was taken from Sifón et al. (2014).

± 4000 km s^{-1}, and then by applying the 3σ clipping method. To finally apply the bi-weight estimator of Beers et al. (1990). This process was iterated until the number of members was stable. That usually happened after the second iteration.

Finally, we calculated dynamical masses by applying the relation between the DM velocity dispersion, σ_{dm}, and the total mass of the halo, M_{200}, from Evrard et al. (2008), which is given by[2]:

$$M_{200} = \frac{10^{15}}{h(z)} \left(\frac{\sigma_{DM}}{\sigma_{15}} \right)^{1/\alpha} M_\odot \tag{3.13}$$

where σ_{15} is the normalization at mass $10^{15} h^{-1} M_\odot$, α is the logarithmic slope, $h(z) = H(z)/100$ km s^{-1} Mpc^{-1} is the normalized Hubble parameter at redshift z for a flat universe, and σ_{DM} is the one-dimension velocity dispersion of the DM particles within r_{200}, which is related to the velocity dispersion of galaxies by a so-called velocity bias factor $b_v = \sigma_{cluster}/\sigma_{DM}$. The best-fit yields $\sigma_{15} = 1082.9 \pm 4.0$ km s^{-1} and $\alpha = 0.3361 \pm 0.0026$.

Based on recent simulation results (e.g., Evrard et al., 2008; White et al., 2010), we assumed no velocity bias ($b_v = \sigma_{cluster}/\sigma_{dm} = 1$) between the galaxy and DM velocity dispersion.

3.3 Strong lensing and dynamical constraints

According to Verdugo et al. (2011), to combine constraints from velocity dispersion and dynamical mass measurements with constraints from strong lensing, we need to define a new likelihood (χ^2) in our modeling procedure. Since we have an independent

[2]This relation was already presented in §2.3.1.1

measurement of the 3D mass of the clusters from the velocity dispersion, we can define this new χ^2 as:

$$\chi^2_{mass}(M^{obs}_{200}, c_{200}, r_s) = \left(\frac{M^{obs}_{200} - M^{pred}_{200}(c_{200}, r_s)}{\Delta M} \right)^2 \tag{3.14}$$

where M^{obs}_{200} is M_{200} described in the previous section, $M^{pred}_{200}(c_{200}, r_s)$ is the 3D mass predicted by the model, given the set of parameters (c_{200}, r_s), and ΔM is the uncertainty in the measurement of the observed 3D mass. Thus, since both the strong lensing masses and the dynamical masses are obtained through independent techniques, we combine both sets of constraints for a given set of free parameters, by adding their χ^2:

$$\chi^2_{tot} = \chi^2_{SL} + \chi^2_{mass} \tag{3.15}$$

In practice, we add this external constraint in our modeling procedure including a gaussian prior in the total mass, centered at $M^{input}_{200} = M_{200}$, with 1σ error equal at the errors of M_{200}.

The Figure 3.1 shows how the parameter distributions change for the cluster PLCK G004.5−19.5 (Sifón et al., 2014) by including dynamical constraints in the SL model. The dynamical mass constraints remarkably decrease the degeneracies in the parameter space, which are very common in strong lensing modeling (e.g., Jullo et al., 2007), ruling out high-M_E, high-concentration and low-ellipticity solutions, which were allowed in the SL only models for low-M_{500}.

It should be noted that this technique has been previously introduced by Verdugo et al. (2011), who implemented the dynamical probability in LENSTOOL software. Verdugo et al. (2011) tested this technique in galaxy groups' masses reconstructions successfully.

3.4 Conclusions

In this chapter we introduced the mass reconstruction methodology that we have used in all the reconstructions presented in this thesis. This consists in the combination of SL constraints that probe the innermost region of the galaxy cluster cores, and dynamical masses derived from the velocity dispersion of the cluster members that probe the mass distribution of clusters at larger radii.

The mass reconstruction results by combining these two observables will be shown in the following chapters.

Chapter 4

New sample of 29 strong lensing selected galaxy clusters

In this chapter we present high quality spectroscopic data of 29 new strong lensing (SL) selected galaxy clusters that were visually identified in the Red-Sequence Cluster Survey-2 (RCS2[1]). We also describe our spectroscopic follow-up methodology, as well as the main results of this campaign.

4.1 The importance of controlled samples of SL selected galaxy clusters

Galaxy clusters are one of the most powerful tool in the modern cosmology. Their number counts are a key test of the standard concordance cosmological model, since they are sensitive to the density fluctuation amplitudes and cosmological parameters. Large surveys of galaxy clusters are now producing catalogs of several clusters, with well-defined selection functions over large fractions of the sky (Gilbank et al., 2011; Gladders and Yee, 2005; Vanderlinde et al., 2010). At the same time, extensive efforts are underway to determine with good accuracy the mass and redshift distributions of these clusters.

One of the most robust and direct ways to map the total mass distribution in massive galaxy clusters is through the analysis of gravitational lensing signatures; with weak lensing (WL) probing at larger radii the density profile of the clusters, while SL yields the most detailed mass reconstructions of the cluster cores (e.g. Bartelmann, 2010; Kneib and Natarajan, 2011, for reviews). WL observations of galaxy clusters have become a

[1]Described in Appendix A

powerful tool in recent years (Dahle, 2006; Hoekstra and Jain, 2008; Okabe et al., 2010b), but galaxy clusters exhibiting SL remain a rare subset of the total cluster population.

In this chapter we present a spectroscopic follow-up of a subset from a large sample of several hundred giant arcs from the Red-Sequence Cluster Survey Giant Arc (RCSGA; Bayliss, 2012), discovered in the RCS2 survey (Gilbank et al., 2011). This SL selected cluster sample is intended primarily to provide statistical samples of SL clusters that can be used to perform robust mass reconstructions of the cluster cores, as well as to address the persistent lack of large, well-selected catalogs of giant arcs which can be compared against of ΛCDM predictions for giant arc statistics. A large sample of SL selected clusters also increases the volume of the high-redshift universe that is available for observations because these clusters act as natural telescopes, magnifying the size and the fluxes of the faint far objects.

4.2 Observations

4.2.1 The SL selected cluster sample

In this section, we present a detailed spectroscopic analysis of a sample of 29 SL selected galaxy clusters from the RCSGA survey, from which 27 clusters are previously unpublished. The clusters in RCSGA survey have been selected through an exhaustive visual inspection in the RCS2 imaging data as those having giant blue arcs around their cores. For more details of this new survey, the reader can go to Bayliss (2012). The RCS2 survey (Gilbank et al., 2011) was designed to detect galaxy clusters at high redshift using the red-sequence technique (Gladders and Yee, 2000) in deep images on a 3.6m class telescope, in the r', g', and z' bands, with limiting magnitudes of 24.3, 24.4, and 22.8, respectively. The median seeing of the RCS-2 survey is $\sim 0.7''$, making it ideal for the detection and classification of giant arcs. The RCSGA survey has discovered hundreds of SL clusters, and we performed a spectroscopic follow-up for some of its most spectacular systems.

Two of our clusters have also been reported in previous studies; RCS2 J0327−1326 in Sharon et al. (2012); Wuyts et al. (2010, 2014); and RCS2 J2111−0114 (or SDSS J2111−0114) in Bayliss et al. (2011); Hennawi et al. (2008); Oguri et al. (2012). This allows us to compare our results and test our innovative technique that will be described in the next chapter. We have adopted a naming convention described in Bayliss et al. (2011) for giant arcs discovered in RCSGA, given by RCSGA − Jhhmmss+ddmmss (e.g. Bayliss, 2012; Wuyts et al., 2010).

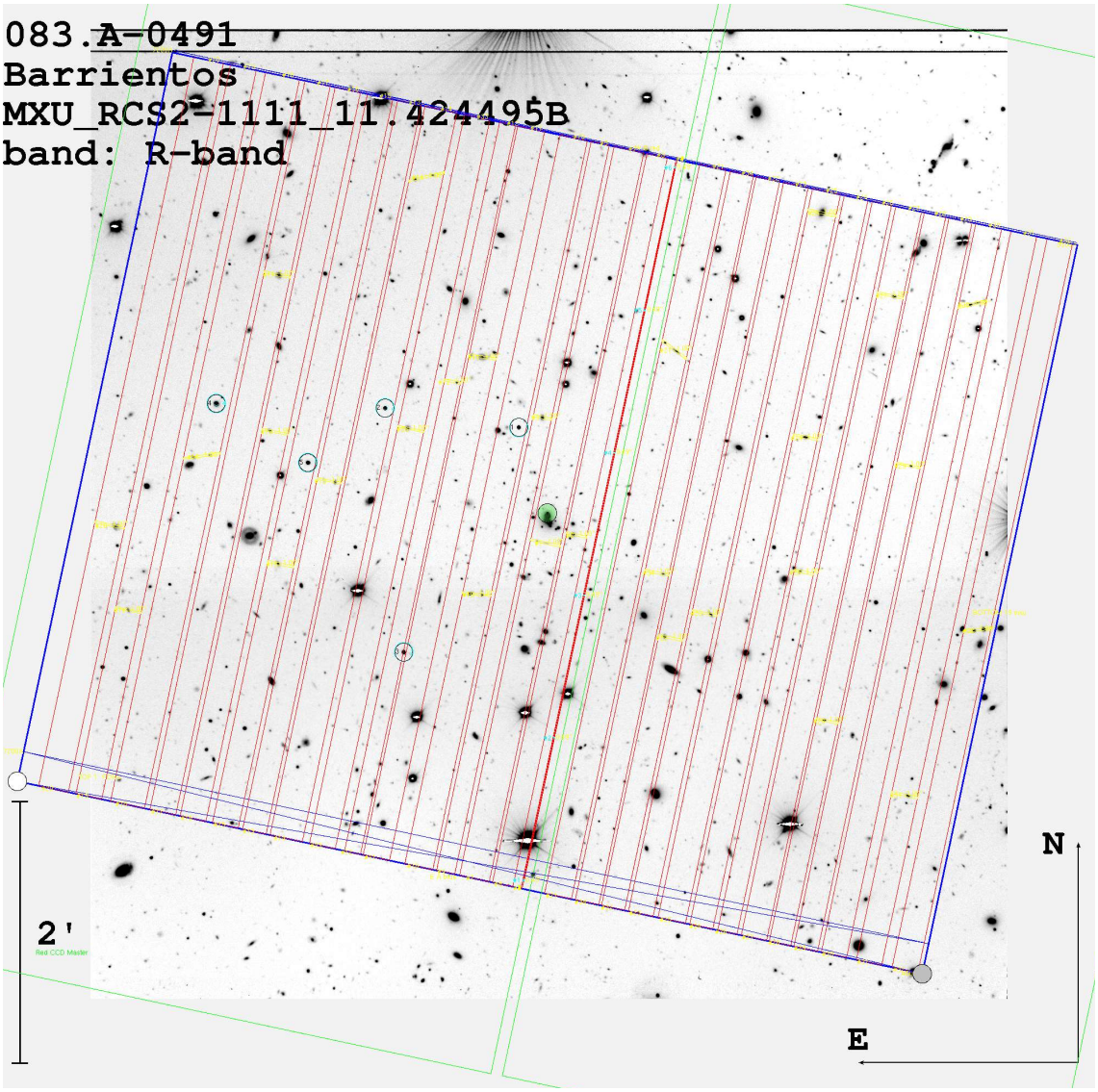

FIGURE 4.1: This figure shows an example of the masks used in MXU mode in this work for the cluster RCS2 J1125−0628.

4.2.2 Imaging

The imaging of our clusters has been obtained from the RCS2 data. They were collected in queue-scheduled mode with MegaCam at the 3.6 m Canada-France-Hawaii Telescope (CFHT), between the semesters 2003A and 2007B inclusive. The RCS2 data (Appendix A.1) consist in single exposure (without dithering) of 4, 8, and 6 minutes, for the g', r', and z' bands, respectively; cosmic rays and chip defects have been identified by visual inspection and removed by interpolation (Gilbank et al., 2011). We used the r' and z' bands to identify the red-sequence cluster member candidates, which have been used as targets in the spectroscopic follow-up and also to perform the mass reconstructions of our SL models (next chapter). While the g'–band was used to identify strongly lensed

arcs, since these tend to be relatively blue. We have also obtained pre-imaging of our clusters in B, R, and I bands, with the Focal Reducer and low dispersion Spectrograph 2 (FORS2; Appenzeller et al., 1998) at ESO[2] 8.2m Very Large Telescope (VLT), in queue mode. The FORS2/VLT pre-imaging data have been used to design the spectroscopic masks and also in the searching for multiple-image systems during the modeling process.

4.2.3 Spectroscopy

The FORS2/VLT observations were carried out during the ESO observing programs P78, P81, P83, and P84 (principal investigator Dr. L. Felipe Barrientos), by using the Multi-object spectroscopy with exchangeable masks (MXU) mode. The MXU mode allows both increase the density of the slits and free manipulation of the width, length, and orientation of the slits, making it ideal for spectroscopy in dense regions as the cluster cores. The spectroscopic masks for each cluster were designed with the FORS Instrument Mask Simulator (FIMS) software. The masks were strategically positioned in the center of each clusters in order to prioritize giant arcs and lensed galaxy candidates.

The slit width was always set to $1''$, while its length varied depending on the arc candidates size, typically between $12''$ to $25''$. The masks were then filled with slits placed in red sequence cluster selected members. The length of these slits was between $6''$ and $12''$, depending on each member size. We have usually built two masks for each cluster, although some of them had up to four masks. In order to increase the giant arcs flux, we have fixed the slits located in the arc positions. On the other hand, with the purpose of increasing the spectroscopically confirmed member galaxies, we have varied the slits located in the cluster galaxy candidates between each masks. Fig. 4.1 shows an example of the mask used in MXU mode in this work.

As one of the main goals of this work is to increase the number of both spectroscopically confirmed lensed galaxies and member galaxies, we have always performed the same instrument setup for medium resolution spectra, by using the GRIS_150I+27 grism and GG435+81 filter, and we have adopted a 2×2 binning in order to improve the signal-to-noise ratio of the spectra. This instrument setup results in a final dispersion of 6.9 Å per image pixel, and covers a spectral range from $\Delta\lambda \sim 4300 - 10500$ Å. Although, our highest sensitivity was in the interval $\Delta\lambda \sim 4500 - 9000$, due to the transmission efficiency of the filter used. This setup is ideal for identifying galaxies at $z \gtrsim 1.0$, which often relies on spectral lines that are redshifted (i.e. $\sim 7000 - 10000$ Å). Depending on the intrinsic features of each clusters, we varied the exposure times between $1200 - 3000$

[2]ESO: the European Southern Observatory; http://www.eso.org/

TABLE 4.1: Summary of FORS2/VLT spectroscopic observations

Target	R.A.[c] (J2000)	Dec[c] (J2000)	Period	Exposures	Comments
RCS2 J0004−0103	00 04 52.001	−01 03 16.58	83	3×2400s	2 masks
RCS2 J0034+0225	00 34 28.134	+02 25 22.34	81	5×2700s, 1×2100s	2 masks
RCS2 J0038+0215	00 38 55.898	+02 15 52.35	84	3×2400s, 3×1800s, 2×2520s	2 masks
RCS2 J0047+0507	00 47 50.787	+05 07 52.30	81	3×2400s	1 masks
RCS2 J0052+0433	00 52 10.352	+04 33 33.31	81	2×3000s	1 masks
RCS2 J0057+0209	00 57 27.869	+02 09 33.98	84	3×1800s, 2×2280s, 1×2580s	2 masks
RCS2 J0252−1459	02 52 41.474	−14 59 30.38	78	2×2400s	1 masks
RCS2 J0309−1437	03 09 44.096	−14 37 34.38	84	3×1980s, 1×1800s	2 masks
RCS2 J0327−1326[a]	03 27 27.174	−13 26 22.90	78	3×2400s	1 masks
RCS2 J0859−0345	08 59 14.486	−03 45 14.63	81	5×2400s	2 masks
RCS2 J1055−0459[d]	10 55 35.647	−04 59 41.60	81 - 83	5×2400s, 2×3300s	4 masks
RCS2 J1101−0602	11 01 54.093	−06 02 32.02	84	3×1200s	1 masks
RCS2 J1108−0456	11 08 16.835	−04 56 37.62	83	3×2400s	2 masks
RCS2 J1111+1408	11 11 24.483	+14 08 50.82	81	3×1800s, 1×2400s	2 masks
RCS2 J1119−0728	11 19 11.925	−07 28 17.51	84	2×2400s, 2×1500s	2 masks
RCS2 J1125−0628	11 25 28.940	−06 28 39.04	83	4×2400s	2 masks
RCS2 J1250+0244	12 50 41.890	+02 44 26.57	84	5×1200s	2 masks
RCS2 J1511+0630	15 11 44.681	+06 30 31.79	83	4×2400s	2 masks
RCS2 J1517+1003	15 17 02.587	+10 03 29.27	84	6×1200s	2 masks
RCS2 J1519+0840[d]	15 19 31.213	+08 40 01.43	81 - 83	2×3600s, 3×2400s	3 masks
RCS2 J1526+0432	15 26 14.914	+04 32 48.01	83	3×2400s	2 masks
SDSS J2111−0114[b]	21 11 19.307	−01 14 23.95	83	2×2400s, 1×3000s	2 masks
RCS2 J2135−0102[d]	21 35 12.040	−01 02 58.27	81 - 83	4×2800s, 2×600s, 4×2400s	4 masks
RCS2 J2147−0102	21 47 37.172	−01 02 51.93	84	2×3000s, 2×2400s	2 masks
RCS2 J2151−0138	21 51 25.950	−01 38 50.14	84	3×1800s	2 masks
RCS2 J2313−0104	23 13 54.514	−01 04 48.46	81	6×2700s	2 masks
RCS2 J2329−1317[d]	23 29 09.528	−13 17 49.26	83 - 84	1×2700s, 2×2400s, 4×1800s	4 masks
RCS2 J2329−0120	23 29 47.782	−01 20 46.89	78	3×2400s	1 masks
RCS2 J2336−0608	23 36 20.838	−06 08 35.81	84	3×2400s, 2×1800s	2 masks

[a] Previously described in Wuyts et al. (2010) and Sharon et al. (2012).
[b] Also reported in Bayliss et al. (2011) and Oguri et al. (2012).
[c] Coordinates are BCG centroids (J2000).
[d] These clusters were observed in more than one period, but with different masks and fixing the slit positions for the lensed galaxies.

seconds. The number of masks and total exposure time for each galaxy clusters are reported in Tab. 4.1

4.2.4 Data reduction

The MXU masks were reduced using the standard ESO data reduction procedures and our own IDL codes. The basic data reduction steps consisted on bias subtraction, flat-fielding, wavelength calibration, and sky subtraction. These steps were carried out by using the ESO Recipe Execution Tool (EsoRex[3]) and the Common Pipeline Library (CPL[4]). The wavelength calibration was done by comparison to the standard He+Ne+Ar

[3]http://www.eso.org/sci/software/cpl/esorex.html
[4]http://www.eso.org/sci/software/cpl

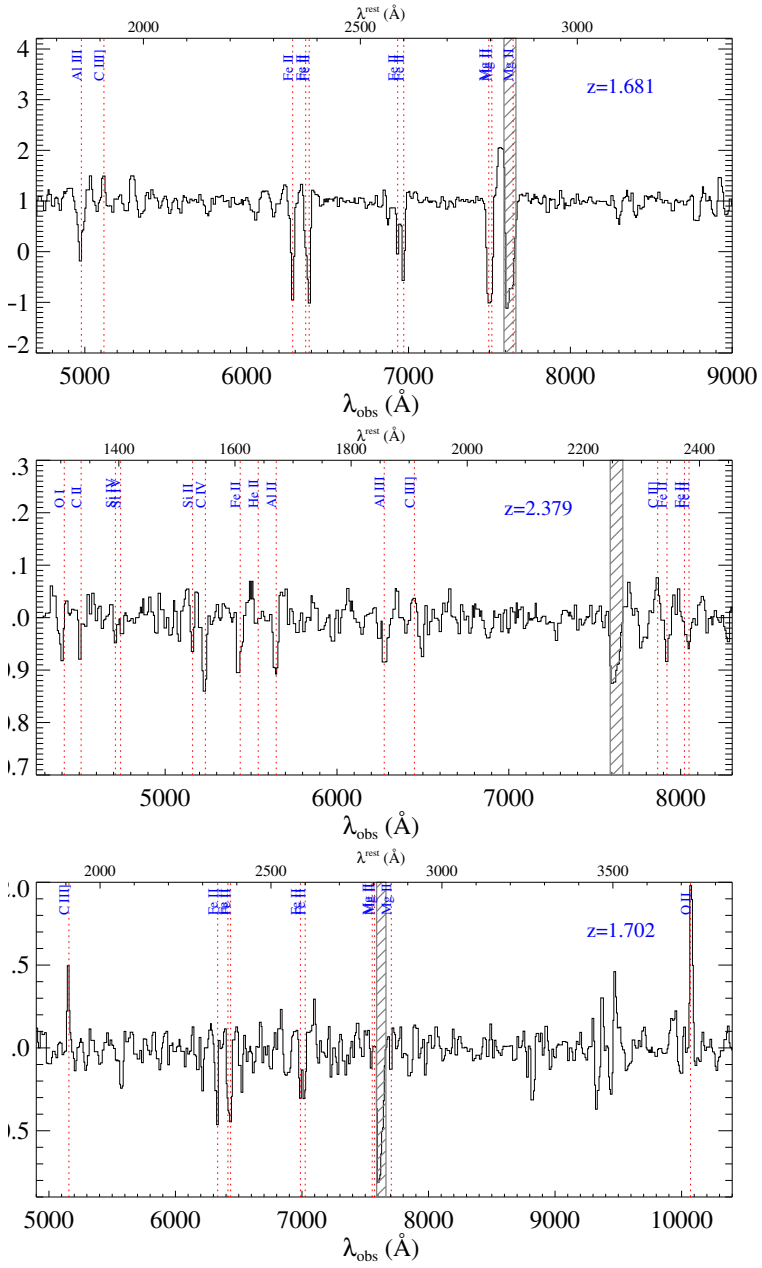

FIGURE 4.2: FORS2/VLT spectra for three lensed galaxies with high confidence redshifts, labeled as class 3. The spectra are displayed in the observer/rest-frame in the bottom/top axis, and smoothed to match the spectral resolution of the data. The locations of spectral lines are identified by dashed red lines and labeled with their corresponding ion. The telluric A Band absorption feature is indicated by a vertical shaded region. From top to bottom the spectra in each panel correspond to the following source/multiple-image objects in Tab. 4.2: a) RCS2 J0004−0103, image S1.1; b) RCS2 J0034+0225, image S1.1; c) RCS2 J0327+1326 image S1.2.

lamp observations. Since the sky subtraction was a complicated task because most of the giant arcs are very long objects and they usually obstructed almost the entire slit, and therefore the background subtraction was sometimes carried out independently. The other advanced steps consisted on the removal of cosmic rays, the 1D spectra extraction

and the average of multiple spectra for each source. These steps were done using our own IDL codes[5], inspired in the optimal extraction algorithm by Horne (1986).

4.3 Analysis and results

4.3.1 Redshift measurements

The spectroscopic redshifts were determined by two independent methods: 1) by cross-correlating the spectra with galaxy spectral templates of the SDSS DR7 using the RVSAO/XCSAO package for IRAF[6] (Kurtz and Mink, 1998). This method yielded accurate redshift measurements for high signal-to-noise spectra. However, half of the lensed galaxies as well as the member galaxies of clusters at high redshift possess a medium/low signal-to-noise, and thus, the redshift results of these cross-correlations have low reliability. 2) In order to determine reliable spectroscopic redshift for all galaxies, we assigned redshifts to individual spectra by identifying a set of lines at a common redshift, fitting a gaussian profile to each line to determine the central wavelength for each line, and taking the mean redshift of the entire set of lines. The redshift measurements for cluster member galaxies are derived from at least three lines, which are the most common in older stellar populations (e.g., CaII H&K λ3934, 3969 Å, g-band λ4306Å, MgI λ5169, 5174, 5185Å, and NaI λ5891, 5894, 5897 Å). Instead, the spectroscopic redshifts of the lensed galaxies were determined by comparison with a varied set of emission and absorption lines. Most of the observed emission lines corresponded to [OII] λ3727 Å, H$-\beta$ λ4862 Å, [OIII] λ4960, 5007Å and H$-\alpha$ λ6563 Å. These are typical emission lines of actively forming stars regions. Due to our instrument setup this set of lines appeared only in the lensed galaxies at $z \lesssim 1.7$. For the background sources at higher redshifts, we had relied on rest-frame UV features to determine their redshifts. The more common absorption lines corresponded to MgII λ2796, 2803 Å, λFeII 2344, 2372, 2384, 2586, 2600 Å, CIV λ1548, 1551 Å, SiII λ1260, 1527 Å, and SiIV λ1394, 1403 Å.

Redshift errors were mainly due to the combination of the uncertainty in our wavelength calibrations and the statistical uncertainty in the identification of line centers. The median RMS in the wavelength calibration was $\sim$ 1.4 Å, which at a central wavelength of $\sim$ 7000 Å, results in redshift errors of $\sim \pm 0.0002$. The redshift errors for the high signal-to-noise spectra were distributed around $\sim \pm 0.0005$. This is in agreement with

[5]http://www.astro.puc.cl/ mcarrasc/RCS/spec/

[6]IRAF is distributed by the National Optical Astronomy Observatories, which are operated by the Association of Universities for Research in Astronomy, Inc., under cooperative agreement with the National Science Foundation.

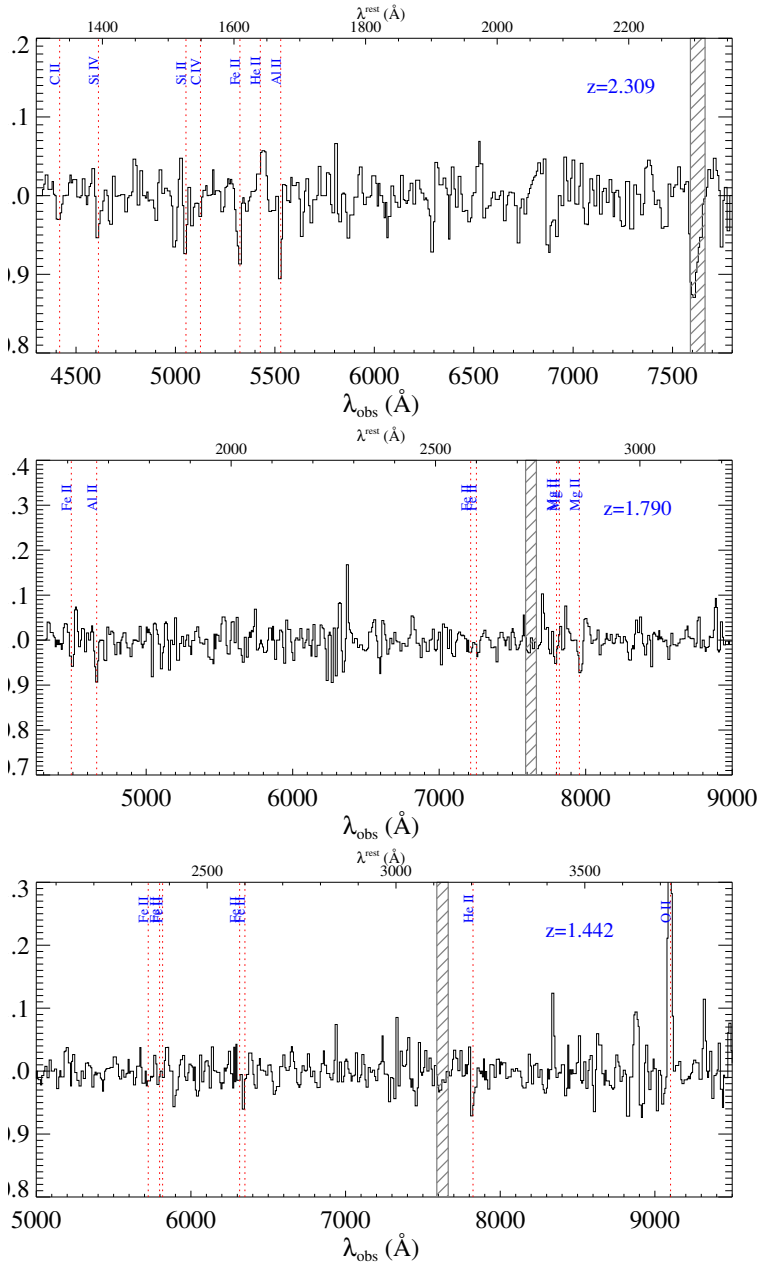

FIGURE 4.3: FORS2/VLT spectra for three lensed galaxies with medium confidence redshift measurements, class 2 objects. The spectra are displayed in the same manner as in Fig. 4.2. From top to bottom the spectra in each panel correspond to the following source/multiple-image objects in Tab. 4.2: RCS2 J1250+0244, image S1.2; RCS2 2329−0102, image S1.2; RCS2 J2329−1317, image S1.1.

the expected ones, since we have to add the uncertainties in the line center identifications. However, these errors increase for low signal-to-noise spectra, which showed errors between $\sim \pm 0.001 - 0.01$.

Following the work done by Bayliss et al. (2011), we classified our redshift measurements into four classes, which describe the confidence level of the redshift measurements. Class

3 redshifts are the highest confidence measurements, typically measured from more than 4 absorption and/or emission features. These redshift measurements are definitive, with essentially no chance of misinterpretation. Most of the redshifts reported here are of this classification. In Fig. 4.2 we show examples of three class 3 spectra. Class 2 redshifts are medium confidence measurements. This classification is based on at least two high-significance lines and/or a larger number of low-significance features. The redshifts with this classification are very likely to be the real redshifts. Fig. 4.3 shows three examples of these class 2 spectra. Class 1 redshifts are low-confidence measurements, which correspond to those displaying few low-significance spectral features. The redshift measurements in these cases represent the "best-guess" redshift using the available spectral data. Three examples of Class 1 spectra are shown in Fig. 4.4. Finally, we have the class 0 redshift for those cases where the spectral analysis shows no evidence of some spectral features.

Our FORS2/VLT spectroscopy have yielded $\gtrsim$ 1500 science spectra which have been used to determine cluster members, cluster redshifts, and velocity dispersion of the clusters, as well as to corroborate that the elongated galaxies and giant arcs correspond to background objects. In fact, our spectroscopy have confirmed that 51 of these lensed galaxies correspond to 34 background sources at high redshifts that are clearly distorted by the gravitational potential of the cluster cores. In Tab. 4.2 we reported our redshift measurements for the giant arcs and the lensed galaxies, which are labeled in Appendix C as those lensed images used to constrain our the SL models (Chapter 5). All spectra corresponding to the 34 background sources are showed in the Appendix B.

4.3.2 Cluster redshift and velocity dispersion

The correctly determination of cluster members is of great importance to avoid biases in the velocity dispersion measurements (Beers et al., 1990). In this analysis, the cluster member galaxies are determined by applying a cut in (rest-frame) velocity space of 4000km s^{-1}, and then by applying the 3σ clipping method. This selection method is iterated until the number of members is stable, which usually occurs after the second iteration. As sanity check, we have also applied the shifting gapper method (Fadda et al., 1996) to those clusters with a large number of galaxies falling into the $\pm$4000km s^{-1}. In this double check we obtained the same number of cluster members, determining the robustness of our method.

Our selection method have recovered $\sim$ 650 member galaxies. Furthermore, we have also included redshift measurements from the Gemini spectroscopy data (García et al 2014 in preparation), of which 39 correspond to the cluster member galaxies of RCS2

TABLE 4.2: Individual lensed galaxies

Cluster Lens	Lensed galaxy[d]	R.A.[c] (J2000)	Dec[c] (J2000)	z	Classification
RCS2 J0004−0103	S1.1	00 04 51.59	-01 03 19.8	1.681	3
RCS2 J0034+0225	S1.1	00 34 27.35	+02 25 14.1	2.379	3
–	S1.2	00 34 27.39	+02 25 22.1	2.379	3
RCS2 J0038+0215	S1.1	00 38 55.92	+02 15 48.9	2.817	3
–	S1.3	00 38 55.90	+02 15 56.8	2.817	3
RCS2 J0047+0507	S1.3	00 47 51.12	+05 08 27.7	1.629	2
RCS2 J0052+0433	S1.2	00 52 07.73	+04 33 34.5	1.853	2
–	S2.1	00 52 10.57	+04 33 25.3	1.732	2
–	S2.2	00 52 10.94	+04 33 28.8	1.732	2
RCS2 J0057+0209	S1.1	00 57 27.98	+02 09 26.6	0.775	1
–	S1.2	00 57 27.66	+02 09 27.5	0.775	1
RCS2 J0252−1459	S1.2	02 52 41.74	-14 59 33.2	1.096	3
RCS2 J0309−1437	S1.1	03 09 44.99	-14 37 16.1	1.519	3
–	S2.1	03 09 45.33	-14 37 16.2	1.413	2
RCS2 J0327−1326[a]	S1.1	03 27 26.63	-13 26 15.4	1.701	3
–	S1.2	03 27 27.19	-13 26 54.3	1.701	3
–	S2.4	03 27 28.36	-13 26 15.6	1.702	3
RCS2 J0859−0345[e]	S1.3	08 59 14.30	-03 45 12.5	2.000	0
RCS2 J1055−0459	S1.1	10 55 36.28	-04 59 41.7	2.804	3
–	S1.2	10 55 35.91	-04 59 38.4	2.804	3
RCS2 J1101−0602	S1.1	11 01 53.95	-06 02 31.3	1.931	1
RCS2 J1108−0456	S1.1	11 08 16.24	-04 56 23.3	1.475	1
–	S4.1	11 08 17.31	-04 56 17.0	1.390	1
RCS2 J1111+1408	S1.1	11 11 24.26	+14 09 01.6	2.140	3
RCS2 J1119−0728	S1.1	11 19 12.26	-07 28 14.0	2.062	1
RCS2 J1125−0628	S1.1	11 25 29.21	-06 28 48.9	1.514	1
–	S1.2	11 25 28.96	-06 28 49.8	1.514	1
RCS2 J1250+0244	S1.2	12 50 42.20	+02 44 31.2	2.309	2
RCS2 J1511+0630	S1.2	15 11 44.39	+06 30 31.2	1.295	1
RCS2 J1517+1003	S1.1	15 17 03.75	+10 03 32.9	2.239	3
–	S1.2	15 17 03.95	+10 03 25.9	2.239	3
RCS2 J1519+0840	S1.1	15 19 30.04	+08 40 05.4	2.371	3
–	S1.2	15 19 30.07	+08 39 53.2	2.371	3
RCS2 J1526+0432	S1.1	15 26 13.94	+04 33 02.0	1.443	3
–	S2.1	15 26 15.73	+04 32 42.7	2.636	2
SDSS J2111−0114[b]	S1.2	21 11 18.91	-01 14 31.9	2.856	3
–	S1.3	21 11 20.22	-01 14 33.0	2.856	3
–	S2.3	21 11 20.40	-01 14 30.8	2.856	3
RCS2 J2135−0102	S1.1	21 35 12.08	-01 03 36.7	2.319	3
–	S1.2	21 35 11.46	-01 03 34.3	2.319	3
–	S1.3	21 35 09.94	-01 03 18.0	2.319	3
–	S2.1	21 35 10.17	-01 03 33.8	0.903	3
RCS2 J2147−0102	S1.2	21 47 37.12	-01 02 56.3	2.699	1
RCS2 J2151−0138	S1.1	21 51 26.87	-01 38 41.1	0.835	2
RCS2 J2313−0104	S1.2	23 13 54.54	-01 04 56.6	1.845	1
RCS2 J2329−1317	S1.1	23 29 10.33	-13 17 44.3	1.441	2
–	S1.2	23 29 10.03	-13 17 41.7	1.441	2
RCS2 J2329−0120	S1.2	23 29 47.18	-01 20 45.4	1.790	2
–	S2.1	23 29 47.87	-01 20 53.6	1.570	3
–	S2.2	23 29 47.74	-01 20 53.6	1.570	3
RCS2 J2336−0608	S1.1	23 36 20.54	-06 08 38.4	1.295	1
–	S1.2	23 36 20.38	-06 08 33.8	1.295	1

[a] Previously described in Wuyts et al. (2010) and Sharon et al. (2012).
[b] Also reported in Bayliss et al. (2011) and Oguri et al. (2012).
[c] Coordinates of the multiple images used in the SL models in the Chapter 5.
[d] Lensed galaxy labels matching those in Figs. C.1 − C.5 (Appendix C).
[e] The spectroscopic redshift measurement failed. Class 0.

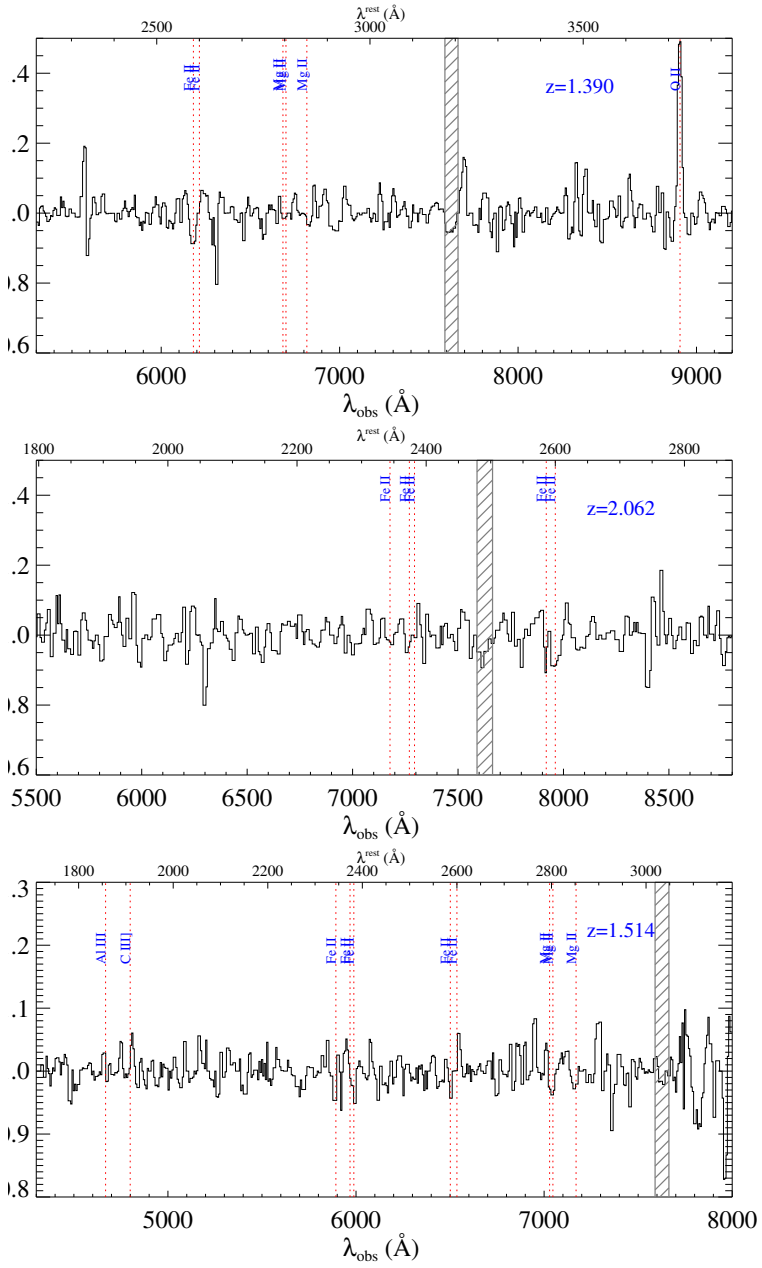

FIGURE 4.4: FORS2/VLT spectra for three lensed galaxies with low confidence redshift measurements, label as class 1. The spectra are displayed in the same manner as in Fig. 4.2. From top to bottom the spectra in each panel correspond to the following source/multiple-image objects in Tab. 4.2: RCS2 J1108−0456, image S4.1; RCS2 J1119−0728, image S1.1; RCS2 J1125−0628, image S1.1.

J0327−1326. Finally, from this exhaustive analysis we have recovered a total of 689 spectroscopically confirmed cluster members, which have been used to compute robust measurements of the cluster redshift, z_c, and the rest-frame velocity dispersion of the clusters, $\sigma_{cluster}$, by applying the biweight estimator (Beers et al., 1990). The redshift results for all cluster members are reported in the Appendix D in Tab. D.1 We summarized the main results of our FORS2/VLT spectroscopy in the Tab. 4.3, while the

TABLE 4.3: Summary of dynamical properties of RCSGA clusters

Name	R.A.[c] (J2000)	Dec[c] (J2000)	z	N[d]	$\sigma_{cluster}$[e] [km s^{-1}]	M_{200} [$h^{-1}10^{14}M_{\odot}$]	r_{200} [$h^{-1}Mpc$]
RCS2 J0004−0103	00 04 52.001	−01 03 16.58	0.5147 ± 0.0009	9	502 ± 144	0.77 ± 0.50	0.57 ± 0.16
RCS2 J0034+0225	00 34 28.134	+02 25 22.34	0.3845 ± 0.0007	26	713 ± 179	2.36 ± 1.53	0.88 ± 0.22
RCS2 J0038+0215	00 38 55.898	+02 15 52.35	0.6962 ± 0.0010	20	778 ± 105	2.54 ± 1.03	0.80 ± 0.11
RCS2 J0047+0507	00 47 50.787	+05 07 52.30	0.4279 ± 0.0012	13	878 ± 279	4.28 ± 2.78	1.05 ± 0.33
RCS2 J0052+0433	00 52 10.352	+04 33 33.31	0.7237 ± 0.0027	5	597 ± 404	1.14 ± 0.74	0.60 ± 0.40
RCS2 J0057+0209	00 57 27.869	+02 09 33.98	0.2931 ± 0.0009	19	939 ± 160	5.65 ± 2.87	1.22 ± 0.21
RCS2 J0252−1459	02 52 41.474	−14 59 30.38	0.2689 ± 0.0017	19	1610 ± 356	28.40 ± 18.50	2.10 ± 0.46
RCS2 J0309−1437	03 09 44.096	−14 37 34.38	0.8078 ± 0.0010	17	669 ± 123	1.52 ± 0.83	0.64 ± 0.12
RCS2 J0327−1326[a]	03 27 27.174	−13 26 22.90	0.5637 ± 0.0020	62	988 ± 122	12.25 ± 4.54	1.80 ± 0.22
RCS2 J0859−0345	08 59 14.486	−03 45 14.63	0.6486 ± 0.0029	8	912 ± 555	4.20 ± 2.73	0.96 ± 0.58
RCS2 J1055−0459	10 55 35.647	−04 59 41.60	0.6078 ± 0.0007	29	692 ± 84	1.89 ± 6.87	0.75 ± 0.09
RCS2 J1101−0602	11 01 54.093	−06 02 32.02	0.4864 ± 0.0013	8	573 ± 201	1.16 ± 0.76	0.67 ± 0.23
RCS2 J1108−0456	11 08 16.835	−04 56 37.62	0.4106 ± 0.0008	32	938 ± 154	5.26 ± 2.58	1.14 ± 0.19
RCS2 J1111+1408	11 11 24.483	+14 08 50.82	0.2207 ± 0.0008	20	907 ± 121	5.30 ± 2.11	1.22 ± 0.16
RCS2 J1119−0728	11 19 11.925	−07 28 17.51	1.0131 ± 0.0033	4	670 ± 338	1.35 ± 0.88	0.57 ± 0.29
RCS2 J1125−0628	11 25 28.940	−06 28 39.04	0.4745 ± 0.0009	13	596 ± 198	1.32 ± 0.86	0.70 ± 0.23
RCS2 J1250+0244	12 50 41.890	+02 44 26.57	0.6910 ± 0.0009	16	655 ± 115	1.53 ± 0.80	0.67 ± 0.12
RCS2 J1511+0630	15 11 44.681	+06 30 31.79	0.5516 ± 0.0009	15	444 ± 210	0.52 ± 0.34	0.50 ± 0.23
RCS2 J1517+1003	15 17 02.587	+10 03 29.27	0.6434 ± 0.0007	31	755 ± 117	2.41 ± 1.11	0.80 ± 0.12
RCS2 J1519+0840	15 19 31.213	+08 40 01.43	0.3177 ± 0.0009	36	1140 ± 117	9.92 ± 3.05	1.45 ± 0.15
RCS2 J1526+0432	15 26 14.914	+04 32 48.01	0.6344 ± 0.0007	30	735 ± 89	2.23 ± 0.81	0.78 ± 0.09
SDSS J2111−0114[b]	21 11 19.307	−01 14 23.95	0.6364 ± 0.0012	28	1072 ± 141	6.85 ± 2.69	1.13 ± 0.15
RCS2 J2135−0102	21 35 12.040	−01 02 58.27	0.3277 ± 0.0006	79	1192 ± 85	11.30 ± 2.41	1.51 ± 0.11
RCS2 J2147−0102	21 47 37.172	−01 02 51.93	0.8832 ± 0.0026	15	908 ± 547	3.61 ± 2.35	0.83 ± 0.50
RCS2 J2151−0138	21 51 25.950	−01 38 50.14	0.3147 ± 0.0008	35	1054 ± 125	7.86 ± 2.78	1.35 ± 0.16
RCS2 J2313−0104	23 13 54.514	−01 04 48.46	0.5279 ± 0.0010	12	625 ± 245	1.47 ± 0.96	0.71 ± 0.28
RCS2 J2329−1317	23 29 09.528	−13 17 49.26	0.3917 ± 0.0007	64	1097 ± 115	8.4 ±7 2.66	1.34 ± 0.14
RCS2 J2329−0120	23 29 47.782	−01 20 46.89	0.5274 ± 0.0010	6	358 ± 213	0.2 ±8 0.18	0.41 ± 0.24
RCS2 J2336−0608	23 36 20.838	−06 08 35.81	0.3927 ± 0.0008	36	1041 ± 113	7.2 ±4 2.36	1.27 ± 0.14

[a] Previously described in Wuyts et al. (2010) and Sharon et al. (2012).
[b] Also reported in Bayliss et al. (2011) and Oguri et al. (2012).
[c] Coordinates are BCG centroids (J2000). The SL models are centered at these coordinates.
[d] Number of spectroscopically confirmed members.
[e] The rest-frame velocity dispersion of the clusters.

velocity histograms for the full sample are plotted in the Figs. 4.7, 4.6, and 4.7.

4.4 Dynamical masses

The computing of dynamical mass from the velocity dispersion of the cluster members requires a good understanding of the relationship between the velocity dispersion of dark matter particles, σ_{DM}, in the cluster-size halos and the velocity dispersion of the cluster members, $\sigma_{cluster}$. This relationship is known as *the velocity bias factor* and it is given by $b_v = \sigma_{cluster}/\sigma_{DM}$. Numerical N-body simulations have shown that this bias factor is in the range of $b_v \sim 1.0 - 1.3$ (Diemand et al., 2004). Although, more recent theoretical works have indicated that the way in which subhalos are tracked and defined in simulations affects the resulting velocity bias predictions (Evrard et al., 2008; White et al., 2010). These recent simulation results have shown no evidence for a velocity bias

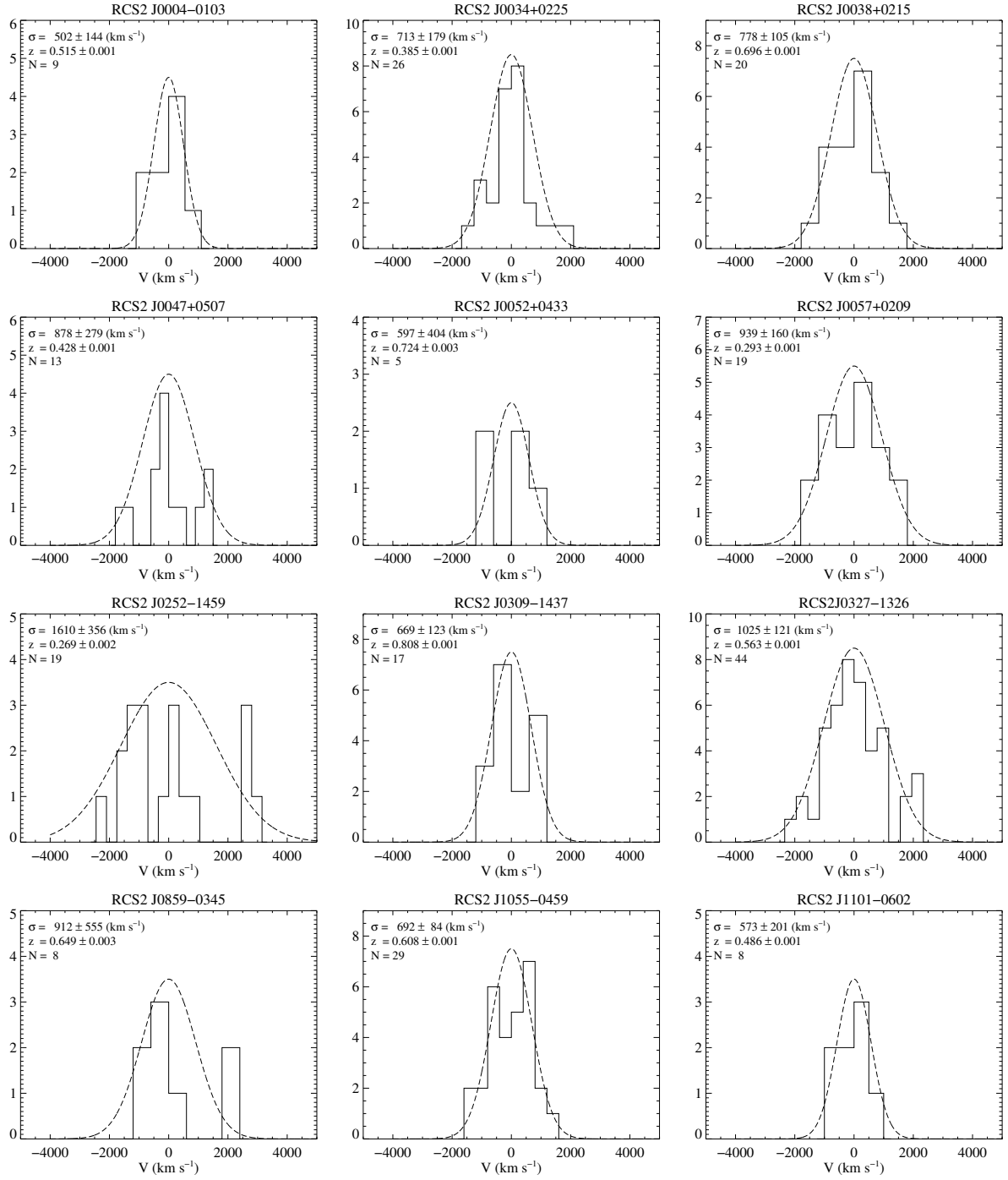

FIGURE 4.5: This figure shows the velocity histograms for 12 of our clusters. Each velocity histogram is labeled at the top with the name of its cluster, its rest-frame velocity dispersion, redshift, and the number of cluster members spectroscopically confirmed. The best-fitting gaussian functions are overplotted for each cluster (dashed line) with the mean and standard deviation values from the bi-weight estimator.

factor, i.e., $b_v \sim 1.0$. Thus, in this thesis we assume no velocity bias when dynamical masses are computed.

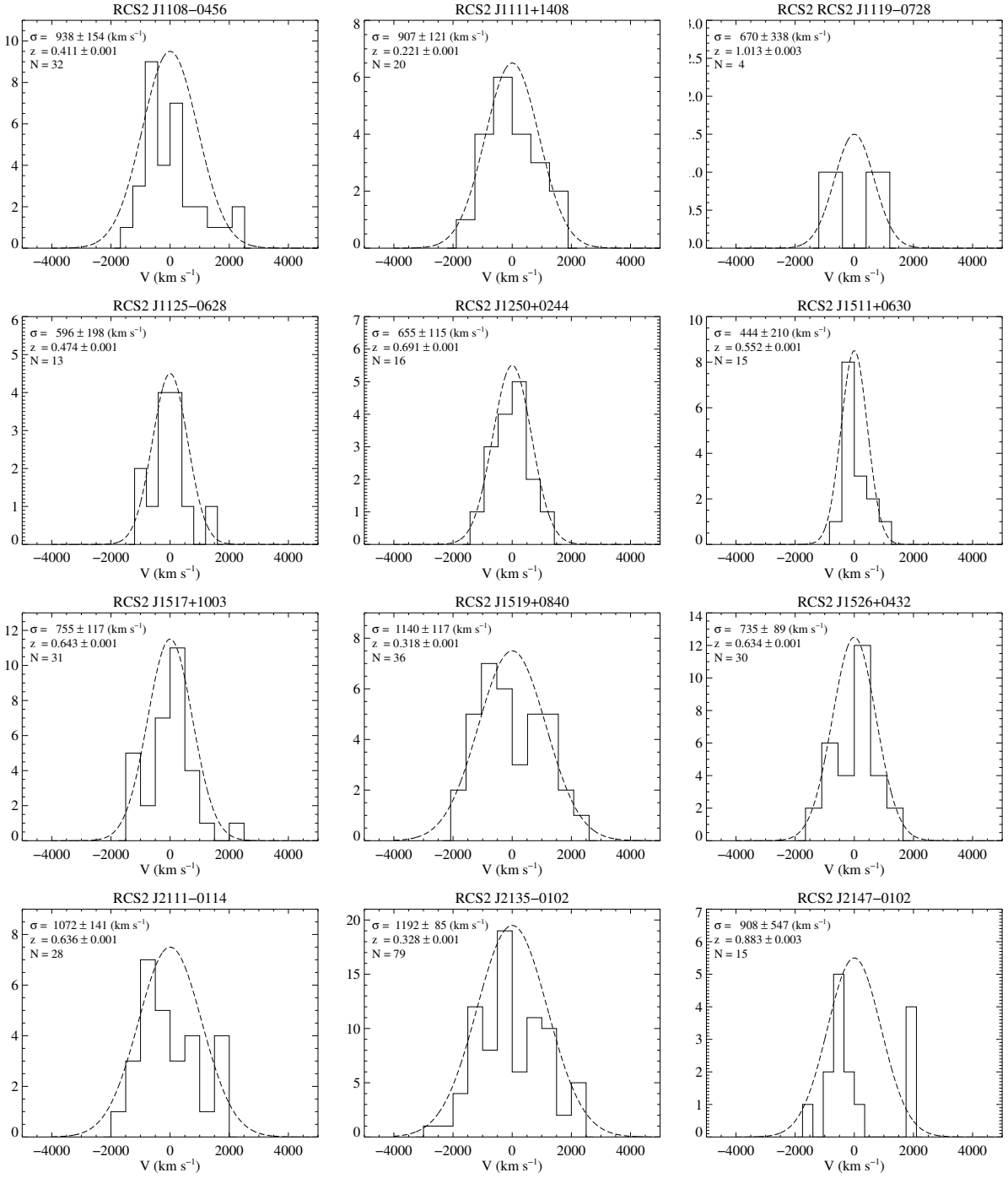

FIGURE 4.6: This figure shows the velocity histograms and gaussian function fits for 12 of our clusters in the same way as those presented in the previous figure.

Therefore, the dynamical masses of our clusters are then calculated by using the relation between the DM velocity dispersion, σ_{DM}, and the total mass of the halo, M_{200}, from Evrard et al. (2008), which is given by[7]:

[7]This relation was already presented in §2.3.1.1

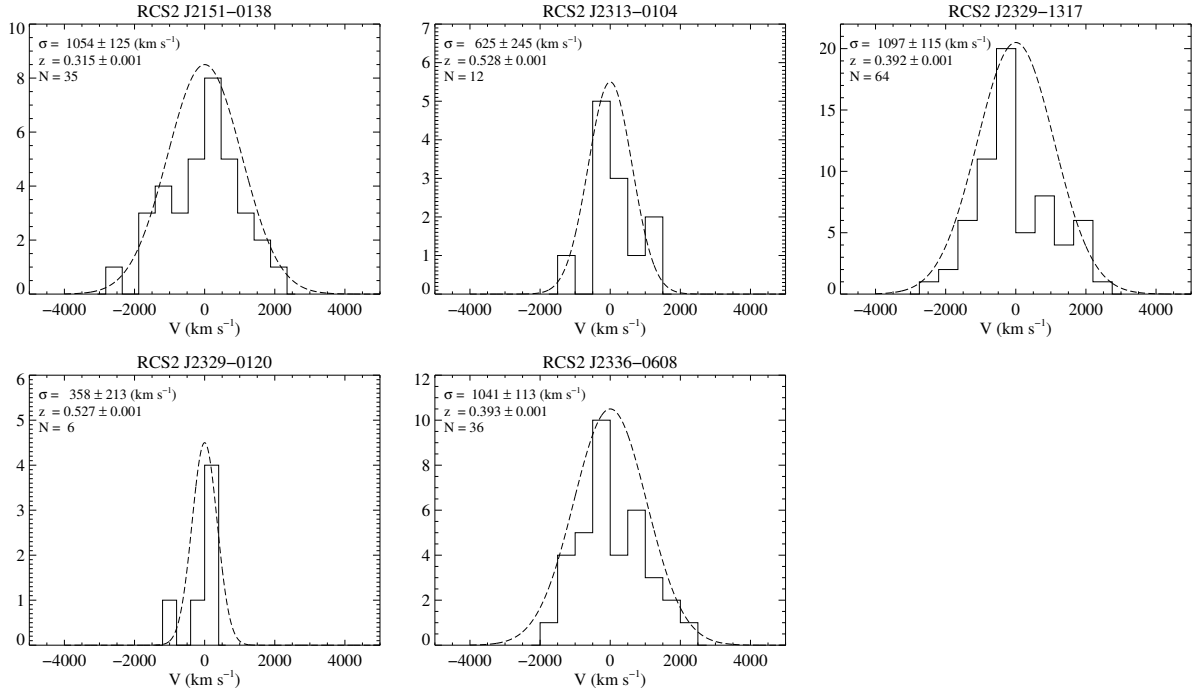

FIGURE 4.7: This figure shows the velocity histograms and gaussian function fits for 5 of our clusters in the same way as those presented in the previous figure.

$$M_{200} = \frac{10^{15}}{h(z)} \left(\frac{\sigma_{DM}}{\sigma_{15}} \right)^{1/\alpha} M_{\odot} \tag{4.1}$$

where σ_{15} is the normalization at mass $10^{15} h^{-1} M_{\odot}$, α is the logarithmic slope, $h(z) = H(z)/100$ km s^{-1} Mpc^{-1} is the normalized Hubble parameter at redshift z for a flat universe, and σ_{DM} is the one-dimension velocity dispersion of the DM particles within r_{200}. The best-fits yielded $\sigma_{15} = 1082.9 \pm 4.0$ km s^{-1} and $\alpha = 0.3361 \pm 0.0026$.

The dynamical masses derived from Eq. 4.1 are also reported in the Tab. 4.3, as well as their respective radius r_{200}, which have been calculated using M_{200} and assuming spherical clusters (i.e., $M_{200} = 200\rho_c \times 4\pi r_{200}^3/3$).

It should be noted that our dynamical mass estimates could be biased mainly by two factors: 1) the modest number of spectroscopically confirmed cluster members to perform the statistic, and 2) the selection function to "select" the sample. To investigate the former, we review the work done by White et al. (2010). They studied the relationship between σ_{DM} and $\sigma_{cluster}$ for individual simulated halos as a function of the number of available spectroscopic cluster members. Their theoretical results showed that cluster-size halos with more than 50 spectroscopic members present an intrinsic scatter of $\sim 15\%$ between the DM particles velocity dispersions and the "observed" ones. They also found that this scatter is a steep function of the number of observed members, reaching a

scatter as high as 30% for halos with less than 10 observed members. However, our sample has on average 24 members per cluster and there are only six systems with less than 10 spectroscopically confirmed members. Therefore, we can conclude that our mass measurements are not strongly biased by systematic errors associated with the modest number of cluster member redshifts available. The second possible source of bias is related to the selection function. The clusters in this sample were selected by SL, and it has been shown that the SL population are on average more concentrated and massive than the rest of the normal cluster population (Hennawi et al., 2007; Meneghetti et al., 2010; Oguri and Blandford, 2009). The excess of concentration in this cluster population is mainly due to triaxiality and projection effects. Numerical simulations have shown that the cluster-size halos appear to be triaxial, and clusters that are efficient strong lenses are more likely to have their major axes aligned along the line of sight with respect to us. Therefore, we assume that our SL selected clusters have this orientation bias. We are measuring the projected velocity dispersion of galaxies that should tend to be preferentially aligned along the major axis of the cluster potential and consequently, our velocity dispersion measurements could be overestimated with respect to velocity dispersions measured for clusters that are randomly oriented on the sky. Bayliss et al. (2011) found that in the worst case scenario (for a total alignment), the measured velocity dispersions could be biased on average about $\sim 18\%$ to higher values than in normal cluster populations, which results in mass estimates that are biased high by $\sim 63\%$ on average, when the Evrard et al. (2008) relation is used. However, this is the most extreme case for orientation bias, corresponding to a sample of clusters that are all aligned with their major axes pointing along the line of sight.

To figure out a possible overestimation in our mass measurements, we compare the relation between dynamical masses derived from the observed velocity dispersions in this work and their corresponding effective Einstein radii (for a source at $z_s = 2.0$), with the relation between WL masses derived by Oguri et al. (2012) and their effective Einstein radii (also for a source at $z_s = 2.0$). These relations are shown in the Fig. 5.1. This figure clearly indicates that the effective Einstein radii and dynamical masses are well correlated with each other, showing that the more massive clusters derived from dynamical analysis have larger effective Einstein radii on average. This figure also shows that both samples present practically the same correlation between total mass and Einstein radius. Since in Oguri et al. (2012) the mass measurements were derived from a WL analysis, these estimates should not be affected by a bias in their velocity dispersions. Therefore, due to this great similarity in both relations, we can conclude that: 1) our dynamical mass measurements are not strongly biased to higher values due to the orientation bias, or 2) both samples are being equally affected by this bias.

Since the probability of the latter is small, we can conclude that our dynamical mass measurements are not strongly affected by the orientation bias.

Once discarded these biases, or at least checked that our sample is not strongly affected by them, we can use these mass estimates for deriving accurate mass distributions from our cluster sample by combining them with spectroscopically confirmed lensed galaxies presented in the cluster cores. This analysis will be presented in the next chapter.

4.5 Summary and conclusions

Here we presented the results of the FORS2/VLT spectroscopy of 29 SL selected galaxy clusters. Our exhaustive analysis yielded a total of 689 cluster members, which were used to measure velocity dispersions and dynamical masses for this cluster sample, covering three orders of magnitude in mass, from $2.80 \times 10^{13} \leq M_{200}/h^{-1}M_{\odot} \leq 2.84 \times 10^{15}$, with a median mass of $M_{200} \sim 3.6 \times 10^{14}h^{-1}M_{\odot}$. This large mass range allows a diverse kinds of studies, such as detailed analysis of the slope and normalization of the $c - M$ relation, and galaxy evolution. Our sample spans a spectroscopic redshift range of $0.22 < z < 1.01$, with a median redshift of $z \sim 0.5$, allowing to explore a possible redshift evolution in the $c - M$ relation. The FORS2/VLT spectroscopy data have also discovered/revealed 51 lensed galaxies, corresponding to 34 background sources at high redshifts that are clearly distorted by the gravitational potential of the cluster cores, and some of them are forming multiple-image systems.

All results presented in this chapter will be used to perform robust mass reconstructions of these clusters by combining SL constraints and dynamical masses. These mass models will be presented in the next chapter.

Chapter 5

The observed concentration-mass relation for 73 galaxy clusters

This thesis aims to contribute with the understanding of the mass distribution in galaxy clusters. In particular, it focuses in the relation between the concentration of the cluster halos and their total masses. In order to derive the most complete analysis of the concentration mass ($c - M$) relation, the results obtained in this thesis are combined with two previously well studied samples of galaxy clusters.

We derive the concentration parameter by a meticulous strong lensing and dynamical mass analysis. We reconstruct the inner mass distribution of our clusters using the well tested parametric method LENSTOOL (Jullo et al., 2007). Furthermore, to fully constrain the density profile and measure accurate and reliable concentration parameters of our clusters, we explore an innovative technique which consists in the combination of strong lensing signatures with velocity dispersions and dynamical masses, implemented in LESNTOOL by Verdugo et al. (2011). As it will be described below, this approach yields results equivalent to those obtained from the combination of strong and weak lensing constrains, allowing us to probe mass distributions at larger radii in a way as good as done by using weak lensing analysis. In practice, we use velocity dispersions, dynamical masses, and virial radii as priors in our models to probe the outer regions in the mass distributions and increasing the number of constraints in our optimization process.

5.1 The sample

In this work we use a new sample of 29 strong lensing (SL) selected galaxy clusters from the RCSGA survey. This sample has been detailed in chapter 4. In brief, the 29 clusters span a spectroscopic redshift range of $0.22 < z < 1.01$, with a median redshift of $z \sim 0.5$. The FORS2/VLT spectroscopic observations have yielded ~ 650 cluster members. Then, we have also include GMOS/Gemini and GISMO/Magellan spectroscopic data to our analysis. In total, we have recovered 689 member galaxies, which are used to measure velocity dispersions and dynamical masses, covering three orders of magnitude in mass, from $2.80 \times 10^{13} \leq M_{200}/h^{-1}M_{\odot} \leq 2.84 \times 10^{15}$, with a median mass of $M_{200} \sim 3.6 \times 10^{14} h^{-1} M_{\odot}$. Besides, we have confirmed 51 lensed galaxies corresponding to 34 background sources at high redshifts that are clearly distorted by the gravitational potential of the cluster cores. This sample and their main features are summarized in Tabs. 4.2 and 4.3.

Furthermore, we have included in our $c-M$ relation analysis the cluster sample studied by Oguri et al. (2012) (hereafter O12) and by Merten et al. (2014) (hereafter M14). The former is a subset of the SL selected clusters from the Sloan Giant Arcs Survey (SGAS; Bayliss et al., 2011; Hennawi et al., 2008), while the second is a subset of the X-ray selected clusters from the Cluster Lensing and Supernova survey with Hubble (CLASH; Postman et al., 2012). We have also included the PLCK G004.5−19.5 cluster (Sifón et al., 2014), in where we have derived the concentration parameter using the same technique described in this thesis.

5.2 Strong lensing and dynamical mass analysis

We have used the parametric method described in Kneib (1993) and implemented in the Markov Chain Monte Carlo (MCMC) code LENSTOOL (Jullo et al., 2007) to perform the models of all clusters studied in this thesis.

The full details of this methodology were presented in chapter 3. All mass models for the RCSGA sample derived by using this technique (in terms of their critical curves and predicted images) together with their best-fitting mass model parameters are presented in the Appendix C.

TABLE 5.1: The effective Einstein radius

Name	z^d_{arc}	SL only		SL and Dy. Mass	
		$\theta_E(z_s = z_{arc})$ $[arcsec]$	$\theta_E(z_s = 2)$ $[arcsec]$	$\theta_E(z_s = z_{arc})$ $[arcsec]$	$\theta_E(z_s = 2)$ $[arcsec]$
RCS2 J0004−0103	1.681 ± 0.001	3.8 ± 0.5	4.4 ± 0.5	3.7 ± 0.4	4.1 ± 0.5
RCS2 J0034+0225	2.374 ± 0.004	18.5 ± 3.8	16.5 ± 3.7	17.5 ± 3.8	15.5 ± 3.6
RCS2 J0038+0215	2.817 ± 0.001	7.0 ± 1.8	5.8 ± 1.2	7.4 ± 1.4	5.6 ± 1.6
RCS2 J0047+0507	1.629 ± 0.001	5.6 ± 1.2	6.4 ± 1.0	5.5 ± 1.3	6.4 ± 1.3
RCS2 J0052+0433	1.853 ± 0.001	16.9 ± 2.4	17.3 ± 2.4	15.9 ± 2.6	17.5 ± 2.6
RCS2 J0057+0209	0.775 ± 0.001	10.4 ± 1.5	19.8 ± 2.8	11.2 ± 1.7	20.4 ± 2.8
RCS2 J0252−1459[g]	1.096 ± 0.001	2.6 ± 0.3	4.3 ± 0.4	2.6 ± 0.4	4.2 ± 0.5
RCS2 J0309−1437	1.519 ± 0.001	14.2 ± 3.2	10.3 ± 2.3	14.2 ± 2.9	10.5 ± 1.8
RCS2 J0327−1326[a]	1.701 ± 0.001	20.6 ± 2.6	22.5 ± 2.8	20.8 ± 2.6	22.6 ± 2.8
RCS2 J0859−0345[e]	2.0 ± 1.0	5.1 ± 0.6	5.1 ± 0.6	5.2 ± 0.6	5.2 ± 0.6
RCS2 J1055−0459[g]	2.800 ± 0.003	7.9 ± 1.7	7.0 ± 2.8	7.1 ± 1.3	4.8 ± 1.6
RCS2 J1101−0602[g]	1.931 ± 0.001	2.6 ± 0.3	2.7 ± 0.3	2.6 ± 0.3	2.7 ± 0.3
RCS2 J1108−0456[f]	1.475 ± 1.0	12.4 ± 2.6	13.2 ± 2.2	10.3 ± 2.2	11.9 ± 1.9
RCS2 J1111+1408	2.140 ± 0.002	10.4 ± 1.9	10.2 ± 2.5	10.4 ± 1.8	9.8 ± 1.6
RCS2 J1119−0728[f]	2.062 ± 1.0	5.6 ± 1.0	5.5 ± 1.1	5.4 ± 1.2	5.3 ± 0.9
RCS2 J1125−0628[f]	1.514 ± 1.0	8.2 ± 1.6	9.7 ± 1.7	7.5 ± 1.5	8.8 ± 2.2
RCS2 J1250+0244	2.309 ± 0.001	3.7 ± 0.5	3.1 ± 0.4	3.8 ± 0.5	3.2 ± 0.5
RCS2 J1511+0630[f]	1.295 ± 1.0	3.5 ± 0.5	5.5 ± 0.6	3.5 ± 0.4	5.2 ± 0.6
RCS2 J1517+1003	2.239 ± 0.002	17.2 ± 2.4	16.8 ± 2.0	17.2 ± 2.7	16.5 ± 2.7
RCS2 J1519+0840	2.371 ± 0.003	10.1 ± 1.6	9.7 ± 1.1	10.8 ± 1.4	10.5 ± 1.4
RCS2 J1526+0432	1.443 ± 0.001	16.0 ± 2.6	21.5 ± 3.2	15.8 ± 2.6	20.5 ± 3.0
SDSS J2111−0114[b]	2.856 ± 0.003	13.8 ± 2.4	9.8 ± 2.0	12.8 ± 2.3	8.0 ± 1.8
RCS2 J2135−0102	2.319 ± 0.001	33.2 ± 4.3	32.0 ± 4.2	30.2 ± 4.0	29.0 ± 3.9
RCS2 J2147−0102[f]	2.699 ± 1.0	5.2 ± 1.3	3.5 ± 1.1	5.2 ± 1.4	3.5 ± 1.0
RCS2 J2151−0138	0.835 ± 0.001	22.2 ± 3.2	37.5 ± 4.8	22.2 ± 3.2	34.8 ± 4.5
RCS2 J2313−0104[f]	1.845 ± 1.0	7.0 ± 1.3	7.4 ± 1.5	7.2 ± 1.5	7.4 ± 1.6
RCS2 J2329−1317	1.441 ± 0.001	17.1 ± 3.4	19.2 ± 4.1	17.2 ± 3.5	19.5 ± 4.5
RCS2 J2329−0120[e]	2.0 ± 1.0	13.4 ± 2.0	13.4 ± 2.0	13.0 ± 2.1	13.0 ± 2.1
RCS2 J2336−0608[f]	1.295 ± 1.0	10.3 ± 1.7	12.2 ± 1.7	11.3 ± 1.7	12.6 ± 2.0
PLCK G004.5−19.5[c]	1.601 ± 0.001	24.5 ± 3.4	27.7 ± 4.2	24.2 ± 3.0	27.7 ± 3.3

[a] Previously described in Wuyts et al. (2010) and Sharon et al. (2012).
[b] Also reported in Bayliss et al. (2011) and O12.
[c] This cluster belongs to the *Planck* Early SZ sample (Planck Collaboration et al., 2011). Previously described in Sifón et al. (2014), where we used the same technique applied in this work.
[d] For some systems we found more than one multiple-image system. In this case we show the redshift of the main arc used in the models.
[e] The redshift measurements failed.
[f] Low-confidence measurements of the redshift. It corresponds to the best-guess redshift using the available spectral data.
[g] Galaxy-galaxy lens, it is not considered to construct the $c - M$ relation.

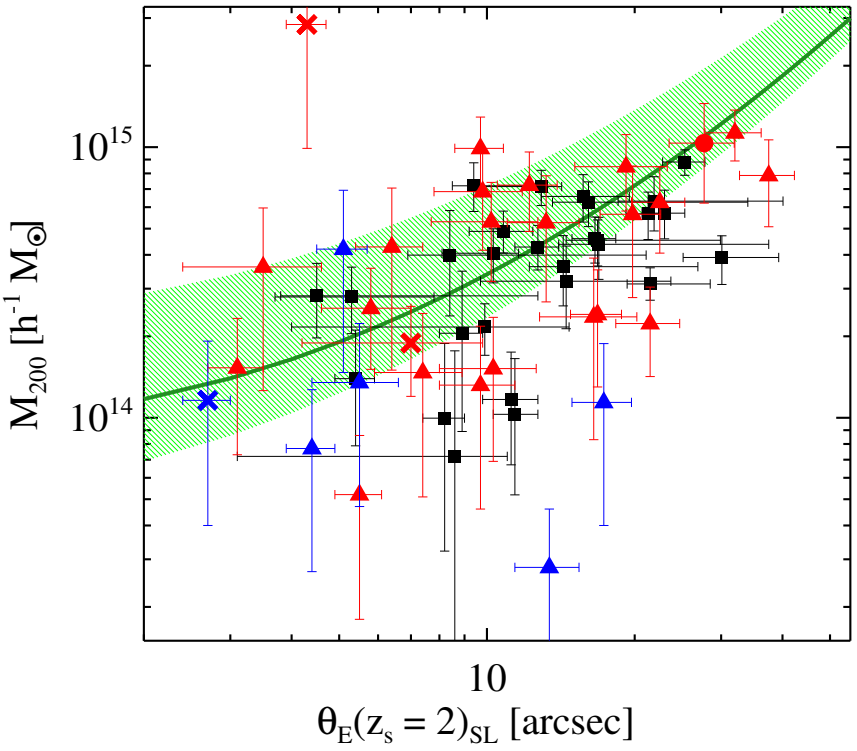

FIGURE 5.1: The correlation between the effective Einstein radius from SL-only analysis and M_{200} from the velocity dispersions derived from the cluster members. The red triangles/crosses correspond to clusters where their velocity dispersions were computed from more than 10 members, while the blue triangles/crosses correspond to systems with a lower number of members. The three crosses correspond to potential galaxy-galaxy lenses, which are left out of our analysis. The red circle corresponds to the PLCK G004.5−19.5 cluster. The black squares represent the Einstein radii derived to the SGAS sample in O12. The green line and shaded region correspond to the expected $Er - M_{200}$ correlation, assuming $c_{200} \simeq 4.9$ and its scatter, respectively.

5.3 Concentration – mass relation of the RCSGA sample

5.3.1 Correlation between the observables

In order to check if dynamical masses are good tracers of the total mass as weak lensing masses are, we compare dynamical masses with Einstein radii, since both quantities measure directly the cluster mass at different radius. We compute the effective Einstein radius θ_E as the radius within which the averaged convergence $\bar{\kappa}(\theta_E)$ is equal to 1 (Meneghetti et al., 2011; Zitrin et al., 2011a),

$$1 - \bar{\kappa}(\theta_E) = 0. \tag{5.1}$$

To normalize the results in our sample and to compare with other cluster samples, we compute convergence maps for all clusters for a source redshift at $z_s = 2.0$. Then, the effective Einstein radius is derived by applying Eq. 5.1. Dynamical masses are directly computed from the cluster velocity dispersions by applying the relation between the total mass of DM halos and their DM velocity dispersion (Chapters 3 and 4, Evrard et al., 2008).

In Fig. 5.1 we visualize the correlation between the effective Einstein radius from SL-only analysis and M_{200} from our dynamical study. The red triangles/crosses correspond to clusters where their velocity dispersions were computed from more than 10 members, while the blue triangles/crosses correspond to systems with a lower number of members. The three crosses in the $Er-M_{200}$ plane correspond to clusters where was found only one multiple-image system per cluster, which seem to be more affected by the gravitational potential of the BCG than by the whole potential of the cluster. Conservatively, we left out these three clusters of our analysis (although they are always shown in the plots), leaving us with 26 RCSGA SL selected clusters to carry out our studies. The red circle corresponds to the PLCK G004.5−19.5 cluster, where its M_{200} was obtained from its X-ray emission (Sifón et al., 2014) and its SL analysis was performed using the same technique used in this work. Then, our final sample consists of 26 clusters from RCSGA sample plus the PLCK G004.5−19.5 cluster. For simplicity, we refer to these 27 clusters as the RCSGA sample.

Fig. 5.1 clearly indicates that the effective Einstein radii and dynamical masses are well correlated with each other, showing that the more massive clusters derived from dynamical analysis have larger effective Einstein radii on average. This figure also shows the observed $Er-M_{weak}$ correlation found by O12 to their cluster sample, as well as the expected $Er-M_{weak}$ correlation for simulated clusters assuming $c_{200} \simeq 4.9$ (typical value for concentration when lensing selection is taken into account, O12) and its scatter. It can be seen that both sample follow quiet well the expected correlation, although there is a slight trend to larger Einstein radii, indicating that both samples are a bit more concentrated than $c_{200} \simeq 4.9$.

Since both samples show practically the same correlation, one can confirm that dynamical masses of SL selected clusters are good tracers of their total masses, allowing us to probe mass distributions at large radii in a way as good as done by using weak lensing masses. Tab. 5.1 lists the effective Einstein radii for all the clusters in our sample derived from SL-only analysis and for SL and dynamical mass analysis, by computing convergence maps for a source at $z_s = z_{arc}$, and for a source at $z_s = 2.0$.

TABLE 5.2: Concentration−mass parameters.

Name	SL only			SL and Dy. Mass		
	$\chi 2/d.o.f.$	c_{200}	M_{200} $[10^{14}h^{-1}M_{\odot}]$	$\chi 2/d.o.f.$	c_{200}	M_{200} $[10^{14}h^{-1}M_{\odot}]$
RCS2 J0004−0103	1.17/3	$4.7^{+9.9}_{-1.9}$	$1.62^{+53}_{-1.62}$	1.17/4	$7.1^{+7.0}_{-3.9}$	$0.74^{+1.11}_{-0.73}$
RCS2 J0034+0225	1.36/1	$5.2^{+4.9}_{-2.1}$	$0.75^{+0.91}_{-0.47}$	1.98/2	$5.2^{+2.9}_{-2.1}$	$1.33^{+0.59}_{-0.94}$
RCS2 J0038+0215	1.35/1	$4.5^{+6.5}_{-1.8}$	$0.84^{+0.11}_{-0.79}$	1.99/2	$5.9^{+3.5}_{-2.4}$	$1.59^{+0.13}_{-1.42}$
RCS2 J0047+0507	1.24/1	$7.4^{+3.0}_{-3.0}$	$0.55^{+0.65}_{-0.39}$	2.38/2	$4.9^{+4.6}_{-2.0}$	$0.96^{+0.33}_{-0.80}$
RCS2 J0052+0433	2.57/2	$17.7^{+7.1}_{-9.4}$	$1.80^{+2.32}_{-0.63}$	2.32/3	$19.4^{+7.8}_{-9.0}$	$1.54^{+1.45}_{-0.34}$
RCS2 J0057+0209	6.89/3	$4.3^{+4.1}_{-1.7}$	$8.97^{+1.67}_{-7.56}$	6.93/4	$5.1^{+2.0}_{-2.0}$	$5.82^{+3.38}_{-3.27}$
RCS2 J0252−1459[d]	1.13/1	$7.6^{+7.1}_{-3.7}$	$0.39^{+1630}_{-0.13}$	2.98/2	$3.5^{+8.1}_{-1.4}$	$1.89^{+70.40}_{-1.66}$
RCS2 J0309−1437	3.96/1	$4.8^{+4.9}_{-1.9}$	$1.18^{+1.43}_{-0.69}$	3.96/2	$4.8^{+4.9}_{-1.9}$	$1.18^{+1.43}_{-0.69}$
RCS2 J0327−1326[a]	2.49/4	$8.1^{+3.2}_{-5.7}$	$2.31^{+0.99}_{-1.53}$	1.43/5	$7.9^{+3.2}_{-5.2}$	$5.50^{+3.55}_{-3.52}$
RCS2 J0859−0345	2.21/3	$3.7^{+1.5}_{-1.5}$	$3.34^{+2.42}_{-1.32}$	2.34/4	$3.0^{+1.2}_{-1.2}$	$4.89^{+0.28}_{-2.16}$
RCS2 J1055−0459[d]	6.32/2	$6.3^{+2.5}_{-2.5}$	$0.30^{+0.52}_{-0.13}$	10.14/3	$6.5^{+3.3}_{-2.6}$	$0.65^{+0.34}_{-0.41}$
RCS2 J1101−0602[d]	1.06/1	$10.9^{+4.4}_{-7.4}$	$0.26^{+6.11}_{-0.24}$	1.11/2	$5.2^{+3.5}_{-2.1}$	$1.06^{+0.18}_{-0.96}$
RCS2 J1108−0456	5.45/1	$3.2^{+1.3}_{-1.3}$	$4.15^{+0.79}_{-2.71}$	5.45/2	$3.2^{+1.3}_{-1.3}$	$4.15^{+0.79}_{-2.71}$
RCS2 J1111+1408	1.06/3	$5.8^{+2.3}_{-2.6}$	$2.87^{+5.96}_{-0.35}$	1.09/4	$4.3^{+1.9}_{-1.7}$	$5.33^{+2.95}_{-2.71}$
RCS2 J1119−0728	1.02/1	$4.7^{+12.0}_{-1.9}$	$0.28^{+2.38}_{-0.21}$	1.31/2	$5.2^{+2.1}_{-2.1}$	$0.91^{+1.41}_{-0.18}$
RCS2 J1125−0628	1.01/2	$14.8^{+5.9}_{-9.6}$	$0.58^{+1.34}_{-0.34}$	1.00/3	$9.7^{+6.1}_{-4.6}$	$1.31^{+0.66}_{-1.02}$
RCS2 J1250+0244	1.03/1	$5.8^{+13.7}_{-2.3}$	$0.61^{+575}_{-0.54}$	1.47/2	$5.8^{+12.5}_{-2.3}$	$0.89^{+2.00}_{-0.82}$
RCS2 J1511+0630	1.01/1	$5.1^{+12.3}_{-2.0}$	$0.95^{+0.69}_{-0.81}$	1.03/2	$7.1^{+9.3}_{-2.8}$	$0.53^{+0.31}_{-0.36}$
RCS2 J1517+1003	1.03/1	$18.9^{+7.6}_{-13.8}$	$2.15^{+2.98}_{-0.48}$	1.06/2	$13.6^{+5.4}_{-6.4}$	$2.43^{+1.35}_{-0.68}$
RCS2 J1519+0840	1.22/1	$3.9^{+1.6}_{-1.6}$	$4.57^{+1.15}_{-4.29}$	2.50/2	$3.0^{+1.6}_{-1.2}$	$6.16^{+0.24}_{-5.30}$
RCS2 J1526+0432	2.52/2	$4.3^{+2.3}_{-1.7}$	$2.21^{+3.55}_{-0.64}$	2.64/3	$5.4^{+2.2}_{-2.2}$	$2.26^{+1.72}_{-0.43}$
SDSS J2111−0114[b]	2.66/1	$4.7^{+1.9}_{-2.1}$	$4.99^{+2.45}_{-2.04}$	2.89/2	$3.2^{+1.7}_{-1.3}$	$6.97^{+0.54}_{-3.94}$
RCS2 J2135−0102	3.03/1	$7.9^{+3.2}_{-4.0}$	$8.78^{+2.76}_{-4.70}$	4.25/2	$6.8^{+2.7}_{-3.1}$	$8.75^{+3.82}_{-3.65}$
RCS2 J2147−0102	1.02/1	$20.5^{+8.2}_{-10.3}$	$0.14^{+1170}_{-0.07}$	2.81/2	$11.2^{+12.8}_{-4.5}$	$0.32^{+0.31}_{-0.26}$
RCS2 J2151−0138	1.03/1	$4.6^{+6.0}_{-1.8}$	$0.70^{+0.49}_{-8.74}$	1.05/2	$6.3^{+3.7}_{-2.5}$	$7.54^{+2.62}_{-5.10}$
RCS2 J2313−0104	1.25/1	$4.9^{+6.2}_{-2.0}$	$0.90^{+1.22}_{-0.85}$	1.40/2	$5.2^{+4.6}_{-2.1}$	$1.24^{+0.37}_{-1.08}$
RCS2 J2329−1317	2.29/1	$3.3^{+4.3}_{-1.3}$	$2.04^{+2.59}_{-1.40}$	4.44/2	$3.5^{+2.9}_{-1.4}$	$4.50^{+1.14}_{-3.58}$
RCS2 J2329−0120	4.07/2	$10.6^{+8.5}_{-4.2}$	$0.78^{+0.50}_{-0.54}$	4.81/3	$10.0^{+7.5}_{-4.0}$	$0.43^{+0.39}_{-0.24}$
RCS2 J2336−0608	3.41/1	$3.0^{+5.0}_{-1.2}$	$7.23^{+1.65}_{-4.99}$	3.37/2	$3.2^{+2.1}_{-1.3}$	$7.09^{+0.83}_{-3.52}$
PLCK G004.5−19.5[c]	1.08/1	$5.2^{+12.4}_{-2.3}$	$7.68^{+3.09}_{-7.00}$	1.09/2	$4.3^{+5.4}_{-1.1}$	$9.81^{+1.69}_{-6.46}$

Note − Summary of the SL only models and SL and dynamical mass analysis models. Errors indicate 1σ errors on each parameter.

[a] Previously described in Wuyts et al. (2010) and Sharon et al. (2012).
[b] Also reported in Bayliss et al. (2011) and O12.
[c] This cluster belongs to the *Planck* Early SZ sample (Planck Collaboration et al., 2011). Previously described in Sifón et al. (2014), where we used the same technique applied in this work.
[d] Galaxy-galaxy lens, it is not considered to construct the $c-M$ relation.

5.3.2 The c – M relation for 27 clusters from the RCSGA sample

In Fig. 5.2 we present the $c - M$ relation for the 27 systems previously described. The concentration parameters were obtained from our SL and dynamical mass analysis, which are listed in Tab. 5.2. The figure shows a evident correlation between the measured concentrations and dynamical masses, with more massive clusters having on average smaller concentrations than less massive clusters, which is consistent with the theoretical expectation, although the dependence on the cluster mass is much stronger. As it has been showed by previous theoretical and observational works, the $c - M$ relation can be fitted very well by a power law. Therefore, we fit our data to a power law with both the normalization, c_n, and mass slope, α, as free parameters,

$$c_{200}(M_{200}) = c_n \times \left(\frac{M_{200}}{M_{piv}\ h^{-1} M_{\odot}} \right)^{\alpha}, \tag{5.2}$$

where M_{piv} corresponds to the median value of M_{200} for our cluster sample. At this stage, we ignore the redshift dependence of the $c - M$ relation, given that theoretical

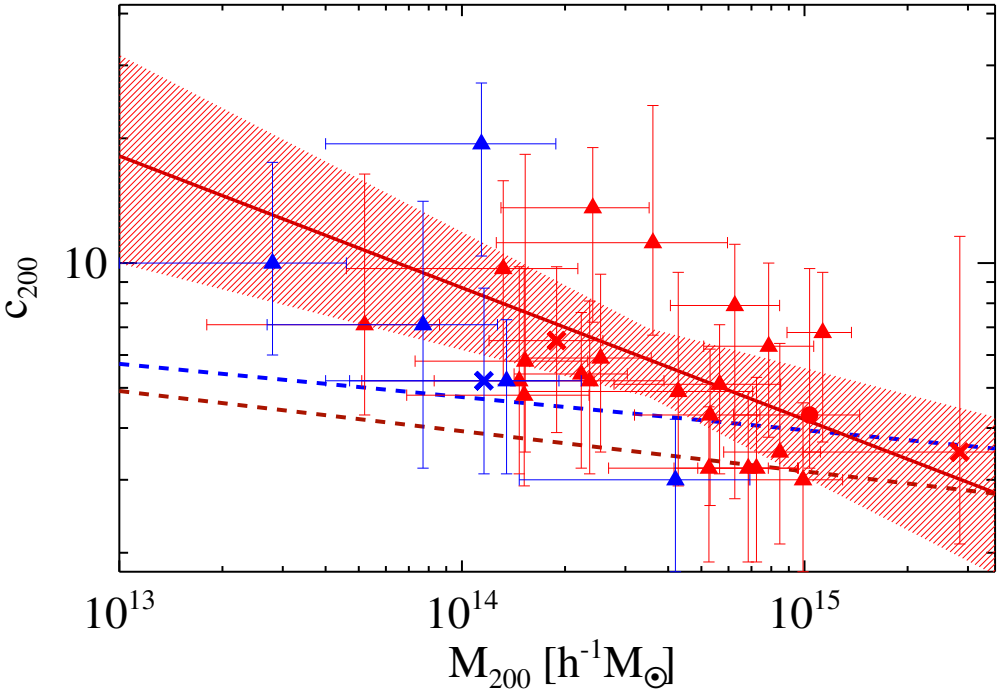

FIGURE 5.2: This figure shows the observed $c - M$ relation for 27 RCSGA clusters. The colors and symbols correspond to the same described in Fig. 5.1. The red line and shaded region correspond to the best-fit, which is described by a $\alpha = -0.32 \pm 0.11$. The figure also shows the expected $c - M$ relations of B13 and D08, blue and brown dashed lines, respectively

predictions show a little evolution of the concentration of massive halos with its redshift (e.g. Meneghetti et al., 2014, hereafter M14Sim), but we will return to this possible redshift evolution in the next sections. We perform a Levenberg-Marquardt least-squares minimization for fitting:

$$\chi^2 = \sum \frac{(c_{200,obs} - c_{200,fit})^2}{\sigma^2_{c_{200}}}, \tag{5.3}$$

where $\sigma^2_{c_{200}}$ is the 1σ error on c_{200}. We find that the best-fit for the observed $c - M$ relation for our 27 RCSGA clusters, including 1σ errors on both the c_n and α, is given by:

$$c_{200} = (5.80 \pm 1.08) \times \left(\frac{M_{200}}{3.61 \times 10^{14}\ h^{-1} M_{\odot}} \right)^{-0.32 \pm 0.11}, \tag{5.4}$$

which is also showed in Fig. 5.2. The best-fitting parameters are reported in Tab. 5.3.

Since theoretical works have shown that velocity dispersions derived from less than 10 members are not likely representative of the cluster velocity dispersion (Evrard et al., 2008; White et al., 2010), we check how much affect to the observed $c - M$ relation clusters with less than 10 members (blue triangles). We probe this by computing a new best-fit excluding five systems from our sample that have less than 10 members. The c_n and α parameters for this new best-fit and their respective 1σ errors are listed in Tab. 5.3. We find a difference on the normalization and the slope are lower than $\sim 4\%$ and $\sim 10\%$, respectively. Therefore, since the inclusion/exclusion of these five clusters with few members do not affect significantly the best-fit of the $c - M$ relation, they will be always included in the next studies.

5.3.2.1 Comparison with N-body simulations

For the theoretical prediction, we adopt results of the N-body simulations of Duffy et al. (2008) (hereafter D08) and Bhattacharya et al. (2013) (hereafter B13). Since both simulations are qualitatively similar and their expected $c - M$ relations are very well fitted by a power law (at $z = 0$), these can be used to analyze our results.

D08 found that their results for the full sample at $z = 0$ are well described by a power law, with $(c_n,\ \alpha,\ M_{piv}) = (3.93, -0.097, 1 \times 10^{14} h^{-1} M_{\odot})$. While B13 found that the normalization for their expected $c - M$ relation of the full sample at $z = 0$, is about 15% higher compared to the results found by D08. But given the statistical limitations and

the different cosmological background model used in D08, we focus our comparison to the simulation results of B13.

The Fig. 5.2 also shows the expected $c-M$ relations of B13 and D08. One can see from this figure that our results are in reasonable agreement with the simulation results for massive clusters of $M_{200} \sim 8 \times 10^{14} h^{-1} M_{\odot}$. In contrast, our results also show that less massive clusters of $M_{200} \sim 1 \times 10^{14} h^{-1} M_{\odot}$ are much more concentrated than theoretical expectations, indicating that our observed $c-M$ relation has a much stronger dependence on the cluster mass than theoretical works. To put these results in more quantitative footing, we calculate the ratio $c_{obs}(M_i)/c_{sim}(M_i)$ for M_1=$8\times10^{14} h^{-1} M_{\odot}$ and M_2=$1\times10^{14} h^{-1} M_{\odot}$, which will serve as prototypes for the next sections. These comparisons are reported in Tab. 5.3. We found that for massive clusters, the measured concentrations are on average about 11% (39%) higher than the simulation results of B13 (D08). In contrast, the concentration of less massive clusters are distributed around $c_{200} \simeq 8.7$, which is almost twice that the expected concentration values for this mass range. This increase in the concentrations, is reflected in the slope of the observed relation, which is four times its expected value. These results are in concordance with previous observational works (Ettori et al., 2010; Okabe et al., 2010a, O12), however, the lensing bias and projection effects should be taken into account before arriving to any conclusion.

5.3.2.2 Comparison with N-body simulations considering SL bias and projection effects

As mentioned, the RCSGA clusters were selected by strong lensing, and it has been shown that this family of clusters represents a strongly biased population such that their measured concentrations are on average much larger than in the normal population, mostly due to the halo triaxiality (Hennawi et al., 2007; Meneghetti et al., 2010; Oguri and Blandford, 2009). Furthermore, since lensing observables can only measure the projected mass distribution of the clusters, substructures and elongation along the line-of-sight may introduce a bias in the 3D mass distribution recovered from the projected mass (Meneghetti et al., 2003).

In order to take into account the selection bias and the projection effects, we compare our observed $c-M$ relation with the simulation results of O12 and M14Sim, which study in detail these biases. They studied $\sim$ 1000 cluster-size halos at high spatial and mass resolution, and each of them was projected along many line-of-sight. Then, they performed several semi-analytic calculations with ray-tracing of extended sources to estimate the effect of the lensing bias (see the references for more details).

In Fig. 5.3, we visualize the expected $c - M$ relations at $z = 0.45$ found by O12 and by M14Sim, which are characterized by the same dependence on the cluster mass of $\alpha \sim -0.2$, which is stronger than the mass slope when the lensing bias is not considered. Although the normalization of these expected relations are a little different, we consider that both are in concordance with each other, and therefore, both will be used in our comparisons that are reported in Tab 5.3. This figure clearly shows a better agreement between our measured concentrations and those derived from simulations. In fact, for massive clusters, the difference between our data and theoretical expectations is reduced to a level of 1%, when the comparison is performed with the results of O12. Despite the reconciliation between the median value of the concentration at the high mass range, there is still a large discrepancy when the slopes are compared, with a difference of $\sim 60\%$. These results reflect a large excess of concentration of lower mass cluster, excess that simulations are still not able to describe, even if the lensing bias and projection effects are considered.

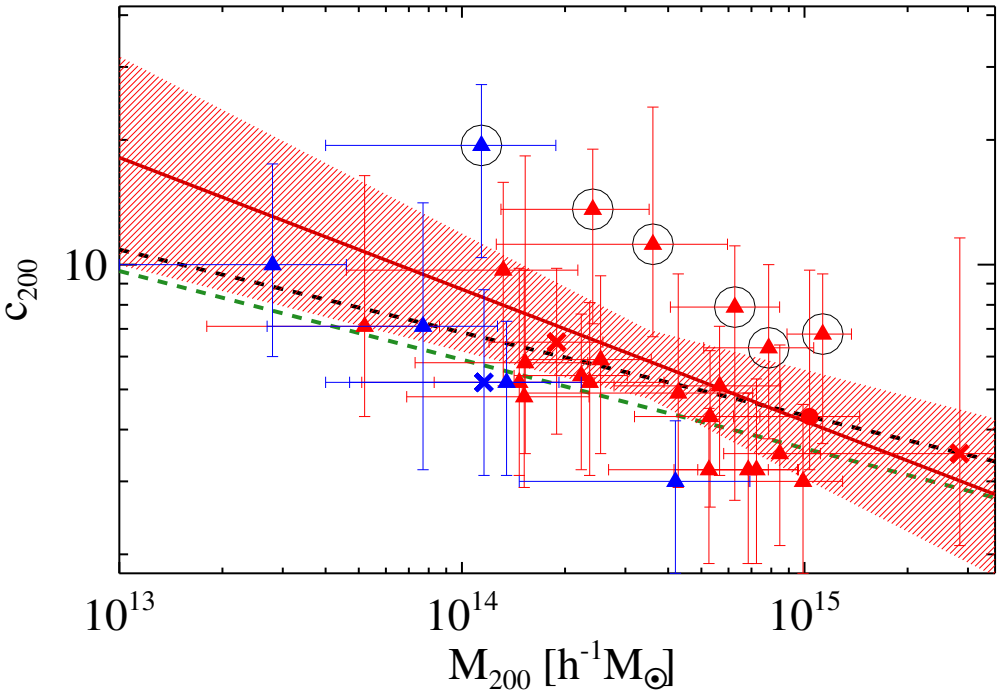

FIGURE 5.3: In this figure we visualize our measured concentrations as well as the expected $c - M$ relations at $z = 0.45$ found by O12 and by M14Sim, which are represented by the black and green dashed lines, respectively. Both expected trends are characterized by the same mass slope of $\alpha \sim -0.2$. This figure clearly shows a better agreement between our measured concentrations and those derived from simulations. Although there is still a large discrepancy when the slopes are compared, with a difference of $\sim 60\%$. Clusters inside the open circles are describing a higher and steeper $c - M$ relation.

The most likely explanation for this excess of concentration for less massive clusters is associated to the baryon cooling effect. The adiabatic contraction of dark matter distribution at the formation time of the central galaxy, enhances the core density of the clusters, resulting in an increase of their concentrations. Cluster halos of lower mass are more affected for this effect because their fraction of the central galaxy mass to the total mass is larger, resulting in a faster and stronger increase of the core density. In fact, simulations with radiative cooling and star formation show that baryon cooling significantly increases the concentration parameter, particularly for low-mass halos (e.g. Mead et al., 2010; Rudd and Nagai, 2009; Zentner et al., 2008), although the effect is strongly dependent on the feedback (Duffy et al., 2010; McCarthy et al., 2010). Therefore, baryon physics could be a good candidate to explain the observed strong dependence on the cluster mass in the $c-M$ relation, although more work needs to be made in this area.

A concern we should discuss is the possibility of false identification of multiple-image systems throughout our modeling methodology, because many of the images used in our analysis have no spectroscopic information, which would introduce systematic errors in our final results. Although, the models were constructed mainly based in the giant arcs, and since most of them were spectroscopically confirmed, one can trust the following steps of modeling as well as the final results.

5.3.2.3 Bimodality in the observed c − M relation

By a visual inspection of the Fig. 5.3, one can see that there is a possible bimodality in the $c-M$ plane. There are six clusters (open circles) that clearly describe a $c-M$ relation with a higher normalization and with a dependence on the cluster mass a bit stronger than the rest of the measured concentrations. Indeed, the best-fit for our RCSGA sample, excluding these six clusters, is in total agreement with the simulation results in both the normalization and the mass slope, with differences in the slopes smaller than 10%, reconciling simulations and real data.

There are few explanations for this bimodality in the $c-M$ relation. Perhaps the most likely are two: 1) this bimodality is caused by an incompleteness in our sample, and therefore, we need to complement our data with another cluster samples before arriving to any conclusion; 2) these six systems belong to a *special* subset of SL clusters, hence, they have to be studied independently. Although, there is not a clear evidence neither in our imaging data nor in our spectroscopy for selecting these systems as *special* SL clusters. Therefore, we can not exclude them from our analysis at this stage. To figure out this, we need deeper and high-quality imaging data as well as more spectroscopic information of the multiple images used to constrain the models.

TABLE 5.3: The best-fitting model parameters for the $c - M$ relations.

Sample	c_n	α	M_{piv} $[10^{14}h^{-1}M_{\odot}]$	$(c_{obs}/c_{sim})_{M=8\times10^{14}M_{\odot}}$ / $(c_{obs}/c_{sim})_{M=1\times10^{14}M_{\odot}}$ B13	D08	$O12_{SL}$	$M14^{sim}_{SL}$	$M14^{sim}_{Xray}$
RCSGA[a]	5.80±1.08	-0.32±0.11	3.61	1.12 / 1.84	1.40 / 2.23	0.99 / 1.28	1.19 / 1.48	1.15 / 1.61
RCSGA (N > 10)[b]	5.58±1.14	-0.29±0.18	3.73	1.10 / 1.71	1.38 / 2.07	0.98 / 1.18	1.18 / 1.38	1.14 / 1.49
RCSGA (low c_n)[c]	5.07±0.76	-0.29±0.13	2.54	0.90 / 1.40	1.13 / 1.69	0.80 / 0.97	0.96 / 1.13	0.93 / 1.22
SGAS[d]	6.07±0.77	-0.68±0.14	4.12	0.96 / 3.35	1.20 / 4.05	0.85 / 2.32	1.02 / 2.70	0.99 / 2.93
CLASH[e]	3.57±0.24	-0.21±0.22	8.00	0.89 / 1.16	1.11 / 1.41	0.79 / 0.81	0.94 / 0.94	0.92 / 1.02
All[f]	4.75±0.84	-0.52±0.09	5.26	0.95 / 2.37	1.19 / 2.87	0.84 / 1.64	1.01 / 1.91	0.98 / 2.07
All (high c_n)[g]	8.90±1.12	-0.69±0.09	3.63	1.28 / 4.56	1.61 / 5.51	1.14 / 3.16	1.37 / 3.67	1.32 / 3.99
All (low c_n)[h]	4.20±0.92	-0.24±0.11	6.10	0.98 / 1.36	1.23 / 1.65	0.87 / 0.95	1.04 / 1.10	1.01 / 1.19

[a]The full RCSGA sample, composed by 26 RCSGA SL selected clusters plus PLCK G004.5−19.5
[b]The RCSGA sample excluding systems with less than 10 members to compute the velocity dispersion.
[c]The RCSGA sample excluding six clusters that are describing a higher and steeper $c - M$ relation.
[d]The SGAS sample, composed by 27 SL selected clusters.
[e]The CLASH sample, compound by 19 X-ray selected clusters.
[f]Combined dataset of 73 concentration parameters.
[g]Dataset composed by $\sim$ 23 system, that describe a higher and steeper $c - M$ relation.
[h]Dataset composed by $\sim$ 50 galaxy clusters, describing a $c - M$ relation that is fully consistent with theoretical expectations.

5.4 The largest robust observed c – M relation

In this section, we combine our results with previous datasets of concentration parameters obtained by O12 from their SGAS SL selected clusters, and with the recent results of M14 for a subset of CLASH X-ray selected clusters, providing the largest robust dataset of concentration parameter for a controlled sample of 73 galaxy clusters, resulting in the most complete analysis for the observed $c - M$ relation hitherto.

5.4.1 Modeling techniques and selection bias

Before to combine these three datasets of concentration parameters, we check possible bias due to the different modeling techniques used and we also study whether the selection function plays a decisive role in the final $c - M$ relation.

5.4.1.1 Different modeling techniques

O12 performed their SL models using the parametric software GLAFIC (Oguri, 2010), assuming a NFW profile for the main DM halo and a pseudo-Jaffe model for the member galaxies. From the derived best-fitting mass model, they computed the effective Einstein radius (by Eq. 5.1), which is then combined with constraints from tangential shear profiles to obtain the final best-fitting model parameters. While M14 used the non-parametric software SaWLens (Merten et al., 2009), which combines strong and weak lensing data, making no a *priori* assumption about the underlying mass distribution

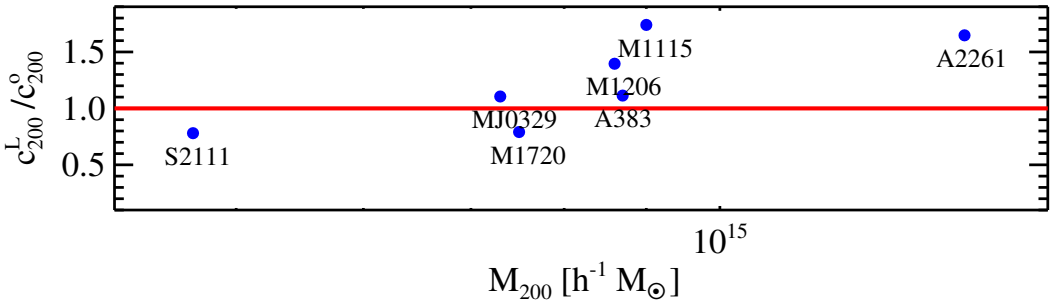

FIGURE 5.4: The ratio between the concentration parameters derived using the technique described in this work and the concentrations derived by M14 and O12. The LENSTOOL model results for Abell 2261 and MACSJ1206−08 were previously presented in Umetsu et al. (2012) and Coe et al. (2013), respectively.

TABLE 5.4: Summary of the LENSTOOL models for CLASH and SGAS clusters.

Name	$\chi^2/d.o.f.$	c_{200}	M_{200} $[10^{14}h^{-1}M_\odot]$
MACSJ1206−08[a]	35/42	6.1± 0.9	9.22± 3.82
MACSJ1115+0129	1.88/1	4.0± 1.4	10.54± 2.81
Abell 2261[b]	3.85/5	5.6± 1.9	12.67± 1.93
Abell 383	2.41/2	4.9± 1.3	8.62± 2.90
MACSJ0329−02	3.89/3	4.2± 1.1	7.48± 2.56
MACSJ1720+3536	2.91/1	3.4± 1.0	1.94± 0.69
SDSS 2111−1114[c]	2.66/1	3.2± 1.5	6.97± 2.24

[a]Previously described in Coe et al. (2013).
[b]Previously described in Umetsu et al. (2012).
[c]This cluster is also included as part of the RCSGA sample. Tab. 5.2

and performing a reconstruction of the lensing potential on an adaptively refined grid. Then, convergence maps are derived from the lensing potential, which are used to fit the NFW profile and to obtain the concentration parameters.

The three used approaches are quite different, making it difficult to see whether there is some bias due to the modeling technique. A possible way to check if there is any discrepancy between these techniques is to perform LENSTOOL models for some clusters used in both researches. Therefore, we perform models for 6 of the 19 CLASH clusters studied in M14 and 1 of 28 SGAS clusters analyzed by O12. Fig. 5.4 shows the ratio between the concentration parameters derived using the technique described in this thesis, c^L_{200}, and the concentrations derived by M14 and O12, c^o_{200}. From the figure one can see that our results are moderately consistent with the results derived by SaWLens and GLAFIC. Although, the models for the clusters Abell 2261, MACSJ1206−08, and MACSJ1115+0129, yielded different results to those presented in M14. However, the

LENSTOOL model results for Abell 2261 and MACSJ1206−08 were previously presented in Umetsu et al. (2012) and Coe et al. (2013), respectively. In both works, these results were compared with concentrations derived from other models, which were always consistent with each other within the statistical errors. Therefore, due to the reasonable agreement between the model results, we can assume that the bias related to the different modeling techniques is negligible, even though we have compared a small fraction of the total sample. The main best-fitting LENSTOOL model parameters for these 7 clusters are tabulated in Tab. 5.4. The LENSTOOL models for the CLASH clusters are described in the next chapter.

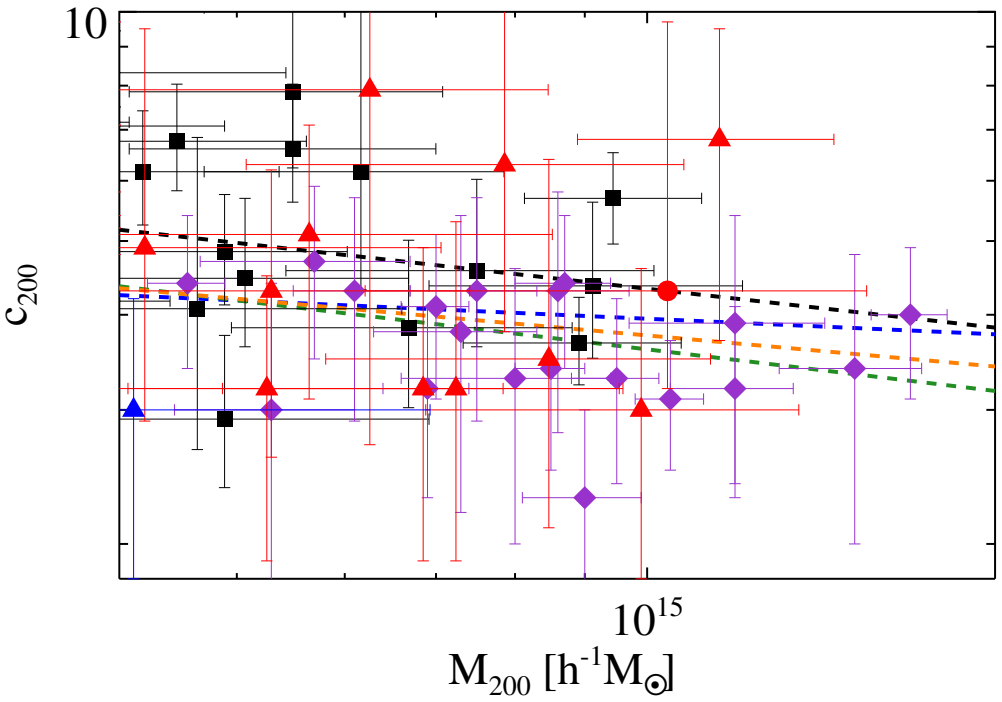

FIGURE 5.5: This figure shows the measured concentrations by M14 (purple diamonds) and by O12 (black squares), as well as our results for the RCSGA sample (same colors and symbols as before). The blue (black, green) dashed line correspond to the expected $c-M$ relation derived from simulation results of B13 (O12, M14Sim). While the orange dashed line correspond to the expected relation derived from M14Sim, for X-ray selected clusters.

5.4.1.2 Selection bias

As mentioned, the RCSGA and SGAS samples selected their clusters by strong lensing, therefore, we expect that both samples are biased at the same order. Otherwise, the CLASH clusters were selected by their X-ray emission, avoiding this bias. Although, they could still be affected by projection effects.

In order to check whether the selection method does not bias the observed $c-M$ relation, we perform a comparison between these three samples in the concentration − high mass plane, since the mass range covered by the CLASH clusters spans only for high masses. Fig 5.5 shows the measured concentrations by M14 and O12, as well as our results for the RCSGA sample. This figure also shows the expected relations derived from simulation results of B13, O12, M14Sim. We have also included a new expected relation derived from M14Sim, for X-ray selected clusters, to perform a better comparison with the CLASH clusters.

From the figure, one can see that the concentrations derived from all the observational works do not have a different behavior. Indeed, they are well distributed in the plane, describing a wide $c - M$ relation with a slight trend to lower values of concentration parameter to higher masses. Although, when the central value of the concentration parameters (in the mass range of $4 < M_{200}/10^{14}h^{-1}M\odot < 16$) of each sample is compared, one begin to see small differences in the distributions, with the CLASH clusters being less concentrated on average, with $\bar{c}_{200} \simeq 3.7$. On the other hand, the SGAS clusters are the most concentrated, with a central value of $\bar{c}_{200} \simeq 4.8$, while the concentrations of the RCSGA clusters are distributed around of $\bar{c}_{200} \simeq 4.3$, just in the middle of the previous ones. The Fig. 5.5 also indicates that all the expected $c - M$ relations from theoretical works, satisfy or are in reasonable agreement with the observational data, even those that do not include the selection bias in these calculations (B13).

Due to the distribution of the concentration parameters in the mass range analyzed and also because the differences on the median values of the concentrations are inside the intrinsic scatter of the $c - M$ relation, we can conclude that the selection method does not play a crucial role in determining the central value of the concentration parameter of the massive clusters. We can also conclude that, given the qualitative agreement between all the expected relations and the data, one can not perform a conclusive study of the slope of the c-M relation in a narrow mass range as showed in the figure, making necessary a study in a wider mass range. Therefore, the combination of these three samples is not only reasonable, but it is even required.

5.4.2 The c – M relation for 73 galaxy clusters

After having determined that the selection methods and different modeling techniques do not bias our results, we give rise to the construction of largest observed $c-M$ relation, composed by 27 RCSGA clusters from this thesis, 27 SGAS clusters from O12 and 19 CLASH clusters from M14. Resulting in the largest robust dataset of 73 concentration parameters, distributed in a wide mass range from $0.28 < M_{200}/10^{14}h^{-1}M\odot < 15.60$,

with a median mass at $M_{200} = 5.26 \times 10^{14} h^{-1} M_{\odot}$, allowing a detailed study of the dependence on the cluster mass in the $c-M$ relation. Furthermore, since its cluster redshift range spans from $0.22 < z < 1.01$, it is also possible to explore the potential redshift evolution in the $c-M$ plane.

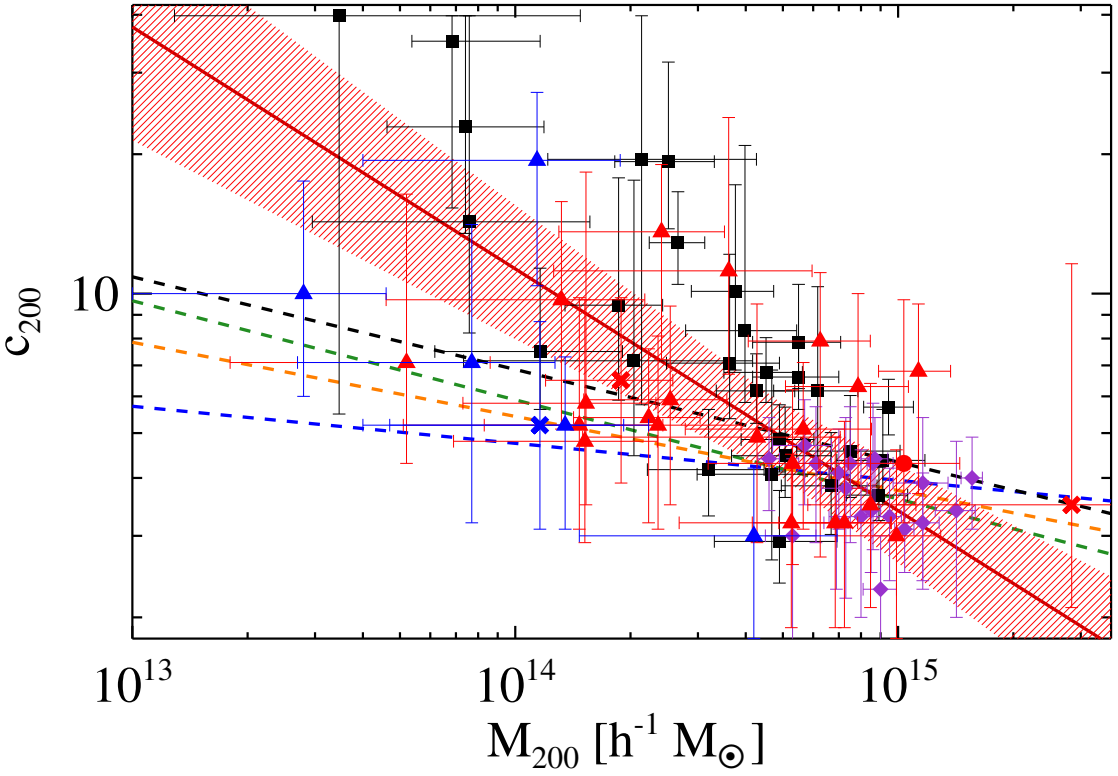

FIGURE 5.6: This figure shows the largest robust dataset of the 73 concentration parameters in the $c-M$ plane by combining 27 RCSGA clusters analyzed in this thesis corresponding to the red/blue symbols, with 27 SGAS clusters from O12 which are represented by black squares, and with 19 CLASH clusters showed by the purple diamonds. The best-fit results a steep $c-M$ relation of $\alpha \sim -0.52$, mainly due to the SGAS sample, in where the clusters present in general more concentrated mass distributions. The best-fit is and its 1σ errors are showed by the red solid line and the shaded region, respectively. The black (green, orange, blue) dashed line corresponds to the expected $c-M$ relation derived from the simulation results by O12 for SL selected clusters at $z = 0.45$ (M14Sim for SL selected clusters at $z = 0.45$, M14Sim for X-ray selected clusters at $z = 0.45$, B13 for all cluster population at $z = 0$).

In Fig. 5.6 we visualize the 73 concentration parameters in the $c-M$ plane. The colors and symbols are the same previously described and the red solid line corresponds to the best-fit for all data. From the figure, we already confirmed that there is a strong correlation between the cluster mass and its concentration, which is consistent with theoretical expectations for massive clusters, whose average concordance is about $\sim 6\%$. This agreement decreases rapidly when the less massive clusters are analyzed, whose concentrations are distributed around a central value of $\bar{c}_{200} \simeq 11$, which is almost

double of the mean expected value at $M_{200} \sim 10^{14}h^{-1}M_{\odot}$. These results confirm our previous conclusions about the excess of the concentration for less massive clusters, which is not yet reproduced by the simulations, even if the lensing bias and projection effects are taken into account. This pronounced dependence on the cluster mass yields a steep mass slope of $\alpha = -0.52 \pm 0.09$, which is stronger than that found in the RCSGA $c-M$ relation, mainly due to the inclusion of the SGAS clusters, which are on average more concentrated than the rest of the sample for masses lower than $M_{200} \sim 7 \times 10^{14}h^{-1}M_{\odot}$.

Although in the previous section we concluded that the samples look similar at the high mass range, the picture is different when the full mass range is analyzed. Some differences appear between these samples, specifically in their mass slopes. For masses lower than $M_{200} \sim 7 \times 10^{14}h^{-1}M_{\odot}$, most of the SGAS clusters start increasing their concentration parameter to higher values than those found in the RCSGA and CLASH clusters, resulting in a mass slope of $\alpha = -0.68 \pm 0.14$, which is more than twice that found for our RCSGA sample alone, and much steeper than the expected slope in simulations. These clusters with higher concentrations are indeed describing the same trend previously found for six of our clusters, as it can be seen in Fig. 5.6. Thereby, the combined analysis highlights the possible bimodality in the $c-M$ relation, which is analyzed next.

5.4.3 The distribution of concentrations and bimodality

In order to study a possible bimodality in the observed $c-M$ relation, and also to understand and quantify the concentration scatter, we perform a series of distributions of the measured concentration parameters.

Numerical simulations have shown that the scatter in the concentration, about the concentration median, is well described by a log-normal for relaxed halos (e.g. Jing, 2000, D08), with a slight decrease in the scatter as a function of mass (Neto et al., 2007). These works also showed that the inclusion of unrelaxed halos adds a tail towards low concentrations. Fig. 5.7 shows the concentration distribution for the 73 clusters, which is well fitted by a log-normal function with $\sigma(log_{10}c_{200}) = 0.14$, which is in a very good quantitative agreement with the previously described theoretical works. Although, the tail is not added to the low concentrations in our distribution, on the contrary, it is added to high values of the concentration parameters, which represent the inclusion of clusters of lower masses.

Theoretical works have also shown that the concentration distribution is also very well described by a Gaussian function, at a given mass bin, with an intrinsic scatter of $\sigma/c_{200} \simeq 0.33$, which remains over a wide mass and redshift range (e.g. Reed

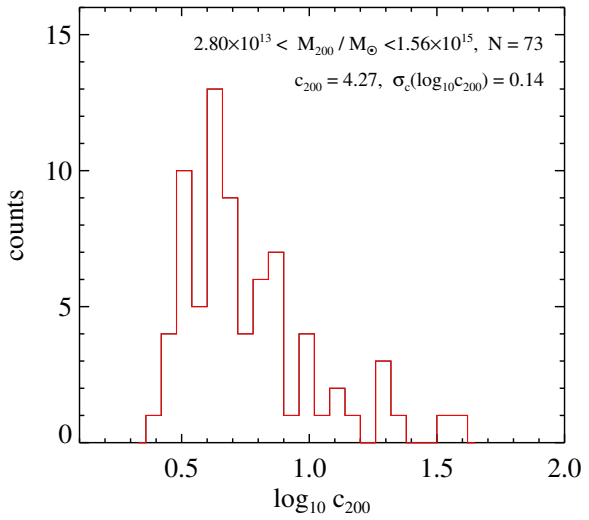

FIGURE 5.7: This figure shows the concentration distribution for the 73 clusters, which is well fitted by a log-normal function with $\sigma(log_{10}c_{200}) = 0.14$, which is in a very good quantitative agreement with the previously described theoretical works. Although, the tail is added to high values of the concentration parameters, associated to clusters of lower masses.

et al., 2011, B13). Therefore, we study the possible bimodality in the observed $c - M$ relation by analyzing the scatter in the concentration distributions, by fitting Gaussian functions. We perform concentration distributions for four mass bins centered at $(9.00, 5.07, 2.04, 0.69) \times 10^{14} h^{-1} M_{\odot}$, which are showed in Fig. 5.8. The concentration distribution centered at the higher mass bin is very well described by a gaussian function, centered at $c_{200} = 4.01$ with a scatter of $\sigma/c_{200} = 0.31$, which are consistent with those found by B13. As noted earlier, in the high mass range, the concentrations of all clusters have relatively the same behavior, therefore, we should expect a very well described Gaussian distribution, centered at the mean/median value of the concentration parameters of these clusters, with a standard desviation similar to the intrinsic scatter of expected $c - M$ relations. For the next mass bin, the concentration distribution is also described by a Gaussian function, but wider and centered at $c_{200} = 5.02$. As we expected, the center of the gaussian fit augmented to a higher value of the concentration parameter, but while the scatter should keep its value of $\sigma/c_{200} \simeq 0.33$, it increases considerably towards $\sigma/c_{200} = 0.47$. In the next two mass bins, due to the lack of data, we could not fit the Gaussian function to the distributions, but by analyzing the standard desviation of these distributions and also by visual inspection, one can see that the distributions are much wider than those for the previous mass bins. Moreover, this increase in both the standard desviation and width correlates with the central mass of the mass bins. This behavior could be interpreted as two distributions whose separation between their peaks increases by decreasing the central mass.

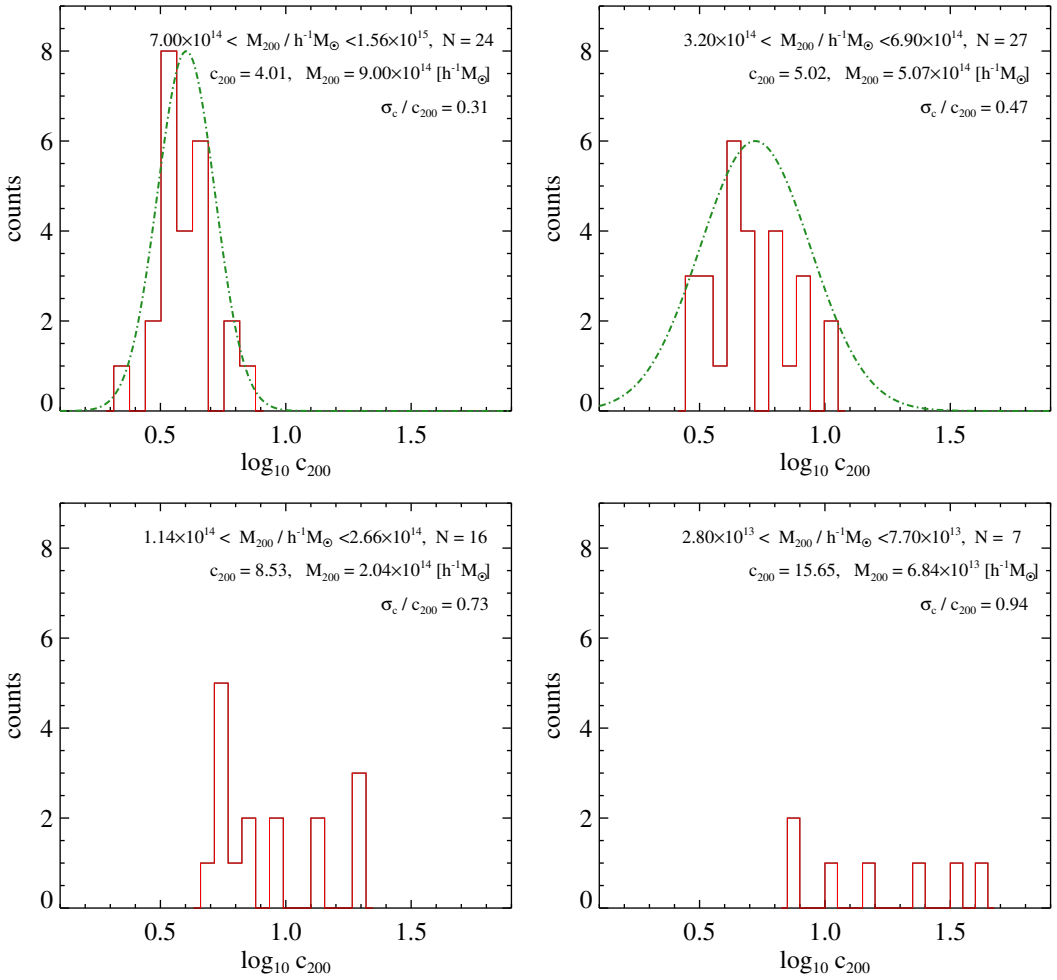

FIGURE 5.8: The concentration distributions for four mass bins centered at (9.00, 5.07, 2.04, 0.69) $\times 10^{14} h^{-1} M_{\odot}$, from the top – left to the bottom – right panel. The top panels are well described by a gaussian function, centered at $c_{200} = 4.01$ and $c_{200} = 5.02$, with a scatter of $\sigma/c_{200} = 0.31$ and $\sigma/c_{200} = 0.47$, for the left and right panels, respectively. The green dotted-dashed lines correspond to the best-fit of the distributions. The bottom panel show the concentration distributions for the lower mass bins, which due to the lack of data we could not fit a Gaussian function to the distributions. The standard deviations of the bottom left and right distribution are $\sigma/c_{200} = 0.73$ and $\sigma/c_{200} = 0.94$, respectively. The constant growth of both the scatter and width of the concentration distributions can be interpreted as a bimodal distribution, where the separation between their peaks is inversely correlated with the central mass of the mass bin, which supports the existence of a bimodality in the observed $c - M$ relation.

Thus, even though one can not see a double peak on the distributions, the constant growth in both the scatter and width, can be interpreted as a bimodal distribution, where the separation between their peaks is inversely correlated with the central mass of the mass bin. Although it could be also associated to the lack of data to perform the statistic. However, the scatter/width of the mass bin centered at $M_{200} \simeq 5 \times 10^{14} h^{-1} M_{\odot}$ turned out to be almost 50% larger than the scatter/width of the mass bin centered at a higher mass, with both mass bins containing practically the same number of clusters

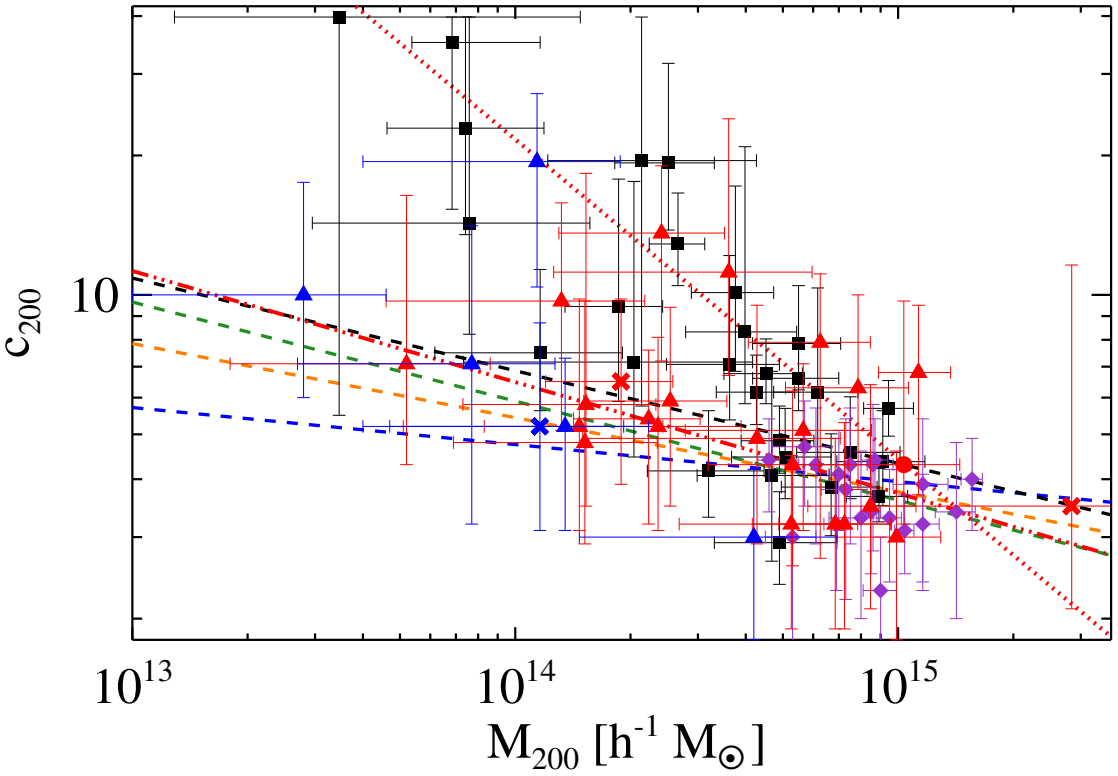

FIGURE 5.9: This figure shows the bimodality in the $c - M$ plane. One of these relations is composed by the full CLASH sample, $\sim 20 - 21$ RCSGA clusters, and $\sim 11 - 15$ clusters from SGAS. The best-fit for this subset of concentration is described by the red dotted-dashed line, which shows a weaker dependence on the cluster mass given by $\alpha = -0.24 \pm 0.11$, resulting in an excellent agreement with theoretical works that have included the selection bias and projection effects, reconciling simulations with observations. The rest of the RCSGA and SGAS clusters describe a higher and steeper $c - M$ relation (red dotted line), with $\alpha \simeq -0.69$, which is far from the theoretical expectations.

to perform the statistic.

Therefore, due to the qualitative analysis to the concentration distributions and also by visual inspection of the observed $c - M$ relation presented in Fig. 5.6, one can confirm the existence of a bimodality in the observed $c - M$ relation. One of these relations is composed by the full CLASH sample, $\sim 20 - 21$ RCSGA clusters, and $\sim 11 - 15$ clusters from SGAS, and shows a lower dependence on the cluster mass, given by $\alpha = -0.24 \pm 0.11$, resulting in an excellent agreement with theoretical works that have included the selection bias and projection effects. The rest of the RCSGA and SGAS clusters describe a higher and steeper $c - M$ relation of $\alpha = -0.69 \pm 0.09$, which is far from any theoretical expectation. Fig. 5.9 shows the best-fit to both $c - M$ relations, while the comparisons are reported in Tab. 5.3.

Since this relation was found in two independent pieces of research, with different modeling techniques, we can confirm the existence of a subset of SL clusters, which are much more concentrated than the rest of the SL population, and therefore, they should be treated independently by theoretical works. Although as it has already been mentioned, there is no evidence or a clear correlation between these clusters and other parameters, like ellipticity, orientation, Einstein radius, etc, that make them special. Therefore, to define these clusters as a *special* SL population, more data analysis needs to be done using deeper and high-quality imaging data as well as more spectroscopic information.

5.4.4 Redshift evolution of the c – M relation

In this section we explore the possible redshift evolution of the observed $c-M$ relation, where theoretical works invoke the existence of a negative dependence on the cluster redshift of the expected $c-M$ relation (e.g. D08, Zhao et al., 2009, M14Sim), due mainly to the combined effect of the density at the formation time and the mass growth. Although, the dependence is small for massive halos.

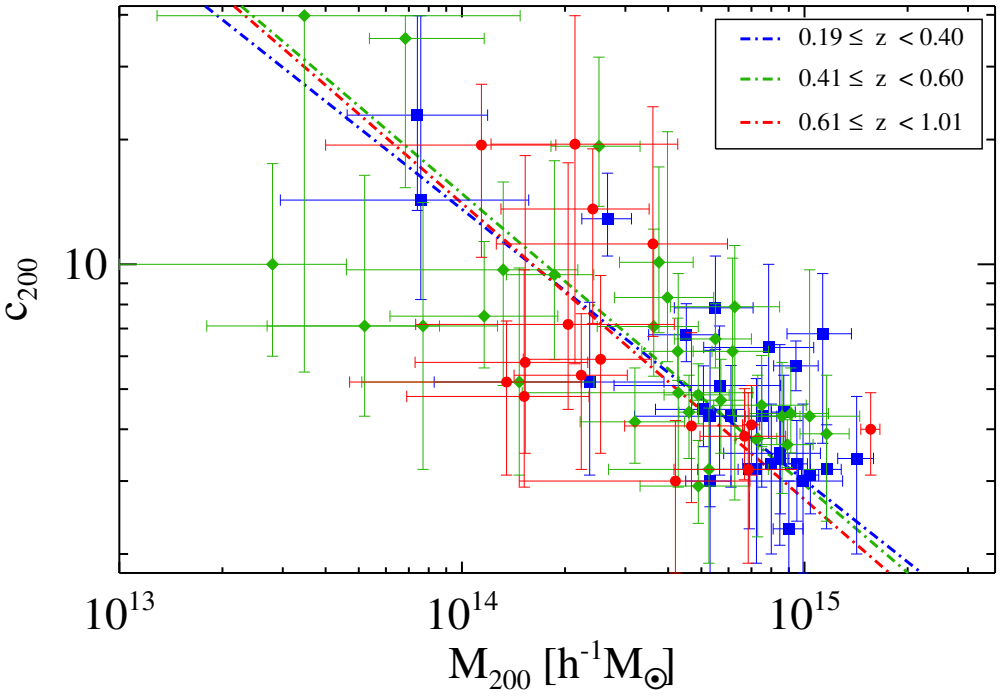

FIGURE 5.10: The figure shows the sample divided in three redshift bins, centered at $z = 0.3, 0.5$, and 0.8, which are showed by the blue squares, green diamonds, and red circles, respectively. The best-fitting $c-M$ relations are showed by the dotted-dashed lines, with the colors corresponding to same redshift bins. The best-fits show no evidence to confirm a redshift evolution of the observed $c-M$ relation.

In order to explore this possible redshift evolution, we divide the full sample in three redshift bins, centered at $z = 0.3, 0.5$, and 0.8. In Fig. 5.10 we visualize these three subsets and their respective best-fitting $c-M$ relations. The derived $c-M$ relations from these subsets describe practically the same trend, with a slight increase in their slope to higher redshifts. However, these differences in the slopes are virtually undetectable, and therefore, one can conclude that there is no evidence to confirm a redshift evolution of the observed $c-M$ relation.

In contrast, if we analyze the full sample in the $c-z$ plane, by dividing it in the same four mass bins studied in the previous section, we can arrive to other conclusion. The Fig. 5.11 shows the $c-z$ plane obtained from the 73 galaxy clusters studied. The figure indicates a positive correlation between the cluster redshift and its concentration, which is well fitted by a power law of $\alpha \sim 0.18$. This correlation is more evident when we focus only in the two higher mass bins, which contain the $\sim 70\%$ of all data. For the other two mass bins, this correlation is lost by the large scatter in the concentration distributions.

Even though our observed $c-M$ relation shows no evidence of some redshift evolution, we find a clear correlation between the cluster redshift and its concentration, which is more obvious for massive clusters. The observed trend appears to be consistent, at least qualitatively, with the theoretical predictions. But a sample with a wider mass and redshift range is needed to study with more detail the dependence on redshift of the $c-M$ relation.

It should be noted that in this analysis we do not take into account the bimodality in the $c-M$ relation, because as mentioned before, we do not find any correlation between the *special* SL population and another parameter or observable, like the cluster redshift. In fact, we can see in Fig. 5.10 that the concentrations from the three redshift bins are presented in both $c-M$ relations.

5.5 Summary and conclusion

We have performed a combined SL and dynamical mass analysis for a sample of 29 SL selected clusters from the RCSGA survey, in the redshift range $0.22 < z < 1.01$ and covering three orders of magnitude in mass. We have derived the concentration parameters by applying an innovative technique, which consists in to probe the inner regions of the mass distribution by SL signatures, while at larger radii it is constrained by the velocity dispersion of the cluster members.

We have found that the observed $c-M$ relation of the RCSGA clusters is well described by a power law of $\alpha = -0.32 \pm 0.11$, indicating a strong dependence on the cluster

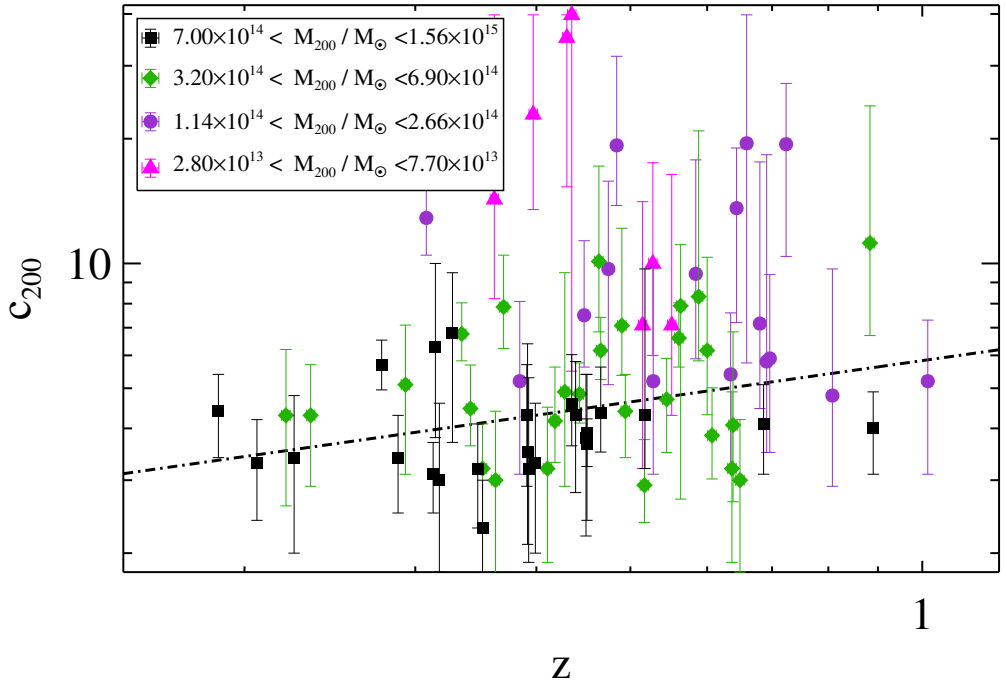

FIGURE 5.11: In this figure we visualize the $c - z$ plane obtained from the 73 galaxy clusters studied. The black squares correspond to concentration parameters of clusters contained in the mass bin centered at $M_{200} = 9 \times 10^{14} h^{-1} M_{\odot}$. While the green diamonds, purple circles and magenta triangles correspond to the mass bins centered at $M_{200} = (5.07, 2.04, 0.69) \times 10^{14} h^{-1} M_{\odot}$, respectively. The figure indicates a evident correlation between the cluster redshift and its concentration for massive clusters.

mass, which is more pronounced than the mass slope derived from theoretical works of $\alpha \simeq -0.2$, even if they have included the lensing bias and projection effects. The steep mass slope derived in this work is the result of a excess of concentration of the less massive clusters of $M_{200} \sim 1 \times 10^{14} h^{-1} M_{\odot}$, whose concentrations appear to be significantly higher than theoretical expectations. In the other hand, the measured concentrations of massive clusters of $M_{200} \sim 8 \times 10^{14} h^{-1} M_{\odot}$, are in reasonable agreement with the simulation results at $\sim 12\%$ level.

A possible bimodality has been detected in the observed $c - M$ relation, described by six clusters with a higher and steeper trend. After excluding these six clusters, we have found a full reconciliation between simulations and observations. Although, there is no evidence in our data to separate these six clusters from the rest of the SL population.

In order to perform the most complete analysis of the observed $c - M$ relation, we have combined concentration parameters of 27 clusters of our RCSGA sample, with results from 27 SGAS clusters studied by O12, and 19 CLASH clusters from M14. Resulting in the largest robust dataset of 73 concentration parameters. The possible

biases due to the different modeling techniques have been discarded by the construction of LENSTOOL models to seven clusters belonging to SGAS and CLASH samples. These mass models have yielded similar results that those in their original researches. We have also concluded that the selection method does not play a crucial role in determining the median concentration of massive clusters, by a simple statistical comparison between these three samples, in the CLASH mass range ($4 < M_{200}/10^{14}h^{-1}M\odot < 16$).

After having ruled out these potential biases, we have derived the best-fit to the full sample, which is also well described by a power law, but with a much stronger dependence on the cluster mass that found for the RCSGA data alone, with $\alpha = -0.52 \pm 0.09$. As our previous results, we have found that clusters in the high mass range, independently of their selection methodology, are reasonable consistent with the ΛCDM predictions. But the picture is different when the low mass range is analyzed, showing a significant contrast.

This steep mass slope found for the observed $c - M$ relation, is mainly due to the inclusion of the SGAS clusters, whose slope is more than twice than the expected slope. The steep behavior of the most of the clusters in the SGAS sample, increases the tension in the $c - M$ plane, adding more concentration parameters to the higher and steeper $c - M$ relation previously found by six clusters in our RCSGA sample. We have solved this concern through the analysis of the scatter of the concentration distributions, which have shown a constant growth by displacing the mass bins to lower masses, which was interpreted as a bimodal distribution. Therefore, we have detected the existence of two trends in the $c-M$ plane. One of these relations is composed by the full CLASH sample, $\sim 20 - 21$ RCSGA clusters, and $\sim 11 - 15$ clusters from SGAS, and shows a weaker dependence on the cluster mass given by $\alpha = -0.24 \pm 0.11$, resulting in an excellent agreement with theoretical works that have included the selection bias and projection effects, reconciling observations with simulation results. The rest of the RCSGA and SGAS clusters describe a higher and steeper $c-M$ relation of $\alpha = -0.69 \pm 0.09$, which is far from any theoretical expectation. Since this relation was found in two independent pieces of research, we can confirm the existence of a subset of SL clusters, which are much more concentrated than the rest of the SL population, and therefore, they should be treated independently by theoretical works. Although, as mentioned earlier there is no evidence or a clear correlation between these clusters and other parameters or observables, that make them special. Therefore, to define these clusters as a *special* SL population, more data analysis needs to be done using deeper and high-quality imaging data, as well as more spectroscopic information.

Our redshift evolution analysis has showed no evidence of a possible redshift dependence on the $c-M$ relation, although we found a clear positive correlation between the cluster

redshift and its concentration, which is more obvious for massive clusters. A broader mass and redshift range sample is necessary to perform a deeper analysis about this concern.

In this thesis we have demonstrated the power of combining SL and dynamical mass analysis to study the SL selected cluster population. This innovative technique can be applied to upcoming SL cluster samples, to fully describe the $c - M$ relation described by galaxy clusters, as well as to characterize their mass distributions. We want also to highlight the importance of combining controlled cluster samples, which allows to analyze in a broad mass and redshift ranges the observed $c - M$ relation. For example, this combined research yielded the discovery of a very likely bimodal $c - M$ relation, posing the existence of a *special* class of SL clusters. Although, we need to deepen these findings in forthcoming researches.

Chapter 6

The CLASH X-ray selected galaxy clusters: robust inner mass measurements

One of the main goals of this thesis is to contribute to the understanding of dark matter distribution in cluster-size halos, by obtaining robust mass reconstructions of galaxy clusters. A detailed understanding of the dark matter distribution is a key test of the current cosmological ΛCDM framework. Furthermore, elaborated mass distributions allow us to search for high-z magnified galaxies which would otherwise be too faint to be observed and studied.

In this chapter we present detailed strong lensing (SL) mass reconstructions for a subset of the X-ray selected galaxy clusters from the Cluster Lensing and Supernova Survey with Hubble (CLASH). We also review some of the most distant objects in the Universe which were found behind these CLASH clusters. Additionally, we check the robustness of our mass reconstructions by performing SL models for a subset of simulated galaxy clusters *like* the CLASH clusters.

6.1 The CLASH X-ray selected clusters

The best and highest resolution maps of DM distribution in massive galaxy clusters come from observations of strong gravitational lensing made by CLASH (Postman et al., 2012), which is a multi-cycle treasury program using 524 Hubble Space Telescope (HST) orbits to target 25 galaxy clusters ($0.18 < z < 0.89$), each in 16 filters with the Wide Field

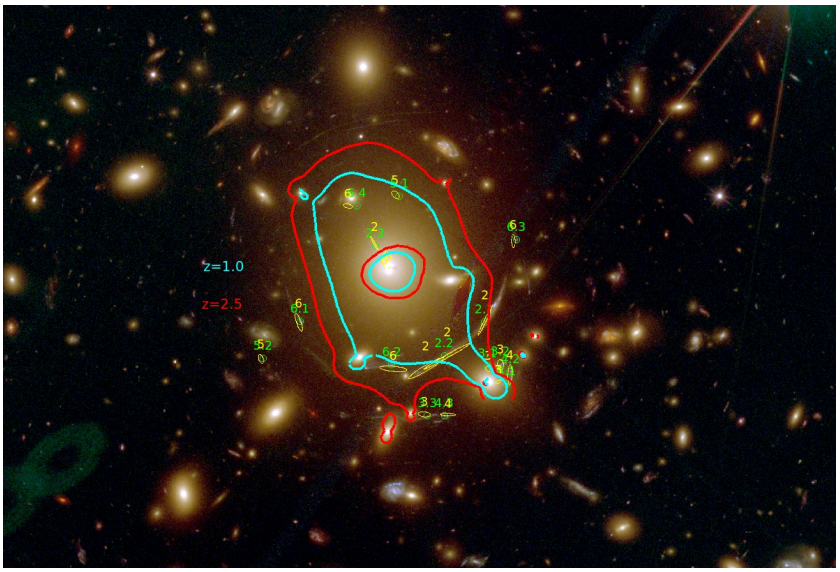

FIGURE 6.1: The best-fitting mass models for the CLASH cluster Abell 383. The multiple-image systems used as constraints in the reconstruction are labeled by green circles, while the predicted images by the current best-fitting mass model are shown by yellow ellipses. The red and cyan lines correspond to critical curves at $z = 2.5$ and $z = 1.0$, respectively.

Camera 3 (WFC3; Kimble et al., 2008) and the Advanced Camera for Surveys (ACS; Ford et al., 2003).

In this survey, 20 clusters were specifically selected by their unperturbed X-ray morphology with the goal of representing a sample of clusters with regular, unbiased density profiles that allow for an optimal comparison with models of cosmological structure formation.

Recently, Merten et al. (2014) (hereafter M14) presented an exquisite strong and weak lensing study on multi-scale grids for 19 CLASH X- ray selected clusters. M14 found that the concentrations derived from these clusters are distributed around a central value of $\bar{c}_{200} \simeq 3.7$ with a mild negative dependence on the cluster mass. These results are fully consistent with theoretical expectations (at 4% level) and they are in reasonable agreement with the mean value of the concentration parameters of our RCSGA clusters ($\bar{c}_{200} \simeq 4.3$).

In order to check whether the lens modeling methodologies bias or not the understanding of the cluster mass distributions, we construct SL models for 7 CLASH clusters by using the SL technique described in chapter 3.

TABLE 6.1: The CLASH X-ray selected cluster subset.

Name	z	$R.A.^a$ ($J2000$)	$Dec.^a$ ($J2000$)
Abell 383	0.188	02 48 03.38	−03 31 45.4
MACSJ0329−02	0.450	03 29 41.57	−02 11 46.4
MACSJ0647.7+7015	0.591	06 47 49.80	+70 14 55.5
MACSJ1115+0129	0.352	11 15 51.90	+01 29 55.0
MACSJ1206−08	0.439	12 06 12.16	−08 48 03.4
MACSJ1720+3536	0.391	17 20 16.75	+35 36 26.2
Abell 2261	0.225	17 22 27.21	+32 07 56.9

[a]Coordinates are BCG centroids (J2000).

6.1.1 Strong lensing mass models for CLASH clusters

In this section we present SL mass reconstructions for 7 CLASH X-ray clusters. The mass models were performed by applying the same technique used in the RCSGA cluster sample. The main features of this subset are listed in Tab. 6.1.

Some SL mass models of CLASH clusters with their respective multiple-image systems have already been published (Coe et al., 2012, 2013; Umetsu et al., 2012; Zitrin et al., 2011c, 2012d) and the full set of SL models and multiple image identifications will be presented in Zitrin et al. (2014 in prep). We use these already known systems to perform our LENSTOOL mass reconstructions. The redshifts for the lensed galaxies are usually taken from the literature, as well as from the spectroscopic CLASH-VLT

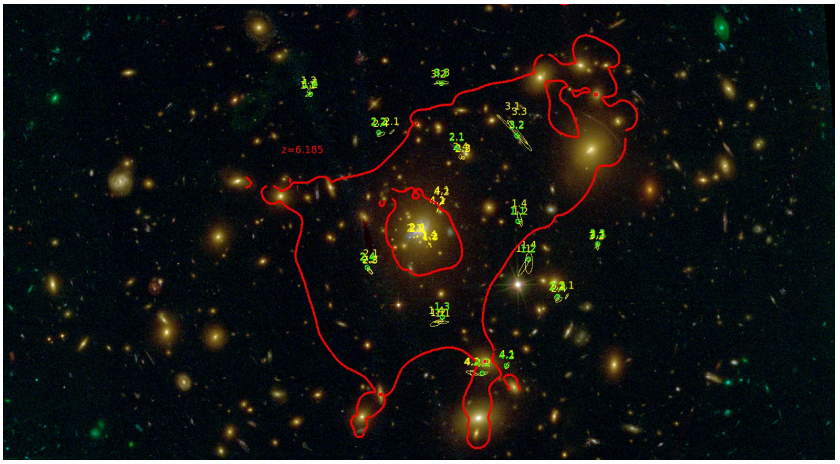

FIGURE 6.2: The best-fitting mass models for the CLASH cluster MACSJ0329−02. The multiple-image systems and predicted images are shown in the same manner as in Fig. 6.1. The red line corresponds to a critical curve at $z \sim 6$.

program (Balestra et al., 2013) or from the CLASH photometry directly, using Bayesian photometric redshifts (BPZ; Benítez, 2000).

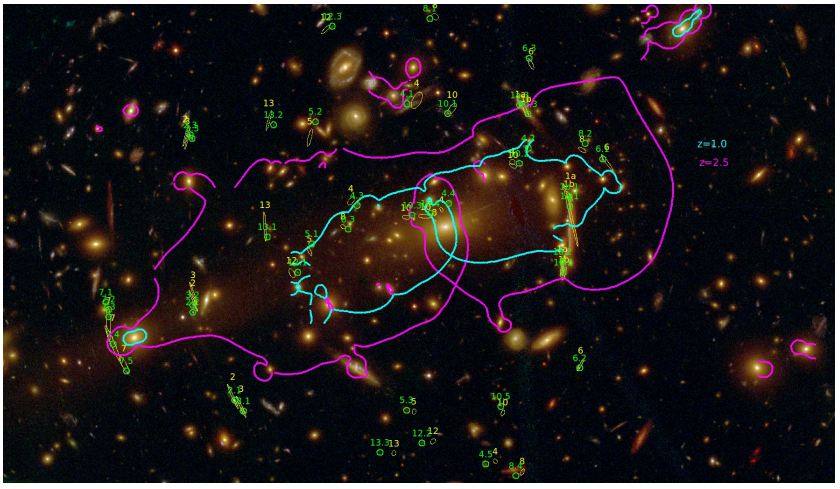

FIGURE 6.3: The best-fitting mass models for the CLASH cluster MACSJ1206−08. The multiple-image systems and predicted images are shown in the same manner as in Fig. 6.1. The magenta and cyan lines correspond to critical curves at $z = 2.5$ and $z = 1.0$, respectively.

As described in chapter 3, the mass reconstructions are performed by assuming an ellipsoidal NFW profile (Navarro et al., 1996, 1997) to describe the projected mass distribution for the main DM halo (Eq. 3.1). Then, we add the mass contributions from the member galaxies (Eq. 3.6) assuming a truncated Pseudo-Isothermal Elliptical Mass Distribution (PIEMD; Kassiola and Kovner, 1993; Kneib et al., 1996) with a constant mass-to-light ratio for all selected cluster members. From the best-fitting mass models, we derive the concentration parameters, the total cluster masses and other important

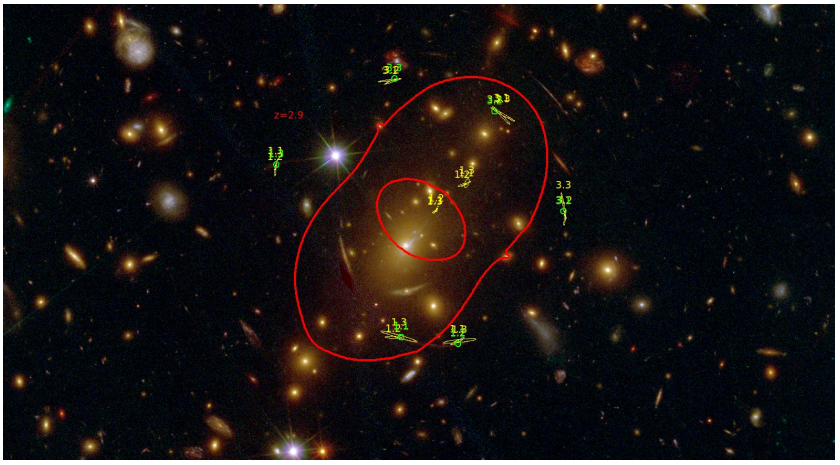

FIGURE 6.4: The best-fitting mass models for the CLASH cluster MACSJ1115+0129. The multiple-image systems and predicted images are shown in the same manner as in Fig. 6.1. The red line corresponds to a critical curve at $z = 2.9$.

TABLE 6.2: Best-fitting model parameters.

Name	$\chi^2/d.o.f.$	c_{200}	M_{200} $[10^{14}h^{-1}M_{\odot}]$
Abell 383	2.41/2	4.9± 1.3	8.62± 2.90
MACSJ0329−02	3.89/3	4.2± 1.1	7.48± 2.56
MACSJ0647.7+7015	13.6/11	3.7± 0.8	8.31 ± 2.10
MACSJ1115+0129	1.88/1	4.0± 1.4	10.54± 2.81
MACSJ1206−08[a]	35/42	6.1± 0.9	9.22± 3.82
MACSJ1720+3536	2.91/1	3.4± 1.0	1.94± 0.69
Abell 2261[b]	3.85/5	5.6± 1.9	12.67± 1.93

[a]Previously described in Coe et al. (2013).
[b]Previously described in Umetsu et al. (2012).
[c]This clusters is also included as part of the RCSGA sample. Tab. 5.2

properties of these clusters, such as the ellipticity of the projected mass distribution and its orientation. The concentration parameters and the total masses derived from the best-fitting mass models are reported in Tab. 6.2. It should be noted that six of these clusters were already presented in the previous chapter (Tab. 5.4).

The best-fitting mass models are shown through their critical lines and predicted images in Figs. 6.1, 6.2, 6.3, 6.4, 6.5, 6.6, and 6.7. The multiple-image systems used as constraints in the reconstruction are labeled by green circles while the predicted images by the current best-fitting mass models are shown by yellow ellipses. The critical curves are shown for different redshifts which are respectively labeled. From these figures we can

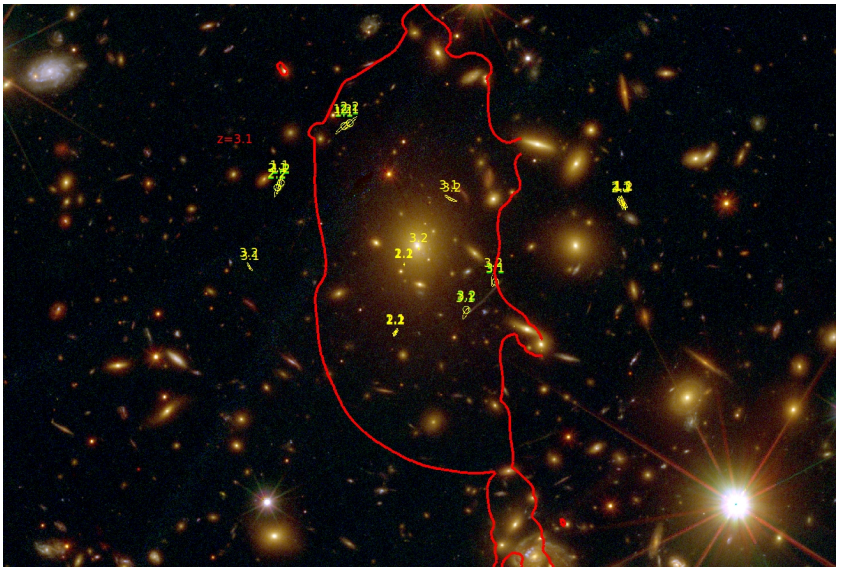

FIGURE 6.5: The best-fitting mass models for the CLASH cluster MACSJ1720+3536. The multiple-image systems and predicted images are shown in the same manner as in Fig. 6.1. The red line corresponds to a critical curve at $z = 3.1$.

already see the excellent image reproduction that we obtain with the best-fitting mass models. In all cases, the rms error in the image reproduction was lower than $\sim 1.5''$, assuming an expected scatter of $\sigma_r = 1.4''$ due to lensing by structures along the line of sights and variation in the mass-to-light ratio of cluster galaxies (Host, 2012; Jullo et al., 2010).

In Fig. 5.4 (chapter 5), we presented the ratio between the concentration parameter results derived by M14 and those derived in this work. From that figure one can see that our results are moderately consistent with the results derived by M14 (by using SaWLens, more details in §5.4.1.1). Although, the models for the clusters Abell 2261, MACSJ1206−08, and MACSJ1115+0129 yielded different results to those presented in M14. However, the LENSTOOL model results for Abell 2261 and MACSJ1206−08 were previously presented in Umetsu et al. (2012) and Coe et al. (2012), respectively. In both works, these results were compared with concentrations derived from other models, which were always consistent with each other within the statistical errors.

Therefore, we can conclude that the mass reconstructions derived in this thesis for the CLASH clusters are reliable measurements of the inner mass distributions of these

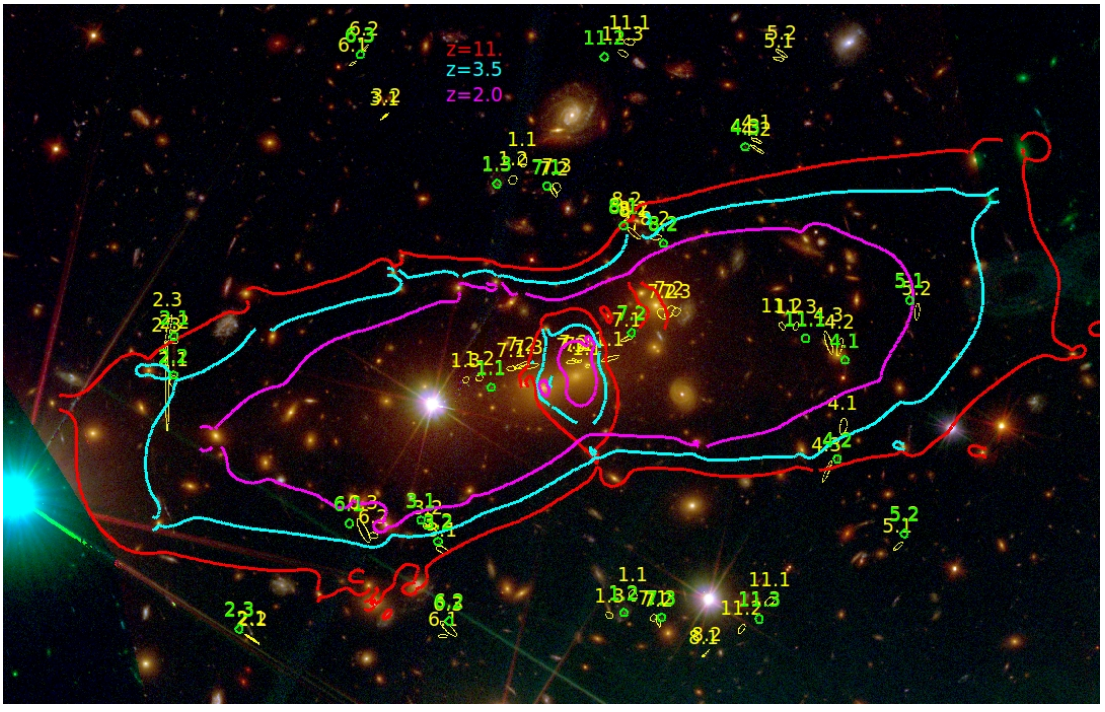

FIGURE 6.6: The best-fitting mass models for the CLASH cluster MACSJ0647.7+7015. The multiple-image systems and predicted images are shown in the same manner as in Fig. 6.1. The magenta, cyan, and red lines correspond to critical curves at $z = 2.0$, $z = 3.5$ and $z = 11.0$, respectively. The system 6 corresponds to a J-dropout at $z = 10.7^{+0.6}_{-0.4}$, at 95% confidence limits.

systems. With these results, we are providing new "tools" to probe the current understanding of our Universe.

Before starting the next section, we should highlight that thanks to the mass reconstruction of the cluster MACJ0647.7+7015 we found a candidate for the most distant galaxy known to date. The full details of this discovery can be found in Coe et al. (2013). In brief, our SL mass model for this cluster predicted a candidate system composed by three multiple images (system 6 in Fig. 6.6) with a rms in the image position reproduction lower than $1''$. Since the redshift was unknown, it was left as a free parameter in the optimization process with a flat wide prior of $1.0 < z < 15.0$. The best-fitting model yielded a redshift of $z \sim 11$, ruling out lower redshift solutions (in terms of rms error in the image reproduction). Then, our CLASH team conducted an exhaustive J-dropout analysis. We found that the most likely photometric redshift for this system should be $z = 10.7^{+0.6}_{-0.4}$, at 95% confidence limits. We also found that galaxies of known types at $z < 9.5$ are ruled out at $7.2 - \sigma$.

Since two independent methods yielded identical results, we can conclude that the most likely redshift for this systems has to be $z \sim 11$. This result together with other high redshift galaxies discovered by CLASH team have helped to characterize the luminosity function of the objects in the early Universe, which is a key test for the ΛCDM cosmological model.

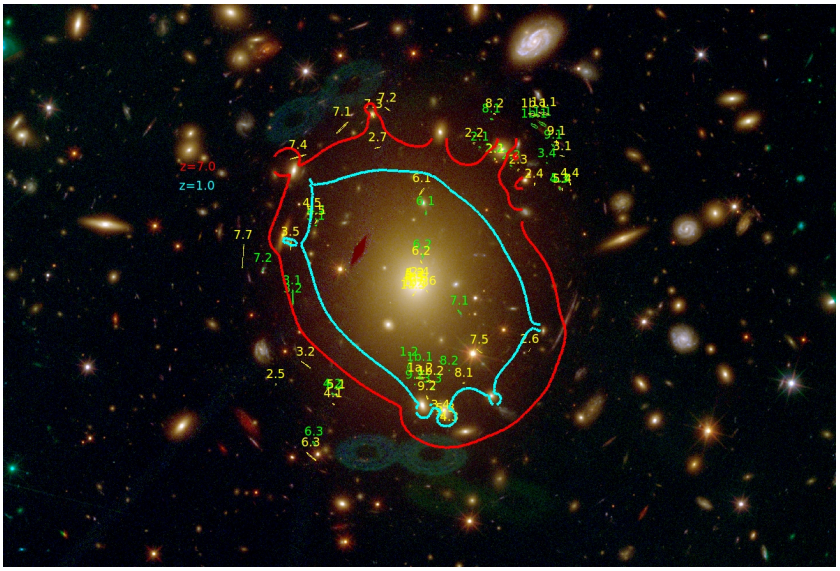

FIGURE 6.7: The best-fitting mass models for the CLASH cluster Abell 2261. The multiple-image systems and predicted images are shown in the same manner as in Fig. 6.1. The red and cyan lines correspond to critical curves at $z = 7.0$ and $z = 1.0$, respectively.

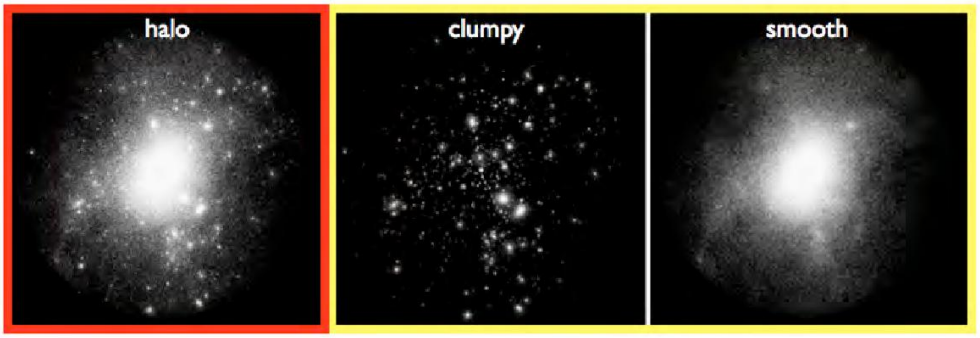

FIGURE 6.8: This figure shows the resulting halo (left panel), clumpy (middle panel) and smooth (right panel) components. This figure was taken from http: //cgiocoli.wordpress.com /research-interests/moka/.

6.2 Synthetic galaxy clusters

In order to double-check the robustness of our mass reconstructions, we perform SL mass models for a subset of simulated galaxy clusters with properties similar to the CLASH clusters. In this way we can corroborate if the mass distributions derived from our SL analysis are able to reproduce the "true" mass of the clusters.

The simulated clusters were taken from the ongoing projects of Massimo Meneghetti together with Carlo Giocoli and CLASH team. Some details of these projects can be found in Meneghetti et al. (2014), Giocoli et al. (2012), and Meneghetti et al. (2010).

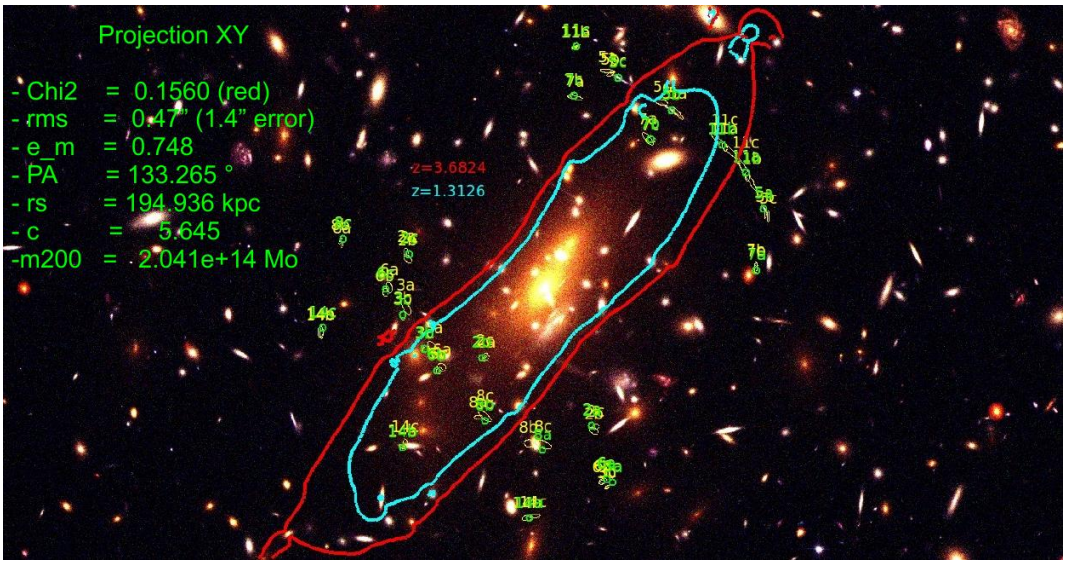

FIGURE 6.9: This figure shows a simulated cluster at $z = 0.29$ in its XY projection. The multiple-image systems, the predicted ones and the critical curves are displayed in the same manner than in Figs. 6.1 − 6.7.

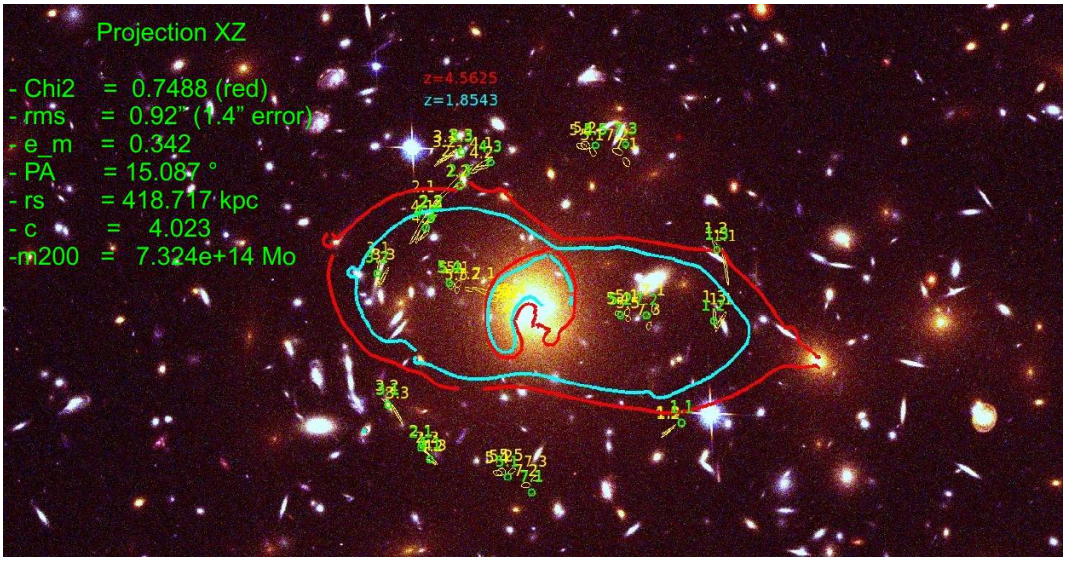

FIGURE 6.10: This figure shows the same simulated cluster at $z = 0.29$, but in its XZ projection. The multiple-image systems, the predicted ones and the critical curves are displayed in the same manner than in Figs. 6.1 − 6.7.

In brief, these clusters were created by using the semi-analytical code Matter density distributiOn Kode for gravitationAl lenses (MOKA, Giocoli et al., 2012). This code produces halos mass distributions by combining a clumpy component, which represents the cluster members, and a smooth component, that stands the DM distribution which in turns is derived from the clumpy component. This algorithm includes features like triaxiality, BCG, adiabatic contraction due to baryon cooling and galaxy halo truncation by dynamical friction. Furthermore, the main dark matter halo is simulated by a triaxial shape NFW density profile, while a Jaffe density profile is used for the BCGs. The substructures (cluster members) are described by a truncated SI profile. Finally, mass distributions are projected on the plane of the sky, since this is the only mass that can be obtained through lensing. Fig. 6.8 shows the resulting halo component plus the smooth and clumpy components.

Then, the lensing signatures are included in these simulated mass distributions by the SkyLens code (Meneghetti et al., 2010). This code creates simulated patches of the sky using real galaxies from the Hubble Ultra-Deep Field (HUDF).

The way we proceeded in this thesis is the following: we used three different projections of one simulated cluster (at z=0.29) to perform SL mass reconstructions of the cluster. The main goals of this study are: 1) investigate how much the parameters derived from SL mass models change with the orientation of the cluster, and 2) determine how robust are the derived mass distributions from the lensing reconstructions.

The SL mass models are shown in the Figs. 6.9, 6.10, and 6.11. The best-fitting mass models are displayed in the same manner as in the figures of the previous section, although this time the parameters derived from the best-fit are also displayed in the figures. By visual inspection, we can directly see the high accuracy in the image prediction. Indeed, the highest rms error in the image position was only $0.92''$ (with $\sigma_r = 1.4''$) for the XZ projection, while for the other two it was about $\sim 0.5''$. The main results can be summarized as follows: the ellipticity of the projected mass distributions varies from $\sim 0.3 - 0.75$, the concentration parameter goes from $c_{200} \sim 0.40$ to $c_{200} \sim 0.56$, and the total mass varies from $2 \lesssim M_{200}/10^{14} h^{-1} M_{\odot} \lesssim 7$. From this simple analysis we can already conclude or corroborate that there is a strong dependence of the SL reconstructions on the cluster halo orientation. Therefore, the projection effects should be taken into account before arriving to any conclusion.

In order to check the robustness of our results, we compare the projected mass distribution derived by our SL modeling technique with the "true" projected mass distribution of these clusters. Fig. 6.12 shows this comparison for the projections XY and XZ, which present the extreme differences in the best-fitting model parameters. In this figure we also visualize the projected mass distribution derived by other SL models (Zitrin et al. 2009b method, in particular). We can see that all methods are able to derive very reliable mass distributions. Although, in both projections our results are closer to the true mass than the others. In fact, we were able to reproduce the projected mass at $\sim 5\%$ level.

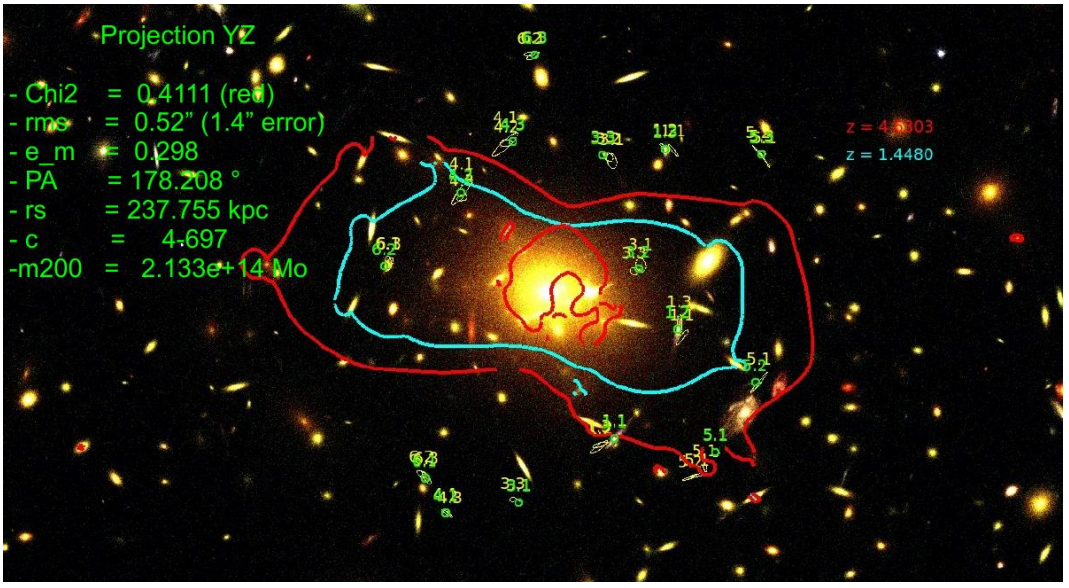

FIGURE 6.11: This figure shows the same simulated cluster at $z = 0.29$, but in its YZ projection. The multiple-image systems, the predicted ones and the critical curves are displayed in the same manner than in Figs. 6.1 – 6.7.

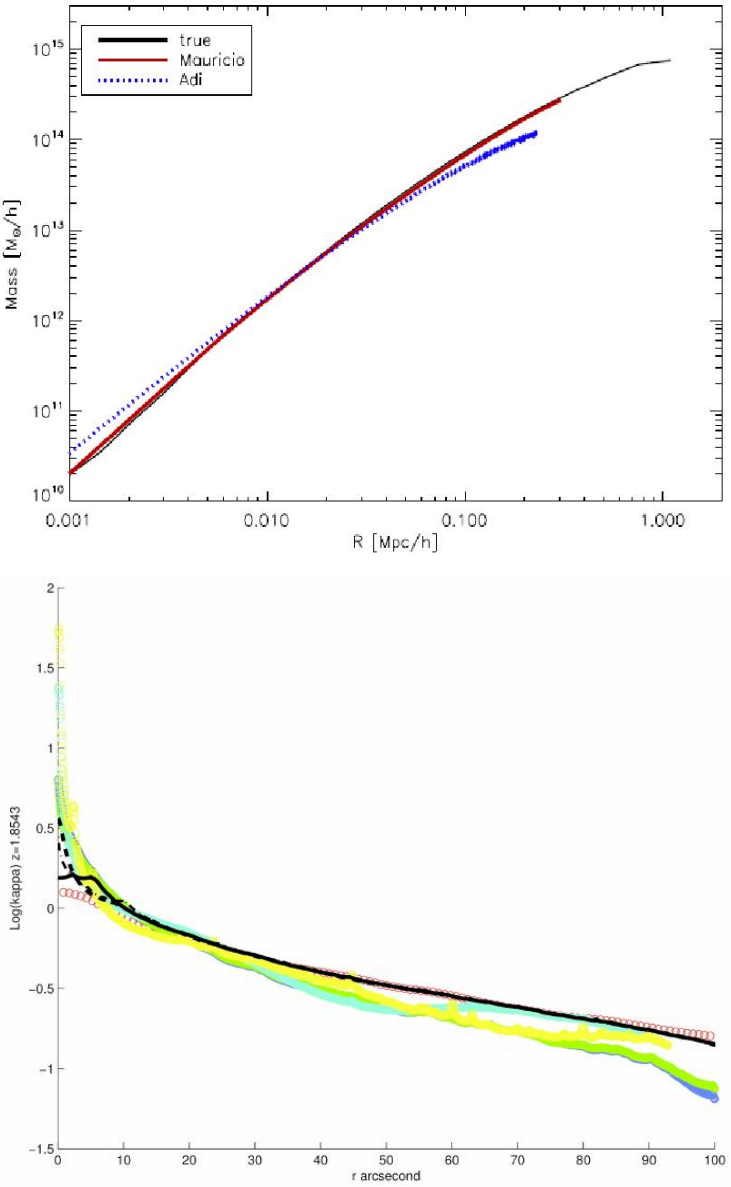

FIGURE 6.12: Top panel: Mass distribution in the XY projection of the simulated cluster at $z = 0.29$. The black line corresponds to the true profile of the projected mass distribution. The red solid line corresponds to results derived from the best-fitting mass models of our mass reconstruction, while the blue dotted line represents the mass distribution derived by using the light-trace-mass method (Zitrin et al., 2009b). Bottom panel: Mass distribution (in terms of κ) in the XZ projection. In this case, the red open circles correspond to the true mass and the black solid line describes the best-fitting mass model derived in this thesis.

Consequently, we can conclude that our mass reconstructions yield accurate mass distributions and therefore, the properties derived from these mass distributions represent (or are very close to) the real characteristics of the galaxy clusters.

It should be noted that all mass models presented in this chapter were performed using

only SL constraints, therefore, all the conclusions presented here are strictly valid in the most inner region of the clusters, although it does not mean that they are not true at larger radii.

6.3 Conclusions

In this chapter we presented detailed SL mass reconstructions for a subset of 7 X-ray selected galaxy clusters from the CLASH survey. From the best-fitting mass models we derived the concentration parameters which were compared with those derived by M14, where they used a different modeling methodology. This comparison resulted in a reasonable agreement indicating that the lens modeling methodologies used to analyze the CLASH clusters do not bias the understanding of their mass distributions.

Thanks to the lens power of the cluster MACJ0647.7+7015, we found a candidate for the most distant galaxy known to date. This result together with other high redshift galaxies discovered by CLASH team have helped to understand and characterize the early Universe.

Finally, we performed SL mass reconstructions for simulated clusters like the CLASH clusters in order to check the robustness of our results. Our mass reconstructions were in excellent agreement with the "true" mass distributions. Even more, our SL mass models were those that provided the most accurate mass reconstructions in our team.

Therefore, we can conclude that the mass reconstructions derived in this thesis for the CLASH clusters are reliable measurements of the inner mass distributions of these systems.

Chapter 7

A fully automated Multiple-Image Finder ALgorithm (MIFAL) for strong-lens modeling

From previous strong lensing studies we have noticed that by constructing a simple *preliminary* lens model, multiple-images can be easily matched by the model, by projecting "manually" each arc-like image to the source plane and back to the image plane, and then searching for similar looking (and similar redshift) objects as the model predicts, i.e., reproduces. Thus, our goal in this chapter is to present a simple algorithm that automatically find multiple-image systems in galaxy clusters.

7.1 The Multiple-Image Finder ALgorithm

We detail here the simple and innovative **M**ultiple-**I**mage **F**inder **AL**gorithm (MIFAL), and its different components.

7.1.1 The lensed galaxy catalogs

The first step we apply here for automatically searching for multiple images is to primarily identify as many lensed galaxy candidates as possible in the cluster or lens field. For that purpose, two independent catalogs were built for each clusters.

7.1.1.1 The arc candidate catalogs

To build the first catalog we use the *Arcfinder* algorithm (Seidel and Bartelmann, 2007), which uses the first and second brightness moments for the detection of elongated objects across the frame. As detailed in Seidel and Bartelmann (2007), the algorithm is sufficiently robust to detect such features even if their surface brightness is near the pixel noise of the image, yet the amount of spurious detections remains (relatively) low.

The algorithm subdivides the image into a grid of overlapping, circular cells (see Fig. 7.1a) which are iteratively shifted towards their local center of brightness in their immediate neighborhood (see Fig. 7.1b to 7.1e). The center of brightness is defined as the first moment $\int_A \vec{x} d^2x = \bar{\vec{x}}$, where A is the cell area and $q(I)$ is a weighting function that dependents on the image intensity $I(\vec{x})$. The code then computes the cell ellipticity $(Q_{11} - Q_{22} + 2iQ_{12})/(Q_{11} + Q_{22})$ using their second brightness moments

$$Q_{ij} = \frac{\int_A (x_i - \bar{x}_i)(x_j - \bar{x}_j) q(I(\vec{x}))\, d^2x}{\int_A q(I(\vec{x}))\, d^2x}. \tag{7.1}$$

The ellipticity of each cell provides a natural measure of its orientation in the image and allows us to compute their angular separation. Cells oriented in the same direction, and spatially aligned, are then combined into initial objects using a simple coherence measure (see Fig. 7.1f); essentially the product of the cosine of the angle between cell orientations and a (scaled) perpendicular cell separation, with a friends-of-friends type algorithm. At this point, the objects are nothing more than sets of correlated cells (see 7.1g) where one cannot directly infer much morphological information, and there are still many spurious detections, e.g. for spatially connected point sources. A large number of spurious detections is removed with a filter interpreting the brightness distribution in each cell to remove those which are unlikely to belong to an elongated object. For objects still containing a sufficient number of valid cells, several consecutive steps compute isophote contours which allow the computation of basic properties like length, length-to-width and signal-to-noise. These are then used to choose the most likely arc-shaped objects, and further reduce the number of spurious detections. Some further filtering and noise cleaning procedures take place, for example to remove elongated objects which are clearly not gravitational arcs (such as diffraction spikes, spiral galaxy arms, edge-on galaxies, etc.), resulting in a final catalog of *arc* candidates (see 7.1i).

It should also be noted, that the arc detection part takes only several seconds on a standard CPU. Two main caveats are entailed, however, by using an arcfinder rather than examining each arc candidate by eye. First, some spurious detections of elongated, un-lensed galaxies may appear in the catalog. These, however, will be filtered out at a later stage based on their photometric redshifts and the mass model. Second,

images with a feeble elongation or distortion may not be detected even if they are multiply lensed (see example the multiply-imaged spiral galaxy in MACS J1149.5+2223, Zitrin and Broadhurst 2009). Our goal throughout, though, is not to test whether all previously known multiple-images are uncovered, but whether enough of them are found to automatically constrain the mass model.

7.1.1.2 The high-redshift galaxy catalogs

To include all the galaxies distorted by the cluster potential, even the multiple images that have a slight deformation, we use another automatic method to build lensed galaxy catalogs taking into account only the photometric redshift of the galaxies in the cluster field.

The construction of these independent catalogs is carried out by selecting all the objects from the CLASH survey catalogs with photometric redshifts higher than $z_l + 0.3$, where z_l is the redshift of the cluster. The selection does not consider the elongation or shape of the galaxy, i.e., without using an *arcfinder* algorithm. It will maximize the number of candidates but could certainly introduce un-lensed objects in the catalog, nevertheless, these will be rejected out in the next step by the algorithm itself.

As we describe below, with both catalogs the algorithm is able to recover the same number of multiple-image systems. However, when the high-redshift galaxy catalogs are used instead the *arc* candidate catalogs, the computation time is increased to reach the final systems.

7.1.2 Photometric redshifts

We use the Bayesian Photometric Redshifts (BPZ; Benítez 2000; Benítez et al. 2004; Coe et al. 2006) of the CLASH survey to populate our catalogs. The CLASH photometry is modeled using the SED templates from PEGASE (Fioc and Rocca-Volmerange, 1997), which have been significantly adjusted and re-calibrated to match the observed photometry of galaxies with known spectroscopic redshifts from FIREWORKS (Wuyts et al., 2008). The FIREWORKS data set includes 0.38 - 24 μm photometry of galaxies down to mag $\sim$ 24.3 (5-σ K-band) and spectroscopic redshifts out to z $\sim$ 3.7. In analysis of large datasets with high quality spectra, this template set yields $\leq$ 1% outliers, demonstrating that it encompasses the range of observed metallicities, extinctions, and star formation histories for the vast majority of real galaxies.

For our *arc* candidate catalogs, we match each *arc* identified by the arcfinder with the corresponding source in the CLASH catalogs to obtain its photometric redshift. In the

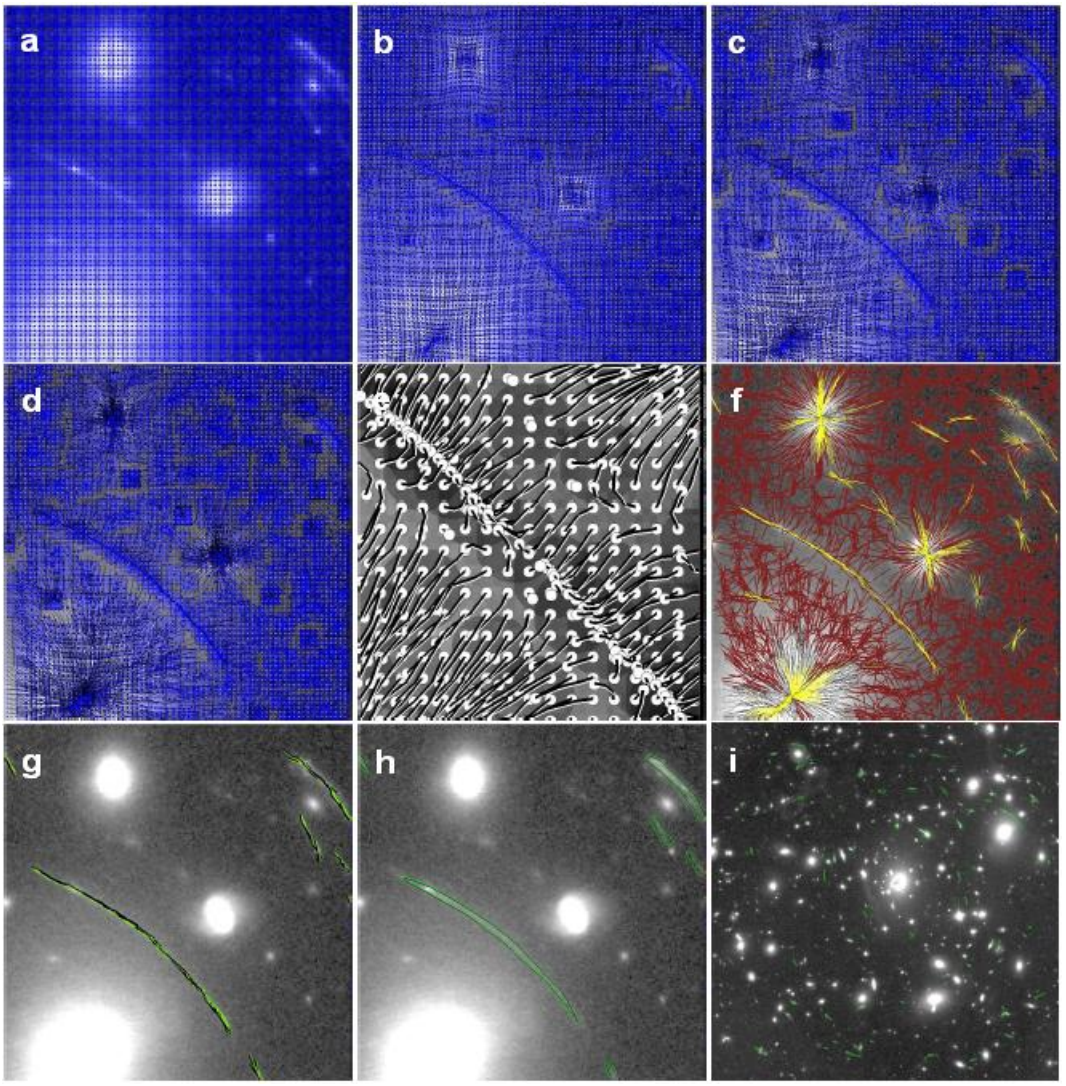

FIGURE 7.1: Example of some key steps in the arcfinder algorithm. The upper-left panel (a) shows the initial division into cells in an equally spaced grid. The following sub figures ("b-e") show the iterative displacement of the cells towards their centers of brightness. "e" shows a zoom-in of the complete process where the black lines trace the path of each cell, shown by a white circle. Then, highly correlated cells are searched for, marked in yellow in sub figure "f". These ensembles of cells are now combined into objects using a friends-of-friends type algorithm, and the resulting objects are shown in "g", where their calculated brightness contours are shown in "h". Sub figure "i" shows the central field of MACS0329 and the arclets found therein in green contours (shown also in Fig. 7.2 for a better view).

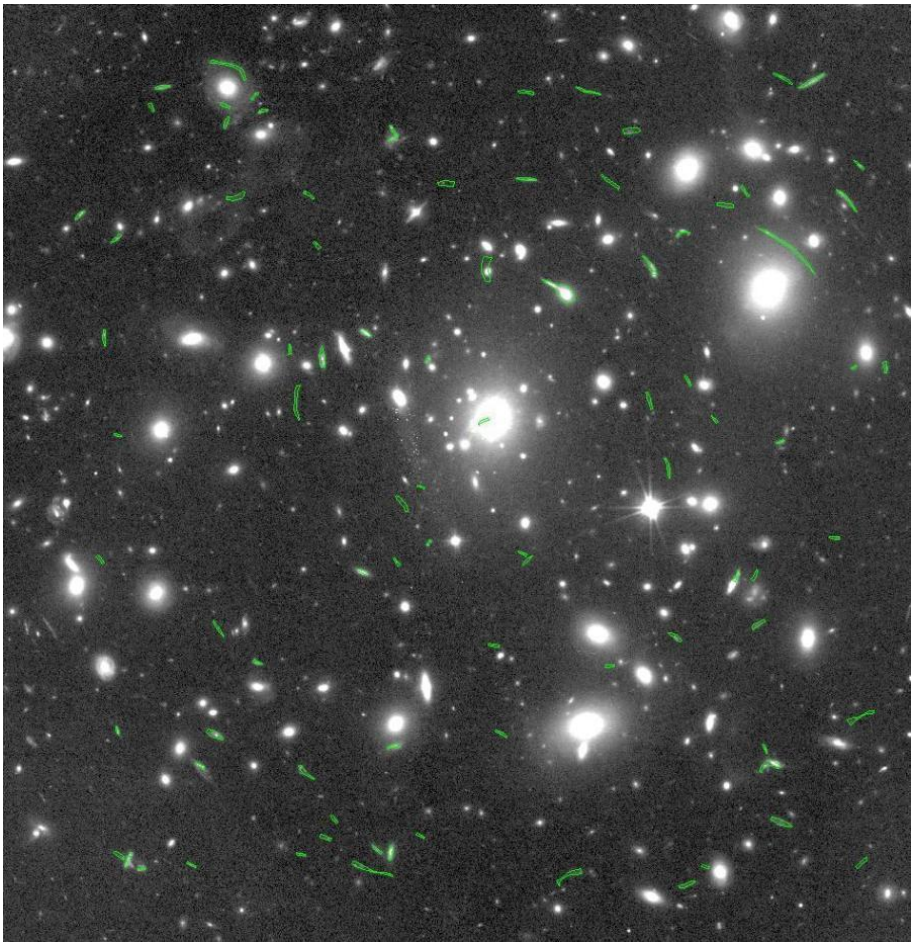

FIGURE 7.2: Same as Fig. 7.1, but enlarged for better view.

case of the high-redshift galaxy catalogs, we build them by selecting all the high-redshift objects in the CLASH catalogs. Therefore, each object in our catalogs corresponds to a source in the CLASH catalogs. These redshifts will then be used to compute the (relative and approximate, see below) lensing distances to project the candidate arcs through the mass model and further constrain the model in the cases where these were matched as multiple images.

7.1.3 The preliminary mass model

The preliminary mass model used in MIFAL is based on the parametric method of Zitrin et al. (2009c) (see also Broadhurst et al. 2005a), which is based on the assumption that light traces mass (hereafter LTM). Then, the mass model can be quickly constructed by adopting a simple representation of the cluster member galaxies and the underlying DM together with a prior guess of the ratio between the two components, K_{gal}, and a certain

mass-to-light ratio (M/L) to account for the overall normalization, K_q. For details of this mass modeling method see Zitrin et al. (2009c) and Zitrin et al. (2011b).

In brief, the mass model consists of three components. The first component are the cluster galaxies, whose surface mass density is modeled as a power-law of slope q, scaled by their luminosity. The superposition of the mass density contribution from all red-sequence galaxies (brighter than a certain threshold: usually $m^\star + 2$, where $m^\star$ is the break in the luminosity function of the members) represents the lumpy, galaxy component. This mass distribution is then smoothed using a 2D polynomial spline of degree S to provide a model for the DM distribution in the cluster halo, which is the second component of the model. These two components are then added together with a relative weight (K_{gal}), and the resulting deflection field of this mass distribution is calculated over the image grid. Finally, the third component is an external shear which can be added to the deflection field for further flexibility. In all, there are six free parameters: the mass scalings of both the smooth and galaxy components, the power law of a unique galaxy density profile, the degree of the smoothing polynomial, and the strength and direction of the external shear.

As we have mentioned in previous work (e.g. Zitrin et al., 2009a), the choice of the power-law (q) and smoothing degree (S) hardly affects the reproduction of multiple images. These parameters mainly affect the mass *profile*, so that all systems can in principle be reproduced with either choice of q and S. The values of q and S will only affect the radius from the mass center at which the multiple images form, but since here we wish to create a preliminary model, we can iterate on different cosmological distances (D_{ls}/D_s normalizations) searching for multiple images with the same effect. We set these two parameters to typical values deduced from our previous analyses (see also Zitrin et al. 2011b); q=1.1 and S=11. Similarly, for the two other parameters: the overall scaling (K_q), and the relative galaxy mass to DM fraction (K_{gal}), we adopt typical values; $K_q = 0.4$ and $K_{gal} = 0.03$. Here, we do not use an external shear, since we do not use any multiple images to constrain the mass model yet. We thus have now a single, preliminary mass model (see Fig 7.3) that can be used to find multiple images. It is also worth mentioning, that once photometry is in hand and the red-sequence member galaxies are chosen, the construction of this initial mass model takes only a few seconds.

7.1.4 Searching for multiple images

With the LTM preliminary mass model described above and the lensed galaxy catalogs in hand, we can start the multiple-images search. Since the following procedures are exactly the same for both catalogs (*arc* candidate and high-redshift galaxies catalogs),

we will refer to the objects in both catalogs just as "candidates", therefore, the next procedures will be described for the compound "candidate catalog".

We use the preliminary mass model to automatically project each candidate in our catalog to the source plane and then back, to predict the location of possible counter images. The program then runs over all the candidates in the catalog searching for objects near the predicted locations and with similar photometric redshift as the re-lensed candidate. The thresholds Δz and Δr used to parametrize this similarity are user defined, but to optimize the number of real multiple-image systems we fix $\Delta z = 0.5$ for the redshift difference and $\Delta r = 10''$ for the search radius.

Once MIFAL has selected all the likely multiple-images for the re-lensed candidate, it calculates the median system redshift, z_{sys}, using the redshift of all members. The code then runs again for the next candidate in the catalog and so forth. At the end of this stage, each candidate in our catalog has its own temporary multiple-image system and its respective z_{sys}.

It should be noted, as we are conducting a blind study, the D_{ls}/D_s normalization for the preliminary mass model can not be fixed because we do not know a-priori any confirmed multiple-image system, i.e., any confirmed source. To explore all the possible normalizations, the code repeats all the processes described above for 25 discrete values of $D_{ls}/D_s(z_s)$, from source redshifts $z_s = z_l + 0.1$ to $z_s = 9$, where z_l is fixed to the cluster redshift and z_s increases logarithmically such that the increments in $D_{ls}/D_s(z_s)$ are linear.

Then, all the temporary systems of the 25 realizations are grouped in five D_{ls}/D_s bins (where each bin contains five realizations corresponding to five different source redshifts), merging those systems that have at least 2 images in common and similar redshift ($z_{sys} \pm \Delta z$). Once it ends, we have five new catalogs of semifinal multiple-image systems, one for each D_{ls}/D_s bin. Now, a new filtering/selection step takes place in our procedure, where the unlikely images in the semifinal systems are removed and the best of these new filtered systems are selected, obtaining the final weighted multiple-image system catalogs. To explore all the possible lensed systems scenarios, two different filtering/selection methods were implemented. The first method selects images only based on their $\chi^2(r_{search}, z_{ima}, color, E_r)$, while the second one selects the images by their lens configuration, taking into account image parity and the previous $\chi^2(r_{search}, z_{ima}, color, E_r)$.

7.1.4.1 χ^2 only method

The χ^2 only method is implemented to study atypical multiple-image configurations that usually appear in complicated mass distributions. For example, the systems 1 in

the cluster MACS J0717.5+3745 (Zitrin et al., 2009c), in where 5 multiple-images are in the same side of the cluster field, and there are no counter-images in the other side. In other words, this method does not consider the position of the multiple images in the lens field to select them.

This method assigns to each multiple-image candidate a χ^2 grade to weight its likelihood of being a member of this family, defined by:

$$\chi^2_{ima} = \chi^2_r + \chi^2_z + \chi^2_{color} + \chi^2_{Er}, \tag{7.2}$$

where the first component is the χ^2 of the image location defined by:

$$\chi^2_r = ((x' - x)^2 + (y' - y)^2) \ / \ \sigma^2_r, \tag{7.3}$$

with [x′,y′] and [x,y] being the position of the candidate, and the model-predicted multiple-image, respectively, and σ_r the expected image-plane reproduction uncertainty due to large-scale structure and matter along the line of sight (e.g. Zitrin et al., 2012c), which we set as $\sigma_r = 1.4''$ throughout. The second component is defined as:

$$\chi^2_z = ((z' - \overline{z})^2) \ / \ \sigma^2_z, \tag{7.4}$$

where z', $\overline{z}$, and σ^2_z, represent the measured photometric redshift, the median system redshift (from the other images found for that system, excluding the image in question), and the redshift error, respectively. The third component is defined as:

$$\chi^2_{color} = \sum_i (color'_i - \overline{color}_i)^2 \ / \ \sigma^2_{color_i}, \tag{7.5}$$

where $color'_i$, $\overline{color}_i$, and $\sigma^2_{color_i}$ are the i color of the candidate in question, the median system color (from the other images found for that system excluding the image in question), and the color error of the i color, respectively, The sum is over the $F814w-F625w$, $F625w - F475w$, and $F814w - F475w$ colors. The fourth component is defined as:

$$\chi^2_{Er} = ((Er' - Er_{mnu})^2) \ / \ \sigma^2_{Er\_mnu}, \tag{7.6}$$

where Er' is the Einstein radius of the candidate, defined as the distance from the brightest cluster galaxy (BCG) to the object. Er_{mnu} and $\sigma^2_{Er\_mnu}$ are the median

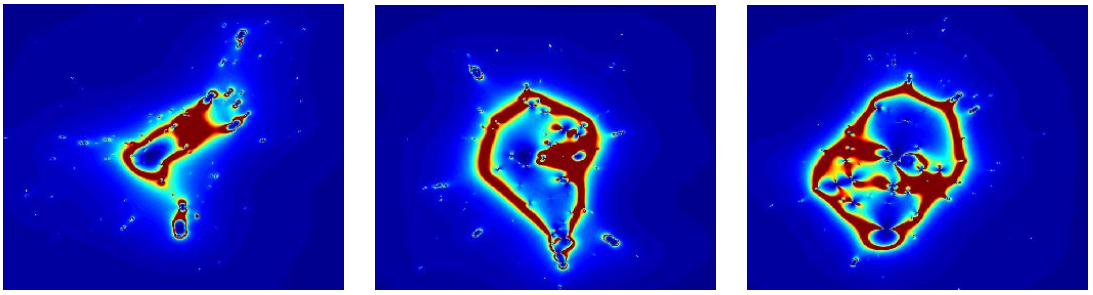

FIGURE 7.3: The preliminary mass models for the cluster M0329 (left panel), M1720 (middle panel), and M1931(right panel). These preliminary mass models are shown in terms of their magnification maps.

Einstein radius and its respective $1-\sigma$ error found by Meneghetti et al. (2011) in their MARENOSTRUM UNIVERSE simulation (Meneghetti et al., 2010) for massive clusters, respectively. We set $Er_{mnu} = 25''$ and $\sigma^2_{Er\_mnu} = 5''$ throughout.

After MIFAL assigns a χ^2 grade to each candidate, it selects the most likely images per system. In practice, if the semifinal system has more than five images (and most of the semifinal systems have them), the algorithm selects the five images with the lowest χ^2_{ima}. Then, it calculates the total χ^2_{sys} of the system, adding in quadrature the χ^2_{ima} of the selected images. If the semifinal system has five multiple-images or less, the program only calculates its χ^2_{sys}.

Once the program has run through all semifinal systems, filtering and updating them, we obtain five final multiple-image systems catalogs, one for each D_{ls}/D_s bin. Henceforth, these final catalogs are named as *the* χ^2 *only catalogs*.

7.1.4.2 Lens configuration, parity and χ^2 method

This method is implemented to study the typical lensed system configurations that are generally produced by smoothed and elliptical mass distributions. Some of the most typical lens configurations are the Einstein cross, cusp arc, and fold arc systems, which have five multiple-images each (four distributed around the lens and one close to the cluster center). As it is common in massive elongated clusters that cusp system only shows the three highly magnified close images, we consider this configuration independently.

This method uses the four lens configurations described above to add position constraints in the selection process of the final multiple images. In practice, the program takes a semifinal system and checks if there are image combinations that match with some of these four lens configurations, and saves the successful image combinations. Then, the program assigns a χ^2 to each successful combination, defined by:

TABLE 7.1: MIFAL results for M0329

Id	R.A.[a] (°)	Dec[a] (°)	z_{ima}	z_{sys}	[b]z_{norm}	R_{find} ($''$)	E_{r_ima} ($''$)	E_{r_sys} ($''$)	χ^2_{col}	χ^2_z	$\chi^2_{R_{find}}$	χ^2_{parity}	$\chi^2_{E_r}$	χ^2_{ima}	χ^2_{sys}
1.1	52.415100	-2.196250	3.010	3.080	1.476	6.9	29.2	30.3	1.01	0.49	24.21	1.64	1.11	28.46	187.10
1.2	52.417500	-2.190630	2.868	3.080	1.476	8.8	28.8	30.3	15.90	5.22	39.18	1.64	1.11	63.05	187.10
1.3	52.424900	-2.187690	3.257	3.080	1.476	5.8	31.3	30.3	1.45	3.05	16.95	1.64	1.11	24.20	187.10
1.4	52.426500	-2.199300	3.151	3.080	1.476	7.6	16.2	30.3	38.74	0.51	29.40	1.64	1.11	71.40	187.10
2.1	52.424900	-2.187690	3.257	3.149	1.476	9.7	31.3	34.4	1.19	1.61	47.56	0.64	3.54	54.53	218.81
2.2	52.433197	-2.196578	3.041	3.149	1.476	10.0	35.9	34.4	7.31	1.77	50.92	0.64	3.54	64.18	218.81
2.3	52.422144	-2.206588	3.013	3.149	1.476	8.8	37.5	34.4	3.56	2.77	39.32	0.64	3.54	49.83	218.81
2.4	52.416600	-2.204170	3.321	3.149	1.476	8.3	37.3	34.4	6.33	4.40	35.35	0.64	3.54	50.26	218.81
3.1	52.421900	-2.201400	6.055	6.032	1.476	5.8	19.3	30.9	2.38	0.06	17.10	359.43	1.40	380.37	1632.49
3.2	52.416800	-2.198060	6.009	6.032	1.476	7.5	24.1	30.9	2.15	0.06	28.81	359.43	1.40	391.85	1632.49
3.3	52.417500	-2.195560	5.781	6.032	1.476	5.4	20.7	30.9	2.57	17.28	14.84	359.43	1.40	395.53	1632.49
3.4	52.429900	-2.188120	6.139	6.032	1.476	3.8	37.8	30.9	95.59	0.78	7.53	359.43	1.40	464.74	1632.49
4.1	52.425725	-2.190436	2.284	2.210	1.476	5.4	22.7	27.6	2.87	6.06	15.01	24.44	0.28	48.66	217.99
4.2	52.426393	-2.198453	2.244	2.210	1.476	6.5	14.0	27.6	0.98	1.04	21.56	24.44	0.28	48.29	217.99
4.3	52.415078	-2.200176	2.162	2.210	1.476	5.7	32.6	27.6	20.72	2.26	16.75	24.44	0.28	64.44	217.99
4.4	52.421065	-2.191334	2.176	2.210	1.476	7.6	19.2	27.6	1.15	1.20	29.53	24.44	0.28	56.59	217.99

[a] Coordinates of each multiple image in (J2000).
[b] Redshift used to normalize the SL model, or the redshift bin in the automated process.

$$\chi^2_{comb} = \left(\sum_i \chi^2_{ima_i} \right) + \chi^2_{Er\_sys} + \chi^2_{parity}, \tag{7.7}$$

where the χ^2_{ima} component is defined as:

$$\chi^2_{ima} = \chi^2_r + \chi^2_z + \chi^2_{color}, \tag{7.8}$$

where χ^2_r, χ^2_z, and χ^2_{color} are defined by the equations 7.3, 7.4, and 7.5, respectively, and the sum is over all members of the successful image combination in question. The second component is defined as:

$$\chi^2_{Er\_sys} = ((Er_{sys} - Er_{mnu})^2) \ / \ \sigma^2_{Er\_mnu}, \tag{7.9}$$

where Er_{sys} is the Einstein radius of the successful image combination in question. In the case of the five image configurations, the Er_{sys} is defined as the mean of the radial distances of the most distant image and its opposite image, while for the three image systems, Er_{sys} is defined as the median of the radial distances of the three members. Er_{mnu} and $\sigma^2_{Er\_mnu}$ are the median Einstein radius and its respective $1-\sigma$ error described above, respectively.

The third component is the χ^2 of the image parity. The image parity describes the relative orientation of the multiple images, which are often formed such that one of the images is a mirror image of the other. This is equivalent to the signs of the eigenvalues of the magnification matrix, where all images can be described as having either positive

TABLE 7.2: MIFAL results for M1720

Id	R.A.[a] (°)	Dec[a] (°)	z_{ima}	z_{sys}	[b]z_{norm}	R_{find} ($''$)	E_{r_ima} ($''$)	E_{r_sys} ($''$)	χ^2_{col}	χ^2_z	$\chi^2_{R_{find}}$	χ^2_{parity}	$\chi^2_{E_r}$	χ^2_{ima}	χ^2_{sys}
1.1	260.079174	35.606614	2.565	2.333	3.881	7.0	33.9	37.5	10.08	9.49	24.69	142.80	6.30	193.36	710.35
1.2	260.067820	35.601192	2.343	2.333	3.881	6.7	23.2	37.5	3.84	0.01	23.10	142.80	6.30	176.05	710.35
1.3	260.058501	35.605402	2.199	2.333	3.881	4.9	41.2	37.5	4.42	1.15	12.44	142.80	6.30	167.11	710.35
1.4	260.062456	35.612745	2.324	2.333	3.881	5.8	32.9	37.5	7.65	0.01	17.07	142.80	6.30	173.83	710.35
2.1	260.061096	35.611111	3.477	3.296	3.881	4.7	34.2	30.0	112.11	1.58	11.13	157.17	0.99	282.99	825.07
2.2	260.073317	35.612099	3.253	3.296	3.881	7.5	21.4	30.0	2.26	0.12	28.77	157.17	0.99	189.32	825.07
2.3	260.076529	35.609749	3.338	3.296	3.881	5.5	25.8	30.0	3.83	0.12	15.60	157.17	0.99	177.71	825.07
2.4	260.069728	35.603732	2.996	3.296	3.881	3.2	12.9	30.0	2.50	9.15	5.25	157.17	0.99	175.06	825.07
3.1	260.076074	35.602565	1.273	1.579	3.881	10.1	28.3	21.9	1.25	173.49	52.41	127.29	0.38	354.82	845.09
3.2	260.067137	35.604648	1.600	1.579	3.881	6.6	13.5	21.9	1.83	0.06	22.29	127.29	0.38	151.85	845.09
3.3	260.065805	35.605677	1.600	1.579	3.881	7.2	15.5	21.9	7.76	0.06	26.77	127.29	0.38	162.25	845.09
3.4	260.067583	35.609483	1.557	1.579	3.881	4.1	11.2	21.9	40.00	0.05	8.46	127.29	0.38	176.18	845.09
4.1	260.079174	35.606614	2.565	2.735	3.881	11.6	33.9	26.0	14.33	1.47	68.15	14.72	0.04	98.71	236.11
4.2	260.069728	35.603732	2.996	2.735	3.881	3.2	12.9	26.0	8.89	7.78	5.22	14.72	0.04	36.66	236.11
4.3	260.066423	35.604602	2.749	2.735	3.881	7.6	15.6	26.0	5.96	0.02	29.72	14.72	0.04	50.46	236.11
4.4	260.059562	35.611026	2.720	2.735	3.881	8.1	39.2	26.0	2.37	0.02	33.14	14.72	0.04	50.29	236.11

[a] Coordinates of each multiple image in (J2000).
[b] Redshift used to normalize the SL model, or the redshift bin in the automated process.

parity or negative parity. But, as we are driving a blind study, we can not check the image parity by visual inspection or by checking their signs in the magnification matrix due to the limited accuracy of the preliminary mass model. The simplest way to check the image parity, is to compare the radial distances of the multiple images, especially those that subtend the smallest angle with respect to the mass center. Indeed, often in the literature mirror arcs shown practically the same radial distances to the center of the lens potential. Considering this, we defined the χ^2 of the image parity as:

$$\chi^2_{parity} = ((r^A_{ima} - r^B_{ima})^2) \ / \ (f_{as} \times \sigma_r)^2, \tag{7.10}$$

where r^A_{ima} and r^B_{ima} are the radial distances from the cluster center to images A and B, respectively. Image A and image B are those that subtend the smallest angle with respect to the mass center of the image combination in question. The component σ_r is the expected image-plane reproduction uncertainty described above, fixed to $\sigma_r = 1.4''$. The factor f_{as} depends on the angular separation of the images A and B, starting from $f_{as} = 0.1$, for the smallest angular separations, and ending with $f_{ag} = 1.0$, for the largest angular separations. The smaller the angular separation is, larger the weight for the parity will be. Thus, all systems where their closest images present significant differences in their radial distances will be deleted (or weighted with a huge χ^2_{parity}).

After each successful image combination has been weighted with its respective χ^2_{comb}, the program selects the best of these configurations for the semifinal system in question. In other words, the combination with the lowest χ^2_{comb} becomes in the final multiple-image system for this semifinal system. The algorithm then runs over all semifinal

TABLE 7.3: MIFAL results for M1931

Id	R.A.[a] (°)	Dec[a] (°)	z_{ima}	z_{sys}	[b]z_{norm}	R_{find} ($''$)	E_{r_ima} ($''$)	E_{r_sys} ($''$)	χ^2_{col}	χ^2_z	$\chi^2_{R_{find}}$	χ^2_{parity}	$\chi^2_{E_r}$	χ^2_{ima}	χ^2_{sys}
1.1	292.943245	-26.577280	5.028	5.388	4.742	3.3	49.2	45.1	28.93	63.68	5.61	76.73	16.17	191.11	608.41
1.2	292.949521	-26.566378	5.458	5.388	4.742	8.0	43.0	45.1	0.87	0.96	32.78	76.73	16.17	127.51	608.41
1.3	292.961578	-26.565480	5.388	5.388	4.742	4.4	41.0	45.1	186.83	0.23	9.85	76.73	16.17	289.79	608.41
2.1	292.946140	-26.580900	5.230	5.230	4.742	9.1	42.6	41.8	0.27	0.16	42.32	8.93	11.29	62.97	263.30
2.2	292.946274	-26.569463	5.186	5.230	4.742	8.2	44.4	41.8	4.91	1.21	34.39	8.93	11.29	60.73	263.30
2.3	292.961578	-26.565480	5.388	5.230	4.742	8.0	41.0	41.8	53.00	33.47	32.92	8.93	11.29	139.60	263.30
3.1	292.944589	-26.578876	6.289	6.192	4.742	4.0	45.4	39.1	15.31	9.70	8.19	138.77	7.91	179.88	587.48
3.2	292.946914	-26.566489	6.192	6.192	4.742	11.6	49.1	39.1	3.73	0.03	68.53	138.77	7.91	218.98	587.48
3.3	292.959282	-26.567086	6.135	6.192	4.742	5.4	32.7	39.1	24.80	2.37	14.77	138.77	7.91	188.62	587.48
4.1	292.971083	-26.570402	5.431	5.390	4.742	8.8	54.9	48.7	30.48	1.14	39.20	50.53	22.56	143.90	431.06
4.2	292.963866	-26.588617	5.390	5.390	4.742	6.1	52.5	48.7	16.77	0.18	19.05	50.53	22.56	109.07	431.06
4.3	292.946140	-26.580900	5.230	5.390	4.742	11.1	42.6	48.7	3.80	38.76	62.44	50.53	22.56	178.09	431.06
5.1	292.966507	-26.568729	5.482	5.482	4.742	8.4	43.2	47.4	31.77	0.12	35.73	22.35	20.09	110.07	302.66
5.2	292.968258	-26.583570	5.590	5.482	4.742	8.1	49.7	47.4	4.74	1.40	33.58	22.35	20.09	82.16	302.66
5.3	292.958990	-26.590005	5.162	5.482	4.742	9.2	51.6	47.4	0.64	23.98	43.36	22.35	20.09	110.43	302.66
6.1	292.968723	-26.587459	5.416	5.130	4.742	8.9	59.9	54.5	9.32	21.83	40.64	35.50	34.84	142.13	369.46
6.2	292.955802	-26.591654	5.130	5.130	4.742	7.4	57.0	54.5	11.22	0.11	28.05	35.50	34.84	109.73	369.46
6.3	292.943245	-26.577280	5.028	5.130	4.742	9.1	49.2	54.5	3.23	1.47	42.55	35.50	34.84	117.59	369.46
7.1	292.968258	-26.583570	5.590	5.390	4.742	6.1	49.7	50.6	3.38	3.79	18.76	264.61	26.27	316.81	1031.90
7.2	292.963866	-26.588617	5.390	5.390	4.742	7.4	52.5	50.6	40.16	0.00	28.20	264.61	26.27	359.24	1031.90
7.3	292.958990	-26.590005	5.162	5.390	4.742	10.6	51.6	50.6	1.75	5.38	57.84	264.61	26.27	355.85	1031.90
8.1	292.968723	-26.587459	5.416	5.220	4.742	8.9	59.9	58.5	10.45	14.34	40.64	98.54	44.76	208.73	594.51
8.2	292.962432	-26.591011	5.220	5.220	4.742	7.1	58.2	58.5	3.56	0.07	26.01	98.54	44.76	172.93	594.51
8.3	292.955802	-26.591654	5.130	5.220	4.742	7.1	57.0	58.5	42.07	1.84	25.63	98.54	44.76	212.85	594.51
9.1	292.949594	-26.570605	1.817	1.817	4.742	7.2	32.1	29.9	0.67	0.00	26.22	52.98	0.95	80.83	274.24
9.2	292.957989	-26.568611	1.829	1.817	4.742	5.8	26.4	29.9	42.75	5.78	16.95	52.98	0.95	119.41	274.24
9.3	292.960596	-26.569164	1.807	1.817	4.742	4.8	27.6	29.9	4.60	3.56	11.92	52.98	0.95	74.00	274.24
10.1	292.967009	-26.578874	2.995	3.109	4.742	7.9	38.2	37.7	11.24	3.55	31.53	4.81	6.45	57.57	219.29
10.2	292.953752	-26.586549	3.109	3.109	4.742	7.7	40.1	37.7	74.92	0.00	30.20	4.81	6.45	116.38	219.29
10.3	292.946810	-26.578311	3.246	3.109	4.742	7.1	37.1	37.7	2.85	5.79	25.43	4.81	6.45	45.33	219.29
11.1	292.969399	-26.579625	2.456	2.534	4.742	10.8	47.3	44.7	13.12	46.72	59.40	419.13	15.59	553.96	2501.88
11.2	292.958152	-26.589497	2.534	2.534	4.742	10.0	49.4	44.7	8.47	0.20	51.49	419.13	15.59	494.88	2501.88
11.3	292.950162	-26.585492	2.552	2.534	4.742	0.2	42.2	44.7	1017.22	1.07	0.02	419.13	15.59	1453.04	2501.88
12.1	292.967009	-26.578873	2.995	3.084	4.742	6.0	38.2	34.4	21.68	10.08	18.32	110.66	3.54	164.27	515.77
12.2	292.955218	-26.583679	3.084	3.084	4.742	11.3	28.8	34.4	0.08	0.04	65.64	110.66	3.54	179.95	515.77
12.3	292.952107	-26.582897	3.135	3.084	4.742	9.9	30.6	34.4	5.16	2.30	49.90	110.66	3.54	171.55	515.77
13.1	292.958152	-26.589497	2.534	2.401	4.742	4.2	49.4	48.8	148.01	2.23	9.02	287.27	22.66	469.19	1154.04
13.2	292.953015	-26.588310	2.401	2.401	4.742	3.8	46.9	48.8	0.81	0.04	7.26	287.27	22.66	318.04	1154.04
13.3	292.950583	-26.587687	2.162	2.401	4.742	8.7	48.2	48.8	7.97	10.55	38.36	287.27	22.66	366.81	1154.04

[a] Coordinates of each multiple image in (J2000).
[b] Redshift used to normalize the SL model, or the redshift bin in the automated process.

systems, performing all possible image combinations and selecting the final multiple-image systems. If there are not combinations that match these four lens configurations, the semifinal system is automatically deleted from the list. Once this ends, we obtain the five final multiple-image systems catalogs (one for each D_{ls}/D_s bin), defined as *the configuration catalogs*.

It should be noted, that we are not considering the central image to constrain the configurations described above due to the limited number of candidates with good photometry near the cluster center.

7.2 MIFAL results

To carry out this study we analyze three CLASH clusters: MACS J0329−0211, MACS J1720+3536, and MACS J1931−2635 (hereafter M0329, M1720, and M1931 respectively). The former one was recently analyzed by Zitrin et al. (2012a), finding six sets of

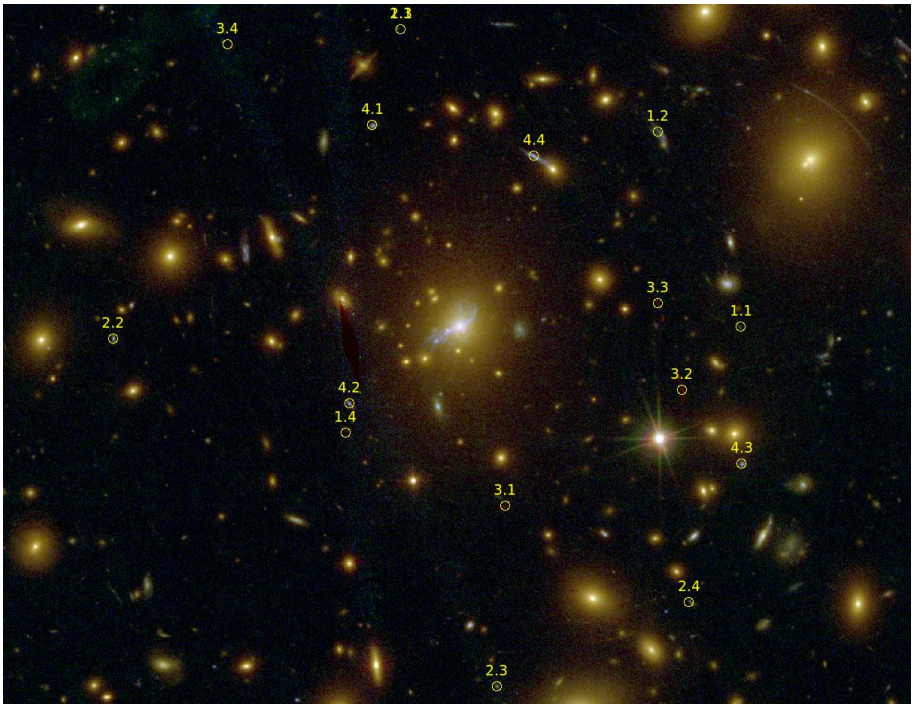

FIGURE 7.4: The figure shows the most likely multiple-image systems found by MIFAL for a normalization redshift of $z_{norm} = 1.476$ labeled by yellow circles. The systems 1, 3, and 4 correspond to three of four systems previously discovery by visual inspection.

multiply-lensed galaxies, but using four of them to constrain their model. The clusters M1720 and M1931 will be fully described in the forthcoming paper Zitrin et al. (2014, in preparation).

Before we run MIFAL we have to find the most likely multiple-image systems by the usual manner. After an exhaustive visual examination and using the preliminary model, we match the most *obvious* multiple-image systems. The preliminary mass models of these clusters are shown in terms of their magnification maps in the Fig. 7.3. Then, we incorporate these multiple images to improve the preliminary mass model and search again for new candidates as it has mentioned in previous work (e.g. Zitrin et al., 2009a). Finally, we include all the found systems to reach the best-fit solution via a long (several dozens of thousands steps) MCMC minimization.

Finally, we apply MIFAL to these three clusters with known multiple-image systems. The most likely multiple-image systems found by our innovative approach are reported in Tabs. 7.1, 7.2, and 7.3. It should be noted that the tables listed all the possible multiple-image systems that satisfy the configuration constraints imposed by MIFAL, but not all of them are considered as likely systems as is described below.

MACS J0329.6-0211: Fig. 7.4 shows the most likely multiple-image systems found by MIFAL for a normalization redshift of $z_{norm} = 1.476$. Zitrin et al. (2012a) reported

six set of likely lensed systems, although, they used only four systems to constrain their models. The systems 1, 3, and 4 (labeled in the figure) correspond to three of these four systems used as constraints. The automated procedure fully recovered systems 4 and 3, while the system 1 was partially identified (images 1.1 and 1.2 are real). Therefore, MIFAL was able to recover the $\sim 75\%$ of the multiple images detected by visual inspection in this cluster.

MACS J1720+3536: Fig. 7.5 shows the most likely multiple-image systems found by MIFAL for a normalization redshift of $z_{norm} = 3.881$. In this cluster, our algorithm recovered in total 3 very likely systems. Although, in this case only system 2 was fully recovered. In total MIFAL found 9 lensed galaxies that correspond to 3 background sources. The photometric redshift of each system, as well as the total χ^2 can be found in Tab. 7.2. The conventional method has found 7 candidate systems in this cluster. Therefore, in this case our algorithm was able to recover $\sim 40\%$ of the "real" multiple images or those ones found by visual inspection.

MACS J1931-2635: In this cluster MIFAL found many candidates of multiple-image systems (see Fig. 7.6). But only 1 system was completely identified, labeled as system 9 in the figure. From the Tab. 7.3 we can see that the system 9 has the second lower

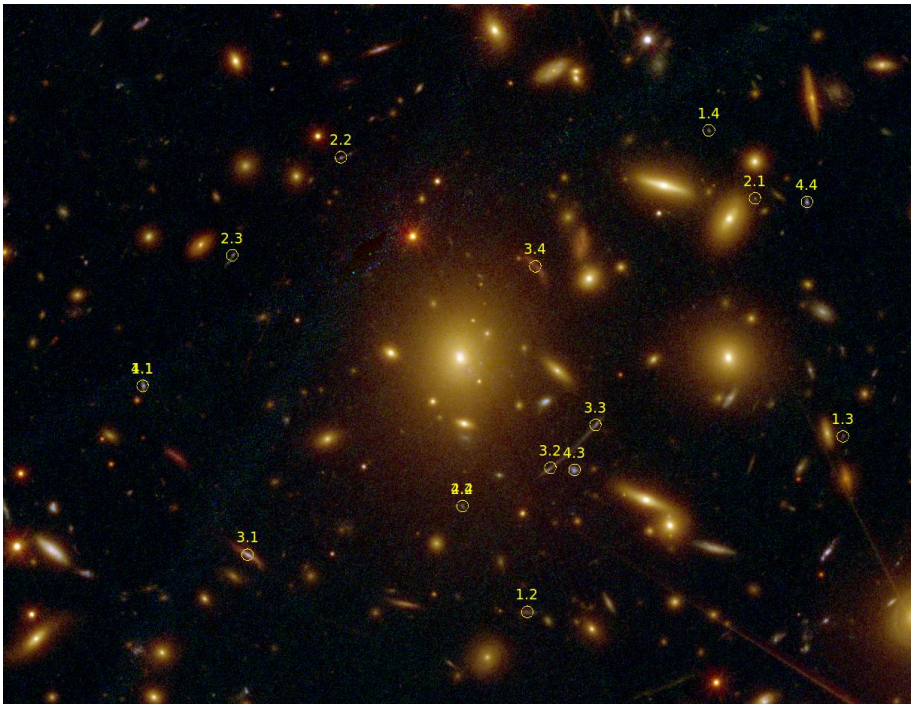

FIGURE 7.5: The figure shows the most likely multiple-image systems found by MIFAL for a normalization redshift of $z_{norm} = 3.881$. In this cluster, our algorithm recovered in total 3 very likely systems. The conventional method has found 7 candidate systems in this cluster.

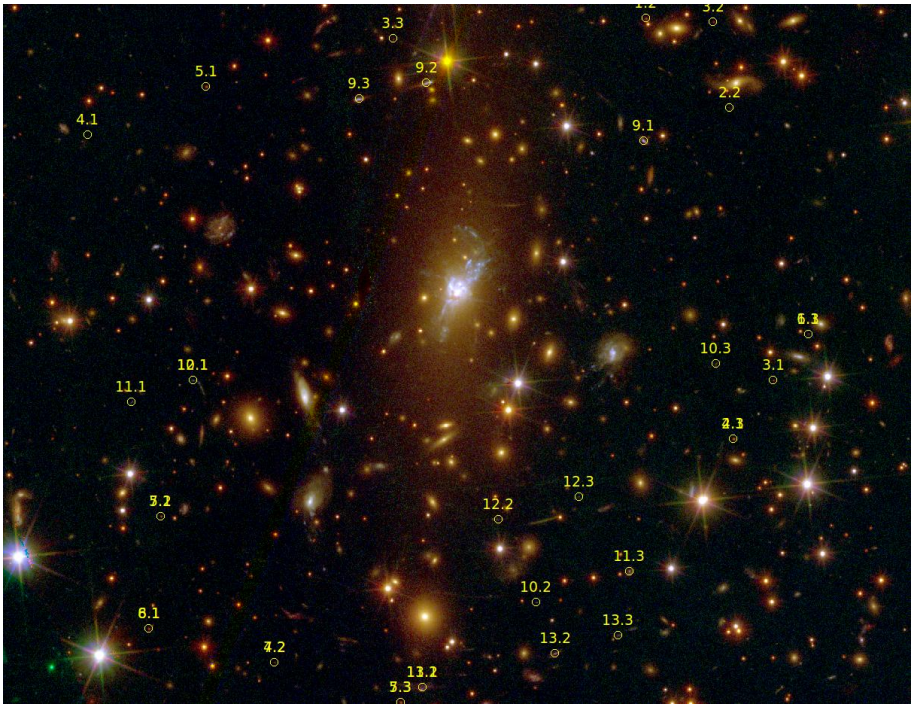

FIGURE 7.6: The figure shows the most likely multiple-image systems found by MIFAL for a normalization redshift of $z_{norm} = 4.742$. Only 1 system was fully recovered, instead the conventional method that found 12 candidate systems.

χ^2_{sys}, suggesting that the way as MIFAL assigns the weights seems right. The system 12 and 13 were partially identified, although their χ^2_{sys} are quite high to be recognized as likely systems through the automated analysis, even though these systems could be real. In this cluster, the visual inspection yields 12 candidate systems. Then, MIFAL was not very successful in this cluster, but still MIFAL was able to recover one very likely system fully automatically and in just 40 minutes.

7.3 Summary and conclusions

In this work we presented an innovative **M**ultiple-**I**mage **F**inder **AL**gorithm (MIFAL) designed to automatically find multiple images in galaxy cluster lenses, so that their mass model could be efficiently and automatically constrained. We combined an *arcfinder* algorithm with CLASH photometric redshift measurements, along with a preliminary mass model, to physically match together multiple-image systems in an automated ("blind") manner. We obtained a robust assessment of the likelihood of each arc to belong to one of the multiple-image systems, as well as the preferred redshift for the different systems. MIFAL then selected the most likely multiple images for each system based

on the assigned weights, to finally construct five catalogs of multiple-image systems for each D_{ls}/D_s normalization.

We applied MIFAL to the recently studied galaxy cluster M0329, as well as to the unprecedented galaxy clusters M1720 and M1931 in deep CLASH/HST images. We compared the results of our automated procedure with the results by the conventional SL analysis where multiple images were verified by eye using the parametric method. Our automated SL analysis blindly recovered 3 out of the 4 systems in M0329, 3 out of the 7 systems in M1720, and 1 out of the 12 candidate systems in M1931.

It should be noted that most of the multiple images and/or systems that were not picked by the automated procedure was mainly due to the ambiguity of the photometric redshift measurements. Another concern that should be taken into account is that our automated procedure yields successful results only for high quality photometric data, i.e., HST data. It is due that the first steps in the selection process are mainly based on the photometric redshifts, and therefore, inaccurate measurements of the photometric redshifts will never allow right combinations of multiple-image systems.

We want to highlight that the the whole automated process takes not more than 1 or 2 hours in a normal CPU, while the conventional SL analysis usually takes days or weeks. Although more comparisons are required for a more robust assessment of the proposed algorithm accuracy, it constitutes another step towards the fully automating SL analysis as a standard tool for studying cluster mass distributions of very large samples, especially with the HST and successors.

Chapter 8

Conclusion and outlook

In this thesis we have studied the mass distribution of galaxy clusters in the context of gravitational lensing. In particular, we have extensively investigated the total mass distribution of clusters, by obtaining robust mass reconstructions of galaxy clusters through a detailed analysis of the SL signatures and dynamical mass information.

We have performed FORS2/VLT spectroscopic observations for a new sample of 29 SL selected galaxy clusters from the RCSGA survey, which were visually identified in the RCS2 survey. Our spectroscopic analysis reveals 51 lensed galaxies corresponding to 34 background sources at high redshift, which are clearly distorted by the gravitational potential of the cluster cores. Our exhaustive analysis has also spectroscopically confirmed 689 cluster members, which were used to measure velocity dispersions, cluster redshift and dynamical masses, covering three orders of magnitude in mass, from $2.80 \times 10^{13} \leq M_{200}/h^{-1}M_{\odot} \leq 2.84 \times 10^{15}$, with a median mass of $M_{200} \sim 3.6 \times 10^{14}h^{-1}M_{\odot}$. The redshift range of these clusters is $0.22 < z < 1.01$, with a redshift median of $z \sim 0.5$.

In order to derive reliable cluster mass distributions we have introduced an innovative mass reconstruction methodology, which consists in the combination of SL constraints from the cluster cores (probing the innermost region of the galaxy clusters) with dynamical masses derived from the velocity dispersion of the cluster members (probing the mass distribution of clusters at larger radii). From the best-fitting mass models we have derived the concentration parameter of the clusters, which is one of the most important properties of the cluster-size halos. The concentration parameter allows us to test the current cosmological ΛCDM framework through its relation with the total mass of the cluster halo.

In this thesis we have provided one of the most complete analysis of the $c-M$ relation by combining results from 27 clusters of our RCSGA sample with the recent analysis of 19

X-ray selected clusters from the CLASH survey, and also with concentration parameter measurements from 27 SL selected clusters from the SGAS survey. This provides the more robust and largest dataset of concentration measurements so far for a controlled population of 73 galaxy clusters. We found that for massive clusters ($M_{200} \sim 8 \times 10^{14} h^{-1} M_{\odot}$), the concentration parameters are distributed around $c_{200} = 4.3 \pm 1.4$, which is in reasonable agreement with theoretical expectations. In contrast, for less massive clusters ($M_{200} \sim 10^{14} h^{-1} M_{\odot}$), the central value of the concentrations is almost twice the mean expected value, even if the selection bias and projection effects are taken into account. This results in a $c - M$ relation with a strong dependence on the cluster mass, given by $c \propto M^{\alpha}$, where $\alpha = -0.52 \pm 0.09$. We found that this steep mass slope is mainly due to ~ 6 RCSGA clusters and ~ 16 clusters from the SGAS survey, which are clearly describing a higher and steeper $c - M$ relation, with a normalization of $c_n = 8.9 \pm 1.12$ and $\alpha = -0.69 \pm 0.09$. This unusual relation is far from any theoretical expectation. The rest of the sample is characterized by a mass slope of $\alpha = -0.24 \pm 0.11$, reconciling simulation results with observations. Since this bimodal behavior has been found in two independent samples with different modeling techniques, we can conclude that there is a subset of SL clusters that are more concentrated than the rest of the SL population. Although, there is no evidence or a clear correlation between these clusters and other parameters or observables that make them special. Therefore, a deeper analysis is required to classify these clusters as a special SL population. This can be done by using deeper and high-quality imaging data, as well as more spectroscopic information of the multiple images used as constraints. However, the most likely explanation for this excess of concentration for less massive clusters can be associated to the baryon cooling effect.

In this thesis we have also detected a clear positive correlation between the cluster redshift and its concentration, which is more obvious for high mass clusters. However, when the redshift dependence on the $c - M$ relation was analyzed, no evidence of a possible redshift evolution was found.

In order to check whether the lens modeling methodologies bias or not the understanding of the cluster mass distributions, we have performed detailed SL mass reconstructions for a subset of 7 X-ray selected galaxy clusters from the CLASH survey. From the best-fitting mass models we derived the concentration parameters, and compared them with those derived in other works, in which different modeling methodologies were used. The results show a reasonable agreement, indicating that the lens modeling methodologies used to analyze the CLASH clusters are consistent with each others and therefore, we derived reliable properties from their mass distributions. We have also performed SL mass reconstructions for simulated clusters with properties similar to the CLASH clusters, in

order to check the robustness of our results. We have found that our mass reconstructions are in excellent agreement with the "true" mass distributions. Even more, our SL mass models provided the most accurate mass reconstructions in our team.

In this thesis we have developed a new innovative algorithm (MIFAL) designed to automatically find multiple images in galaxy cluster lenses, so that their mass model could be efficiently and automatically constrained. We have combined an arcfinder algorithm with high-quality photometric redshift measurements, along with a simple preliminary mass model, to physically match together multiple-image systems in an automated procedure. We have applied MIFAL to three CLASH clusters with successful results. MIFAL was able to automatically recover 1 – 3 systems (completely or partially), becoming the first algorithm able to automatically find multiple-image systems in galaxy clusters. Although more comparisons are required for a more robust assessment of the accuracy of this algorithm, it constitutes another step towards the fully automatizing SL analysis as a standard tool for studying cluster mass distributions of very large samples, especially with the HST and successors.

The mass modeling methodology presented in this thesis can be also applied to other cluster samples that present SL signatures. In fact, the closest project will be to perform mass reconstructions of all CLASH clusters using this technique. The next step in our modeling methodology will be to include weak lensing analysis and the BCG velocity dispersion information, in order to fully constrain the density profile of galaxy clusters to test the universal form of the cluster mass distributions. Then, we want to perform a detailed study of the orientation and triaxiality of the cluster-size halos, and therefore, we want to include X-ray information in our SL analysis.

In order to fully automate the SL analysis of galaxy clusters we will improve our algorithm by adding another step in the procedure. We will refine the preliminary mass model by using the most likely multiple-image systems found in the first steps. This refined mass model will be then used to find again multiple-image systems, in an iterate mode. Finally, the best systems in the last iteration will be used as input into the regular minimization procedure. In this manner, we could derive fully automatically robust mass reconstructions of galaxy clusters in only a couple of hours, getting ready for the next generation of large samples of clusters.

Appendix A

Galaxy cluster surveys

As explained earlier, galaxy clusters are ideal tracers of the largest density fluctuations in the universe and their abundances can be used to constrain cosmological parameters (e.g. Eke et al., 1996). The building of large and well-defined samples of galaxy clusters become extremely necessary. The first systematic searches of clusters consisted in the visual identification of overdensities of optical galaxies on photographic plates (Abell, 1958; Abell et al., 1989). In the 1970s, with the advent of X-ray telescopes above Earth's atmosphere, selection of clusters from their extended X-ray emission was possible (Mitchell et al., 1976; Serlemitsos et al., 1977). Recently, a combination of large format CCD detectors and objective algorithms to search efficiently for signatures of galaxy clusters has led to a revival in the use of optical selection in cluster surveys (Gladders and Yee, 2000; Kepner et al., 1999; Postman et al., 1996). A variety of techniques have been suggested to exploit the expected luminosity and/or color distribution of galaxies in clusters. In this appendix we will briefly describe two of them, which are the cornerstones of this thesis. The information provided in this appendix is mainly based in Gilbank et al. (2011) and Postman et al. (2012).

A.1 The Red-sequence Cluster Survey-2 (RCS2)

The second Red-sequence Cluster Survey (RCS2) is a ~ 1000 deg^2 , multi-color imaging survey using the square-degree image, MegaCam, on the Canada-France-Hawaii Telescope.

It was designed to detect clusters of galaxies over a large redshift range, from $0.1 \lesssim z \lesssim 1$. The primary aim was to build a statistically complete, large (~ 10000) sample of clusters, covering a sufficiently long redshift baseline to be able to put constraints on cosmological parameters via the evolution of the cluster mass function.

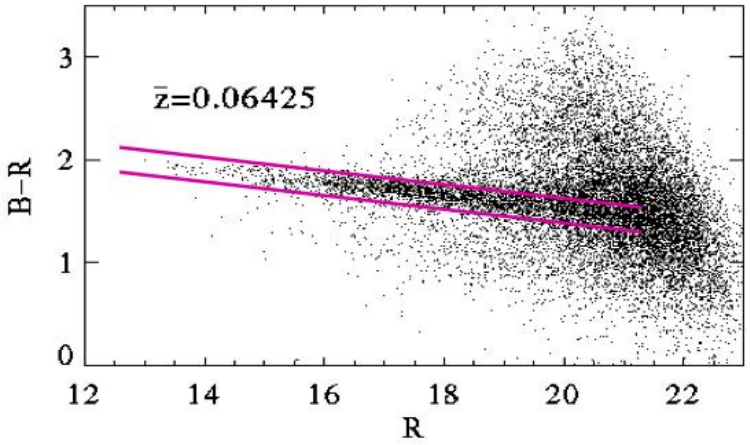

FIGURE A.1: This figure shows an example of the red-sequence from a composite of low-redshift clusters. The color of the red-sequence depends on the cluster redshift. This means that the color can be used to estimate the redshift of the cluster. This figure was taken from Gladders and Yee (2000)

The second main science goals include building a large sample of high surface brightness, strongly gravitationally lensed arcs associated with these cluster lenses, and construct an unprecedented sample of several tens of thousands of galaxy clusters and groups, spanning a large range of halo masses, in order to study the properties and evolution of their member galaxies.

The survey uses the well defined red-sequence of early-type galaxies to identify clusters with a well-understood selection function (Gladders and Yee, 2000). This technique was used with great success in the 90 square degree R and z survey, RCS1 (Gladders and Yee, 2005). The red-sequence method involves the construction of many color slices from the survey data and searching for overdensities of galaxies in these slices. Once significant overdensities are found, the slice containing the peak signal for the overdensity gives the cluster candidate's most probable redshift. Fig. A.1 shows an example of the red-sequence from a composite of low-redshift clusters. The color of the red-sequence depends on the cluster redshift. This means that the color can be used to estimate the redshift of the cluster. The typical accuracy obtained in the Red-sequence Cluster Surveys using $R-z$ color is ~ 0.05.

RCS2 reaches average 5σ point-source limiting magnitudes of $griz = [24.4, 24.3, 23.7, 22.8]$, approximately $1-2$ mag deeper than the SDSS. Due to the queue-scheduled nature of the observations, the data are highly uniform and taken in excellent seeing, mostly FWHM $\lesssim 0.7''$ in the r band, making it ideal for the detection and classification of giant arcs.

In this thesis we have worked with a new sample of 29 strong lensing galaxy clusters, which have been selected through an exhaustive visual inspection of the RCS2 imaging

data as those having prominent blue arcs around their cores. This search has resulted in hundreds of strong lensing clusters, which have giving rise to a new survey; the Red-Sequence Cluster Survey Giant Arc (RCSGA; Bayliss, 2012). From this new survey, we have selected this subset of 29 clusters to perform a spectroscopic follow-up, in order to confirm giant arcs and lensed galaxies, as well as to match up multiple-image systems. A detailed description of this new sample of 29 SL selected galaxy clusters is presented in chapters 4 and 5.

A.2 The Cluster Lensing and Supernova Survey with Hubble (CLASH)

The Cluster Lensing and Supernova Survey with Hubble (CLASH; Postman et al., 2012) is a multi-cycle treasury program, using 524 Hubble Space Telescope (HST) orbits to target 25 galaxy clusters ($0.18 < z < 0.89$), each in 16 filters with the Wide Field Camera 3 (WFC3; Kimble et al., 2008) and the Advanced Camera for Surveys (ACS; Ford et al., 2003) over the course of three years (HST cycles 18-20). They are largely drawn from Abell and MACS cluster catalogs (Abell, 1958; Abell et al., 1989; Ebeling et al., 2007, 2001). 20 clusters were specifically selected by their unperturbed X-ray morphology with the goal of representing a sample of clusters with regular, unbiased density profiles that allow for an optimal comparison with models of cosmological structure formation. As reported in Postman et al. (2012) all the clusters in the sample are fairly X-ray luminous with X-ray temperatures $T_x \geq 5$ keV and show a smooth morphology in their X-ray surface brightness. For all the systems the separation between the brightest cluster galaxy (BCG) and the X-ray luminosity centroid is < 20 kpc.

In this thesis we study some of these clusters, specifically we construct strong lensing models of seven of these CLASH clusters to analyze the concentration-mass relation of the massive dark matter halos.

Appendix B

RCSGA: spectroscopically confirmed lensed galaxies

Our FORS2/VLT spectroscopy analysis has discovered/revealed 51 lensed galaxies, corresponding to 34 background sources at high redshift that are clearly distorted by the gravitational potential of the cluster cores.

In this appendix we present the spectra for those 34 background sources in the Figs. B.1, B.2, B.3, and B.4.

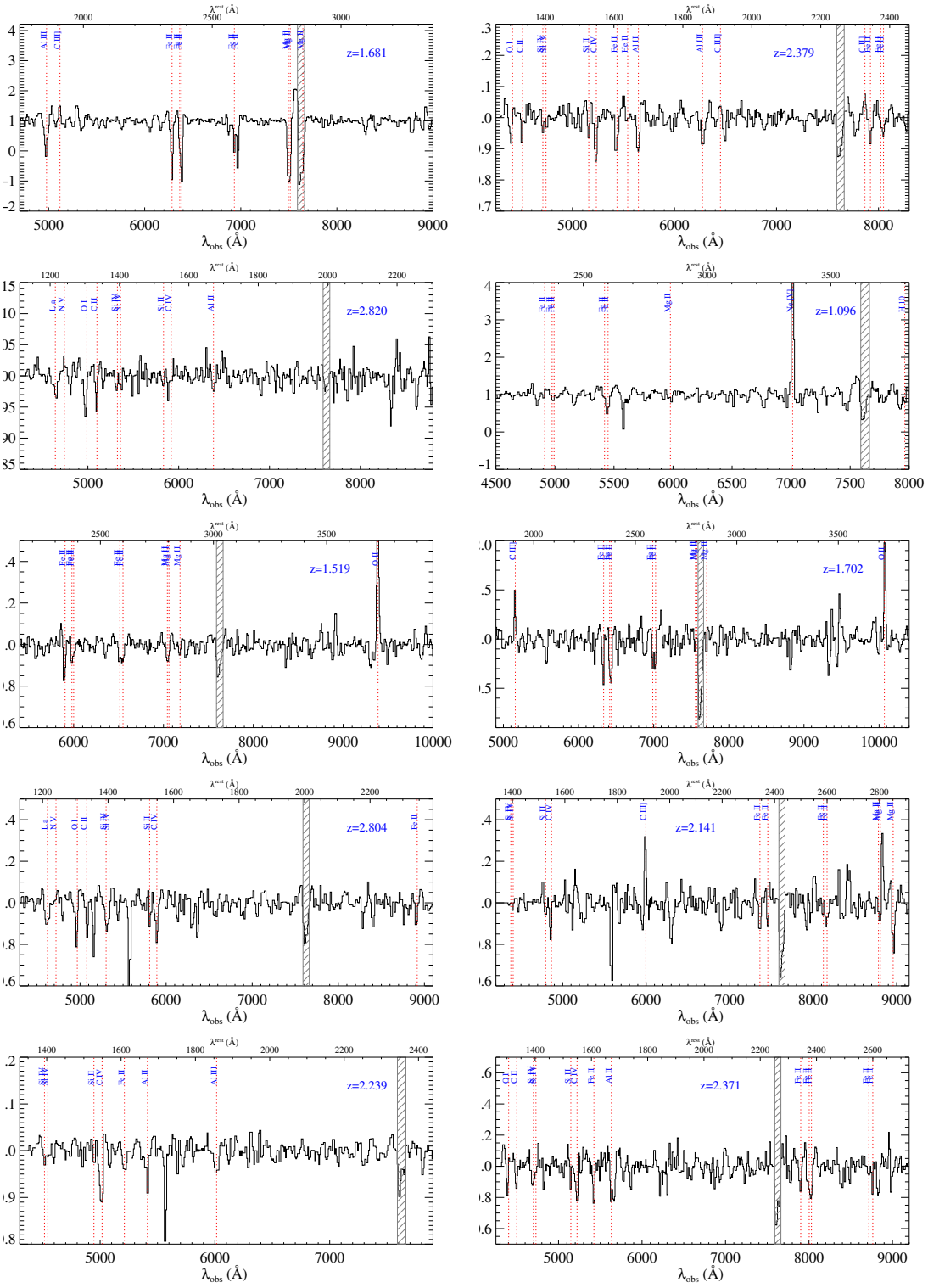

FIGURE B.1: FORS2/VLT spectra for ten lensed galaxies with high confidence redshifts, labeled as class 3. The spectra are displayed in the observer/rest-frame in the bottom/top axis, and smoothed to match the spectral resolution of the data. The locations of spectral lines are identified by red dashed lines and labeled with their corresponding ion. The telluric A Band absorption feature is indicated by a vertical shaded region. From top to bottom − left to right the spectra in each panel correspond to the following source/multiple-image objects in Tab. 4.2: 1) RCS2 J0004−0103, S1.1; 2) RCS2 J0034+0225, S1.1; 3) RCS2 J0038+0215, S1.1; 4) RCS2 J0252−1459, S1.2; 5) RCS2 J0309−1437, S1.1; 6) RCS2 J0327−1326, S1.2; 7) RCS2 J1055−0459, S1.1; 8) RCS2 J1111+1408, S1.1; 9) RCS2 J1517+1003, S1.1; 10)RCS2 J1519+0840, S1.1.

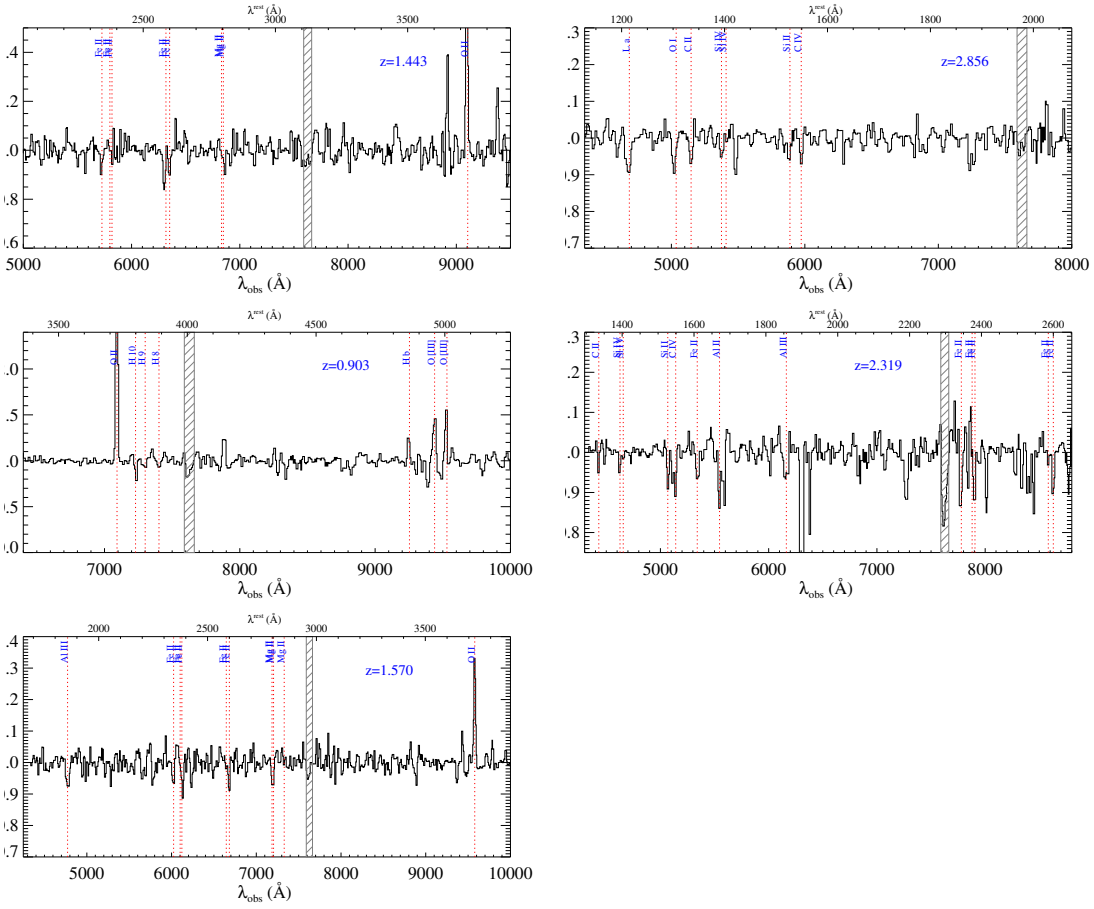

FIGURE B.2: FORS2/VLT spectra for five lensed galaxies with high confidence redshifts, labeled as class 3. The spectra are displayed in the same manner as in the previous figure. From top to bottom − left to right the spectra in each panel correspond to the following source/multiple-image objects in Tab. 4.2: 11) RCS2 J1526+0432, S1.1; 12) RCS2 J2111−0114, S1.2; 13) RCS2 J2135−0102, S1.1; 14) RCS2 J2135−0102, S2.1; 15) RCS2 J2329−0102, S2.1.

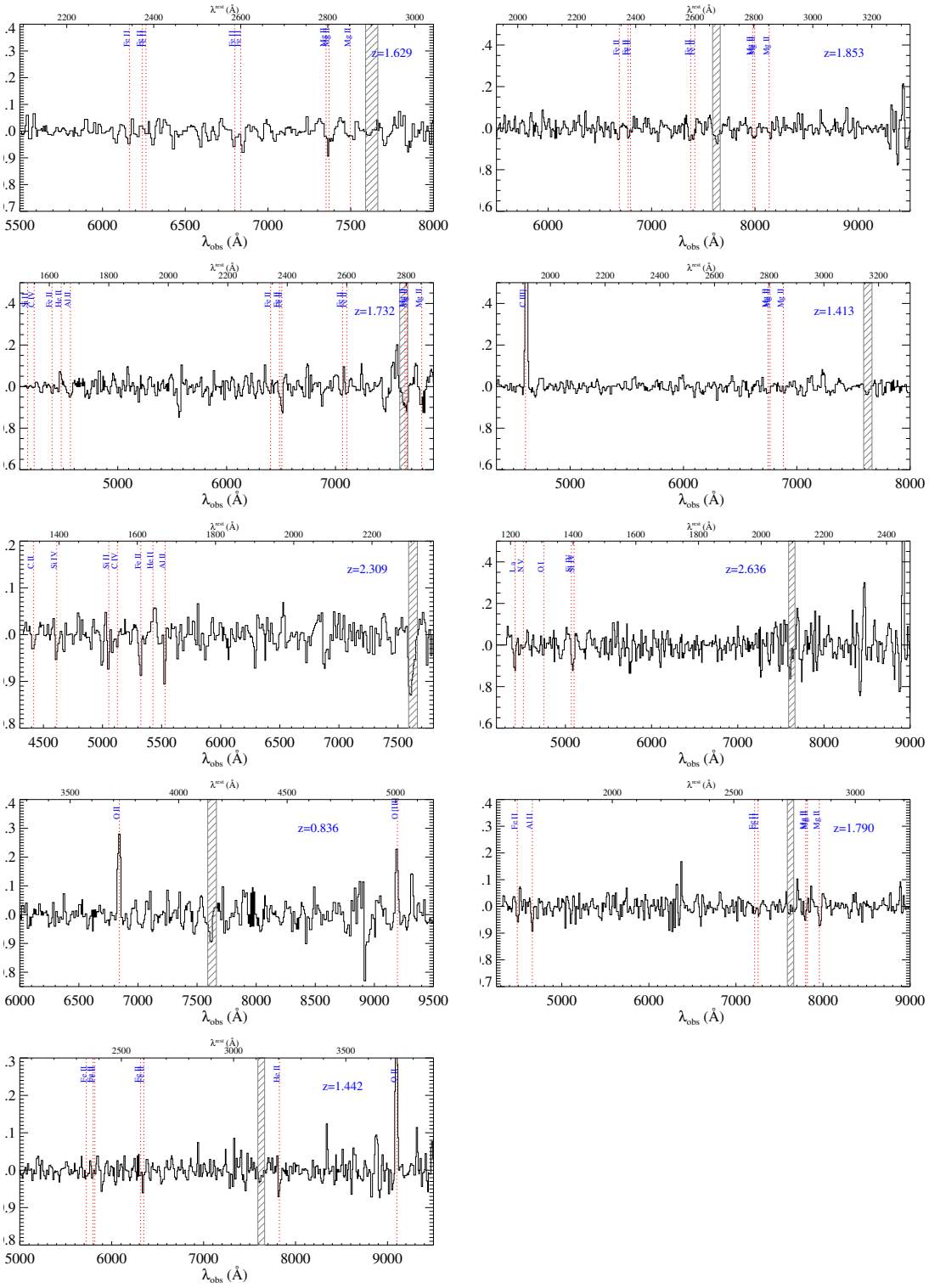

FIGURE B.3: FORS2/VLT spectra for nine lensed galaxies with medium confidence redshifts, labeled as class 2. The spectra are displayed in the same manner as in the previous figure. From top to bottom − left to right the spectra in each panel correspond to the following source/multiple-image objects in Tab. 4.2: 1) RCS2 J0047+0507, S1.3; 2) RCS2 J0052+0433, S1.2; 3) RCS2 J0052+0433, S2.1; 4) RCS2 J0309−1437, S1.1; 5) RCS2 J1250+0244, S1.2; 6) RCS2 J1526+0432, S2.1; 7) RCS2 J2151−0138, S1.1; 8) RCS2 J2329−0102, S1.1; 9) RCS2 J2329−1317, S1.2.

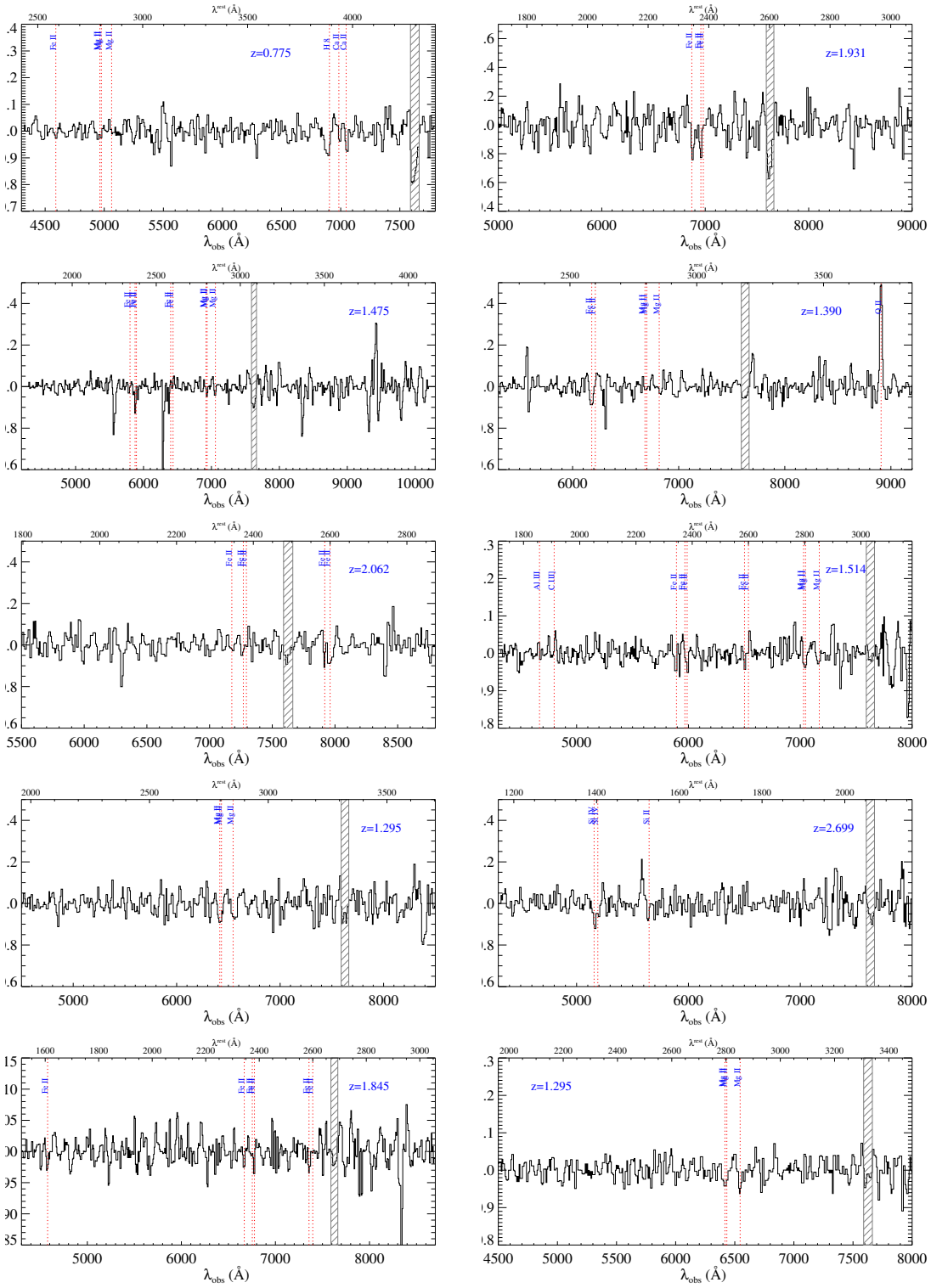

FIGURE B.4: FORS2/VLT spectra for ten lensed galaxies with low confidence redshifts, labeled as class 1. The spectra are displayed in the same manner as in the previous figure. From top to bottom − left to right the spectra in each panel correspond to the following source/multiple-image objects in Tab. 4.2: 1) RCS2 J0057+0209, S1.1; 2) RCS2 J1101−0602, S1.1; 3) RCS2 J1108−0456, S1.1; 4) RCS2 J1108−0456, S4.1; 5) RCS2 J1119−0728, S1.1; 6) RCS2 J1125−0628, S1.1; 7) RCS2 J1511+0630, S1.2; 8) RCS2 J2147−0102, S1.2; 9) RCS2 J2313−0104, S1.2; 10)RCS2 J2336−0608, S1.1.

Appendix C

RCSGA: strong lensing and dynamical mass models

In this appendix we present the complete results of our innovative technique by combining strong lensing (SL) signatures and velocity dispersion information of the cluster members. We perform our models with the parametric software LENSTOOL (Jullo et al., 2007).

We report the best-fitting model parameters derived of the analysis where SL information of the giant arcs were used alone, as well as when they were combined with dynamical mass of the cluster members. These results are tabulated in the Tab. C.1 and C.2, respectively.

We also present the multiple-image systems used to constrain our models, as well as the derived critical curves from our best-fitting models computed at $z_s = z_{arc}$. In all figures, multiple images are labeled by yellow ID numbers and critical lines are displayed by red curves. It should be noted that the ID of the lensed galaxies reported in the Tab. 4.2 correspond to the same ID displayed in these figures.

TABLE C.1: The best-fitting model parameters for the SL only analysis

Name	$\chi^2/d.o.f.$	$x_{offset}{}^d$ ["]	$y_{offset}{}^d$ ["]	e_Σ	$\theta_e{}^e$ [deg]	r_s [kpc]	c_{200}	r_{cut} [kpc]	σ_{gal} [km s^{-1}]	$z_{arc,2}$	$r_{arc,3}$
RCS2 J0004−0103	1.17/3	–	–	$0.26^{+0.13}_{-0.06}$	312^{+2}_{-7}	156^{+37}_{-142}	$4.7^{+9.9}_{-1.9}$	–	–	–	–
RCS2 J0034+0225	1.36/1	–	–	$0.28^{+0.06}_{-0.17}$	38^{+0}_{-18}	116^{+27}_{-64}	$5.2^{+4.9}_{-2.1}$	88^{+107}_{-6}	162^{+3}_{-63}	–	–
RCS2 J0038+0215	1.35/1	$8.4^{+0.5}_{-3.3}$	$-1.4^{+2.2}_{-2.3}$	$0.06^{+0.13}_{-0.05}$	9^{+19}_{-7}	108^{+4}_{-77}	$4.5^{+6.5}_{-1.8}$	55^{+53}_{-43}	191^{+98}_{-45}	$2.2^{+3.1}_{-0.7}$	–
RCS2 J0047+0507	1.24/1	$0.4^{+2.3}_{-1.3}$	$-0.5^{+4.4}_{-0.3}$	$0.55^{+0.00}_{-0.19}$	80^{+9}_{-9}	71^{+56}_{-20}	$7.4^{+4.0}_{-3.0}$	33^{+101}_{-11}	150^{+67}_{-49}	–	–
RCS2 J0052+0433	2.57/2	$5.5^{+3.4}_{-2.2}$	$-3.3^{+4.7}_{-5.5}$	$0.49^{+0.15}_{-0.15}$	64^{+14}_{-10}	39^{+65}_{-8}	$17.7^{+7.1}_{-9.4}$	16^{+88}_{-5}	294^{+20}_{-139}	$1.2^{+1.0}_{-0.2}$	–
RCS2 J0057+0209	6.89/3	–	–	$0.24^{+0.00}_{-0.13}$	82^{+12}_{-9}	329^{+59}_{-222}	$4.3^{+4.1}_{-1.7}$	48^{+126}_{-15}	60^{+89}_{-8}	–	–
RCS2 J0252−1459	1.13/1	–	–	$0.44^{+0.10}_{-0.09}$	204^{+19}_{-9}	66^{+613}_{-0}	$7.6^{+7.1}_{-3.7}$	105^{+41}_{-43}	52^{+161}_{-0}	–	–
RCS2 J0309−1437	3.96/1	$-0.1^{+0.0}_{-3.5}$	$-0.2^{+0.1}_{-4.5}$	$0.20^{0+.09}_{-0.05}$	108^{00}_{-18}	122^{048}_{-71}	$4.8^{04.9}_{-1.9}$	49^{038}_{-26}	205^{023}_{-46}	$2.6^{+1.6}_{-0.1}$	$3.1^{+0.2}_{-1.4}$
RCS2 J0327−1326[a]	2.49/4	$-1.8^{+3.8}_{-5.9}$	$-0.1^{+2.8}_{-3.4}$	$0.38^{+0.29}_{-0.02}$	4^{+0}_{-9}	100^{+212}_{-1}	$8.1^{+3.2}_{-5.7}$	91^{+97}_{-67}	142^{+77}_{-3}	–	–
RCS2 J0859−0345	2.21/3	$-1.4^{+2.5}_{-0.1}$	$1.5^{+0.0}_{-1.2}$	$0.10^{+0.10}_{-0.06}$	-2^{+11}_{-1}	242^{+142}_{-89}	$3.7^{+1.5}_{-1.5}$	–	–	–	–
RCS2 J1055−0459	6.32/2	$-1.0^{+1.8}_{-0.0}$	$-0.9^{+1.8}_{-0.0}$	$0.75^{+0.00}_{-0.32}$	126^{+6}_{-11}	63^{+33}_{-13}	$6.3^{+2.5}_{-2.5}$	184^{+8}_{-142}	147^{+59}_{-65}	–	–
RCS2 J1101−0602	1.06/1	–	–	$0.07^{+0.22}_{-0.05}$	27^{+10}_{-17}	36^{+127}_{-5}	$10.9^{+4.4}_{-7.4}$	118^{+2}_{-111}	31^{+134}_{-6}	–	–
RCS2 J1108−0456	5.45/1	$4.6^{+0.3}_{-6.4}$	$2.4^{+1.5}_{-3.6}$	$0.46^{+0.28}_{-0.05}$	21^{+7}_{-8}	328^{+21}_{-126}	$3.2^{+1.3}_{-1.3}$	15^{+128}_{-4}	101^{+26}_{-59}	–	–
RCS2 J1111+1408	1.06/3	–	–	$0.46^{+0.13}_{-0.24}$	56^{+5}_{-8}	170^{+264}_{-17}	$5.8^{+2.3}_{-2.6}$	–	–	–	–
RCS2 J1119−0728	1.02/1	–	–	$0.21^{+0.18}_{-0.16}$	143^{+10}_{-7}	71^{+85}_{-52}	$4.7^{+12.0}_{-1.9}$	189^{+6}_{-135}	271^{+32}_{-215}	–	–
RCS2 J1125−0628	1.01/2	–	–	$0.54^{+0.11}_{-0.22}$	88^{+8}_{-7}	36^{+110}_{-4}	$14.8^{+5.9}_{-9.6}$	173^{+0}_{-161}	33^{+102}_{-1}	–	–
RCS2 J1250+0244	1.03/1	–	–	$0.53^{+0.16}_{-0.22}$	136^{+8}_{-5}	85^{+206}_{-62}	$5.8^{+13.7}_{-2.3}$	4^{+91}_{-1}	125^{+68}_{-101}	–	–
RCS2 J1511+0630	1.01/1	–	–	$0.51^{+0.03}_{-0.16}$	-9^{+8}_{-10}	119^{+9}_{-98}	$5.1^{+12.3}_{-2.0}$	181^{+13}_{-127}	83^{+81}_{-69}	–	–
RCS2 J1517+1003	1.03/1	$-3.9^{+8.4}_{-0.9}$	$-5.0^{+4.6}_{-1.6}$	$0.40^{+0.19}_{-0.16}$	30^{+6}_{-3}	40^{+148}_{-1}	$18.9^{+7.6}_{-3.8}$	93^{+49}_{-88}	67^{+113}_{-21}	–	–
RCS2 J1519+0840	1.22/1	$-18.0^{+4.4}_{-0.9}$	$-2.3^{+2.2}_{-2.6}$	$0.24^{+0.06}_{-0.22}$	-2^{+15}_{-2}	289^{+140}_{-137}	$3.9^{+1.6}_{-1.6}$	95^{+77}_{-43}	83^{+127}_{-2}	$1.5^{+0.3}_{-0.3}$	$1.2^{+0.1}_{-0.3}$
RCS2 J1526+0432	2.52/2	$-0.5^{+2.1}_{-2.4}$	$2.5^{+1.8}_{-3.0}$	$0.50^{+0.14}_{-0.28}$	119^{+5}_{-4}	182^{+51}_{-51}	$4.3^{+2.3}_{-1.7}$	127^{+64}_{-65}	201^{+36}_{-88}	$1.1^{+1.8}_{-0.1}$	–
SDSS J2111−0114[b]	2.66/1	$-3.6^{+3.6}_{-0.3}$	$6.5^{+2.1}_{-10.1}$	$0.10^{+0.24}_{-0.02}$	103^{+3}_{-5}	217^{+192}_{-31}	$4.7^{+1.9}_{-2.1}$	84^{+62}_{-31}	57^{+39}_{-45}	–	–
RCS2 J2135−0102	3.03/1	$-5.7^{+7.8}_{-0.2}$	$6.7^{+1.0}_{-13.0}$	$0.20^{+0.10}_{-0.06}$	114^{+1}_{-11}	176^{+192}_{-24}	$7.9^{+3.2}_{-4.0}$	20^{+77}_{-15}	76^{+110}_{-32}	$0.7^{+2.9}_{-0.1}$	–
RCS2 J2147−0102	1.02/1	–	–	$0.60^{+0.04}_{-0.34}$	76^{+12}_{-10}	13^{+355}_{-1}	$20.5^{+8.2}_{-0.3}$	82^{+187}_{-58}	163^{+168}_{-118}	–	–
RCS2 J2151−0138	1.03/1	$0.6^{+1.4}_{-0.6}$	$-5.9^{+3.0}_{-2.0}$	$0.05^{+0.09}_{-0.02}$	79^{+14}_{-3}	325^{+6}_{-232}	$4.6^{+6.0}_{-1.8}$	140^{+55}_{-39}	120^{+45}_{-14}	–	–
RCS2 J2313−0104	1.25/1	–	–	$0.29^{+0.10}_{-0.25}$	95^{+3}_{-19}	122^{+57}_{-81}	$4.9^{+6.2}_{-2.0}$	35^{+91}_{-3}	125^{+44}_{-82}	–	–
RCS2 J2329−1317	2.29/1	$-0.9^{+2.7}_{-1.5}$	$4.7^{+0.1}_{-4.6}$	$0.55^{+0.04}_{-0.22}$	72^{+15}_{-2}	252^{+89}_{-178}	$3.3^{+4.3}_{-1.3}$	59^{+37}_{-38}	182^{+28}_{-60}	$3.2^{+2.7}_{-0.5}$	–
RCS2 J2329−0120	4.07/2	–	–	$0.65^{+0.00}_{-0.16}$	58^{+5}_{-10}	54^{+23}_{-30}	$10.6^{+8.5}_{-4.2}$	155^{+0}_{-93}	111^{+55}_{-20}	–	–
RCS2 J2336−0608	3.41/1	$-12.0^{+1.4}_{-0.0}$	$11.5^{+0.4}_{-6.2}$	$0.19^{+0.21}_{-0.08}$	121^{+3}_{-8}	424^{+22}_{-317}	$3.0^{+5.0}_{-1.2}$	131^{+36}_{-66}	85^{+18}_{-20}	$1.4^{+0.1}_{-0.1}$	$2.9^{+0.1}_{-0.2}$
PLCK G004.5−19.5[c]	1.08/1	–	–	$0.38^{+0.15}_{-0.22}$	53^{+49}_{-2}	237^{+134}_{-196}	$5.2^{+12.4}_{-2.3}$	33^{+34}_{-25}	117^{+171}_{-58}	–	–

Note – Summary of the SL only models. Errors indicates 1σ errors on each parameter.

[a]Previously described in Wuyts et al. (2010) and Sharon et al. (2012).
[b]Also reported in Bayliss et al. (2011) and Oguri et al. (2012).
[c]This clusters belongs to the *Planck* Early SZ sample (Planck Collaboration et al., 2011). Previously described in Sifón et al. (2014), where we used the same technique applied in this work.
[d]The offsets are measured from the BCG centroids.
[e]The direction of the elliptical mass distribution measured counterclockwise from the West and is related to the position angle (P.A.) by P.A $= \theta_e - 90°$.

TABLE C.2: The best-fitting model parameters for the SL and M_{200} analysis

Name	$\chi^2/d.o.f.$	$x_{offset}{}^d$ [']	$y_{offset}{}^d$ [']	e_Σ	$\theta_e{}^e$ [deg]	r_s [kpc]	c_{200}	r_{cut} [kpc]	σ_{gal} [km s^{-1}]	$z_{arc,2}$	$r_{arc,3}$
RCS2 J0004−0103	1.17/4	–	–	$0.32^{+0.07}_{-0.12}$	311^{+3}_{-5}	80^{+97}_{-65}	$7.1^{+7.0}_{-3.9}$	–	–	–	–
RCS2 J0034+0225	1.98/2	–	–	$0.17^{+0.17}_{-0.06}$	34^{+4}_{-14}	140^{+13}_{-69}	$5.2^{+2.9}_{-2.1}$	91^{+103}_{-9}	141^{+19}_{-44}	–	–
RCS2 J0038+0215	1.99/2	$8.7^{+0.2}_{-3.6}$	$-1.5^{+2.3}_{-2.2}$	$0.08^{+0.12}_{-0.06}$	15^{+13}_{-14}	130^{+9}_{-79}	$5.9^{+3.5}_{-2.4}$	17^{+90}_{-6}	184^{+99}_{-72}	$2.2^{+3.1}_{-0.7}$	–
RCS2 J0047+0507	2.38/2	$0.6^{+2.1}_{-1.5}$	$1.2^{+2.7}_{-2.0}$	$0.47^{+0.08}_{-0.11}$	79^{+9}_{-8}	123^{+9}_{-72}	$4.9^{+4.6}_{-2.0}$	25^{+108}_{-4}	152^{+67}_{-51}	–	–
RCS2 J0052+043	2.32/3	$5.0^{+3.8}_{-1.8}$	$-2.6^{+4.0}_{-5.5}$	$0.44^{+0.21}_{-0.02}$	66^{+12}_{-9}	34^{+41}_{-1}	$19.4^{+7.8}_{-9.0}$	29^{+47}_{-18}	271^{+56}_{-100}	$1.2^{+1.0}_{-0.1}$	–
RCS2 J0057+0209	6.93/4	–	–	$0.23^{+0.01}_{-0.11}$	88^{+6}_{-14}	243^{+98}_{-86}	$5.1^{+2.0}_{-2.0}$	98^{+28}_{-65}	82^{-31}	–	–
RCS2 J0252−1459	2.98/2	–	–	$0.49^{+0.06}_{-0.13}$	203^{+20}_{-8}	243^{+370}_{-179}	$3.5^{+8.1}_{-1.4}$	76^{+70}_{-14}	52^{+162}_{-0}	–	–
RCS2 J0309−1437	3.96/2	$-0.1^{+0.0}_{-3.5}$	$-0.2^{+0.1}_{-4.5}$	$0.20^{+0.09}_{-0.05}$	108^{+0}_{-18}	122^{+48}_{-71}	$4.8^{+4.9}_{-1.9}$	49^{+38}_{-26}	205^{+23}_{-46}	$2.2^{+0.2}_{-1.4}$	$3.7^{+0.9}_{-0.7}$
RCS2 J0327−1326	1.43/5	$-2.2^{+2.2}_{-3.2}$	$-1.9^{+2.6}_{-2.5}$	$0.21^{+0.18}_{-0.09}$	8^{+2}_{-12}	137^{+245}_{-33}	$7.9^{+3.2}_{-5.2}$	79^{+12}_{-70}	55^{+137}_{-35}	–	–
RCS2 J0859−0345	2.34/4	$-1.3^{+2.4}_{-0.2}$	$1.5^{+0.0}_{-1.1}$	$0.10^{+0.08}_{-0.06}$	-2^{+10}_{-2}	339^{+2}_{-137}	$3.0^{+1.2}_{-1.2}$	–	–	–	–
RCS2 J1055−0459	10.14/3	$-1.0^{+1.7}_{-0.0}$	$-1.0^{+1.9}_{-0.0}$	$0.72^{+0.02}_{-0.29}$	122^{+9}_{-7}	94^{+8}_{-43}	$6.5^{+3.3}_{-2.6}$	44^{+148}_{-1}	130^{+59}_{-48}	–	–
RCS2 J1101−0602	1.11/2	–	–	$0.04^{+0.15}_{-0.03}$	25^{+13}_{-14}	125^{+12}_{-73}	$5.2^{+3.5}_{-2.1}$	97^{+0}_{-90}	26^{+113}_{-2}	–	–
RCS2 J1108−0456	5.45/2	$4.6^{+0.3}_{-6.4}$	$2.4^{+1.5}_{-3.6}$	$0.46^{+0.28}_{-0.05}$	21^{+7}_{-8}	328^{+21}_{-126}	$3.2^{+1.3}_{-1.3}$	15^{+128}_{-4}	101^{+26}_{-59}	$1.5^{+1.0}_{-0.2}$	$2.8^{+1.3}_{-0.5}$
RCS2 J1111+1408	1.09/4	–	–	$0.40^{+0.19}_{-0.17}$	56^{+6}_{-7}	288^{+142}_{-130}	$4.3^{+1.9}_{-1.7}$	–	–	–	–
RCS2 J1119−0728	1.31/2	–	–	$0.14^{+0.16}_{-0.09}$	137^{+16}_{-2}	95^{+31}_{-14}	$5.2^{+2.1}_{-2.1}$	86^{+108}_{-4}	232^{+4}_{-149}	–	–
RCS2 J1125−0628	1.00/3	–	–	$0.32^{+0.32}_{-0.01}$	89^{+9}_{-8}	71^{+73}_{-40}	$9.7^{+6.1}_{-4.6}$	57^{+115}_{-45}	32^{+104}_{-0}	–	–
RCS2 J1250+0244	1.47/2	–	–	$0.35^{+0.34}_{-0.04}$	136^{+8}_{-5}	96^{+27}_{-75}	$5.8^{+12.5}_{-2.3}$	9^{+86}_{-6}	51^{+142}_{-27}	–	–
RCS2 J1511+0630	1.03/2	–	–	$0.51^{+0.03}_{-0.16}$	-8^{+7}_{-10}	70^{+6}_{-48}	$7.1^{+9.3}_{-2.8}$	180^{+14}_{-107}	95^{+49}_{-82}	–	–
RCS2 J1517+1003	1.06/2	$-3.7^{+8.4}_{-1.0}$	$-5.5^{+4.9}_{-1.1}$	$0.38^{+0.21}_{-0.13}$	31^{+4}_{-4}	58^{+62}_{-13}	$13.6^{+5.4}_{-6.4}$	54^{+52}_{-47}	95^{+73}_{-30}	–	–
RCS2 J1519+0840	2.50/2	$-18.2^{+3.6}_{-0.7}$	$-2.7^{+2.2}_{-2.2}$	$0.23^{+0.02}_{-0.20}$	-1^{+11}_{-3}	412^{+19}_{-228}	$3.0^{+1.6}_{-1.2}$	67^{+96}_{-5}	100^{+82}_{-0}	$1.5^{+0.3}_{-0.3}$	$1.2^{+0.1}_{-0.3}$
RCS2 J1526+0432	2.64/3	$-1.2^{+2.6}_{-1.7}$	$2.4^{+2.0}_{-2.9}$	$0.46^{+0.13}_{-0.23}$	119^{+5}_{-4}	146^{+26}_{-6}	$5.4^{+2.2}_{-2.2}$	93^{+100}_{-11}	205^{+12}_{-68}	$1.1^{+1.5}_{-0.1}$	–
SDSS J2111−0114	2.89/2	$-3.5^{+3.3}_{-0.4}$	$6.5^{+2.2}_{-10.1}$	$0.12^{+0.22}_{-0.03}$	103^{+3}_{-5}	355^{+53}_{-171}	$3.2^{+1.7}_{-1.3}$	69^{+77}_{-17}	80^{+16}_{-68}	–	–
RCS2 J2135−0102	4.25/2	$-6.8^{+8.9}_{-0.8}$	$8.8^{+0.8}_{-15.3}$	$0.26^{+0.03}_{-0.07}$	114^{+2}_{-8}	205^{+185}_{-29}	$6.8^{+2.7}_{-3.1}$	66^{+30}_{-61}	82^{+108}_{-39}	$0.7^{+2.2}_{-0.2}$	–
RCS2 J2147−0102	2.81/2	–	–	$0.33^{+0.31}_{-0.01}$	73^{+15}_{-7}	33^{+7}_{-21}	$11.2^{+12.8}_{-4.5}$	245^{+25}_{-211}	147^{+83}_{-92}	–	–
RCS2 J2151−0138	1.05/2	$1.4^{+1.1}_{-1.4}$	$-6.3^{+2.8}_{-1.9}$	$0.04^{+0.08}_{-0.02}$	84^{+9}_{-9}	209^{+65}_{-106}	$6.3^{+3.7}_{-2.5}$	102^{+93}_{-1}	119^{+39}_{-29}	–	–
RCS2 J2313−0104	1.40/2	–	–	$0.22^{+0.18}_{-0.16}$	91^{+6}_{-15}	129^{+5}_{-78}	$5.2^{+4.6}_{-2.1}$	33^{+82}_{-2}	109^{+48}_{-57}	–	–
RCS2 J2329−1317	4.44/2	$0.1^{+1.7}_{-2.5}$	$0.2^{+4.5}_{-0.1}$	$0.43^{+0.16}_{-0.16}$	83^{+5}_{-12}	306^{+6}_{-203}	$3.5^{+2.9}_{-1.4}$	20^{+74}_{-0}	174^{+36}_{-82}	$3.3^{+2.8}_{-0.6}$	–
RCS2 J2329−0120	4.81/3	–	–	$0.65^{+0.00}_{-0.14}$	56^{+6}_{-8}	46^{+16}_{-23}	$10.0^{+7.5}_{-4.0}$	139^{+8}_{-57}	145^{+26}_{-39}	–	–
RCS2 J2336−0608	3.37/2	$-12.0^{+1.0}_{-0.0}$	$11.3^{+0.6}_{-4.6}$	$0.18^{+0.11}_{-0.06}$	121^{+2}_{-8}	391^{+5}_{-215}	$3.2^{+2.1}_{-1.3}$	132^{+25}_{-58}	81^{+20}_{-10}	$1.4^{+0.1}_{-0.1}$	$3.0^{+0.1}_{-0.2}$
PLCK G004.5−19.5	1.09/2	–	–	$0.35^{+0.15}_{-0.16}$	53^{+7}_{-2}	311^{+63}_{-214}	$4.3^{+5.4}_{-1.1}$	53^{+12}_{-46}	93^{+162}_{-40}	–	–

Note – Summary of the SL and M_{200} models. Errors indicates 1σ errors on each parameter.

[a] Previously described in Wuyts et al. (2010) and Sharon et al. (2012).
[b] Also reported in Bayliss et al. (2011) and Oguri et al. (2012).
[c] This clusters belongs to the *Planck* Early SZ sample (Planck Collaboration et al., 2011). Previously described in Sifón et al. (2014), where we used the same technique applied in this work.
[d] The offsets are measured from the BCG centroids.
[e] The direction of the elliptical mass distribution measured counterclockwise from the West and is related to the position angle (P.A.) by P.A $= \theta_e - 90°$.

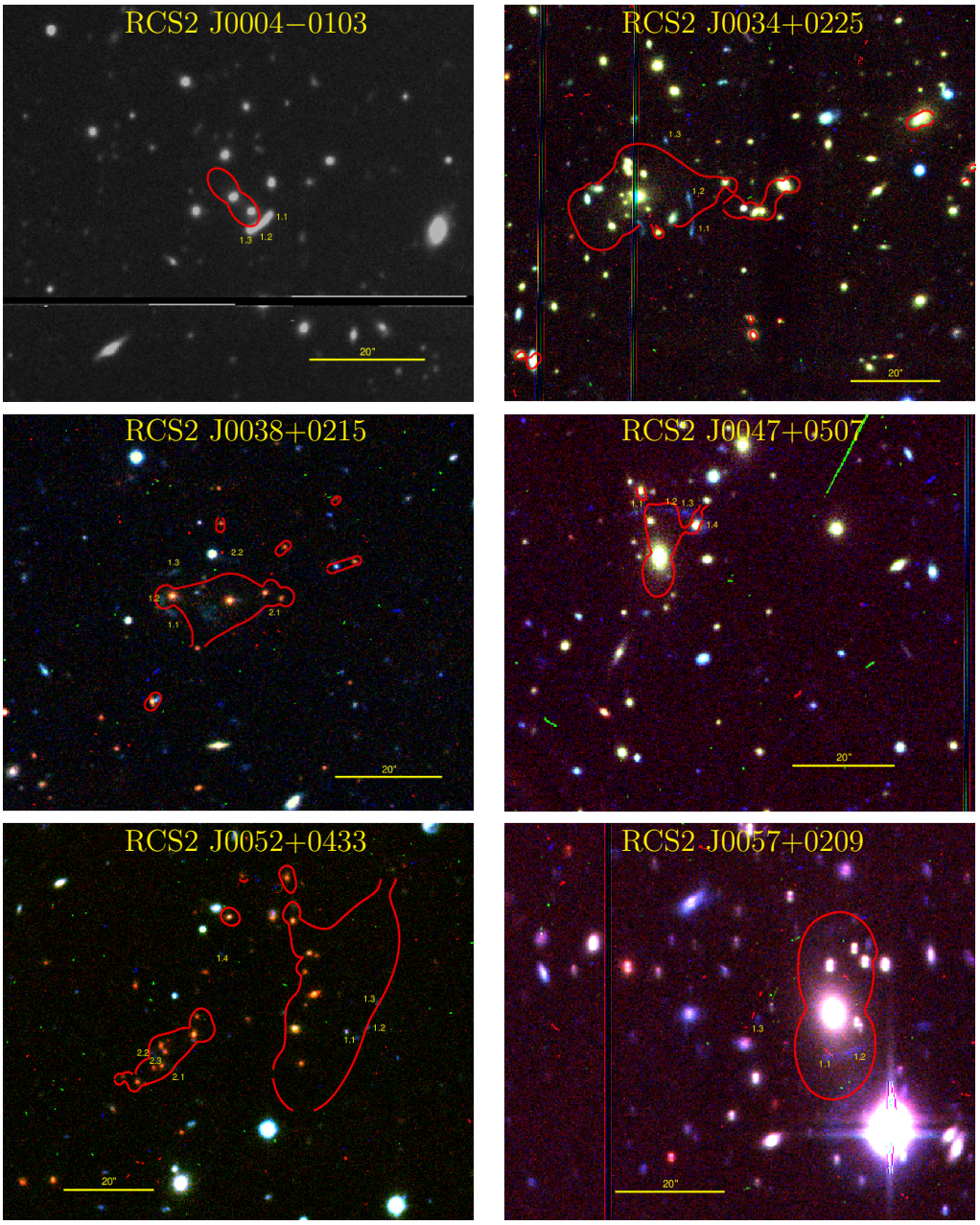

FIGURE C.1: The best model derived from our SL and dynamical analysis. The multiple images are labeled by yellow ID numbers while critical curves are displayed by red curves. Each cluster is labeled at the top with its cluster name.

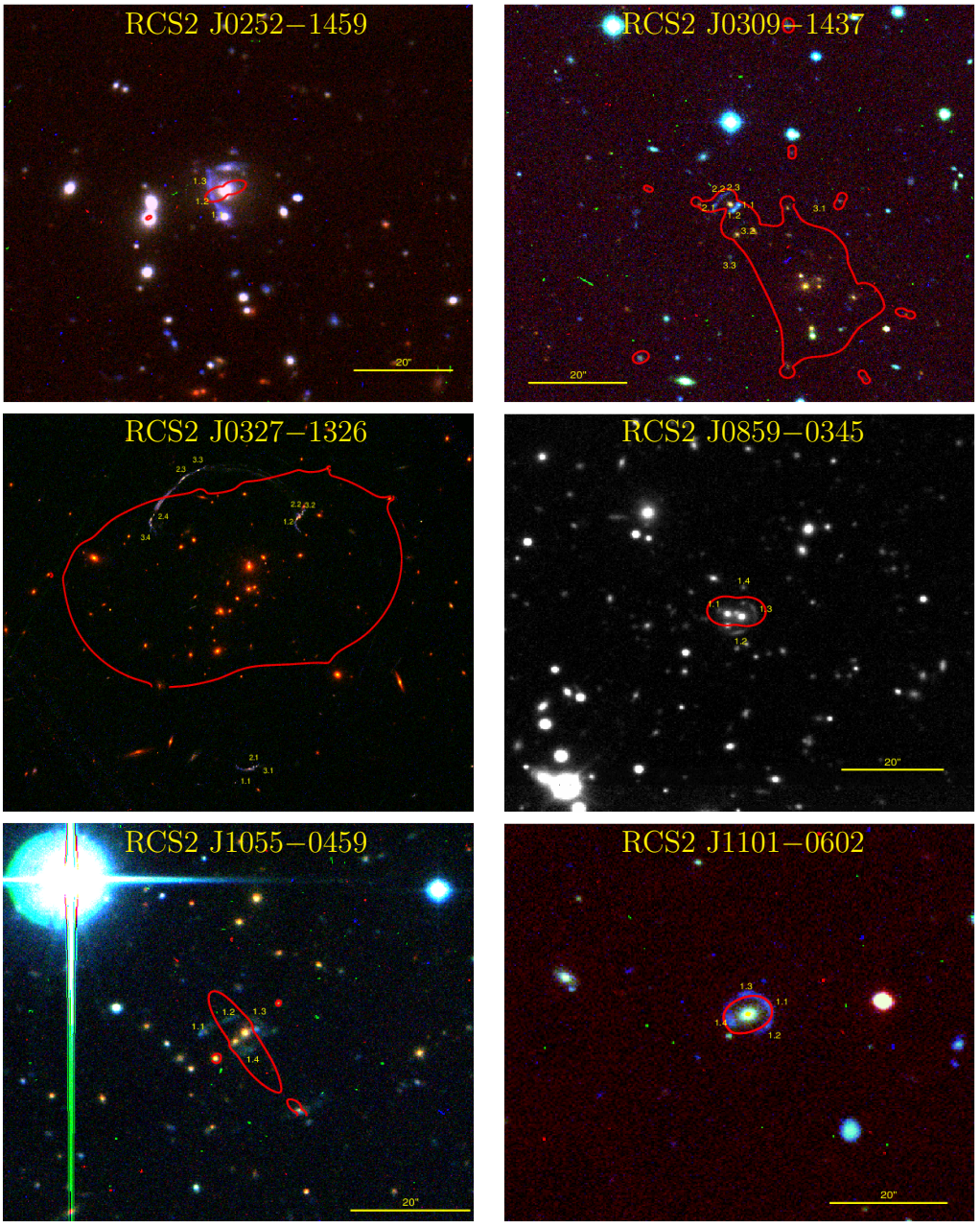

FIGURE C.2: The best model derived from our SL and dynamical analysis. The multiple images are labeled by yellow ID numbers while critical curves are displayed by red curves. Each cluster is labeled at the top with its cluster name. The images of the cluster RCS2J0327−1326 were taken from the HST website. The clusters RCS2J0252−1459, RCS2J1055−0459, and RCS2J1101−0602 present a small effective Einstein radius and their arcs seem to be more affected by the central galaxies than the hole clusters. Conservatively, we left out these three systems of our $c - M$ relation analysis, although they are always shown in the plots.

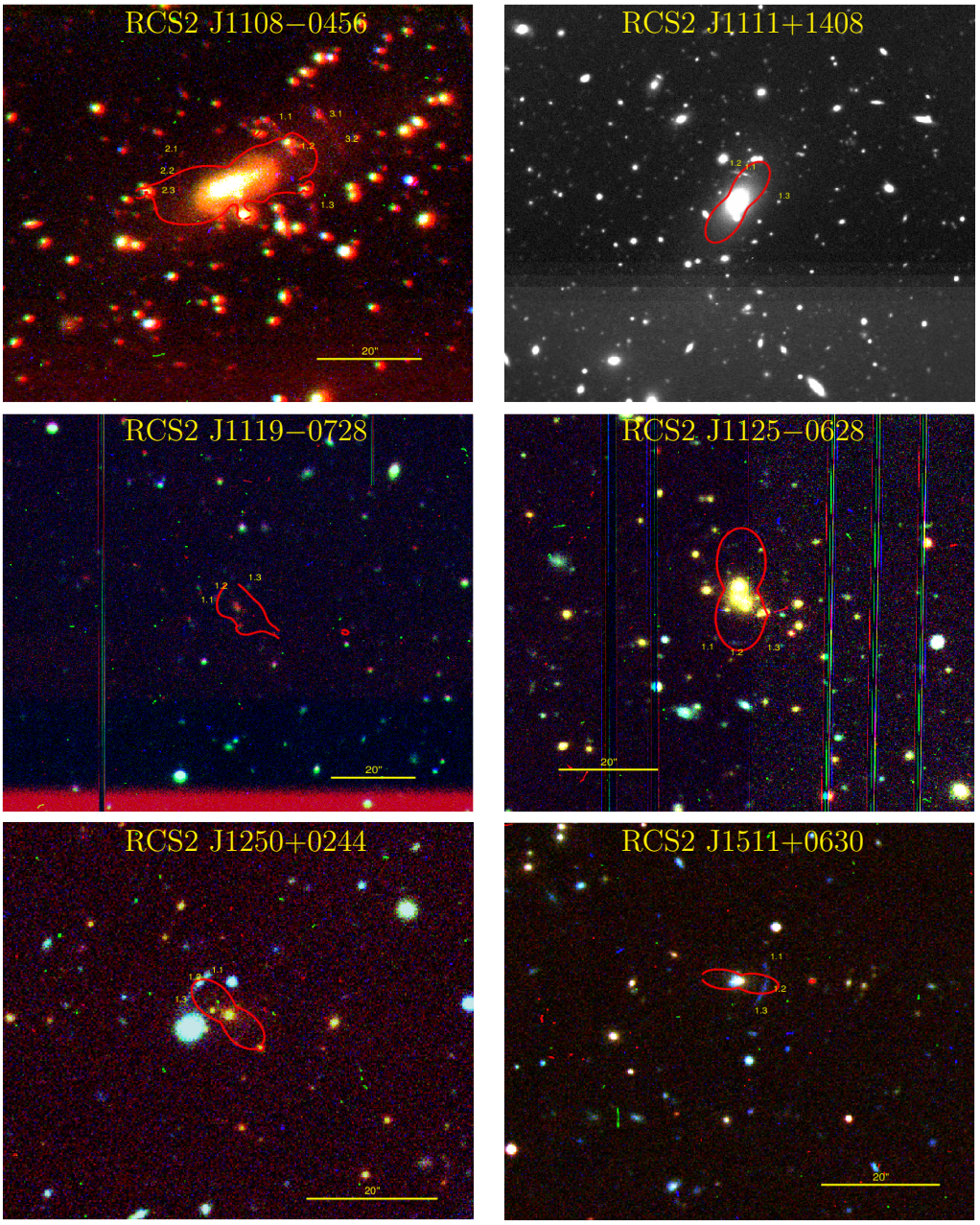

FIGURE C.3: The best model derived from our SL and dynamical analysis. The multiple images are labeled by yellow ID numbers while critical curves are displayed by red curves. Each cluster is labeled at the top with its cluster name.

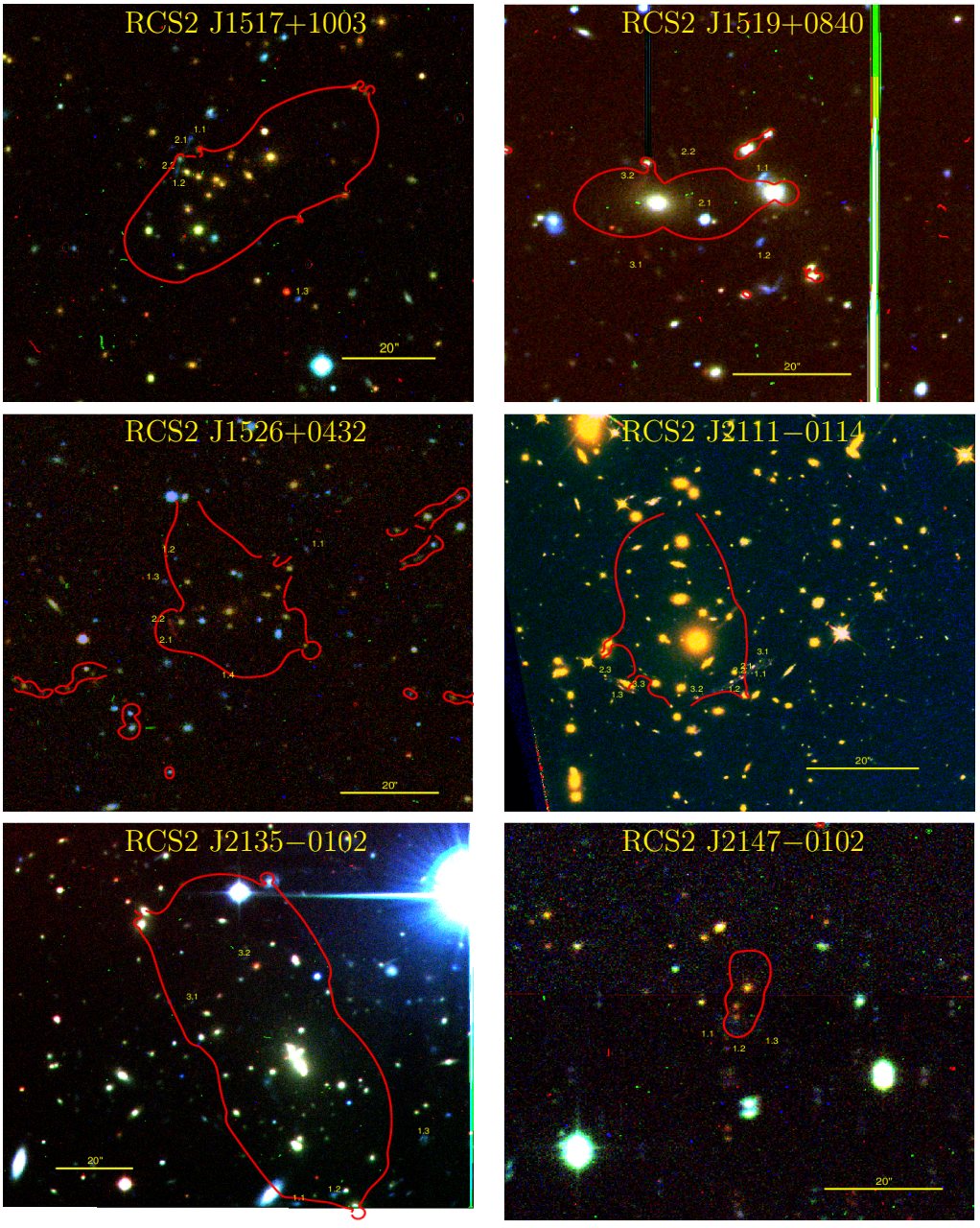

FIGURE C.4: The best model derived from our SL and dynamical analysis. The multiple images are labeled by yellow ID numbers while critical curves are displayed by red curves. Each cluster is labeled at the top with its cluster name. The images of the cluster RCS2J2111−011 were taken from the HST website.

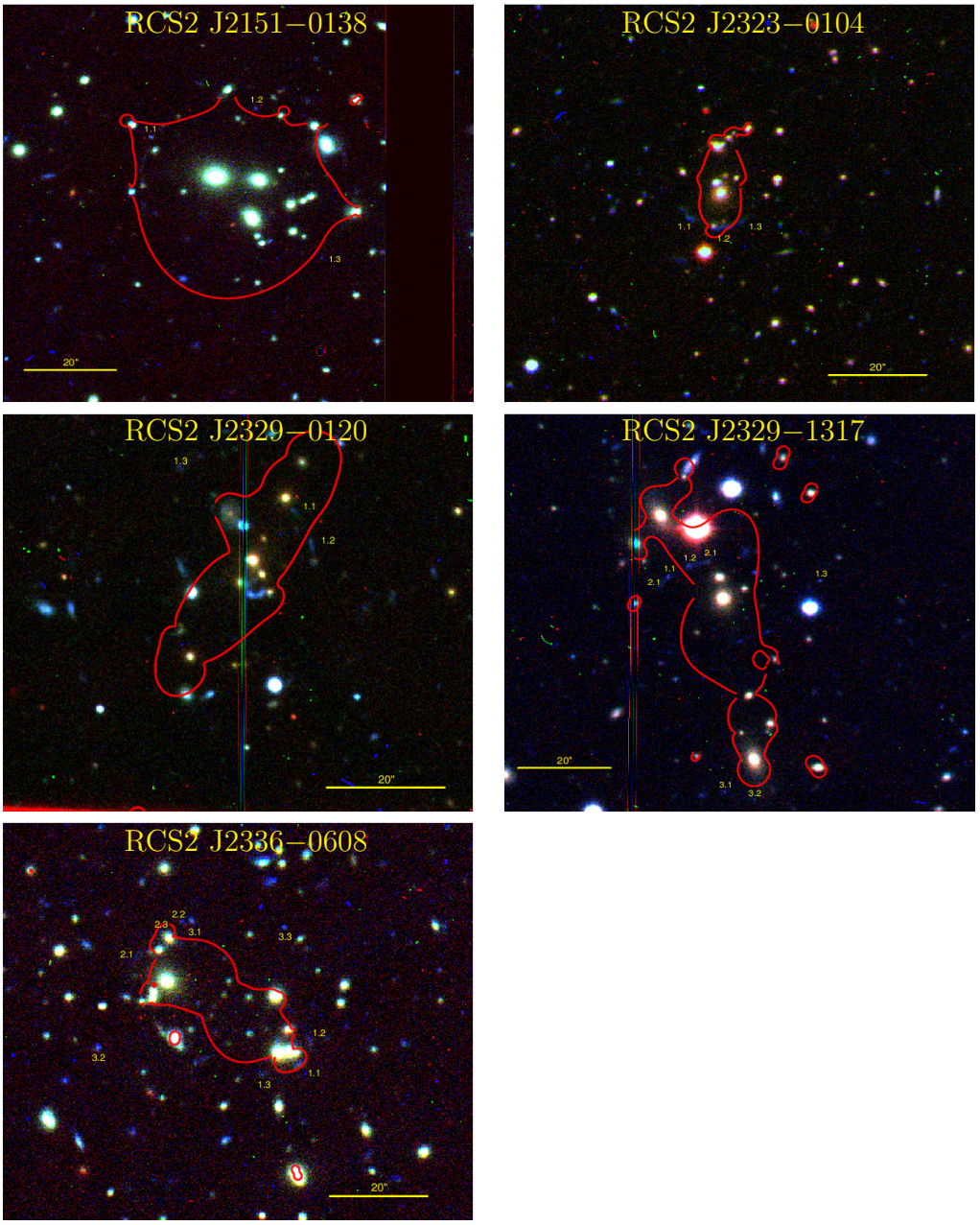

FIGURE C.5: The best model derived from our SL and dynamical analysis. The multiple images are labeled by yellow ID numbers while critical curves are displayed by red curves. Each cluster is labeled at the top with its cluster name.

Appendix D

RCSGA: spectroscopically confirmed cluster members

The FORS2/VLT spectroscopy observations of the RCSGA cluster sample have yielded $\sim$ 700 cluster members. This spectroscopic information has been used to measure velocity dispersions and dynamical masses.

In this appendix we report all the spectroscopically confirmed cluster members in Tab. D.1.

Table D.1: The FORS2/VLT Spectroscopic redshifts for cluster members

Cluster	R.A. (°)	Dec. (°)	z z
RCS2J0004−0103	–	–	–
–	1.164037228	-1.031056523	0.5178
–	1.187413931	-1.032596350	0.5175
–	1.218209743	-1.074513793	0.5110
–	1.252925158	-1.056319118	0.5151
–	1.268463135	-1.058558226	0.5106
–	1.264403820	-1.068215370	0.5160
–	1.263284087	-1.077172756	0.5165
–	1.172435999	-1.036445022	0.5143
–	1.177335262	-1.039104342	0.5130
RCS2J0034+0225	–	–	–
–	8.60755825	2.47035551	0.3848

Continued on next page

Table D.1 – *Continued from previous page*

Cluster	R.A. (°)	Dec. (°)	z z
–	8.61596298	2.46720552	0.3836
–	8.61582470	2.45824718	0.3860
–	8.63711643	2.45523882	0.3788
–	8.61848736	2.44866109	0.3771
–	8.61498356	2.42948627	0.3848
–	8.60545826	2.42612505	0.3881
–	8.59978294	2.41640019	0.3819
–	8.62744999	2.40961123	0.3902
–	8.62941265	2.40513062	0.3831
–	8.62535000	2.39197516	0.3804
–	8.63494587	2.38826680	0.3823
–	8.58542538	2.37783909	0.3873
–	8.58773708	2.37021112	0.3856
–	8.60755825	2.47035551	0.3845
–	8.62345791	2.46811676	0.3828
–	8.64559174	2.45677781	0.3838
–	8.63536644	2.44117236	0.3806
–	8.58983707	2.43795276	0.3849
–	8.59971237	2.42787504	0.3829
–	8.62247944	2.41597795	0.3855
–	8.64237118	2.40828061	0.3854
–	8.58269215	2.40492225	0.3921
–	8.64139175	2.40170288	0.3932
–	8.63697529	2.39078617	0.3843
–	8.58773708	2.37028074	0.3858
RCS2J0038+0215	–	–	–
–	9.710704803	2.284380198	0.6930
–	9.713926315	2.281441212	0.6990
–	9.715467453	2.278501749	0.6926
–	9.719669342	2.276262283	0.6919
–	9.730455399	2.268284321	0.7009
–	9.7328366	2.2645053	0.6931
–	9.731716156	2.261846066	0.6970
–	9.735918045	2.256667376	0.7019

Continued on next page

Table D.1 – *Continued from previous page*

Cluster	R.A. (°)	Dec. (°)	z z
–	9.731575966	2.254567862	0.6893
–	9.747263908	2.245050192	0.6985
–	9.719949722	2.238331795	0.7046
–	9.721350670	2.232453346	0.7026
–	9.695717812	2.220416069	0.6978
–	9.691093445	2.301945686	0.6976
–	9.692354202	2.299146414	0.6904
–	9.7328366	2.2645053	0.6931
–	9.740119934	2.256317377	0.6916
–	9.738719940	2.247639418	0.6969
–	9.735077858	2.243860483	0.6946
–	9.692635536	2.234622478	0.6973
RCS2J0047+0507	–	–	–
–	11.99014187	5.15903902	0.4276
–	11.97510433	5.15134192	0.4292
–	11.97229576	5.15015268	0.4279
–	11.95683765	5.15449190	0.4347
–	11.95985794	5.14056396	0.4259
–	11.95985794	5.14056396	0.4267
–	11.96393299	5.11159420	0.4198
–	11.94672108	5.11614180	0.4300
–	11.94172955	5.11222219	0.4217
–	11.95149612	5.09962797	0.4269
–	11.93793774	5.10564423	0.4262
–	11.92992878	5.10424423	0.4323
–	11.93337059	5.09066963	0.4345
RCS2J0052+0433	–	–	–
–	13.06461620	4.57020283	0.7178
–	13.05008316	4.57629156	0.7271
–	13.04671669	4.56215572	0.7196
–	13.04545021	4.55781698	0.7238
–	13.03569126	4.56159735	0.7273
RCS2J0057+0209	–	–	–
–	14.327603340	2.176548958	0.2904

Continued on next page

Table D.1 – *Continued from previous page*

Cluster	R.A. (°)	Dec. (°)	z z
–	14.344270706	2.188446283	0.2942
–	14.352395058	2.178369045	0.3001
–	14.346652985	2.152475357	0.2941
–	14.362059593	2.178929090	0.2957
–	14.351835251	2.140858412	0.2946
–	14.370182991	2.156254768	0.2975
–	14.369202614	2.142678022	0.2899
–	14.371583939	2.138478994	0.3005
–	14.389162064	2.165352345	0.2911
–	14.392804146	2.159333706	0.2925
–	14.392663956	2.147016764	0.2882
–	14.398825645	2.147716522	0.2958
–	14.335797310	2.185297012	0.2943
–	14.351063728	2.172280550	0.2877
–	14.357787132	2.183617830	0.2930
–	14.369273186	2.153105497	0.2860
–	14.372353554	2.147926807	0.2893
–	14.393083572	2.171230793	0.2939
RCS2J0252-1459	–	–	–
–	43.17150497	-14.94787788	0.2800
–	43.17324066	-14.95137787	0.2701
–	43.15259552	-14.96915054	0.2798
–	43.17193604	-14.97216129	0.2812
–	43.16411591	-14.97923088	0.2805
–	43.18657684	-14.98175049	0.2698
–	43.17903900	-14.98524761	0.2643
–	43.19975662	-14.98839760	0.2718
–	43.17721558	-14.99704170	0.2682
–	43.17164993	-14.99858093	0.2635
–	43.17143250	-14.99942017	0.2650
–	43.17267609	-15.00986958	0.2657
–	43.18434525	-15.01230240	0.2590
–	43.16131973	-15.02514172	0.2732
–	43.16632462	-15.02863312	0.2620

Continued on next page

Table D.1 – *Continued from previous page*

Cluster	R.A. (°)	Dec. (°)	z z
–	43.17618179	-15.03155804	0.2695
–	43.15764618	-15.03921127	0.2647
–	43.17779922	-15.04436398	0.2636
–	0.00000000	0.00000000	0.2628
RCS2J0309-1437	–	–	–
–	47.488540649	-14.582889557	0.8111
–	47.486816406	-14.641256332	0.8033
–	47.484069824	-14.654832840	0.8070
–	47.481323242	-14.654973984	0.8057
–	47.477416992	-14.655533791	0.8073
–	47.458457947	-14.599270821	0.8042
–	47.452819824	-14.613548279	0.8099
–	47.439874	-14.621141	0.8036
–	47.438064575	-14.621106148	0.8126
–	47.433727264	-14.626145363	0.8046
–	47.424903870	-14.603610039	0.8116
–	47.419261932	-14.610467911	0.8053
–	47.415355682	-14.624744415	0.8134
–	47.404651642	-14.611865997	0.8045
–	47.439874	-14.621141	0.8036
–	47.438064575	-14.621106148	0.8126
–	47.438064575	-14.621106148	0.8125
RCS2J0327-1326	–	–	–
–	51.86061478	-13.43758106	0.5624
–	51.87525177	-13.45442772	0.5537
–	51.90061951	-13.48007298	0.5618
–	51.91069031	-13.47627831	0.5604
–	51.91142654	-13.48418617	0.5643
–	51.84401703	-13.46564198	0.5577
–	51.88822937	-13.46377468	0.5583
–	51.84124756	-13.46314716	0.5720
–	51.86796951	-13.45788860	0.5724
–	51.84029770	-13.45658875	0.5600
–	51.85223389	-13.45660019	0.5634

Continued on next page

Table D.1 – *Continued from previous page*

Cluster	R.A. (°)	Dec. (°)	z z
–	51.87660217	-13.45558357	0.5641
–	51.84815216	-13.45533657	0.5601
–	51.88372040	-13.45484734	0.5551
–	51.85322952	-13.45486641	0.5614
–	51.86703873	-13.45384121	0.5625
–	51.83876038	-13.45234203	0.5679
–	51.86246490	-13.45211124	0.5619
–	51.85461044	-13.45181370	0.5590
–	51.87912369	-13.44970512	0.5597
–	51.88410568	-13.44788361	0.5744
–	51.86850739	-13.44762802	0.5668
–	51.89250565	-13.44725800	0.5630
–	51.83625793	-13.44524956	0.5737
–	51.86742783	-13.44476128	0.5577
–	51.84402466	-13.44420528	0.5617
–	51.85091400	-13.44293880	0.5604
–	51.84140015	-13.44239140	0.5646
–	51.86442566	-13.44153023	0.5678
–	51.88077545	-13.43953609	0.5660
–	51.84952545	-13.43935299	0.5669
–	51.89400101	-13.43850803	0.5583
–	51.86323547	-13.43645859	0.5682
–	51.87012863	-13.43568039	0.5674
–	51.89244080	-13.43462467	0.5686
–	51.87011337	-13.43076134	0.5649
–	51.84202194	-13.42878342	0.5688
–	51.87432861	-13.42666149	0.5640
–	51.85435104	-13.42581081	0.5596
–	51.85784912	-13.42388630	0.5529
–	51.84763718	-13.42356682	0.5642
–	51.86972046	-13.42245865	0.5566
–	51.88482666	-13.42052460	0.5745
–	51.87628555	-13.41940022	0.5631
RCS2J0859-0345	–	–	–

Continued on next page

Table D.1 – *Continued from previous page*

Cluster	R.A. (°)	Dec. (°)	z z
–	134.795593262	-3.736541986	0.6589
–	134.796569824	-3.741720438	0.6433
–	134.792358398	-3.757816076	0.6488
–	134.804855347	-3.747738838	0.6454
–	134.809616089	-3.753477335	0.6437
–	134.843566895	-3.767752647	0.6606
–	134.798812866	-3.758236170	0.6484
–	134.805831909	-3.752917528	0.6454
RCS2J1055-0459	–	–	–
–	163.87594604	-4.96433258	0.6052
–	163.89898682	-4.98308802	0.6119
–	163.89672852	-4.98994637	0.6105
–	163.90234375	-4.99652481	0.6030
–	163.90684509	-4.99918413	0.6009
–	163.91372681	-4.99974346	0.6091
–	163.92300415	-5.00254250	0.6087
–	163.93241882	-5.00996017	0.6079
–	163.94900513	-5.01485777	0.6042
–	163.87608337	-4.96433258	0.6052
–	163.88984680	-4.96615267	0.6061
–	163.89364624	-4.97399092	0.6031
–	163.88577271	-4.99456501	0.6113
–	163.89433289	-4.99078608	0.6149
–	163.91372681	-4.99974346	0.6102
–	163.93142700	-5.01415920	0.6076
–	163.93916321	-5.01163960	0.6087
–	163.86785889	-5.00203943	0.6041
–	163.89237976	-4.98055553	0.6056
–	163.88851929	-4.99623108	0.6114
–	163.89785767	-4.98650408	0.6075
–	163.90411377	-4.99448156	0.6009
–	163.90959167	-4.99889088	0.6121
–	163.91128540	-5.01309681	0.6078
–	163.92231750	-5.00343943	0.6077

Continued on next page

Table D.1 – *Continued from previous page*

Cluster	R.A. (°)	Dec. (°)	z z
–	163.89877319	-4.98811340	0.6135
–	163.90039062	-5.00085020	0.6102
–	163.91662598	-4.99210215	0.6047
–	163.90916443	-5.01806593	0.6105
RCS2J1101-0602	–	–	–
–	165.467132568	-6.018191814	0.4843
–	165.475387573	-6.034847736	0.4858
–	165.483612061	-6.046044827	0.4899
–	165.470169067	-6.049823761	0.4814
–	165.461868286	-6.057101727	0.4887
–	165.491836548	-6.060390472	0.4829
–	165.470169067	-6.068509102	0.4887
–	165.452011108	-6.100700378	0.4881
RCS2J1108-0456	–	–	–
–	167.120620728	-4.917506695	0.4212
–	167.102630615	-4.911419392	0.4202
–	167.086547852	-4.907710552	0.4094
–	167.078750610	-4.919397831	0.4122
–	167.082260132	-4.936333656	0.4127
–	167.076721191	-4.938922882	0.4136
–	167.06649	-4.9409874	0.4070
–	167.06713	-4.94484	0.4075
–	167.066879272	-4.945431232	0.4118
–	167.066741943	-4.950119972	0.4119
–	167.050018311	-4.956418037	0.4153
–	167.047073364	-4.960826874	0.4085
–	167.049102783	-4.979022503	0.4098
–	167.039474487	-4.994627953	0.4110
–	167.089645386	-4.908410549	0.4070
–	167.098419189	-4.936822891	0.4073
–	167.066467285	-4.912329674	0.4084
–	167.083389282	-4.936123371	0.4051
–	167.071945190	-4.929965019	0.4046
–	167.091476440	-4.952009201	0.4115

Continued on next page

Table D.1 – *Continued from previous page*

Cluster	R.A. (°)	Dec. (°)	z z
–	167.091476440	-4.952009201	0.4049
–	167.06649	-4.9409874	0.4070
–	167.06713	-4.94484	0.4075
–	167.066955566	-4.945291519	0.4118
–	167.067306519	-4.951589584	0.4103
–	167.051574707	-4.948230267	0.4213
–	167.065475464	-4.967825413	0.4055
–	167.032455444	-4.944660187	0.4125
–	167.039199829	-4.954108238	0.4072
–	167.064834595	-4.981751919	0.4173
–	167.016586304	-4.952497482	0.4148
–	167.043777466	-4.994627953	0.4105
RCS2J1111+1408	–	–	–
–	167.905502319	14.182679176	0.2182
–	167.868103027	14.160989761	0.2237
–	167.861465454	14.172607422	0.2167
–	167.849624634	14.137617111	0.2149
–	167.834625244	14.147414207	0.2170
–	167.835342407	14.123060226	0.2164
–	167.832168579	14.118721008	0.2197
–	167.804458618	14.121096611	0.2193
–	167.900726318	14.184848785	0.2197
–	167.889602661	14.160918236	0.2194
–	167.883544922	14.119070053	0.2268
–	167.879226685	14.126208305	0.2270
–	167.857421875	14.140625954	0.2210
–	167.865509033	14.129849434	0.2255
–	167.850936890	14.135867119	0.2164
–	167.849334717	14.131808281	0.2246
–	167.817291260	14.180373192	0.2213
–	167.835205078	14.123270035	0.2230
–	167.820617676	14.136005402	0.2232
–	167.796081543	14.155595779	0.2202
RCS2J1119-0728	–	–	–

Continued on next page

Table D.1 – *Continued from previous page*

Cluster	R.A. (°)	Dec. (°)	z z
–	169.787857056	-7.467146397	1.0062
–	169.800354004	-7.466726780	1.0194
–	169.809677124	-7.469526291	1.0090
–	169.778610229	-7.474214554	1.0171
RCS2J1125-0628	–	–	–
–	171.383819580	-6.441330910	0.4740
–	171.382553101	-6.465124607	0.4743
–	171.380294800	-6.479260921	0.4771
–	171.376220703	-6.473382473	0.4733
–	171.373123169	-6.475481987	0.4816
–	171.367202759	-6.478561401	0.4763
–	171.361145020	-6.488079071	0.4760
–	171.332824707	-6.466243267	0.4762
–	171.388610840	-6.466384411	0.4695
–	171.380447388	-6.487518787	0.4692
–	171.380447388	-6.487518787	0.4736
–	171.371292114	-6.464984894	0.4725
–	171.367202759	-6.479960918	0.4753
RCS2J1250+0244	–	–	–
–	192.667953491	2.762478590	0.6907
–	192.660736084	2.740713835	0.6923
–	192.680068970	2.750511408	0.6857
–	192.676712036	2.745332718	0.6964
–	192.683914185	2.740503788	0.6923
–	192.684265137	2.733995438	0.6903
–	192.683853149	2.715240002	0.6870
–	192.701583862	2.724407673	0.6930
–	192.721405029	2.721117973	0.6890
–	192.674743652	2.766047716	0.6909
–	192.679153442	2.748831987	0.6926
–	192.682174683	2.740364075	0.6846
–	192.682174683	2.740364075	0.6961
–	192.664306641	2.719858885	0.6950
–	192.687423706	2.735045195	0.6923

Continued on next page

Table D.1 – *Continued from previous page*

Cluster	R.A. (°)	Dec. (°)	z z
–	192.685943604	2.719858885	0.6861
RCS2J1511+0630	–	–	–
–	227.952606201	6.532571793	0.5513
–	227.963592529	6.529911995	0.5551
–	227.955139160	6.520395279	0.5533
–	227.942047119	6.505838871	0.5541
–	227.936691284	6.501500130	0.5502
–	227.934783936	6.491003036	0.5500
–	227.945770264	6.487223625	0.5473
–	227.935211182	6.451113224	0.5534
–	227.941696167	6.519065857	0.5499
–	227.944503784	6.516266346	0.5498
–	227.944503784	6.516266346	0.5529
–	227.918090820	6.493802071	0.5498
–	227.918655396	6.488903046	0.5580
–	227.967407227	6.484563828	0.5512
–	227.935287476	6.453072548	0.5500
RCS2J1517+1003	–	–	–
–	229.237045288	10.104122162	0.6376
–	229.223037720	10.084175110	0.6456
–	229.240600586	10.088445663	0.6469
–	229.240524292	10.084457397	0.6458
–	229.237899780	10.077178955	0.6354
–	229.250839233	10.074729919	0.6488
–	229.256317139	10.067381859	0.6454
–	229.258026123	10.065562248	0.6453
–	229.262207031	10.064653397	0.6490
–	229.278137207	10.067312241	0.6456
–	229.265335083	10.045967102	0.6423
–	229.270599365	10.046596527	0.6460
–	229.277633667	10.045826912	0.6384
–	229.287796021	10.044707298	0.6373
–	229.272933960	10.027491570	0.6460
–	229.292556763	10.031619072	0.6431

Continued on next page

Table D.1 – *Continued from previous page*

Cluster	R.A. (°)	Dec. (°)	z z
–	229.282104492	10.017483711	0.6552
–	229.276275635	10.010625839	0.6439
–	229.290145874	10.011674881	0.6396
–	229.276779175	10.003067970	0.6436
–	229.246429443	10.108181000	0.6469
–	229.239685059	10.080958366	0.6407
–	229.235275269	10.076548576	0.6379
–	229.249771118	10.069271088	0.6427
–	229.254318237	10.068572044	0.6460
–	229.255523682	10.065002441	0.6411
–	229.255737305	10.062273026	0.6375
–	229.266265869	10.057864189	0.6426
–	229.282745361	10.045967102	0.6469
–	229.263198853	9.998799324	0.6435
–	229.280761719	10.003486633	0.6411
RCS2J1519+0840	–	–	–
–	229.87594604	8.71224117	0.3240
–	229.86956787	8.69873619	0.3127
–	229.83332825	8.67941952	0.3096
–	229.84344482	8.67766953	0.3143
–	229.86291504	8.67781162	0.3111
–	229.87686157	8.67864990	0.3265
–	229.88337708	8.67557240	0.3160
–	229.87509155	8.66773319	0.3201
–	229.89746094	8.63505268	0.3166
–	229.89002991	8.62245560	0.3146
–	229.84362793	8.67804432	0.3149
–	229.85383606	8.67776489	0.3195
–	229.86317444	8.67818546	0.3112
–	229.84985352	8.66684723	0.3162
–	229.86146545	8.66908741	0.3210
–	229.87591553	8.66222954	0.3223
–	229.87733459	8.65817070	0.3271
–	229.89036560	8.65894032	0.3120

Continued on next page

Table D.1 – *Continued from previous page*

Cluster	R.A. (°)	Dec. (°)	z z
–	229.89276123	8.65544128	0.3227
–	229.87081909	8.64158440	0.3235
–	229.87860107	8.64200497	0.3153
–	229.87321472	8.63654613	0.3123
–	229.87294006	8.62226963	0.3238
–	229.88653564	8.61793041	0.3153
–	229.83351135	8.67972279	0.3093
–	229.88320923	8.69610119	0.3160
–	229.86593628	8.67664623	0.3173
–	229.85162354	8.66670799	0.3170
–	229.88589478	8.67972469	0.3149
–	229.89213562	8.67986488	0.3207
–	229.88560486	8.66628838	0.3203
–	229.87924194	8.66069031	0.3194
–	229.91505432	8.66040802	0.3260
–	229.91590881	8.65788841	0.3153
–	229.90698242	8.63339520	0.3196
–	229.87980652	8.61520100	0.3212
RCS2J1526+0432	–	–	–
–	231.552291870	4.601474285	0.6363
–	231.559875488	4.596435547	0.6281
–	231.560012817	4.580479622	0.6413
–	231.592315674	4.570541382	0.6306
–	231.550186157	4.560464382	0.6304
–	231.552856445	4.543669224	0.6346
–	231.538803101	4.542618752	0.6378
–	231.581634521	4.530722141	0.6357
–	231.581634521	4.530722141	0.6307
–	231.563232422	4.529462814	0.6351
–	231.567733765	4.522744179	0.6365
–	231.560165405	4.522884369	0.6352
–	231.544006348	4.520644665	0.6365
–	231.587387085	4.506368160	0.6267
–	231.551162720	4.588457584	0.6387

Continued on next page

Table D.1 – *Continued from previous page*

Cluster	R.A. (°)	Dec. (°)	z z
–	231.577285767	4.578660011	0.6347
–	231.591049194	4.568161964	0.6331
–	231.607757568	4.561023235	0.6420
–	231.553558350	4.562424183	0.6394
–	231.538253784	4.561863899	0.6350
–	231.538253784	4.561863899	0.6375
–	231.577850342	4.549407482	0.6302
–	231.568725586	4.540449619	0.6297
–	231.547103882	4.540729523	0.6332
–	231.578689575	4.531212330	0.6316
–	231.548645020	4.534711361	0.6363
–	231.575042725	4.520854950	0.6319
–	231.585296631	4.511896610	0.6372
–	231.559036255	4.508677959	0.6288
–	231.544708252	4.499300003	0.6369
RCS2J2111-0114	–	–	–
–	317.837829590	-1.198773265	0.6312
–	317.820068359	-1.195414066	0.6301
–	317.823272705	-1.203812003	0.6369
–	317.844696045	-1.229285359	0.6320
–	317.841888428	-1.232364655	0.6438
–	317.836303711	-1.229985356	0.6357
–	317.83133	-1.2314199	0.6366
–	317.83067	-1.2319798	0.6323
–	317.831268311	-1.234604120	0.6347
–	317.82997	-1.2411824	0.6460
–	317.82815	-1.2429669	0.6414
–	317.828186035	-1.249020457	0.6316
–	317.784698486	-1.236423254	0.6353
–	317.784698486	-1.245940804	0.6401
–	317.847564697	-1.199682951	0.6330
–	317.859466553	-1.215638757	0.6363
–	317.846588135	-1.225296378	0.6302
–	317.836517334	-1.218858123	0.6275

Continued on next page

Table D.1 – *Continued from previous page*

Cluster	R.A. (°)	Dec. (°)	z z
–	317.831329346	-1.226276159	0.6285
–	317.831329346	-1.226276159	0.6333
–	317.830474854	-1.230755091	0.6354
–	317.831481934	-1.235933661	0.6462
–	317.82997	-1.2411824	0.6460
–	317.82815	-1.2429669	0.6414
–	317.800659180	-1.221517324	0.6403
–	317.821105957	-1.255038857	0.6377
–	317.821105957	-1.258817911	0.6320
–	317.814819336	-1.258257985	0.6472
RCS2J2135-0102	–	–	–
–	323.75717163	-1.04473603	0.3212
–	323.76681519	-1.03598881	0.3268
–	323.76779175	-1.05124438	0.3224
–	323.77899170	-1.02779996	0.3190
–	323.77758789	-1.04263604	0.3330
–	323.77572632	-1.06174159	0.3329
–	323.78228760	-1.04942501	0.3224
–	323.78671265	-1.05187500	0.3304
–	323.79440308	-1.04172778	0.3343
–	323.79693604	-1.05922222	0.3248
–	323.79782104	-1.05957222	0.3222
–	323.80981445	-1.03332782	0.3388
–	323.81204224	-1.05320275	0.3373
–	323.81799316	-1.04963326	0.3275
–	323.82553101	-1.05705273	0.3210
–	323.84078979	-1.05054438	0.3272
–	323.85409546	-1.04459441	0.3226
–	323.81317139	-1.01296389	0.3320
–	323.80105591	-1.01107502	0.3264
–	323.81231689	-1.02472222	0.3286
–	323.81155396	-1.03864717	0.3341
–	323.80581665	-1.03836668	0.3338
–	323.80218506	-1.04011667	0.3275

Continued on next page

Table D.1 – *Continued from previous page*

Cluster	R.A. (°)	Dec. (°)	z z
–	323.80615234	-1.04697502	0.3221
–	323.80090332	-1.04816389	0.3289
–	323.80068970	-1.04879439	0.3257
–	323.80020142	-1.04949439	0.3298
–	323.80047607	-1.05572212	0.3371
–	323.79693604	-1.05922222	0.3234
–	323.79623413	-1.06048048	0.3227
–	323.79067993	-1.06202221	0.3387
–	323.78671265	-1.06299996	0.3317
–	323.77572632	-1.06174159	0.3321
–	323.79299927	-1.08266675	0.3237
–	323.78256226	-1.08049726	0.3280
–	323.79315186	-1.08966398	0.3230
–	323.77935791	-1.08861399	0.3320
–	323.77682495	-1.09337223	0.3185
–	323.75808716	-1.08651388	0.3329
–	323.75415039	-1.08868337	0.3225
–	323.74374390	-1.03792500	0.3265
–	323.75982666	-1.02028978	0.3219
–	323.77899170	-1.01861048	0.3317
–	323.76849365	-1.04310405	0.3327
–	323.75463867	-1.07263625	0.3267
–	323.79452515	-1.02182972	0.3361
–	323.79522705	-1.02560866	0.3189
–	323.78375244	-1.04758298	0.3210
–	323.78991699	-1.04604352	0.3288
–	323.78234863	-1.06059968	0.3237
–	323.80154419	-1.06077468	0.3265
–	323.80139160	-1.07711554	0.3340
–	323.81777954	-1.05934000	0.3260
–	323.82882690	-1.06591833	0.3322
–	323.84130859	-1.06241906	0.3224
–	323.83526611	-1.08243394	0.3274
–	323.82940674	-1.10006952	0.3343

Continued on next page

Table D.1 – *Continued from previous page*

Cluster	R.A. (°)	Dec. (°)	z z
–	323.83010864	-1.10440826	0.3261
–	323.83737183	-1.09992945	0.3244
–	323.76556396	-1.05409122	0.3264
–	323.76528931	-1.00517380	0.3309
–	323.75646973	-1.02350903	0.3266
–	323.76290894	-1.02952754	0.3304
–	323.75241089	-1.04996204	0.3367
–	323.76123047	-1.04408371	0.3277
–	323.74749756	-1.06913710	0.3265
–	323.79159546	-1.01189220	0.3301
–	323.76107788	-1.06185925	0.3155
–	323.77227783	-1.04996228	0.3248
–	323.76907349	-1.06017971	0.3240
–	323.78094482	-1.05010235	0.3293
–	323.78796387	-1.04702318	0.3277
–	323.80154419	-1.06077468	0.3265
–	323.79580688	-1.08369374	0.3274
–	323.80938721	-1.08285403	0.3246
–	323.80630493	-1.09209168	0.3315
–	323.82882690	-1.06591833	0.3316
–	323.82199097	-1.08453345	0.3223
–	323.84579468	-1.06801748	0.3351
RCS2J2147-0102	–	–	–
–	326.947509766	-1.017211556	0.8775
–	326.945983887	-1.027429104	0.8829
–	326.923706055	-1.050663710	0.8803
–	326.913757324	-1.042545676	0.8744
–	326.912384033	-1.044085264	0.8803
–	326.906341553	-1.043665409	0.8787
–	326.899353027	-1.057382107	0.8809
–	326.876678467	-1.067039728	0.8956
–	326.855834961	-1.029668450	0.8962
–	326.951293945	-1.002095103	0.8810
–	326.945556641	-1.022110343	0.8801

Continued on next page

Table D.1 – *Continued from previous page*

Cluster	R.A. (°)	Dec. (°)	z z
–	326.917968750	-1.013432741	0.8847
–	326.922454834	-1.052483320	0.8817
–	326.855834961	-1.029668450	0.8957
–	326.850921631	-1.030228138	0.8947
RCS2J2151-0138	–	–	–
–	327.824035645	-1.633788347	0.3165
–	327.840118408	-1.624690771	0.3100
–	327.817718506	-1.654923320	0.3130
–	327.847961426	-1.637427807	0.3146
–	327.849639893	-1.642186642	0.3140
–	327.857360840	-1.641626835	0.3083
–	327.856994629	-1.663251758	0.3162
–	327.875213623	-1.649254918	0.3083
–	327.858123779	-1.674029112	0.3184
–	327.869476318	-1.666610837	0.3174
–	327.879272461	-1.659472346	0.3180
–	327.861755371	-1.685506344	0.3085
–	327.890319824	-1.658632517	0.3089
–	327.880676270	-1.674308896	0.3141
–	327.898162842	-1.660451889	0.3140
–	327.897888184	-1.664230943	0.3205
–	327.896362305	-1.671369314	0.3117
–	327.876464844	-1.706921101	0.3096
–	327.903076172	-1.680327058	0.3148
–	327.801361084	-1.621610761	0.3162
–	327.799530029	-1.649464130	0.3151
–	327.842498779	-1.608594656	0.3107
–	327.821380615	-1.644285917	0.3205
–	327.849090576	-1.623151183	0.3113
–	327.863372803	-1.622451425	0.3153
–	327.847839355	-1.647925258	0.3105
–	327.854278564	-1.643306375	0.3226
–	327.856445312	-1.665771008	0.3175
–	327.865417480	-1.661991954	0.3153

Continued on next page

Table D.1 – *Continued from previous page*

Cluster	R.A. (°)	Dec. (°)	z z
–	327.880950928	-1.649814725	0.3182
–	327.854614258	-1.684806466	0.3191
–	327.893280029	-1.647015214	0.3034
–	327.899291992	-1.644775629	0.3209
–	327.878997803	-1.681307197	0.3234
–	327.890899658	-1.680467248	0.3151
RCS2J2313-0104	–	–	–
–	348.42761230	-1.08599174	0.5279
–	348.43960571	-1.06919730	0.5308
–	348.46499634	-1.08018339	0.5273
–	348.48318481	-1.08760285	0.5260
–	348.49398804	-1.08899999	0.5257
–	348.50064087	-1.08284175	0.5289
–	348.50390625	-1.12917221	0.5334
–	348.42761230	-1.08599174	0.5282
–	348.46499634	-1.08018339	0.5262
–	348.48318481	-1.08760285	0.5260
–	348.48992920	-1.07479453	0.5344
–	348.51553345	-1.10383618	0.5216
RCS2J2329-0120	–	–	–
–	352.47549438	-1.33600008	0.5226
–	352.43594360	-1.35132778	0.5288
–	352.43325806	-1.34768891	0.5264
–	352.41577148	-1.34096944	0.5294
–	352.41192627	-1.34992778	0.5283
–	352.40280151	-1.34733617	0.5275
RCS2J2329-1317	–	–	–
–	352.23699951	-13.25346756	0.3866
–	352.30560303	-13.24619484	0.4006
–	352.29711914	-13.25739288	0.3871
–	352.30242920	-13.25907230	0.3866
–	352.28375244	-13.26593113	0.3931
–	352.27929688	-13.27628803	0.3903
–	352.28820801	-13.27740765	0.3902

Continued on next page

Table D.1 – *Continued from previous page*

Cluster	R.A. (°)	Dec. (°)	z z
–	352.30343628	-13.27796745	0.3862
–	352.30432129	-13.28118610	0.3954
–	352.28433228	-13.29014397	0.3919
–	352.28762817	-13.29140377	0.3900
–	352.28805542	-13.30316067	0.3953
–	352.25195312	-13.31778526	0.3915
–	352.27279663	-13.31596661	0.3937
–	352.29138184	-13.31624794	0.3895
–	352.29956055	-13.31778717	0.3895
–	352.30072021	-13.32086563	0.3794
–	352.29336548	-13.32436562	0.3906
–	352.28359985	-13.32884407	0.3904
–	352.28286743	-13.34382057	0.3909
–	352.33868408	-13.33975697	0.3836
–	352.33639526	-13.34339619	0.3990
–	352.24118042	-13.24934006	0.3870
–	352.32241821	-13.23996544	0.3902
–	352.29711914	-13.25732327	0.3886
–	352.31567383	-13.25536156	0.4003
–	352.27984619	-13.26642036	0.3870
–	352.30343628	-13.26404095	0.3868
–	352.28604126	-13.27565765	0.3915
–	352.29193115	-13.27957726	0.3965
–	352.28433228	-13.28335571	0.3964
–	352.28604126	-13.28783512	0.3980
–	352.29638672	-13.28923512	0.3861
–	352.29638672	-13.28923512	0.3835
–	352.28344727	-13.30477142	0.3914
–	352.28619385	-13.31274891	0.3932
–	352.30978394	-13.31484699	0.3917
–	352.30502319	-13.31792736	0.4009
–	352.28820801	-13.32520485	0.3890
–	352.29553223	-13.33094406	0.3890
–	352.28836060	-13.34284115	0.3912

Continued on next page

Table D.1 – *Continued from previous page*

Cluster	R.A. (°)	Dec. (°)	z z
–	352.29956055	-13.34871864	0.3979
–	352.24676514	-13.28339481	0.3898
–	352.25711060	-13.26996040	0.4014
–	352.25927734	-13.29025459	0.4004
–	352.26803589	-13.29319477	0.4009
–	352.27996826	-13.27639961	0.3907
–	352.30642700	-13.29347610	0.3910
–	352.30889893	-13.29655457	0.3946
–	352.31204224	-13.29725456	0.3945
–	352.32141113	-13.31138992	0.3948
–	352.24734497	-13.24854374	0.3891
–	352.23394775	-13.30550671	0.3982
–	352.26086426	-13.28241730	0.3883
–	352.28240967	-13.27779961	0.3966
–	352.29119873	-13.27752018	0.3942
–	352.30355835	-13.28962708	0.3853
–	352.30615234	-13.29956532	0.3866
–	352.30111694	-13.31286144	0.3901
–	352.31204224	-13.30362320	0.3914
–	352.30529785	-13.32741833	0.3874
–	352.32067871	-13.30796146	0.3916
–	352.33578491	-13.29312325	0.3883
–	352.31649780	-13.35667038	0.4037
RCS2J2336-0608	–	–	–
–	354.036224365	-6.103911877	0.3989
–	354.053375244	-6.117769718	0.3923
–	354.080139160	-6.105874062	0.3986
–	354.055938721	-6.126167774	0.3973
–	354.083648682	-6.114971638	0.4010
–	354.089019775	-6.115391731	0.3962
–	354.088745117	-6.123649597	0.3991
–	354.077880859	-6.135966301	0.3917
–	354.091552734	-6.130507946	0.3884
–	354.083099365	-6.139465809	0.3928

Continued on next page

Table D.1 – *Continued from previous page*

Cluster	R.A. (°)	Dec. (°)	z z
–	354.093383789	-6.142125130	0.3971
–	354.107299805	-6.141984463	0.3968
–	354.087036133	-6.156821251	0.3896
–	354.093383789	-6.157101154	0.3911
–	354.098999023	-6.155981541	0.3927
–	354.112670898	-6.152901649	0.3955
–	354.111938477	-6.157660484	0.4014
–	354.095336914	-6.170398235	0.3944
–	354.083526611	-6.184254646	0.3909
–	354.079986572	-6.190972805	0.3875
–	354.089019775	-6.188033581	0.3882
–	354.136871338	-6.168996334	0.3909
–	354.042755127	-6.109091282	0.3923
–	354.082611084	-6.089918137	0.3904
–	354.062194824	-6.111752033	0.3864
–	354.096405029	-6.100135326	0.3867
–	354.096405029	-6.100135326	0.3858
–	354.079071045	-6.119170666	0.3911
–	354.084564209	-6.119730473	0.4020
–	354.113159180	-6.118750095	0.3893
–	354.093383789	-6.142125130	0.3971
–	354.093444824	-6.142264843	0.3844
–	354.095397949	-6.152902126	0.3885
–	354.092742920	-6.162419796	0.3927
–	354.133148193	-6.161858082	0.3906
–	354.134399414	-6.171935558	0.3907

Bibliography

(1994). Book Review: Principles of physical cosmology / Princeton U Press, 1993. *Sky and Telescope*, 87:58.

Abdelsalam, H. M., Saha, P., and Williams, L. L. R. (1998). Non-parametric reconstruction of cluster mass distribution from strong lensing - Modelling Abell 370. *Monthly Notices of the Royal Astronomical Society*, 294:734–+.

Abell, G. O. (1958). The Distribution of Rich Clusters of Galaxies. *The Astrophysical Journal Supplement Series*, 3:211–+.

Abell, G. O., Corwin, Jr., H. G., and Olowin, R. P. (1989). A catalog of rich clusters of galaxies. *The Astrophysical Journal Supplement Series*, 70:1–138.

Allen, S. W. (2002). Cosmological constraints from Chandra observations of galaxy clusters. *Royal Society of London Philosophical Transactions Series A*, 360:2005.

Anguita, T. (2009). *A combined observational and theoretical study of gravitationally lensed quasars*. PhD thesis, , The Heidelberg University, 141 pages.

Appenzeller, I., Fricke, K., Fürtig, W., Gässler, W., Häfner, R., Harke, R., Hess, H.-J., Hummel, W., Jürgens, P., Kudritzki, R.-P., Mantel, K.-H., Meisl, W., Muschielok, B., Nicklas, H., Rupprecht, G., Seifert, W., Stahl, O., Szeifert, T., and Tarantik, K. (1998). Successful commissioning of FORS1 - the first optical instrument on the VLT. *The Messenger*, 94:1–6.

Balestra, I., Vanzella, E., Rosati, P., Monna, A., Grillo, C., Nonino, M., Mercurio, A., Biviano, A., Bradley, L., Coe, D., et al. (2013). CLASH-VLT: spectroscopic confirmation of a z = 6.11 quintuply lensed galaxy in the Frontier Fields cluster RXC J2248.7-4431. *arXiv:astro-ph*, 559:L9.

Bartelmann, M. (2010). TOPICAL REVIEW Gravitational lensing. *Classical and Quantum Gravity*, 27(23):233001.

Bartelmann, M. and Schneider, P. (2001). Weak gravitational lensing. *Physics Reports*, 340:291–472.

Bayliss, M. B. (2012). Broadband Photometry of 105 Giant Arcs: Redshift Constraints and Implications for Giant Arc Statistics. *The Astrophysical Journal*, 744:156.

Bayliss, M. B., Hennawi, J. F., Gladders, M. D., Koester, B. P., Sharon, K., Dahle, H., and Oguri, M. (2011). Gemini/GMOS Spectroscopy of 26 Strong-lensing-selected Galaxy Cluster Cores. *The Astrophysical Journal Supplement Series*, 193:8.

Beers, T. C., Flynn, K., and Gebhardt, K. (1990). Measures of location and scale for velocities in clusters of galaxies - A robust approach. *The Astronomical Journal*, 100:32–46.

Benítez, N. (2000). Bayesian Photometric Redshift Estimation. *The Astrophysical Journal*, 536:571–583.

Benítez, N. (2000). Bayesian Photometric Redshift Estimation. *The Astrophysical Journal*, 536:571–583.

Benítez, N., Ford, H., Bouwens, R., Menanteau, F., Blakeslee, J., Gronwall, C., Illingworth, G., Meurer, G., Broadhurst, T. J., Clampin, M., et al. (2004). Faint Galaxies in Deep Advanced Camera for Surveys Observations. *The Astrophysical Journal Supplement Series*, 150:1–18.

Bertin, G. and Lombardi, M. (2001). Double Lenses. *The Astrophysical Journal*, 546:47–62.

Bhattacharya, S., Habib, S., Heitmann, K., and Vikhlinin, A. (2013). Dark Matter Halo Profiles of Massive Clusters: Theory versus Observations. *The Astrophysical Journal*, 766:32.

Bradač, M., Erben, T., Schneider, P., Hildebrandt, H., Lombardi, M., Schirmer, M., Miralles, J., Clowe, D., et al. (2005). Strong and weak lensing united. *arXiv:astro-ph*, 437:49–60.

Broadhurst, T., Benítez, N., Coe, D., Sharon, K., Zekser, K., White, R., Ford, H., Bouwens, R., Blakeslee, J., Clampin, M., et al. (2005a). Strong-Lensing Analysis of A1689 from Deep Advanced Camera Images. *The Astrophysical Journal*, 621:53–88.

Broadhurst, T., Takada, M., Umetsu, K., Kong, X., Arimoto, N., Chiba, M., and Futamase, T. (2005b). The Surprisingly Steep Mass Profile of A1689, from a Lensing Analysis of Subaru Images. *The Astrophysical Journal Letters*, 619:L143–L146.

Broadhurst, T., Umetsu, K., Medezinski, E., Oguri, M., and Rephaeli, Y. (2008). Comparison of Cluster Lensing Profiles with ΛCDM Predictions. *The Astrophysical Journal Letters*, 685:L9–L12.

Bryan, G. L. and Norman, M. L. (1998). Statistical Properties of X-Ray Clusters: Analytic and Numerical Comparisons. *The Astrophysical Journal*, 495:80–+.

Bullock, J. S., Kolatt, T. S., Sigad, Y., Somerville, R. S., Kravtsov, A. V., Klypin, A. A., Primack, J. R., and Dekel, A. (2001). Profiles of dark haloes: evolution, scatter and environment. *Monthly Notices of the Royal Astronomical Society*, 321:559–575.

Carlberg, R. G., Yee, H. K. C., Ellingson, E., Morris, S. L., Abraham, R., Gravel, P., Pritchet, C. J., Smecker-Hane, T., Hartwick, F. D. A., Hesser, J. E., Hutchings, J. B., and Oke, J. B. (1997). The Average Mass Profile of Galaxy Clusters. *The Astrophysical Journal Letters*, 485:L13–L16.

Chae, K.-H., Biggs, A. D., Blandford, R. D., Browne, I. W., de Bruyn, A. G., Fassnacht, C. D., Helbig, P., Jackson, N. J., et al. (2002). Constraints on Cosmological Parameters from the Analysis of the Cosmic Lens All Sky Survey Radio-Selected Gravitational Lens Statistics. *Physical Review Letters*, 89(15):151301–+.

Clowe, D. and Schneider, P. (2001). Wide field weak lensing observations of A1689. *arXiv:astro-ph*, 379:384–392.

Coe, D., Benítez, N., Sánchez, S. F., Jee, M., Bouwens, R., and Ford, H. (2006). Galaxies in the Hubble Ultra Deep Field. I. Detection, Multiband Photometry, Photometric Redshifts, and Morphology. *The Astronomical Journal*, 132:926–959.

Coe, D., Fuselier, E., Benítez, N., Broadhurst, T., Frye, B., and Ford, H. (2008). LensPerfect: Gravitational Lens Mass Map Reconstructions Yielding Exact Reproduction of All Multiple Images. *The Astrophysical Journal*, 681:814–830.

Coe, D., Umetsu, K., Zitrin, A., Donahue, M., Medezinski, E., Postman, M., Carrasco, M., Anguita, T., et al. (2012). CLASH: Precise New Constraints on the Mass Profile of Abell 2261. *arXiv*, 1201.1616.

Coe, D., Zitrin, A., Carrasco, M., Shu, X., Zheng, W., Postman, M., et al. (2013). CLASH: Three Strongly Lensed Images of a Candidate z Astronomy & Physics 11 Galaxy. *The Astrophysical Journal*, 762:32.

Comerford, J. M. and Natarajan, P. (2007). The observed concentration-mass relation for galaxy clusters. *Monthly Notices of the Royal Astronomical Society*, 379:190–200.

Dahle, H. (2006). The Cluster Mass Function from Weak Gravitational Lensing. *The Astrophysical Journal*, 653:954–962.

Diego, J. M., Protopapas, P., Sandvik, H. B., and Tegmark, M. (2005). Non-parametric inversion of strong lensing systems. *Monthly Notices of the Royal Astronomical Society*, 360:477–491.

Diemand, J., Moore, B., and Stadel, J. (2004). Velocity and spatial biases in cold dark matter subhalo distributions. *Monthly Notices of the Royal Astronomical Society*, 352:535–546.

Duffy, A. R., Schaye, J., Kay, S. T., and Dalla Vecchia, C. (2008). Dark matter halo concentrations in the Wilkinson Microwave Anisotropy Probe year 5 cosmology. *Monthly Notices of the Royal Astronomical Society*, 390:L64–L68.

Duffy, A. R., Schaye, J., Kay, S. T., Dalla Vecchia, C., Battye, R. A., and Booth, C. M. (2010). Impact of baryon physics on dark matter structures: a detailed simulation study of halo density profiles. *Monthly Notices of the Royal Astronomical Society*, 405:2161–2178.

Ebeling, H., Barrett, E., Donovan, D., Ma, C., Edge, A. C., and van Speybroeck, L. (2007). A Complete Sample of 12 Very X-Ray Luminous Galaxy Clusters at z $>$ 0.5. *The Astrophysical Journal Letters*, 661:L33–L36.

Ebeling, H., Edge, A. C., and Henry, J. P. (2001). MACS: A Quest for the Most Massive Galaxy Clusters in the Universe. *The Astrophysical Journal*, 553:668–676.

Eke, V. R., Cole, S., and Frenk, C. S. (1996). Cluster evolution as a diagnostic for Omega. *Monthly Notices of the Royal Astronomical Society*, 282:263–280.

Eliasdottir, A., Limousin, M., Richard, J., Hjorth, J., Kneib, J.-P., Natarajan, P., Pedersen, K., Jullo, E., and Paraficz, D. (2007). Where is the matter in the Merging Cluster Abell 2218? *ArXiv e-prints*.

Ettori, S., Gastaldello, F., Leccardi, A., Molendi, S., Rossetti, M., Buote, D., and Meneghetti, M. (2010). Mass profiles and c-M_{DM} relation in X-ray luminous galaxy clusters. *arXiv:astro-ph*, 524:A68+.

Evrard, A. E., Bialek, J., Busha, M., White, M., Habib, S., Heitmann, K., Warren, M., Rasia, E., Tormen, G., Moscardini, L., Power, C., Jenkins, A. R., Gao, L., Frenk, C. S., Springel, V., White, S. D. M., and Diemand, J. (2008). Virial Scaling of Massive Dark Matter Halos: Why Clusters Prefer a High Normalization Cosmology. *The Astrophysical Journal*, 672:122–137.

Fadda, D., Girardi, M., Giuricin, G., Mardirossian, F., and Mezzetti, M. (1996). The Observational Distribution of Internal Velocity Dispersions in Nearby Galaxy Clusters. *The Astrophysical Journal*, 473:670.

Falco, M. (2013). *Dynamics of Galaxy Clusters and their Outskirts: beyond the virialization regime*. PhD thesis, , The University of Copenhagen, 105 pages.

Fioc, M. and Rocca-Volmerange, B. (1997). PEGASE: a UV to NIR spectral evolution model of galaxies. Application to the calibration of bright galaxy counts. *arXiv:astro-ph*, 326:950–962.

Ford, H. C., Clampin, M., Hartig, G. F., Illingworth, G. D., Sirianni, M., Martel, A. R., Meurer, G. R., McCann, W. J., et al. (2003). Overview of the Advanced Camera for Surveys on-orbit performance. In J. C. Blades & O. H. W. Siegmund, editor, *Society of Photo-Optical Instrumentation Engineers (SPIE) Conference Series*, volume 4854, pages 81–94.

Frieman, J. and Dark Energy Survey Collaboration (2013). The Dark Energy Survey: Overview. In *American Astronomical Society Meeting Abstracts*, volume 221 of *American Astronomical Society Meeting Abstracts*, page 335.01.

Gilbank, D. G., Gladders, M. D., Yee, H. K. C., and Hsieh, B. C. (2011). The Red-sequence Cluster Survey-2 (RCS-2): Survey Details and Photometric Catalog Construction. *The Astronomical Journal*, 141:94.

Giocoli, C., Meneghetti, M., Bartelmann, M., Moscardini, L., and Boldrin, M. (2012). MOKA: a new tool for strong lensing studies. *Monthly Notices of the Royal Astronomical Society*, 421:3343–3355.

Gladders, M. D. and Yee, H. K. C. (2000). A New Method For Galaxy Cluster Detection. I. The Algorithm. *The Astronomical Journal*, 120:2148–2162.

Gladders, M. D. and Yee, H. K. C. (2005). Red-Sequence Cluster Survey (Gladders+, 2005). *VizieR Online Data Catalog*, 215:70001.

Golse, G. and Kneib, J.-P. (2002). Pseudo elliptical lensing mass model: Application to the NFW mass distribution. *arXiv:astro-ph*, 390:821–827.

Heisler, J., Tremaine, S., and Bahcall, J. N. (1985). Estimating the masses of galaxy groups - Alternatives to the virial theorem. *The Astrophysical Journal*, 298:8–17.

Hennawi, J. F., Dalal, N., Bode, P., and Ostriker, J. P. (2007). Characterizing the Cluster Lens Population. *The Astrophysical Journal*, 654:714–730.

Hennawi, J. F., Gladders, M. D., Oguri, M., Dalal, N., Koester, B., Natarajan, P., Strauss, M. A., Inada, N., Kayo, I., Lin, H., Lampeitl, H., Annis, J., Bahcall, N. A., and Schneider, D. P. (2008). A New Survey for Giant Arcs. *The Astronomical Journal*, 135:664–681.

Hoekstra, H., Franx, M., Kuijken, K., and Squires, G. (1998). Weak Lensing Analysis of CL 1358+62 Using Hubble Space Telescope Observations. *The Astrophysical Journal*, 504:636–+.

Hoekstra, H. and Jain, B. (2008). Weak Gravitational Lensing and Its Cosmological Applications. *Annual Review of Nuclear and Particle Science*, 58:99–123.

Hogg, D. W. (1999). Distance measures in cosmology. *ArXiv Astrophysics e-prints*, astro-ph/9905116.

Horne, K. (1986). An optimal extraction algorithm for CCD spectroscopy. *Publications of the Astronomical Society of the Pacific*, 98:609–617.

Host, O. (2012). Galaxy cluster strong lensing: image deflections from density fluctuations along the line of sight. *Monthly Notices of the Royal Astronomical Society*, 420:L18–L22.

Hubble, E. (1929). A Relation between Distance and Radial Velocity among Extra-Galactic Nebulae. *Contributions from the Mount Wilson Observatory, vol. 3, pp.23-28*, 3:23–28.

Jing, Y. P. (2000). The Density Profile of Equilibrium and Nonequilibrium Dark Matter Halos. *The Astrophysical Journal*, 535:30–36.

Jing, Y. P. and Suto, Y. (2002). Triaxial Modeling of Halo Density Profiles with High-Resolution N-Body Simulations. *The Astrophysical Journal*, 574:538–553.

Jullo, E., Kneib, J.-P., Limousin, M., Elíasdóttir, Á., Marshall, P. J., and Verdugo, T. (2007). A Bayesian approach to strong lensing modelling of galaxy clusters. *New Journal of Physics*, 9:447.

Jullo, E., Natarajan, P., Kneib, J.-P., D'Aloisio, A., Limousin, M., Richard, J., and Schimd, C. (2010). Cosmological Constraints from Strong Gravitational Lensing in Clusters of Galaxies. *Science*, 329:924–927.

Kaiser, N. (1995). Nonlinear cluster lens reconstruction. *The Astrophysical Journal Letters*, 439:L1–L3.

Kassiola, A. and Kovner, I. (1993). Elliptic Mass Distributions versus Elliptic Potentials in Gravitational Lenses. *The Astrophysical Journal*, 417:450.

Keeton, C. R. (2001). Computational Methods for Gravitational Lensing. *ArXiv Astrophysics e-prints*, arXiv:astro-ph/0102340.

Kellogg, E., Gursky, H., Leong, C., Schreier, E., Tananbaum, H., and Giacconi, R. (1971). X-Ray Observations of the Virgo Cluster, NGC 5128, and 3c 273 from the UHURU Satellite. *The Astrophysical Journal Letters*, 165:L49.

Kepner, J., Fan, X., Bahcall, N., Gunn, J., Lupton, R., and Xu, G. (1999). An Automated Cluster Finder: The Adaptive Matched Filter. *The Astrophysical Journal*, 517:78–91.

Kimble, R. A., MacKenty, J. W., O'Connell, R. W., and Townsend, J. A. (2008). Wide Field Camera 3: a powerful new imager for the Hubble Space Telescope. In *Society of Photo-Optical Instrumentation Engineers (SPIE) Conference Series*, volume 7010 of *Society of Photo-Optical Instrumentation Engineers (SPIE) Conference Series*.

King, L. J., Clowe, D. I., and Schneider, P. (2002). Parameterised models for the lensing cluster Abell 1689. *arXiv:astro-ph*, 383:118–124.

Kneib, J.-P. (1993). *Multiple Arcs and arclets as a diagnostic of the mass distribution in clusters of galaxies*. PhD thesis, Ph. D. thesis, Université Paul Sabatier, Toulouse, (1993).

Kneib, J.-P., Ellis, R. S., Smail, I., Couch, W. J., and Sharples, R. M. (1996). Hubble Space Telescope Observations of the Lensing Cluster Abell 2218. *The Astrophysical Journal*, 471:643–+.

Kneib, J.-P. and Natarajan, P. (2011). Cluster lenses. *Astronomy and Astrophysics Reviews*, 19:47.

Knop, R. A., Aldering, G., Amanullah, R., Astier, P., Blanc, G., Burns, M. S., Conley, A., Deustua, S. E., et al. (2003). New Constraints on Ω_M, Ω_Λ, and w from an Independent Set of 11 High-Redshift Supernovae Observed with the Hubble Space Telescope. *The Astrophysical Journal*, 598:102–137.

Kochanek, C. S. (1991). Systematic effects in lens inversions - Aleph(1) exact models for 0957 + 561. *The Astrophysical Journal*, 382:58–70.

Kochanek, C. S. (1996). Is There a Cosmological Constant? *The Astrophysical Journal*, 466:638.

Koopmans, L. V. E. (2005). Gravitational imaging of cold dark matter substructures. *Monthly Notices of the Royal Astronomical Society*, 363:1136–1144.

Kurtz, M. J. and Mink, D. J. (1998). RVSAO 2.0: Digital Redshifts and Radial Velocities. *Publications of the Astronomical Society of the Pacific*, 110:934–977.

Limousin, M., Kneib, J.-P., and Natarajan, P. (2005). Constraining the mass distribution of galaxies using galaxy-galaxy lensing in clusters and in the field. *Monthly Notices of the Royal Astronomical Society*, 356:309–322.

Limousin, M., Richard, J., Jullo, E., Kneib, J.-P., Fort, B., Soucail, G., Elíasdóttir, Á., Natarajan, P., et al. (2007). Combining Strong and Weak Gravitational Lensing in Abell 1689. *The Astrophysical Journal*, 668:643–666.

Macciò, A. V., Dutton, A. A., and van den Bosch, F. C. (2008). Concentration, spin and shape of dark matter haloes as a function of the cosmological model: WMAP1, WMAP3 and WMAP5 results. *Monthly Notices of the Royal Astronomical Society*, 391:1940–1954.

McCarthy, I. G., Schaye, J., Ponman, T. J., Bower, R. G., Booth, C. M., Dalla Vecchia, C., Crain, R. A., Springel, V., et al. (2010). The case for AGN feedback in galaxy groups. *Monthly Notices of the Royal Astronomical Society*, 406:822–839.

Mead, J. M. G., King, L. J., Sijacki, D., Leonard, A., Puchwein, E., and McCarthy, I. G. (2010). The impact of AGN feedback and baryonic cooling on galaxy clusters as gravitational lenses. *Monthly Notices of the Royal Astronomical Society*, 406:434–444.

Meneghetti, M., Bartelmann, M., and Moscardini, L. (2003). Cluster cross-sections for strong lensing: analytic and numerical lens models. *Monthly Notices of the Royal Astronomical Society*, 340:105–114.

Meneghetti, M., Fedeli, C., Pace, F., Gottlöber, S., and Yepes, G. (2010). Strong lensing in the MARENOSTRUM UNIVERSE. I. Biases in the cluster lens population. *arXiv:astro-ph*, 519:A90+.

Meneghetti, M., Fedeli, C., Zitrin, A., Bartelmann, M., Broadhurst, T., Gottlöber, S., Moscardini, L., and Yepes, G. (2011). Comparison of an X-ray-selected sample of massive lensing clusters with the MareNostrum Universe ΛCDM simulation. *arXiv:astro-ph*, 530:A17+.

Meneghetti, M., Rasia, E., Vega, J., Merten, J., Postman, M., Yepes, G., Sembolini, F., Donahue, M., Ettori, S., Umetsu, K., et al. (2014). The MUSIC of CLASH: predictions on the concentration-mass relation. *ArXiv e-prints*.

Merten, J., Cacciato, M., Meneghetti, M., Mignone, C., and Bartelmann, M. (2009). Combining weak and strong cluster lensing: applications to simulations and MS 2137. *arXiv:astro-ph*, 500:681–691.

Merten, J., Meneghetti, M., Postman, M., Umetsu, K., Zitrin, A., Medezinski, E., et al. (2014). CLASH: The Concentration-Mass Relation of Galaxy Clusters. *ArXiv e-prints*.

Mitchell, R. J., Ives, J. C., and Culhane, J. L. (1976). The Relation Between Temperature and X-ray Luminosity for Clusters of Galaxies. In *Bulletin of the American Astronomical Society*, volume 8 of *Bulletin of the American Astronomical Society*, page 553.

Narayan, R. and Bartelmann, M. (1996). Lectures on Gravitational Lensing. *ArXiv Astrophysics e-prints*.

Natarajan, P., Kneib, J., Smail, I., and Ellis, R. S. (1998). The Mass-to-Light Ratio of Early-Type Galaxies: Constraints from Gravitational Lensing in the Rich Cluster AC 114. *The Astrophysical Journal*, 499:600–+.

Natarajan, P., Kneib, J., Smail, I., Treu, T., Ellis, R., Moran, S., Limousin, M., and Czoske, O. (2009). The Survival of Dark Matter Halos in the Cluster Cl 0024+16. *The Astrophysical Journal*, 693:970–983.

Navarro, J. F., Frenk, C. S., and White, S. D. M. (1996). The Structure of Cold Dark Matter Halos. *The Astrophysical Journal*, 462:563–+.

Navarro, J. F., Frenk, C. S., and White, S. D. M. (1997). A Universal Density Profile from Hierarchical Clustering. *The Astrophysical Journal*, 490:493–+.

Neto, A. F., Gao, L., Bett, P., Cole, S., Navarro, J. F., Frenk, C. S., White, S. D. M., Springel, V., et al. (2007). The statistics of Λ CDM halo concentrations. *Monthly Notices of the Royal Astronomical Society*, 381:1450–1462.

Oguri, M. (2004). *Strong Gravitational Lenses in a Cold Dark Matter Universe*. PhD thesis, , The University of Tokyo, 174 pages.

Oguri, M. (2010). glafic: Software Package for Analyzing Gravitational Lensing. Astrophysics Source Code Library.

Oguri, M., Bayliss, M. B., Dahle, H., Sharon, K., Gladders, M. D., Natarajan, P., Hennawi, J. F., and Koester, B. P. (2012). Combined strong and weak lensing analysis of 28 clusters from the Sloan Giant Arcs Survey. *Monthly Notices of the Royal Astronomical Society*, 420:3213–3239.

Oguri, M. and Blandford, R. D. (2009). What is the largest Einstein radius in the universe? *Monthly Notices of the Royal Astronomical Society*, 392:930–944.

Oguri, M., Hennawi, J. F., Gladders, M. D., Dahle, H., Natarajan, P., Dalal, N., Koester, B. P., Sharon, K., et al. (2009). Subaru Weak Lensing Measurements of Four Strong Lensing Clusters: Are Lensing Clusters Overconcentrated? *The Astrophysical Journal*, 699:1038–1052.

Okabe, N., Takada, M., Umetsu, K., Futamase, T., and Smith, G. P. (2010a). LoCuSS: Subaru Weak Lensing Study of 30 Galaxy Clusters. *Publications of the Astronomical Society of Japan*, 62:811–.

Okabe, N., Zhang, Y., Finoguenov, A., Takada, M., Smith, G. P., Umetsu, K., and Futamase, T. (2010b). LoCuSS: Calibrating Mass-observable Scaling Relations for Cluster Cosmology with Subaru Weak-lensing Observations. *The Astrophysical Journal*, 721:875–885.

Ostriker, J. P. and Peebles, P. J. E. (1973). A Numerical Study of the Stability of Flattened Galaxies: or, can Cold Galaxies Survive? *The Astrophysical Journal*, 186:467–480.

Planck Collaboration, Ade, P. A. R., Aghanim, N., Armitage-Caplan, C., Arnaud, M., Ashdown, M., Atrio-Barandela, F., Aumont, J., Baccigalupi, C., Banday, A. J., and et al. (2013). Planck 2013 results. XVI. Cosmological parameters. *ArXiv e-prints*.

Planck Collaboration, Aghanim, N., Arnaud, M., Ashdown, M., Aumont, J., Baccigalupi, C., Balbi, A., Banday, A. J., Barreiro, R. B., Bartelmann, M., and et al. (2011). Planck early results. XII. Cluster Sunyaev-Zeldovich optical scaling relations. *arXiv:astro-ph*, 536:A12.

Postman, M., Coe, D., Benítez, N., Bradley, L., Broadhurst, T., et al. (2012). The Cluster Lensing and Supernova Survey with Hubble: An Overview. *The Astrophysical Journal Supplement Series*, 199:25.

Postman, M., Lubin, L. M., Gunn, J. E., Oke, J. B., Hoessel, J. G., Schneider, D. P., and Christensen, J. A. (1996). The Palomar Distant Clusters Survey. I. The Cluster Catalog. *The Astronomical Journal*, 111:615.

Reed, D. S., Koushiappas, S. M., and Gao, L. (2011). Non-universality of halo profiles and implications for dark matter experiments. *Monthly Notices of the Royal Astronomical Society*, 415:3177–3188.

Riess, A. G., Strolger, L.-G., Tonry, J., Casertano, S., Ferguson, H. C., Mobasher, B., Challis, P., Filippenko, A. V., et al. (2004). Type Ia Supernova Discoveries at z $>$ 1 from the Hubble Space Telescope: Evidence for Past Deceleration and Constraints on Dark Energy Evolution. *The Astrophysical Journal*, 607:665–687.

Rubin, V. C., Burstein, D., Ford, Jr., W. K., and Thonnard, N. (1985). Rotation velocities of 16 SA galaxies and a comparison of Sa, Sb, and SC rotation properties. *The Astrophysical Journal*, 289:81–98.

Rubin, V. C. and Ford, W. K. J. (1970). Rotation of the Andromeda Nebula from a Spectroscopic Survey of Emission Regions. *The Astrophysical Journal*, 159:379–+.

Rudd, D. H. and Nagai, D. (2009). Nonequilibrium Electrons and the Sunyaev-Zel'Dovich Effect of Galaxy Clusters. *The Astrophysical Journal Letters*, 701:L16–L19.

Saha, P. and Williams, L. L. R. (1997). Non-parametric reconstruction of the galaxy lens in PG 1115+080. *Monthly Notices of the Royal Astronomical Society*, 292:148–+.

Saha, P. and Williams, L. L. R. (2004). A Portable Modeler of Lensed Quasars. *The Astronomical Journal*, 127:2604–2616.

Sand, D. J., Treu, T., Smith, G. P., and Ellis, R. S. (2004). The Dark Matter Distribution in the Central Regions of Galaxy Clusters: Implications for Cold Dark Matter. *The Astrophysical Journal*, 604:88–107.

Schechter, P. (1976). An analytic expression for the luminosity function for galaxies. *The Astrophysical Journal*, 203:297–306.

Schneider, P., Ehlers, J., and Falco, E. E. (1992). Gravitational Lenses.

Seidel, G. and Bartelmann, M. (2007). Arcfinder: an algorithm for the automatic detection of gravitational arcs. *arXiv:astro-ph*, 472:341–352.

Serlemitsos, P. J., Smith, B. W., Boldt, E. A., Holt, S. S., and Swank, J. H. (1977). X-radiation from clusters of galaxies - Spectral evidence for a hot evolved gas. *The Astrophysical Journal Letters*, 211:L63–L66.

Sharon, K., Gladders, M. D., Rigby, J. R., Wuyts, E., Koester, B. P., Bayliss, M. B., and Barrientos, L. F. (2012). Source-plane Reconstruction of the Bright Lensed Galaxy RCSGA 032727-132609. *The Astrophysical Journal*, 746:161.

Sifón, C., Menanteau, F., Hasselfield, M., Marriage, T. A., Hughes, J. P., Barrientos, L. F., et al. (2013). The Atacama Cosmology Telescope: Dynamical Masses and Scaling Relations for a Sample of Massive Sunyaev-Zel'dovich Effect Selected Galaxy Clusters. *The Astrophysical Journal*, 772:25.

Sifón, C., Menanteau, F., Hughes, J. P., Carrasco, M., and Barrientos, L. F. (2014). Strong lensing analysis of PLCK G004.5-19.5, a Planck-discovered cluster hosting a radio relic at z = 0.52. *arXiv:astro-ph*, 562:A43.

Spergel, D. N., Bean, R., Doré, O., Nolta, M. R., Bennett, C. L., Dunkley, J., Hinshaw, G., Jarosik, N., et al. (2007). Three-Year Wilkinson Microwave Anisotropy Probe (WMAP) Observations: Implications for Cosmology. *The Astrophysical Journal Supplement Series*, 170:377–408.

Spergel, D. N., Verde, L., Peiris, H. V., Komatsu, E., Nolta, M. R., Bennett, C. L., Halpern, M., Hinshaw, G., et al. (2003). First-Year Wilkinson Microwave Anisotropy Probe (WMAP) Observations: Determination of Cosmological Parameters. *The Astrophysical Journal Supplement Series*, 148:175–194.

Squires, G., Kaiser, N., Fahlman, G., Babul, A., and Woods, D. (1996). A Weak Gravitational Lensing Analysis of Abell 2390. *The Astrophysical Journal*, 469:73.

Suyu, S. H., Marshall, P. J., Hobson, M. P., and Blandford, R. D. (2006). A Bayesian analysis of regularized source inversions in gravitational lensing. *Monthly Notices of the Royal Astronomical Society*, 371:983–998.

Tegmark, M., Blanton, M. R., Strauss, M. A., Hoyle, F., Schlegel, D., Scoccimarro, R., Vogeley, M. S., Weinberg, D. H., et al. (2004). The Three-Dimensional Power Spectrum of Galaxies from the Sloan Digital Sky Survey. *The Astrophysical Journal*, 606:702–740.

Trotter, C. S., Winn, J. N., and Hewitt, J. N. (2000). A Multipole-Taylor Expansion for the Potential of the Gravitational Lens MG J0414+0534. *The Astrophysical Journal*, 535:671–691.

Umetsu, K. and Broadhurst, T. (2008a). Combining Lens Distortion and Depletion to Map the Mass Distribution of A1689. *The Astrophysical Journal*, 684:177–203.

Umetsu, K. and Broadhurst, T. (2008b). Combining Lens Distortion and Depletion to Map the Mass Distribution of A1689. *The Astrophysical Journal*, 684:177–203.

Umetsu, K., Broadhurst, T., Zitrin, A., Medezinski, E., Coe, D., and Postman, M. (2011). A Precise Cluster Mass Profile Averaged from the Highest-quality Lensing Data. *The Astrophysical Journal*, 738:41.

Umetsu, K., Medezinski, E., Broadhurst, T., Zitrin, A., Okabe, N., Hsieh, B., and Molnar, S. M. (2010). The Mass Structure of the Galaxy Cluster Cl0024+1654 from a Full Lensing Analysis of Joint Subaru and ACS/NIC3 Observations. *The Astrophysical Journal*, 714:1470–1496.

Umetsu, K., Medezinski, E., Nonino, M., Merten, J., Zitrin, A., Molino, A., Grillo, C., Carrasco, M., et al. (2012). CLASH: Mass Distribution in and around MACS J1206.2-0847 from a Full Cluster Lensing Analysis. *arXiv*, 1204.3630.

Vanderlinde, K., Crawford, T. M., de Haan, T., Dudley, J. P., Shaw, L., Ade, P. A. R., Aird, K. A., Benson, B. A., et al. (2010). Galaxy Clusters Selected with the Sunyaev-Zel'dovich Effect from 2008 South Pole Telescope Observations. *arXiv*, 1003.0003.

Verdugo, T., Motta, V., Muñoz, R. P., Limousin, M., Cabanac, R., and Richard, J. (2011). Gravitational lensing and dynamics in SL2S J02140-0535: probing the mass out to large radius. *arXiv:astro-ph*, 527:A124.

Wetzel, A. R. and White, M. (2010). What determines satellite galaxy disruption? *Monthly Notices of the Royal Astronomical Society*, 403:1072–1088.

White, M., Cohn, J. D., and Smit, R. (2010). Cluster galaxy dynamics and the effects of large-scale environment. *Monthly Notices of the Royal Astronomical Society*, 408:1818–1834.

White, S. D. M., Navarro, J. F., Evrard, A. E., and Frenk, C. S. (1993). The Baryon Content of Galaxy Clusters - a Challenge to Cosmological Orthodoxy. *Nature*, 366:429–+.

Wuyts, E., Barrientos, L. F., Gladders, M. D., Sharon, K., Bayliss, M. B., Carrasco, M., Gilbank, D., Yee, H. K. C., Koester, B. P., and Muñoz, R. (2010). A Bright, Spatially Extended Lensed Galaxy at z = 1.7 Behind the Cluster RCS2 032727-132623. *The Astrophysical Journal*, 724:1182–1192.

Wuyts, E., Rigby, J. R., Gladders, M. D., and Sharon, K. (2014). A Magnified View of the Kinematics and Morphology of RCSGA 032727-132609: Zooming in on a Merger at z = 1.7. *The Astrophysical Journal*, 781:61.

Wuyts, S., Labbé, I., Schreiber, N. M. F., Franx, M., Rudnick, G., Brammer, G. B., and van Dokkum, P. G. (2008). FIREWORKS U_{38}-to-24 μm Photometry of the GOODS Chandra Deep Field-South: Multiwavelength Catalog and Total Infrared Properties of Distant K_s-selected Galaxies. *The Astrophysical Journal*, 682:985–1003.

Zentner, A. R., Rudd, D. H., and Hu, W. (2008). Self-calibration of tomographic weak lensing for the physics of baryons to constrain dark energy. *Physical Review D*, 77(4):043507.

Zhao, D. H., Jing, Y. P., Mo, H. J., and Börner, G. (2009). Accurate Universal Models for the Mass Accretion Histories and Concentrations of Dark Matter Halos. *The Astrophysical Journal*, 707:354–369.

Zheng, W., Postman, M., Zitrin, A., Moustakas, J., Shu, X., Jouvel, S., Host, O., Molino, A., et al. (2012). A highly magnified candidate for a young galaxy seen when the Universe was 500 Myrs old. *arXiv*, 1204.2305.

Zitrin, A. and Broadhurst, T. (2009). Discovery of the Largest Known Lensed Images Formed by a Critically Convergent Lensing Cluster. *The Astrophysical Journal Letters*, 703:L132–L136.

Zitrin, A., Broadhurst, T., Bartelmann, M., Rephaeli, Y., Oguri, M., Benítez, N., Hao, J., and Umetsu, K. (2011a). The Universal Einstein Radius Distribution from 10,000 SDSS Clusters. *arXiv*, 1105.2295.

Zitrin, A., Broadhurst, T., Bartelmann, M., Rephaeli, Y., Oguri, M., Benítez, N., Hao, J., and Umetsu, K. (2011b). The Universal Einstein Radius Distribution from 10,000 SDSS Clusters. *arXiv*, 1105.2295.

Zitrin, A., Broadhurst, T., Coe, D., Umetsu, K., Postman, M., Benítez, N., Meneghetti, M., et al. (2011c). The Cluster Lensing and Supernova Survey with Hubble (CLASH): Strong-lensing Analysis of A383 from 16-band HST/WFC3/ACS Imaging. *The Astrophysical Journal*, 742:117.

Zitrin, A., Broadhurst, T., Coe, D., Umetsu, K., Postman, M., Benítez, N., Meneghetti, M., Medezinski, E., et al. (2011d). The Cluster Lensing and Supernova Survey with Hubble (CLASH): Strong-lensing Analysis of A383 from 16-band HST/WFC3/ACS Imaging. *The Astrophysical Journal*, 742:117.

Zitrin, A., Broadhurst, T., Rephaeli, Y., and Sadeh, S. (2009a). The Largest Gravitational Lens: MACS J0717.5+3745 (z = 0.546). *The Astrophysical Journal Letters*, 707:L102–L106.

Zitrin, A., Broadhurst, T., Umetsu, K., Coe, D., Benítez, N., Ascaso, B., Bradley, L., Ford, H., et al. (2009b). New multiply-lensed galaxies identified in ACS/NIC3 observations of Cl0024+1654 using an improved mass model. *Monthly Notices of the Royal Astronomical Society*, 396:1985–2002.

Zitrin, A., Broadhurst, T., Umetsu, K., Coe, D., Benítez, N., Ascaso, B., Bradley, L., Ford, H., Jee, J., Medezinski, E., et al. (2009c). New multiply-lensed galaxies identified in ACS/NIC3 observations of Cl0024+1654 using an improved mass model. *Monthly Notices of the Royal Astronomical Society*, 396:1985–2002.

Zitrin, A., Moustakas, J., Bradley, L., Coe, D., et al. (2012a). CLASH: Discovery of a Bright z $\simeq$ 6.2 Dwarf Galaxy Quadruply Lensed by MACS J0329.6-0211. *The Astrophysical Journal Letters*, 747:L9.

Zitrin, A., Moustakas, J., Bradley, L., Coe, D., Moustakas, L. A., Postman, M., Shu, X., Zheng, W., et al. (2012b). CLASH: Discovery of a Bright z $\approx$ 6.2 Dwarf Galaxy Quadruply Lensed by MACS J0329.6-0211. *The Astrophysical Journal Letters*, 747:L9.

Zitrin, A., Rephaeli, Y., Sadeh, S., Medezinski, E., Umetsu, K., Sayers, J., Nonino, M., Morandi, A., et al. (2012c). Cluster-cluster lensing and the case of Abell 383. *Monthly Notices of the Royal Astronomical Society*, 420:1621–1629.

Zitrin, A., Rosati, P., Nonino, M., Grillo, C., Postman, M., Coe, D., Seitz, S., Eichner, T., et al. (2012d). CLASH: New Multiple Images Constraining the Inner Mass Profile of MACS J1206.2–0847. *The Astrophysical Journal*, 749:97.

Zwicky, F. (1933). Die Rotverschiebung von extragalaktischen Nebeln. *Helvetica Physica Acta*, 6:110–127.

List of Figures

List of Tables